DIRECT CURRENT HYBRID
VACUUM BREAKER

THESIS PRESENTED TO

THE DEPARTMENT OF ELECTRONIC & ELECTRICAL ENGINEERING

AND THE COMMITTEE FOR POSTGRADUATE STUDIES

IN FULFILMENT OF THE REQUIREMENTS FOR DEGREE OF

DOCTOR OF PHILOSOPHY

UNIVERSITY OF STRATHCLYDE

By

Yunhai Shan

May 2014

Glasgow, UK

Dedicated to my family

DECLARATION OF AUTHENTICITY AND AUTHOR'S RIGHTS

Acknowledgments

Abstract

Hybrid DC circuit breaker switching techniques have been proposed for use in multi-terminal HVDC networks, to create an efficient, reliable and controllable system. There are two DC hybrid switching techniques. The first is arc interruption based on current oscillation. The second is interruption without an arc, like with a voltage commutation approach. The main difference is whether or not the interruption mechanism deals with the arc. Interrupting the arc not only causes erosion of the electrode surface, therefore reducing useful lifetime, but also introduces uncertainty to the process of successful interruption. This thesis therefore focuses on determination of the best switching technique for HVDC applications.

To highlight the advantages of interruption without an arc, this thesis uses a vacuum circuit breaker (VCB) as the main breaker to investigate arc effects on interruption performance, when employing a forced current commutation method. The vacuum arc characteristics are detailed, thereby giving the VCB operation understanding needed. The VCB opening time is reduced from approximately 50ms to 13ms by employing a coil DC activation method. This allows the coil counter-EMF to be observed and utilised to optimally trigger the auxiliary commutation circuit.

An active commutation test circuit is proposed, and in simulation and experimentally, the VCB interruption properties are investigated in terms of varied interruption current, di/dt, dv_{VCB}/dt, and gap distance. Experimental results elicit that the key parameters determining arc interruption probability is di/dt , where even if dv_{VCB}/dt is low, successful interruption become impossible if di/dt is above a certain level. By analysing the post-arc current based on its electrical behaviour, the reason why di/dt and dv_{VCB}/dt dominate successful interruption probability is explained.

A cascaded commutation circuit is proposed, and its validity is confirmed by simulation and experimentally, showing the interruption probability is improved compared to the test circuit, even with small circuit inductance.

List of symbols

A	Cross section area (mm^2)
A_{EL}	Electrode surface area (mm^2)
A_i	Cross section area of the steel (mm^2)
A_A	Cross section area of the air-gap (mm^2)
B	Magnetic flux density (Wb/m^2)
B_r	Saturation residual field (Wb/m^2)
B_{r0}	Unsaturated residual field (Wb/m^2)
B_i	Residual field through the steel (Wb/m^2)
B_A	Residual field through the air-gap (Wb/m^2)
B_θ	Azimuthal magnetic field (Wb/m^2)
B_s	Saturation flux density (Wb/m^2)
C	Capacitance (F)
C_C	Commutation capacitance (F)
$C_{C1,2,3}$	Cascaded commutation capacitance (F)
C_s	Snubber capacitance (F)
C_{bank}	Capacitor bank (F)
d	The distance between two sets of contacts (mm)
di/dt	Decline rate of current before current-zero (kA/μs)
dv/dt	Rise rate of voltage across the opening contacts immediately after current-zero (kV/μs)
dv_{VCB}/dt	Rise rate of voltage across the VCB immediately after current-zero (kV/μs)
ds/dt	The expanding speed of the sheath (mm/s)
e	The electronic charge (C)
E_{nor}	Energy losses (mJ)
E_{CE}	IGBT conduction energy losses (mJ)

E_D	Diode conduction energy losses (mJ)
E_L	Line resistance energy losses (mJ)
F	Mechanical force (N)
g	Gap distance (mm)
H	Magnetic field strength (A/m)
H_A	Magnetic field strength in the air-gap (A/m)
H_C	Coercive force (A/m)
H_S	Magnetic field strength in the steel during excitation (A/m)
H_i	Magnetic field strength in the steel after excitation (A/m)
i	Current (A)
i_0	Coil output current (A)
$\bar{I}_0$	Mean output current (A)
I_{rms}	RMS current
I_{peak}	Maximum counter-current
$\hat{i}_C$	Maximum cascaded counter-current
i_{SC}	Short-circuit current (kA)
i_B	Current passing through the main breaker (A)
i_C	Counter current (A)
$i_{C1/2/3}$	Cascaded counter current (A)
i_{ce}	Current through IGBT
i_{L_C}	Current through cascaded commutation inductor (A)
i_D	Current through diode
i_T	Current through the solid-state switches
i_{FAULT}	Fault current (A)
i_{line}	Line current (kA)
I_m	Maximum mean coil current (A)
i_{DC}	Source current (A)

i_s	Current through the snubber capacitor (A)
$\check{I}$	Minimum coil current (A)
$\hat{I}$	Maximum coil current (A)
i_{VCB}	Current through the VCB (A)
i_1	Current for charging the commutation capacitor (A)
i_{FW}	Current through the freewheel diode (A)
i_{pc}	Post-arc current after current-zero
J	Current density (A/m^2)
L	Inductance (H)
L_S	Solenoid coil (H)
L_C	Commutation inductance (µH)
L_{LOAD}	Load inductance (mH)
L_M	Magnetising inductance (H)
L_L	Lumped inductance (mH)
L_{LOAD}	Load inductance (mH)
l	Length (mm)
l_{MFP}	Mean free path (µm)
l_{l_1}	Length of steel portion 1 (mm)
l_{d2}	Length of air-gap portion 2 (mm)
l_{l_3}	Length of steel portion 3 (mm)
l_{d4}	Length of air-gap portion 4 (mm)
l_{l_5}	Length of air-gap portion 5 (mm)
l_{l_6}	Length of air-gap portion 6 (mm)
l_A	Air-gap distance (mm)
l'_A	Air-gap distance during VCB closed (mm)
l_i	Total length of steel (mm)
M	Magnetisation (A/m)

M_s	Saturation magnetisation (A/m)
n	The concentration of the electrons or ions (m^{-3})
N	Turns number
R	Anode diameter electrodes (mm)
R_{LOAD}	Load resistor (Ω)
R_{FAULT}	Fault resistor (Ω)
R_L	Solenoid coil load resistor (Ω)
R_S	Solenoid coil resistance (Ω)
R_C	Commutation circuit resistance (mΩ)
$\Re$	Reluctance (H^{-1})
$\Re_A$	Magnetic reluctance in the air-gap (H^{-1})
$\Re_S$	Magnetic reluctance in the steel (H^{-1})
r_c	IGBT on-state resistance (mΩ)
r_D	Diode on-state resistance (mΩ)
s	Sheath thickness (mm)
s_q	The quantity of electrons through the acceleration zone
S	Spacing between turns (mm)
T	Absolute temperature (K)
T_C	A critical temperature in the superconducting element (K)
T_{con}	Temperature of the contact spot (K)
T_0	Original temperature of the electrode (K)
T_e	The electron temperature (K)
$T_{C1/2/3/4/5/6}$	Cascaded time intervals (μs)
t_m	Time to reach maximum fault current (ms)
t_{CZ1}	Time to the first VCB current-zero (μs)
t_{CZ2}	Time to the first VCB current-zero (μs)
t_d	Freewheel diode conduction time (ms)

μ	Permeability (H/m)
μ_r	Relative permeability
μ_0	Permeability of air (H/M)
U_e	The voltage across the electrodes (V)
μ_{eff}	Effective permeability (H/M)
U_{REC}	The transient recovery voltage (kV)
v	Velocity of the electrons or ions (m/s)
v_a	Air-gap volume (mm^3)
v_i	Ion velocity (m/s)
v_0	Coil mean output voltage (V)
v_{rms}	RMS load circuit voltage (V)
v_a	Armature separation speed (m/s)
v_{CE}	IGBT conduction voltage (V)
v_D	Diode conduction voltage (V)
V_{DC}	An idealised DC source (V)
V_{sh}	The sheath voltage (kV)
V_S	Voltage across the solenoid coil (V)
$V_{C_{bank}}$	Voltage across the capacitor bank (V)
V_{VCB}	Voltage across the VCB (V)
V_{C_C}	Voltage across the commutation capacitor (V)
$V_{C_{C1/2/3}}$	Voltage across the cascaded commutation capacitor (V)
W_L	Energy stored in the solenoid coil (J)
w_a	Energy density in the air-gap (J/mm^3)
Z	Surge impedance (Ω)
Z_{mn}	The mean ion charge number
ΔW_{magn}	A change in the system magnetic energy (J)
ΔW_{mech}	A change in the system mechanical energy (J)

Δx	An additional distance (mm)
Δt	Time difference
Δd	Displacement difference
Δi	Difference between the normal and fault current (kA)
β	Damped nature frequency (1/s)
δ	Damping constant (1/s)
ε_0	Permittivity in a vacuum (F/m)
ϕ	The work function (eV)
ϕ_0	The thermionic work function (W)
κ	Boltzmann's constant (joules/K)
θ	Angle ($^\circ$)
τ	Time constant
ω	Angular frequency (rad/s)
Φ	Magnetic flux (Wb)
Φ_i	Magnetic flux through the steel (Wb)
Φ_A	Magnetic flux through the air-gap (Wb)
Λ	Flux linkage (Wb)

List of abbreviations

ABB	Asea Brown Boveri Ltd
AC	Alternating current
AMF	Axial magnetic field
CBs	Circuit breakers
DC	Direct current
EMF	Electromotive force
GTO	Gate turn-off thyristor
GCT	Gate commutated thyristor
HVDC	High voltage direct current
IGBT	Insulated gate bipolar transistor
LC	Inductor-capacitor
MOSFET	Metal oxide semiconductor field effect transistor
MOV	Metal oxide varistor
MFP	mean free path
MMF	Magneto-motive force
PTCR	Positive temperature coefficient resistor
PWM	Pulse width modulation
PI	Proportional plus integral
RMS	Root mean square
SCCL	Superconducting current limiters
SCR	Silicon controlled rectifier or Thyristor
TMF	Transverse magnetic field
T-F	Temperature-field
TRV	Transient recovery voltage
T_1,T_2,T_3,T_4,T_5,T_6	Solid-state switches
VCB	Vacuum circuit breaker
VSC	Voltage source converter

Table of Contents

1 Circuit breaker concepts for high-power DC applications

1.1 Introduction

The first commercial high voltage direct current (HVDC) network in 1954 was rated at 100kV, 20MW and was commissioned between the mainland of Sweden and the Isle of Gotland [1.1]. It utilised a 60 mile submarine cable weighing approximately 1,000 tons. Today, the transmission capacity in HVDC operation has reached 200 GW in total, and the Asea Brown Boveri Ltd. (ABB) has acquired around 90 orders among the 170 projects in world and has installed transmission capacity of approximately 120 GW [1.2].

The major electric power transmission method is still based on three-phase alternating current (AC) that is produced by power stations and transmitted to the consumers by the AC transmission systems. Why has the HVDC system become popular [1.3]? The reasons to select HVDC rather than AC for transmitting power in some cases are numerous and complex, but the most common arguments for choosing HVDC are: firstly, HVDC permits long distant power transmission with low losses, with less environmental pollution, since the transmission line HVDC requirement is much smaller and needs less space than AC at the same power rating; secondly, HVDC realises the possibility of accurately controlling active power by utilising converter stations that convert AC to direct current (DC) and vice-versa, without reactive power conduction and losses hence improves power quality; thirdly, HVDC not only has the capability of limiting short circuit currents but also allows interconnection of asynchronous ac systems; moreover, the investment cost is less. However, the key element to establish multi-terminal HVDC networks in terms of efficiency and reliability as well as controllability, is the realisation of viable HVDC circuit breakers (CBs) [1.4].

The requirements of AC and DC CBs are significantly different, where the main differences are due to the absence of a natural current-zero crossing in DC applications. It is difficult to interrupt large DC currents. Due to lack of large

inductance in DC grids involving voltage source converters, a DC breaker has to interrupt the fault current very quickly to avoid excessive overcurrent and needs to dissipate the stored magnetic energy without producing an excessive high voltage [1.5].

This chapter gives an overview of present electric current limiting and interruption techniques of DC breaker designs. Most technologies are a hybrid circuit topology which comprises a traditional AC interrupter and semiconductor devices, as well as commutation elements involving a series combination of a capacitors and inductors. This hybrid circuit technology involves the traditional AC interrupter component operating (gap opening) with interruption current. Paul G. Slade [1.6] stated that an arc will always form during breaker separation as long as basic conditions are satisfied. Since a vacuum is considered an environment-friendly arc-quenching medium, the vacuum interrupter demands attention in HVDC applications. Thus, the objectives of this thesis are to investigate the interruption performance of the vacuum interrupter.

1.2 Fundamentals on switching in DC-grids

There are three levels in the classification of DC voltages [1.7], namely low voltage and medium voltages as well as high voltage, where the range of low voltage is up to 1200V, and the range of medium voltage is from 1500V to 3000V and possibly up to 15kV, above which is generally classified as high voltage. HVDC is suitable for high power transmission and for the 'back-to-back' stations of AC systems. Medium voltage DC is suitable for electric traction and electric heating devices as well as some drives. Low voltage DC is suitable for most sorts of urban applications and mine electric traction, in various drives and converter systems. Hence the fault parameters vary from situation to situation. The time constant in the HVDC situation is usually large compared to low and medium voltage situations that have a time constants in the range of 5 to 30ms and prospective fault amplitudes in the range of 10 to 150kA [1.8].

Figure 1.1 illustrates an equivalent circuit for a DC system, comprising an ideal DC source, lumped resistance and inductance, with a circuit breaker as well as a fault circuit.
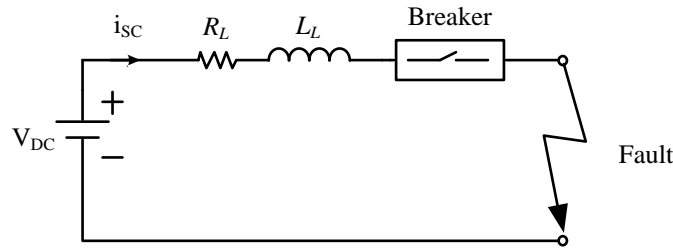
Figure 1.1 Equivalent circuit of a DC grid.

Assuming the voltage drop across the breaker is zero, the fault current is defined by:

$$V_{DC} = R_L \cdot i_{SC} + L_L \cdot \frac{di_{SC}}{dt} \text{ (A)} \tag{1.1}$$

In general, AC grids have large generators and transformers which introduce inductance. Consequently, the time constant is large and the amplitude of the fault current is suppressed. The resulting impedance also restricts the thermal fault current. However, a DC grid involving a voltage source converter (VSC) does not possess this inductance and only R_L limits the fault current. VSC based systems not only have small DC-side inductance but also any dc fault current is aggravated by DC capacitor discharge [1.9, 10]. For instance, if the value of V_{DC} is 30kV and the normal current is 2kA, with lumped resistance R_L=10mΩ, the theoretical maximum fault current will be 3000kA. But if the lumped inductance is $L_L = 1$mH and a turn-off time of 20ms is required, the maximum current will rise to 545.4kA.

Although it is impossible for the fault current to reach to this level due to the limited short circuit power of sources [1.5], it is apparent that fast fault isolation action is needed in DC systems. The main devices in a DC grid system are the converter stations, with the main function to convert AC to direct current (DC) and vice-versa. They can, however, shut down their load current within a few microseconds. However, in advanced systems, shutdown leading to a loss of power in the entire grid at each fault, is unacceptable. Furthermore, in order to ensure the converter station

operates normally, a reasonable level of HVDC voltage is needed post fault isolation. This means a short-circuit fault must be cleared within a few ms [1.11].

A fast switching AC circuit breaker has been possible for the last decade [1.12]. But it has not been commercialised. The reason seems to be the cost and the fact that faster switching is not essential in AC power grids.

1.3 Current limiting techniques

A current limiting device can be considered as a series of elements in the line. During normal operation, it presents low impedance to the load current. When a fault occurs, it presents large impedance to the fault current. The purpose of the current limiting device is not necessarily to finally give zero current, because an auxiliary series interrupter can interrupt near zero currents. A number of current limiting techniques are discussed in the following sub-sections.

1.3.1 Fuses

There is no doubt that the fuse is the most familiar and simplest current limiting device [1.13]. It not only supports a continuous current conduction with low losses but also clears a fault automatically. A current limiting fuse possesses fast action and rapid interruption, where thermal and electrodynamic effects on circuit components are minimised. However, due to fuses having low continuous current ratings, they only apply to low and medium voltage systems.

Self-recovery fuses using sodium had been proposed [1.14], but a viable outcome is uncertain. This is because a fuse arc voltage occurs produced by the stored magnetic energy which causes an increase in the system voltage, which must be suppressed to avoid excessive overvoltage. That is, the fuse arc voltage can raise to twice the line to neutral voltage due to energy considerations and fuse size limitations. A fuse has two obvious disadvantages: first, the continuous current rating cannot reach a high value due to its size; and second, it has to be replaced after each fault.

1.3.2 Positive temperature coefficient resistors (PTCR)

The positive temperature coefficient resistor (PTCR) is a mixture of polymer and metal materials. It is connected into the line in series and carries current continuously. Under normal circumstances, the PTCR presents a stable low resistance. When the current starts to increase and its internal temperature rises, a critical temperature is reached where the polymer resistor has a higher resistance, eventually reaching ten times the normal magnitude. When this occurs the amplitude of current is sharply decreased and a load breaker interrupts the limited current. After the fault has been cleared, the PTCR regains normal low resistance at room temperature. Consequently, the PTCR can be considered as a repetitive current limiter.

Skindhoj [1.15] has analysed these devices in 220V AC systems where a prospective current of 16kA is limited to 3kA. For a high voltage 12kV system, Strumpler [1.16] restrained the prospective currents between 4 to 14kA within approximately 1ms. However, these devices are not generally accepted in terms of economy and reliability, and for DC networks their performance is uncertain.

1.3.3 Superconducting current limiters (SCCL)

Since the operating temperature of superconducting materials is well below room temperature, in order to maintain a superconducting state cooling equipment is mandatory. The fault current forces the superconducting material to enter its resistive state. There are two superconducting current limitation types as shown in Figure 1.2, where figure (a) presents the resistive type where the fault current is transferred to a shunt resistor and thereby is limited, and figure (b) illustrates the inductive type where the superconducting material is connected to the secondary side of coupled coils [1.17-19].
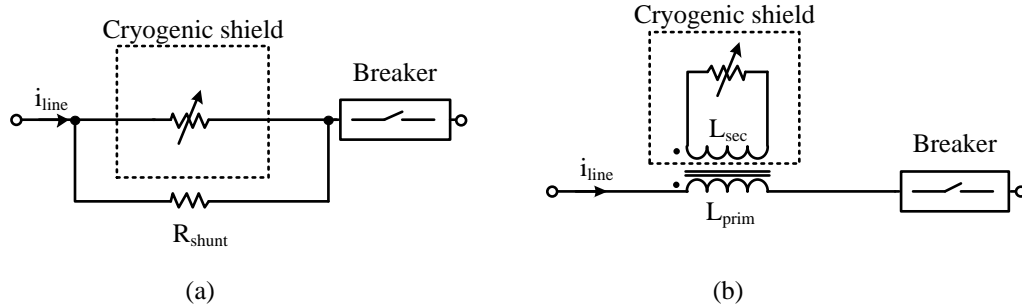
Figure 1.2 Schematic of the superconducting current limitation types: (a) resistive and (b) inductive.

Resistive type

There is a critical temperature T_C in the superconducting element, where the value of T_C is dominated by the superconducting material. Under normal operating conditions, the superconductor has zero resistance, provided its temperature is below T_C. When the fault occurs, the current density exceeds the superconducting limit, the internal temperature of the superconductor exceeds T_C, and the resistance of the superconductor exceeds the shunt resistance. Thus, the fault current is commutated into the parallel path and only a small current remains in the superconducting element. The limited current is finally interrupted by a suitable breaker.

Inductive type

Under normal conditions, coupled coils comprise a conducting primary coil and a superconducting secondary coil which creates a short-circuited transformer. The coupled coils transfer the low impedance secondary into the primary circuit. However, as primary current is increased to a certain level, the secondary current density will reaches a level causing a change in the state of the superconducting material. A resulting high impedance is reflected into the primary side, which limits the fault current. Finally, the breaker interrupts this current. A stack of short-circuit rings composed of superconducting material can be applied to the secondary side [1.20].

The features of these current limiting devices can be concluded as follows: they do not have moving parts; and the energy losses are low, but they need a permanently

cooled device. Economically the superconducting current limiter could be suitable for medium voltage AC networks, but, the coupled inductive type cannot be utilised in DC systems.

1.4 Current interruption methods

Current interruption in DC systems is more difficult than in AC systems due to the absence of a natural current-zero. Since there is no large inductive device in the VSC based DC system, DC breakers have to interrupt the fault current quickly to avoid excessive overcurrent and to dissipate the stored magnetic energy without producing an excessive high voltage.
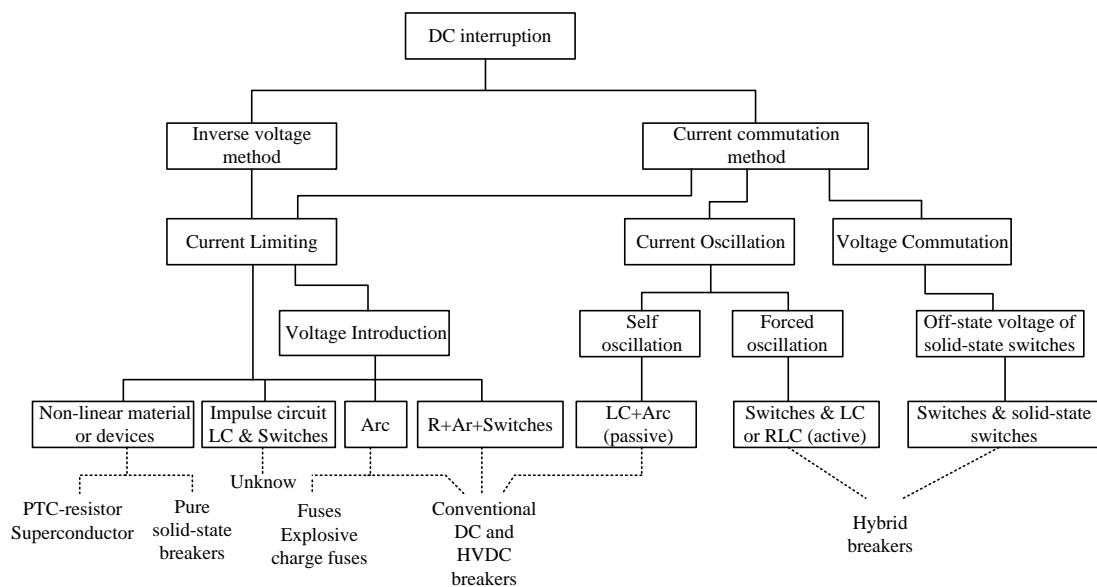
Figure 1.3 Classification of DC interrupting methods; PTC: Positive Temperature Coefficient, R: resistor, RLC and LC: oscillating loops with and without damping.

Numerous proposals for introducing a current-zero have been presented in articles and patent applications [1.21-25]. Based on the literature [1.24], these methods can be divided into two groups as shown in Figure 1.3. The first group can be addressed as the inverse voltage method where the classic AC interrupter creates an arc voltage significantly in excess of the system voltage. The second group can be interpreted as

employing a current commutation method where a virtual current-zero is developed by utilising auxiliary means which include current oscillation and voltage commutation, and where the current oscillation is accomplished by switching parallel commutation circuits to produce a counter-current through the breaker. Voltage commutation means the current commutation is achieved by introducing a voltage which exceeds the on-state voltage of the parallel commutation path.

1.4.1 Conventional direct current breakers

An arc plasma is utilised in classical direct current interruption in order to produce an inverse voltage in excess of the system voltage for the current-zero [1.26]. Under normal conditions, the AC interrupter is closed to support the high continuous currents flow with low power losses. Once a fault is detected the AC interrupter starts to switch (gap separation). An arc plasma is developed causing erosion on the contact surface and is always accompanied by acoustic noise and gasses. Such interrupters have slow reaction. Hence, it is difficult to limit the maximal fault current due to said slow opening and long arcing times. If based on the solution proposed in [1.12], which uses a fast mechanical breaker, although the reaction time is reduced the erosion rate is still high because of the high inverse voltage produced to create the current-zero.

This method can be used in low and medium-voltage applications. There is some suggestion of its use in high-voltage systems, but prototypes have not been transferred to a real application [1.4].

1.4.2 Solid-state circuit breaker

With development of power semiconductors including the power diode, thyristor, GTO-thyristor, IGBT, power MOSFET, and recently the IGCT, these devices have acquired attention in power system applications [1.27-30] since they offer a fast acting arcless mechanism, high reliability, and reduced maintenance. Figure 1.4 illustrates the basic breaker topology, which includes power semiconductors and a voltage suppressor MOV.
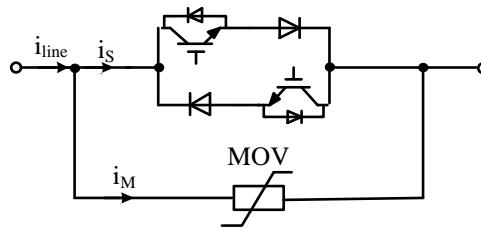
Figure 1.4 Solid-state circuit breaker.

During on-state operation, the power semiconductors are able to conduct continuous currents. Once a fault is detected, the power semiconductors are turned off, resulting in a fast increasing voltage until the voltage suppressor MOV starts to conduct. The MOV clamps the voltage to 1.5 times its nominal value, thereby clamping the grid overvoltage and absorbing the energy stored in the line inductance [1.26].

Since the solid-state solution provides fast operation with switching times of a few μs, the maximum prospective fault current can be avoided. However, it also possesses some disadvantages. The costs are high and the on-state losses are high compared to mechanical breakers. Device cooling is necessary. Additionally, solid-state switches are sensitive to transient overvoltage and overcurrent. Figure 1.5 illustrates an overview of the electrical operating bounds of solid-state devices [1.31]. The IGCT has almost the same rating as the GTO.
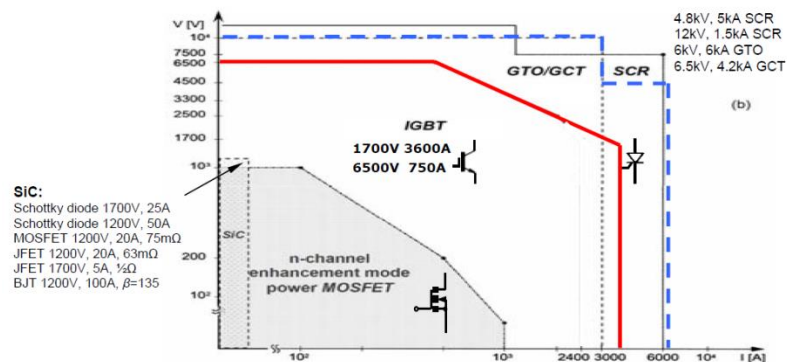
Figure 1.5 Application ranges of power semiconductor devices, where SCR: Silicon Controlled Rectifier or Thyristor; GTO/GCT: Gate Turn-Off thyristor/ Gate Commutated thyristor; IGBT: Insulated Gate Bipolar Transistor; and MOSFET: Metal Oxide Semiconductor Field Effect Transistor; (adapted from[1.31]).

9

In order to interrupt at high powers, a combination of both series and parallel arrangements of the solid-state switches is utilised. However, a new problem arises: how are voltages and currents shared among the switches?

1.4.3 Hybrid solution

As previously described, purely mechanical and solid-state switches possess both specific advantages and disadvantages. In order to effectively utilise the advantages and eliminate the disadvantages, a hybrid circuit breaker has been proposed, based on a fast-acting mechanical switch, as shown in Figure 1.6 [1.5].
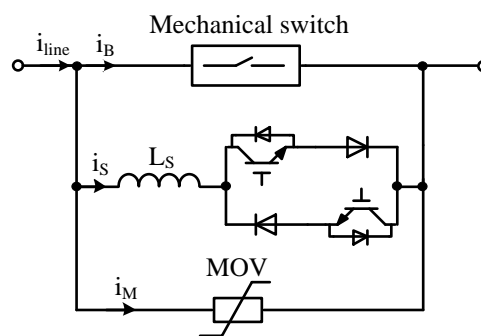
Figure 1.6 Conventional hybrid circuit breaker.

During normal operation, the mechanical switch conducts the current, with low losses. When a fault is monitored, the current is transferred into the solid-state path by the arc voltage produced when the mechanical switch is opened. This means that the mechanical switch requires no other components to extinguish the resulting arc, and contact erosion is minimised. The solid-state switches conduct the current until the mechanical switch gains ability to block the system voltage. At this time, the solid-state switches are turned off, causing an increasing voltage with fast rate until the voltage suppressor MOV clamps. The MOV clamping voltage is 1.5 times the grid voltage thereby clamping the overvoltage and the demagnetising energy stored in the line inductance. The inductance L_S can be the line inductance of the path or a specific element.

The advantage of this method is that the on-state power losses are minimal. A natural current-zero is produced by the arc voltage. The arc voltage must exceed the on-state voltage of solid-state switches, for the current to commutate from the arc to the semiconductor path. For interruption at high power rating, the power rating of the solid-state switches is increased by adding a combination of series and parallel devices, thereby increasing the on-state voltage. Series connection decreases the commutation rate, but the arc voltage could be increased by various means, such as for the vacuum interrupter by using a transverse magnetic field (TMF) [1.32] or for an air interrupter by applying an airblast [1.26]. However, the mass of the mechnism is increased. The mainly disadvantage of this method is that a time is needed for arc recovery and for the contacts to adequately separate after current commutation. This time duration is determined by the type of the mechnical breaker and external electrical conditions.

1.4.4 Hybrid HVDC breaker

Voltage commutation

ABB has proposed a hybrid DC breaker to fulfil HVDC grid requirements [1.11]. This hybrid configuration has negligible on-state power losses and provides current interruption capability within 4ms, at 70kV. Figure 1.7 shows the topology of the hybrid HVDC breaker. There are two branches: one includes a bypass branch that contains a series combination of a semiconductor-based load commutation switch and a fast mechanical disconnector, and the other branch is the main semiconductor-based breaker that comprises several sections with individual arrester banks. Each independent section in the main breaker branch is designed for full voltage and current breaking capability whereas the load commutation switch branch is dimensioned for lower voltage and energy capability. The disconnecting circuit offers dielectric separation of the load after fault clearance thereby protecting the arrester banks of the hybrid HVDC breaker from thermal overload.
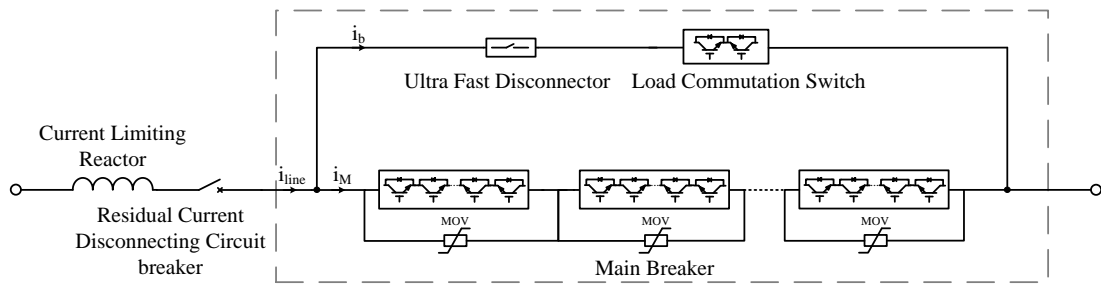
Figure 1.7 Hybrid HVDC breaker.

The fast mechanical switch is opened without experiencing current thereby it can be accomplished by a lightweight contact system. When the mechanical switch reaches the open position the main HVDC breaker interrupts the current. The dielectric separation means the load commutation switch has a low voltage requirement. Proactive control of the hybrid HVDC breaker is utilised to compensate for the time delay of the fast disconnector.

Comparing with the method described in Section 1.4.3, the topologies are the same, in addition to extra solid-state switches in the nominal path. They both have same commutation method, termed voltage commutation, to produce a current-zero in the mechanical breaker. The different is that the former utilises arc voltage the later use the off-state voltage of the solid-state switches to commutate the current. Consequently, assuming interruption at same power rating, the hybrid presents better performance than the former, in terms of commutation rate and cost. Additionally, if the mechanical switch has same opening speed in both topologies, the total interruption time in the later (hybrid) is less because the former needs wait for arc recovery.

Current oscillation

Another method [1.35-38] to produce current-zero in the mechanical switch is termed current oscillation. Figure 1.8 illustrates the basic arrangement of the hybrid HVDC breaker based on this method. In general, this topology comprises two mechanical switches: a main breaker and an isolation switch. The main breaker is parallel connected to commutation and energy absorbing paths.
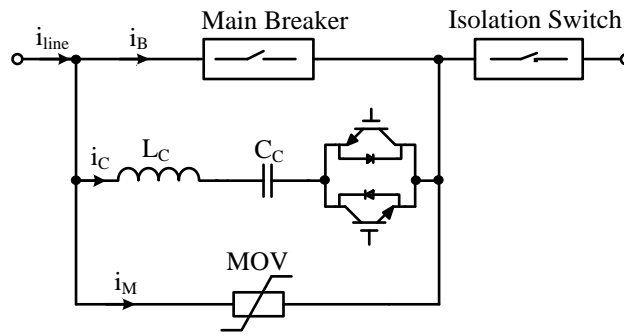
Figure 1.8 Basic arrangement of the hybrid HVDC breaker.

The main breaker supports the continuous current i_B flow; the isolation switch provides dielectric separation of the load after fault clearance thereby avoiding MOV thermal overload while the solid-state switches in the commutation path only conduct during the interruption process. A series combination of a capacitance C_C and inductance L_C is incorporated into the commutation path: thus there will be an oscillating current i_C with a frequency $\omega^2 = 1/L_C C_C$ between the main breaker and commutation path. The line current i_{line} originally flows through the main breaker and is sinusoidally transferred into the commutation path until the amplitude of i_C is increased to same as i_B. At this point, a current-zero arises in the nominal path and the main breaker can interrupt with zero current. As the line current i_{line} continues to flow through the LC commutation circuit, the voltage across the capacitor C_C charges to a voltage within the capability of the grid. At this voltage, the remaining energy stored in the line inductance is dissipated in the energy absorption path (MOV), forcing the line current to decrease.

There are two current commutation modes: namely active commutation if C_C is pre-charged; or passive commutation otherwise. Due to solid-state switches having a fast reaction time, the mechanical drive of the hybrid breakers must be as fast as possible [1.33]. The mass of the mechanism must be increased for interrupting higher current. The Section 4.2.1 gives a detailed description of this current commutation technology. Since the main mechanical part is separated with some current flow, this method also needs to deal with the arc situation. This means the main breakers must

13

have capability to withstand the large transient recovery voltage at the time immediately following the first current-zero.

In term of system voltage rating, the main breaker can be one single unit [1.22] or the series connection of several mechanical interrupters [1.26, 34]. The performance of various classical AC interrupters as a main breaker has been investigated and include an oil breaker [1.4], air-blast breaker [1.26], vacuum interrupter [1.25, 35-38], and an SF_6 gas CB [1.34, 39]. Although the test conditions vary, the experiment results are acceptable. They all concluded that the interruption capability of the interrupter is dominated by two factors: namely the current slope di/dt before the current-zero, and the rate of rise of the transient recovery voltage dv/dt across the mechanical breaker after the current zero. The factor di/dt is based on the oscillation frequency and amplitude which can vary over a large range. The factor dv/dt depends on the voltage of the capacitor C_C. Thus it has been proposed [1.40] that the vacuum interrupter is applicable to HVDC applications since it offers high interruption performance (large di/dt and $/dt$) with low breaker times (< 5ms) [1.35].

Comparison

Previously, the current oscillation approach, especially active commutation, dominated the development of the hybrid HVDC breaker. Since the current oscillation involves an arc situation, the vacuum interrupter becomes a possible as a building element for HVDC CBs due to its excellent insulating properties after the current-zero. However, this trend is broken by the approach proposed by ABB. Rather than interruption with an arc based on current oscillation, the ABB approach is interruption without an arc voltage. Assuming interruption at the same power rating, the two approaches (traditional and ABB approaches) compare as follows.

- The mass of mechanical switch in the traditional approach is large compared to the ABB approach. Therefore the ABB opening speed is faster.
- Since the first approach has to deal with an arc, the interruption performance is uncertain, unlike the ABB approach.
- The conduction power loss in the traditional approach is smaller, but both are negligible.

- Both need solid-state switches in the commutation bypass path, and the traditional approach needs large capacitance.

For interruption at high power rating, the hybrid HVDC breaker proposed by ABB appears the only way to meet the requirement of HVDC grids. However, from an economical view, the hybrid HVDC breaker adopting current commutation may be more suitable for the low and medium voltage applications, such as electric traction, various drives, and converter systems.

Consequently, the objective of this thesis is to seek some positive aspects of active commutation applied to the vacuum interrupter, to compete with and circumvent the patented ABB approach.

In summary, in order to develop a high-speed current limiting vacuum circuit breaker based on a hybrid current commutation concept, the features and properties listed in Table 1.1 [1.7] are necessary.

Table 1.1 Design requirements for hybrid breakers.

Subject	Purpose	Methods
High-speed operation	fast fault detection time	• define suitable criteria for faults in a certain network in terms of parameters Δi, di/dt
	fast main breaker opening time	• speed up the coil discharge time if solenoid operated mechanisms applied • introduce counter-current before full gap distance is reached • adoption of a fast electrodynamic drive system • decrease the entire mass of the moving parts of the main breaker
High-current interruption	fast current commutation from main breaker to commutation path	• decrease the commutation inductance • increase the arc voltage in the main breaker • increase the commutation capacitor initial voltage
	adaption of main breaker and commutating devices	• obtain optimum commutation parameters. If parameters are too large, commutation time increases. This can be compensated by initiating the counter-current in advance
	suppression of overvoltage during the interruption	• utilise proper overvoltage protection device (non-linear resistance) • utilise freewheel diode to transfer the load stored inductive energy • increase the commutation capacitance and decrease initial voltages

1.5 Objectives

In this research, an AC vacuum circuit breaker (VCB) is used to analyse arc effects on fault clearance. Based on a hybrid breaker using active current commutation, the following should be achieved:

- The opening time should be reduced (since the DC energising circuit only speeds up the discharge rate of coil current rather accelerating the opening speed).

- In order to create an efficient, reliable and controllable HVDC system, several hybrid DC circuit breaker switching techniques have been proposed. Determination of the best technique for HVDC applications is necessary.

- A current-zero is produced by introducing a counter-current from a bypass commutation circuit, where optimal commutation initiation is needed to minimise the LC requirements. An adaptive control method is needed.

- Although the vacuum interrupter offers large values of di/dt and dv/dt, their limits are uncertain. The relationship between the interruption performance and $di/dt - dv/dt$ should therefore be investigated.

- Although hybrid breaker technology adopting current commutation appears mature, further investigation of the arc behaviour under different conditions to optimise this technology is needed. In addition, the commutation parameters including capacitance and inductance should be optimised.

1.6 Outline of thesis

The main subjects of each chapter are as follows.

Chapter 2 describes the characteristics of the vacuum arc including its formation and models as well as post-arc properties.

Chapter 3 presents the VCB drive mechanism. Based on the DC energising circuit, the opening time of the VCB is accelerated. Using detection of the plunger

movement counter-EMF, an adaptive control circuit is developed to trigger the commutation circuits at the optimal moment.

Chapter 4 describes the active and passive commutation circuits in detail. A test circuit is built to investigate the interruption properties of the vacuum interrupter in terms of varied interruption current, di/dt and dv_{VCB}/dt, as well as arcing time.

Chapter 5 presents a cascaded commutation circuit without a snubber circuit. The size of commutation parameters, including capacitor and inductor, are optimised.

Chapter 6 gives general conclusions and recommendations for the future research.

References

[1.1]   B.O.N. Hansson, "Submarine cable for 100-kv D-C power transmission," *Electrical Engineering,* vol. 73, pp. 602-602, 1954.

[1.2]   ABB. (April). *HVDC Classic - Reference list Thyristor valve projects and upgrades*. Available: http://search-ext.abb.com/library/Download.aspx?DocumentID=POW-0013&LanguageCode=en&DocumentPartID=&Action=Launch

[1.3]   ABB. *Why HVDC*. Available: http://www.abb.com/industries/us/9AAF400103.aspx

[1.4]   C.M. Franck, "HVDC Circuit Breakers: A Review Identifying Future Research Needs," *Power Delivery, IEEE Transactions on,* vol. 26, pp. 998-1007, 2011.

[1.5]   C.K. Meyer, M. De Doncker, and R.W., "Circuit breaker concepts for future high-power DC-applications," *Industry Applications Conference, 2005. Fourtieth IAS Annual Meeting. Conference Record of the 2005,* vol. 2, pp. 860-866, Oct. 2005.

[1.6]   P.G. Slade, "The Vacuum Interrupter: Theory, Design, and Application," *CRC Press and Taylor & Francis Group,* pp. 130-170, 2008.

[1.7]   A.M.S. Atmadji, "Direct Current Hybrid Breakers: A design and its realization," in *Eindhoven, The Netherlands: Department of Electrical Engineering, Eindhoven University of Technology*, 2000.

[1.8]   M. Bartosik, "Progress in D. C. breaking," in *Proc. 8th Int. Conf. Switching Arc Phenomena, Summary of discussed items on fuses, Lodz, Poland 3-6,* vol. 2, pp. 24-41, Sept. 1997, (Published in 1998).

[1.9]   Lianxiang Tang, and Boon-Teck Ooi, "Protection of VSC multi-terminal HVDC against DC faults," in *Proc. IEEE 33rd Annu. Power Electronics Specialists Conf.,* vol. 2, pp. 719-724, 2002.

[1.10] R.H.S. Allebrod, and R. Marquardt, "New transformerless, scalable modular multilevel converters for HVDC-transmission," In *Proc. IEEE Power Electronics Specialists Conf.,* pp. 174-179, Jun. 2008.

[1.11] ABB. *The Hybrid HVDC Breaker An innovation breakthrough enabling reliable HVDC grids*. Available: http://www05.abb.com/global/scot/scot221.nsf/veritydisplay/c9d5ba256e7e9671c1257ab6004b1feb/$file/hybrid-hvdc-breaker---an-innovation-breakthrough-for-reliable-hvdc-gridsnov2012.pdf

[1.12] W. Holaus, and K. Frohlich, "Ultra-fast switches- a new element for medium voltage fault current limiting switchgear," *Power Engineering Society Winter Meeting, 2002. IEEE* vol. 1, pp. 299-304, 2002.

[1.13] P.A.W. Newbery, "Electric fuses," *Proc. IEE,* vol. 124, pp. 909-924, November 1977.

[1.14] H. Nakayama, T. Fukazu, Y. Wada, Y. Shinozaki, and K. Ibuki, "Development of high voltage, self-healing current limiting element and verification of its operating parameters as a CLD for distribution substations," *IEEE Trans. on Power Delivery,* vol. 4, pp. 342-348, January 1989.

[1.15] J. Skindhoj, J. Glatz-Reichenbach, and R. Strumpler, "Repetitive current limiter based on polymer PTC resistor," *Power Delivery, IEEE Transactions on* vol. 13, pp. 489-494, Apr 1998.

[1.16] R.S. Strumpler, J. Glatz-Reichenbach, J. Kuhlefelt, and J.H.W. Perdoncin, "Novel medium voltage fault current limiter based on polymer PTC resistors," *Power Delivery, IEEE Transactions on* vol. 14, pp. 425-430, Apr 1999.

[1.17] P. Tixador, Y. Brunet, J. Leveque, and V.D. Pham, "Hybrid superconducting AC fault current limiter principle and previous studies," *Magnetics, IEEE Transactions on* vol. 28, pp. 446-449, Jan 1992.

[1.18] P. Manohar, and W. Ahmed, "Superconducting fault current limiter to mitigate the effect of DC line fault in VSC-HVDC system," *Power, Signals, Controls and Computation (EPSCICON), 2012 International Conference on* pp. 1-6, 3-6 Jan. 2012.

[1.19] Z. Hong, J. Sheng, L. Yao, J. Gu, and Z. Jin, "The Structure, Performance and Recovery Time of a 10 kV Resistive Type Superconducting Fault Current Limiter," *Applied Superconductivity, IEEE Transactions on* vol. 23, pp. 5601304-5601304, June 2013.

[1.20] T. Tanaka, "Electrical insulation in HTS power cables, fault-current limiters and transformers," *Electra,* pp. 11-29, October 1999.

[1.21] D. Andersson, and A. Henriksson, "Passive and active DC breakers in the three Gorges-Changzhou HVDC project," in *Proc. Int. Conf. Power Systems,* pp. 391-395, 2001.

[1.22] K. Arimatsu, Y. Yoshioka, S. Tokuyama, Y. Kato, and K. Hirata, "Development and Interrupting Tests on 250KV 8KA HVDC Circuit Breaker," *Power Apparatus and Systems, IEEE Transactions on,* vol. PAS-104, pp. 2452-2459, Sept. 1985.

[1.23] B. Pauli, E. Ruoss, G. Mauthe, G. Ecklin, and J. Porter, "Development of a high current HVDC circuit breaker with fast fault clearing capability," *IEEE Trans. Power Del.,* vol. 3, pp. 2072-2080, Oct. 1988.

[1.24] W. Pucher, "Fundamentals of HVDC interruption," *Electra,* pp. 24-38, Jun. 1968.

[1.25] W.J. Premerlani, "Forced Commutation Performance of Vacuum Switches for HVDC Breaker Application," *IEEE TRANS.,* vol. PAS-101, pp. 2721-2727, Aug. 1982.

[1.26] G.M.B. Bachmann, E. Ruoss, H. Lips, J. Porter, and J. Vithayathil, "Development of a 500 kV airblast HVDC circuit breaker," *IEEE Trans. Power App. Syst.,* vol. 104, pp. 2460-2466, Sep. 1985.

[1.27] R.K. Smith, P.G. Slade, M. Sarkozi, E.J. Stacey, J.J. Bonk, and H. Mehta, "Solid-state distribution current limiter and circuit breaker: application requirements and control strategies," *Power Delivery, IEEE Transactions on* vol. 8, pp. 1155-1164, July 1993.

[1.28] T. Ueda, M. Morita, H. Arita, J. Kida, Y. Kurosawa, and T. Yamagiwa, "Solid-state current limiter for power distribution system," *Power Delivery, IEEE Transactions on,* vol. 8, pp. 1796-1801, Oct 1993.

[1.29] F.W. Holroyd, and V.A.K. Temple, "Power Semiconductor Devices for Hybrid Breakers," *Power Apparatus and Systems, IEEE Transactions on* vol. PAS-101, pp. 2103-2108, July 1982.

[1.30] C. Meyer, S. Schroder, and Rik W. De Doncker, "Solid-state circuit breakers and current limiters for medium-voltage system having distributed power

systems," *IEEE Transaction on Power Electronics,* vol. 19, pp. 1333-1340, Sept. 2004.

[1.31] B.W. Williams, "POWER ELECTRONICS: Devices, Drivers, Applications, and Passive components," pp. 107-130, 2006.

[1.32] J.G. Gorman, C.W. Kimblin, R.E. Voshall, R.E. Wein and P.G. Slade, "The interaction of vacuum arcs with magnetic fields and applications," *IEEE Transactions on Power Apparatus and Systems,* vol. PAS-102, pp. 257-266, February 1983.

[1.33] J. Czucha, and J. Zyborski, "Ultra fast hybrid circuit breaker for AC network theorectical analysis," *29th University Power Engineering Conf, UPEC 1994, Galway Ireland,* vol. 1, pp. 173-176, 1994.

[1.34] A. Lee, P.G. Slade, K.H. Yoon, J. Porter, and J. Vithayathil, "The Development of a HVDC SF6 Breaker," *IEEE Trans. Power App. Syst.,* vol. 104, pp. 2721-2729, Oct. 1985.

[1.35] A.N. Greenwood, P. Barkan, and W.C. Kracht, "HVDC Vacuum Circuit Breakers," *Power Apparatus and Systems, IEEE Transactions on* vol. PAS-91, pp. 1575-1588, July 1972.

[1.36] J. Jadidian, "A Compact Design for High Voltage Direct Current Circuit Breaker," *Plasma Science, IEEE Transactions on,* vol. 37, pp. 1084-1091, 2009.

[1.37] Y. Niwa, T. Funahashi, K. Yokokura, J. Matsuzaki, M. Homma and E. Kaneko, "Basic investigation of a high-speed vacuum circuit breaker and its vacuum arc characteristics," *Generation, Transmission and Distribution, IEE Proceedings,* vol. 153, pp. 11-15, 12 Jan. 2006.

[1.38] J.M. Anderson, and J.J. Carroll, "Applicability of a Vacuum Interrupter as the Basic Switch Element in HVDC Breakers," *Power Apparatus and Systems, IEEE Transactions on,* vol. PAS-97, pp. 1893-1900, Sept. 1978.

[1.39] H. Nakao, Y. Nakagoshi, M. Hatano, T. Koshizuka, S. Nishiwaki, A. Kobayashi, T. Murao, and S. Yanabu, "DC Current Interruption in HVDC SF6 Gas MRTB by Means of Self-Excitation," *Power Engineering Review, IEEE* vol. 21, pp. 687-693, Aug. 2001.

[1.40]   L. T. W. Falkingham, and M. Waldron, "Vacuum for HV applications - Perhaps not so new? - Thirty Years Service Experience of 132kV Vacuum Circuit breaker," *Discharges and Electrical Insulation in Vacuum, 2006. ISDEIV '06. International Symposium on* vol. 1, pp. 200-203, Sept. 2006.

2 Vacuum insulation

2.1 Introduction

When introducing the vacuum interrupter it is necessary to understand and interpreting the vacuum arc. The name vacuum arc is improper, being a contradiction since there are no conducting media in a vacuum. It is more accurate to be addressed as a metal vapour arc because metal vapour burns in the vacuum as the current-carrying contacts separate. However, since the name vacuum arc is prevalent and accepted, it is used throughout this thesis.

The internal model of a vacuum arc is discussed in detail in this chapter, including the diffuse arc mode and the constricted arc mode. The vacuum arc is relatively stable once started, and like arcs arising in a gaseous media, it is self-sustaining. It will continuously transmit energy from the electrical source to load until the external conditions are changed, such as the occurrence of a current zero or removal of its energy source. However, at low defined current level, the arc becomes unstable and suddenly extinguishes rapidly. This phenomenon is termed *current chopping* and is discussed in Appendix B.2.3 Finally, the vacuum arc can be characterised as a self-sustained electrical discharge through the inter-electrode region, keeping the current flowing by the burning of vapour and charge carriers drawn from one or both of the electrodes.

Vacuum breakdown, especially in a period immediately following arc interruption, is also determined by the vacuum arc. The vacuum interrupter needs time for the recovery of dielectric strength after interruption. Consequently, the post-arc model is illustrated to help understand vacuum arc recovery.

2.2 Definition

If an electron is released from a solid and starts to move it away, a force exists between the electron and the positively charged region vacated. Thus, work is applied to the electron for movement. This not only results in a change in potential energy of the electron but also causes the formation of a potential well, and therefore confines electrons close to the solid surface. Consequently, the potential of the departed electron is defined as the vacuum energy (0eV), and to some extent it is interpreted as *barrier potential* (typically 3.8eV for copper) [2.1]. According to the band theory of metals, the metal electrons will fill the band structure and follow Fermi-Dirac statistics, where the Fermi energy level is defined as the highest level occupied by an electron at 0K, and also is equal to the energy distribution midpoint of electrons at temperatures above 0K. Consequently, for electrons to escape from a solid, they must overcome a barrier of several voltages, known as the *work function*, which is defined as the difference between the vacuum energy and the Fermi energy. In other words, it represents the additional energy the electron requires to escape from the solid. Fortunately, there are no electrons with this energy at room temperature, except those influenced by a change in the external conditions, such as metal being heated, an externally applied field, etc.

The energy distribution of the conduction band electrons is proportional to an increasing temperature as metal is heated. Thus, some electrons can escape from metal to the surrounding space when they achieve sufficient energy to overcome the work function. This process is referred to as *thermionic emission* [2.2], and was first proposed by Richardson and generally quantified by Dushman, who proved why refractory metals, such as tungsten and molybdenum, can bring high thermionic emission, which is described by:

$$J = A_1 \times T^2 \times e^{(-\frac{\phi_0 e}{\kappa T})} \tag{2.1}$$

This expression describes the relationship between current density, $J(A/m^2)$ and the absolute temperature $T(K)$, where ϕ_0 represents the thermionic work function, κ is Boltzmann's constant $(1.37 \times 10^{-23} joules/K)$, and e is the electronic charge. The

constant A_1 is derived from experimentally, and is approximately 6×10^5 for most metals.

Field emission is when electrons move away from a metal due to a strong electric field, which is capable of reducing the barrier potential. This is understood by considering Figure 2.1 [2.3, 4]. Figure 2.1 (a) describes conditions at an ideal boundary between the metal (left side) and the vacuum (right side). The cross-hatched region represents the metal conduction band within which electrons are located, and the conduction band extends down from the Fermi level. The Fermi level itself is ϕV below the surface potential, where ϕ represents the work function. Consequently the Fermi level is at $-\phi$V if the potential in metal surface is considered as zero volts. To pull away from the metal, Fermi electrons must acquire at least ϕeV of energy.
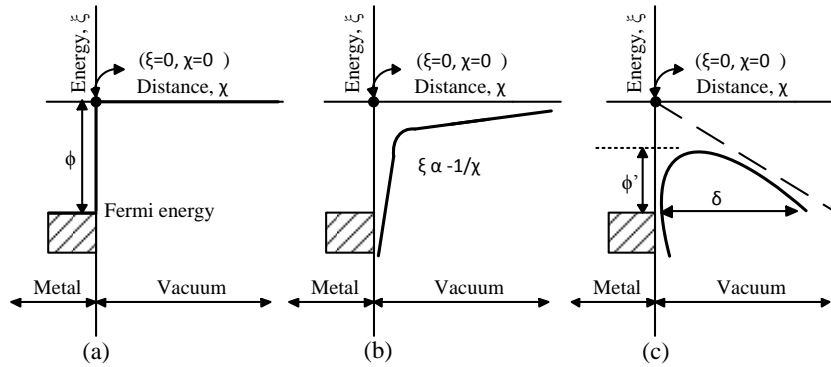
Figure 2.1 Potential energy against distance for electron near metal surface [2.5]: (a) without image charge field; (b) with image charge field; and (c) with image charge and external field.

The electron will escape from the metal when it gains enough energy, and then affect the field due to its charge. Consequently, the electron field and its image within the metal dominate the potential profile form, as shown in Figure 2.1 (b). In Figure 2.1 (c), an external electrical field results in the linear change of potential profile, represented by the dashed line. The solid line indicates the combined potential profile after superposition. Consequently, the effect of the external field is not only to reduce the maximum height of the potential barrier to a level below the work function, (where the potential barrier is further reduced if the field is increased), but also produces an area where the potential falls as electrons move away from the solid.

As the external field increases, the width of the barrier is reduced to the point where quantum tunnelling occurs across the barrier, based on a finite probability. The width change dominates this probability, which increases as the width narrows, i.e. probability increases with increasing field. For Fermi energy electrons, this is shown as δ in Figure 2.1 (c), and this behaviour obeys the following function [2.6]:

$$J = K_1 \times E^2 \times e^{\left(-K_2/E\right)} \qquad (2.2)$$

where J represents the current density and E is the applied field. The constants K_1 and K_2 depend on the work function and vary slightly as applied field is changed.

Arc formation, different types of arc, electrode spots, arc voltage and current chopping, etc. are important physical contact mechanisms and involve complicated processes. Detailed information on all of these arc processes and characteristics are detailed in Appendix B.

2.3 Vacuum breakdown and its recovery

Breakdown voltage is the minimum voltage across a given gap distance that results in a portion of an insulator becoming electrically conductive. The factors that influence the breakdown strength of a vacuum are electrode effects, gap distance, vacuum pressure, and 'conditioning'.

- Electrode effects: for a given gap distance, the breakdown voltage varies from electrode material to material. In general, the breakdown strength is proportional to the melting point of a metal. The condition of the contact surface also affects the breakdown strength. Even on new polished contacts, its surface is full of asperities and protrusions which will become a source to enhanced electron emission [2.7]. Spolaore and Bisoffi [2.8] established that the breakdown strength reduces as the electrode diameter increases, as shown in Figure 2.2.
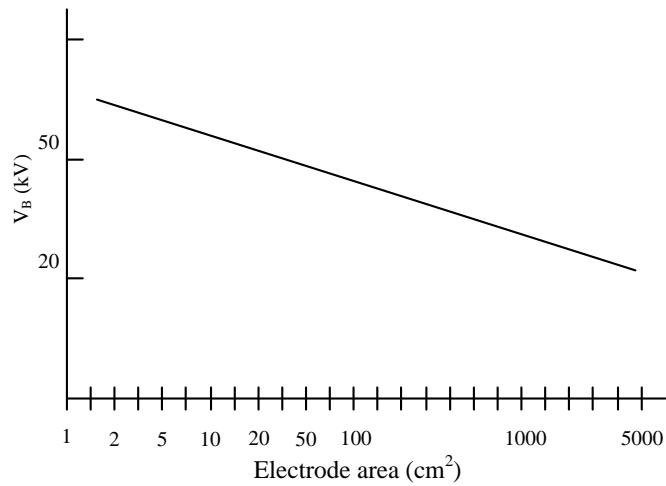
Figure 2.2 Breakdown voltage with increasing electrode size.

- Gap distance. Figure 2.3 illustrates the relationship between vacuum breakdown voltage, V_B and the contact gap d based on many sources [2.7-14]. For a small gap, $d < 0.4$mm, V_B is in proportion in gap d. For larger gaps, 0.4mm $< d < 100$mm, V_B is in proportion in gap d^η, where η is between 0.3 and 0.7. $\eta \cong 0.58$ for 0.4mm $< d < 40$mm and $\eta \cong 0.34$ for 40mm $< d < 100$mm.
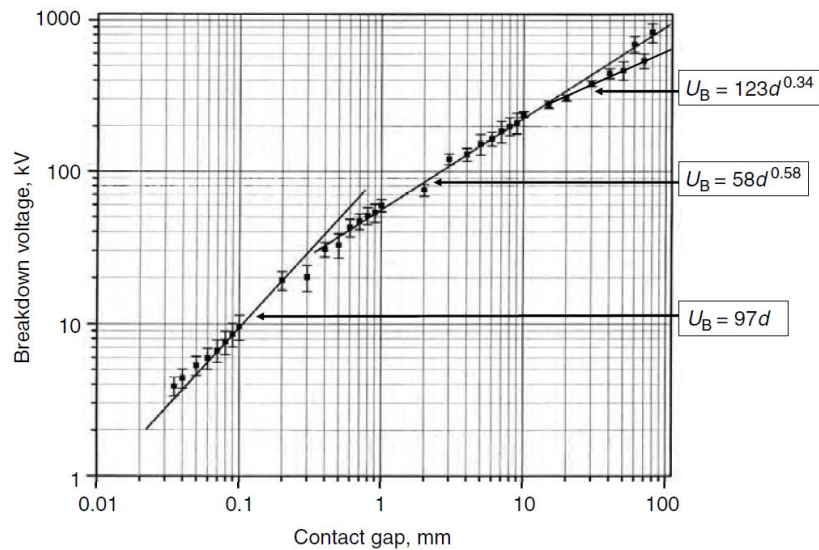
Figure 2.3 log-log plot of breakdown voltage, V_B , as a function of contact gap in a vacuum [2.8].

27

- Vacuum pressure dominates the mean free path which determines the probability of collision between electrons and metal atoms. Normally, the vacuum interrupter operates with a vacuum $10^{-2} \sim 10^{-4}$Pa, which is a low gas density and introduces few collisions. Thus electron avalanche does not develop in the residual gas between the contacts [2.9].

- 'Conditioning' is a method used to increase the ability to withstand high voltages between two electrodes before breakdown occurs in a vacuum following multiple discharges [2.15]. Conditioning operations eliminate sources of pre-breakdown current such as from micro-projections and protrusions on the contact surfaces. Methods for conditioning are spark conditioning by using a high-voltage AC power supply and high-voltage pulsing, as well as current conditioning [2.16].

The difficult phase in vacuum breakdown is a period that immediately follows arc interruption. The vacuum interrupter needs time for dielectric strength recovery to withstand the transient recovery voltage (TRV). A re-ignition may occur that indicates a failure to interrupt if the recovery time is not sufficient, since there is no vacuum state immediately after current-zero in the vacuum interrupter. In other words, the gap is still in a conductive state due to a residual plasma in the gap from the prior arcing. Parts of the contacts are capable of emitting electrons and ions as well as metal particles due to the hot electrode surface.

Farrall [2.17] analysed the recovery of dielectric strength after current interruption in a vacuum by performing experiments based on a few electrode materials, for given conditions. An AC power source was utilised to a produce a high current arc through the contact during electrode separation, keeping the AC source switched on until arc extinction. A high-voltage DC supply or a short pulse for a few microseconds, where both could be delayed to any time after the arc extinction, was introduced across the vacuum interrupter. In order to quickly reduce the current through the vacuum contact to zero after its sinusoidal peak, an auxiliary circuit was used to produce a fixed ramp current opposing the AC current direction. The experiment results revealed that contacts made from refractory metals, such as tungsten and molybdenum, perform better than metals like copper and silver, in recovery rate and

breakdown strength. However, the refractory metals readily exhibit the current chopping phenomenon. The recovery performance is not only determined by the electrode metal but also dominated by the gap geometry and conducting current. The recovery time reduces as the electrode diameter increases, but increases as the gap distance increases or as the measured current decreases. Zalucki and Seidel [2.18] also analysed the recovery period, but with the high-voltage DC supply connected with opposite polarity across the gap. This produces higher breakdown voltage (10 to 20%). Since the experiment is with a diffused arc, only cathode spots occur, so arc cathode tracking roughens the surface and increases the breakdown voltage.

2.4 Post-arc model

A critical moment for dielectric recovery in a vacuum interrupter is the post-arc phase, which involves the residual ions and electrons between the electrodes after the circuit current-zero. To understand the residual arc, the simplified one-dimensional post-arc model is proposed [2.19-21] as shown in Figure 2.4. After current reduces to zero, there is neutral plasma within the vacuum interrupter. Also there is a space charged sheath (s) expanding from the new cathode to the new anode if a transient recovery voltage (U_{REC}) arises. This sheath should only consist of ions. The sheath not only withstands the whole transient recovery voltage (TRV), but also sustains the post-arc current due to freely moving ions. Although the remaining gap is neutral, with zero voltage drop, the electrons are influenced by new anode potential. Thus, the post-arc current in neutral plasma occurs as the electrons enter the new anode.
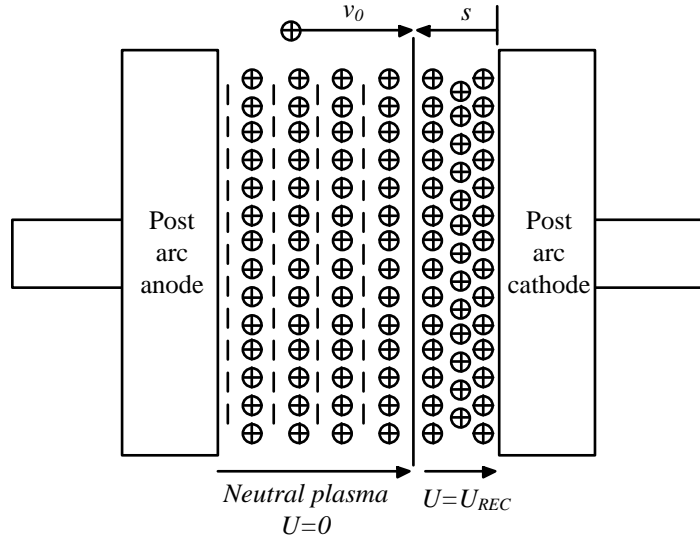
Figure 2.4 Model for sheath growth after current zero.

Gerd and Manfred [2.22] proposed a mathematical model of sheath growth, confirmed experimentally by employing a chamber which contained two sets of contacts with variable distances (*d*) between the sets. One set was the main contacts for experiencing arc stress, whilst the other set were the high-voltage electrodes for experiencing the TRV that can have a positive or negative potential, as shown in Figure 2.5. This experiment was based on an assumption that the residual plasma is independent of the thermal stress and melting on the contact surface. Thus the mathematical expression for the current density *j* is:

$$j = n \times Z_{mn} \times e \times (v_i + {ds}/{dt})$$ (2.3)

where *j* represents current density; n is the ion density at the boundary between the sheath and the neutral plasma; Z_{mn} is the mean ion charge number, which varies from material to material; e is the elementary charge; v_i represents the ion velocity at the sheath boundary; and s is the sheath thickness.
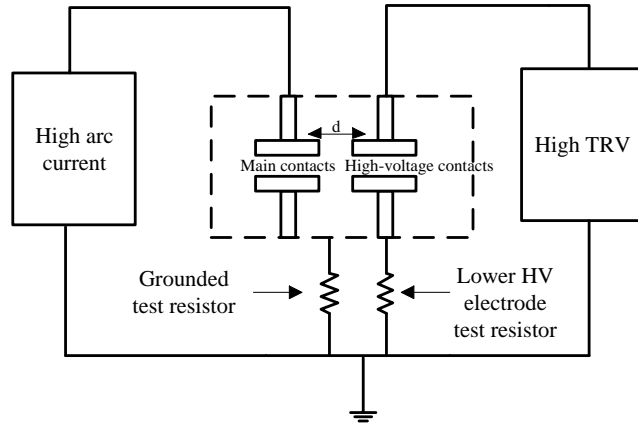
Figure 2.5 Model of test chamber.

The ion velocity v_0 (typically 10^4ms^{-1}) at the sheath boundary arises from the high pressure [2.17] that results from the movement and reformation of cathode spots in the former cathode electrode (now the new anode) of the VCB. It reduces to zero once the ions have arrived at the new cathode after travelling a gap distance of a few millimetres in the first few μs. The ion velocity is considered as zero with respect to the time scale of several μs to several tens of μs. For the simplest case or for short times, the ion density n is assumed constant, where the ion density is dominated by the electrode material and the level of current through the inter-electrodes region. The one-dimensional model of Figure 2.4 and equation (2.3) also indicate that the post-arc current will drop to zero suddenly as the sheath arrives at the anode electrode, since there is no more gap into which the sheath can expand ($ds/dt = 0$). If the surface area of the planar electrodes is A_{EL}, then equation (2.3) can be written as:

$$i(t) = A_{EL} \times n \times Z_{mn} \times e \times (^{ds}/_{dt}) \tag{2.4}$$

where $i(t)$ represents post-arc current and A_{EL} is electrode surface area.

The experimental results verified the mathematical model and confirmed the effect of the vacuum interrupter shield, shown in Figure 2.6 (a). Due to the negative bias attracting ions, a current flowing to the shield was observed when the shield was grounded, confirming that there are ions in the residual plasma. Since the test vessel had a larger surface than the test electrode, the post-arc current in the test vessel was

large compared to that in the test electrode. Thus the post-arc current is proportional to the surface area. With increasing test voltage, all three post-arc current traces displayed similar appearance, all rising together to a certain level and abruptly dropping at the same time, because the positive space charge sheath started to rise when it moved from the new cathode electrode and could no longer expand as it had arrived at the new anode electrode. The distance, *d*, between the main contacts and high voltage electrodes was adjustable to enable study of the ion density distribution in the test chamber after conducting current reduces to zero.

(a)

(b)
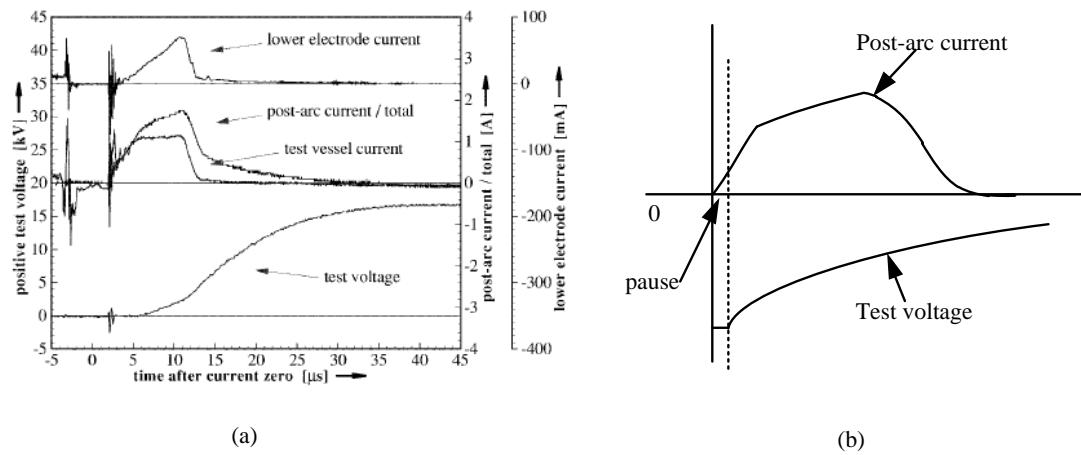
Figure 2.6 (a) Post-arc current measurement: main current I=7.5kA RMS, test voltage U=+18kV, test vessel grounded [2.22] and (b) the voltage zero before the development of the TRV.

With a main current of 10kA RMS and a positive TRV with different time delay after current zero, the results show the residual plasma is uniformly distributed in the test chamber centre after current zero.

However, the model is incomplete. The model excludes the effects from thermal stress and melting of the contact surface after experiencing the arc. It also does not consider the effect of collisions during sheath expansion if the sheath thickness is greater than the ion mean free path [2.23, 24]. Since it assumed that ion velocity v_0 is zero in terms of the µs time scale, the observable pause before the development of the TRV, shown in Figure 2.6 (b), is ignored. The residual plasma has to be prepared to produce the sheath for the forthcoming TRV. The voltage-zero period immediately following current interruption was explained and formulated by Ezra and Lanen

[2.25]. The displacement current caused by the time change of the electric field inside the sheath could be modelled by sheath capacitance, given by

$$C_{sh} = \frac{K_0}{V_{sh}^{3/4}} \tag{2.5}$$

where $K_0 \approx 0.42(Zn\varepsilon_0)^{1/2}(\frac{\kappa T_e}{Z})^{1/4}A_{EL}$ (2.6)

κ is the Boltzmann's constant; T_e is electron temperature; Z is average ion charge; n is ion density at the plasma-sheath boundary; A_{EL} represents surface area of the electrodes; ε_0 is the permittivity in vacuum; and V_{sh} is the sheath voltage.

However this thesis questions one of initial conditions for equations (2.4) and (2.6); that the ion density is only determined by its natural decay and the post-arc current. Niwa and Funahashi [2.26, 27] found that the vacuum interruption is not only dependent on the rate of TRV after current zero, but is also reliant on the current decline rate before current zero. The change in current decline rate affects the residual plasma.

2.5 The merit of the vacuum circuit breaker

As previously mentioned, a number of factors affect the properties of a vacuum interrupter, including electrode material, electrode dimensions, gap distance, and the level of conducting current. In order to maintain the vacuum, VCBs are permanently sealed, which makes it difficult to directly measure the vacuum arc. Many researchers [2.26-29] have investigated the vacuum circuit breaker by considering it as a black box. The figure of merit for describing one property of a VCB, is the product:

$$\xi = \frac{di}{dt} \times \frac{dv}{dt} \tag{2.7}$$

where di/dt represents the rate of decline of current immediately before current-zero, and dv/dt represents the rate of rise of voltage across the opening contacts immediately after current zero.

The higher this product, the better the performance of the vacuum interrupter. Figure 2.7 illustrates the definition of di/dt and dv/dt. The relationship between them is popular with the researchers, since di/dt and dv/dt are convenient electrical behaviour measurements.
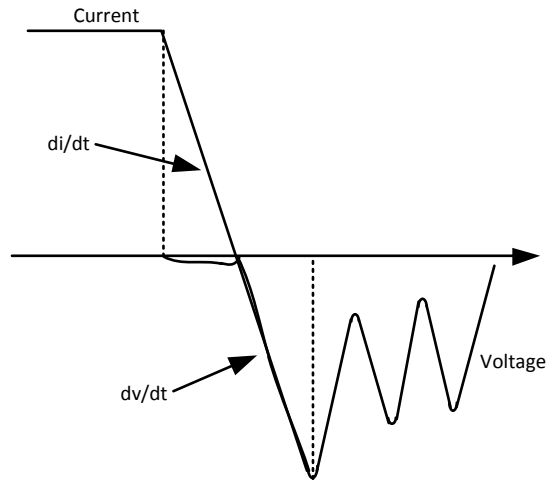
Figure 2.7 Definition of *di/dt* and *dv/dt*

Although the properties of the VCB have been investigated by several researchers, all experiment results conclude that to achieve successful interruption using the VCB, the value of di/dt must be increased as dv/dt reduces. The dielectric strength starts to recover as the conducting current through the electrodes reduces. The relationships between di/dt and the gap distance and the conducting current level have been investigated, and show that di/dt increases as the gap distance increases, but reduces as the conducting current level increases. However, di/dt cannot reach too high a level, otherwise the vacuum interrupter behaves as a short circuit and dv/dt loses its function in the recovery of dielectric strength [2.29]. di/dt is key in the interruption of the vacuum circuit breaker. These VCB property conclusions are based on high power rating operation. The objective in this thesis is to study the fundamental properties of the VCB at lower currents, and to find the optimum gap distance for the vacuum interrupter for faster fault clearing.

2.6 Summary

This chapter utilised graphical evidence to describe the mode transition of the vacuum arc which is dominated by electrode materials and the internal dimensions of the vacuum interrupter, as well as the conducting current level. The diffuse mode of the vacuum arc has two distinct advantages, namely less electrode surface erosion and easier interruption when compared to the constricted mode. Methods to keep the arc diffuse were described, such as the application of magnetic field and carefully designed in electrode structures [2.30, 31]. The post-arc model illustrated that there is an approximately uniform distribution of the residual plasma in the electrodes after current-zero. The recovery time is material dependent.

The vacuum arc characteristics considered in this chapter, although incomplete, are sufficient for the understanding of VCB operation needed in the following chapters.

References

[2.1] A.N. Greenwood, "Vacuum Switchgear," *the insitution of electrical engineers,* vol. 18, pp. 25-47, 1994.

[2.2] O. W. Richardson, "Emission of electricity from hot bodies," *Proc. Cambridge Philos. Soc.,* vol. 11, p. 173, 1901.

[2.3] James M. Lafferty, "Vacuum arcs - theory and application," *Wiley,* pp. 21-24, 1980.

[2.4] J. D. Cobine, "Gaseous conductors," *McGraw-Hill,* pp. 106-122, 1941.

[2.5] James M. Lafferty, "Vacuum arcs- theory and application," *Wiley,* pp. 137-145, 1980.

[2.6] R. H. Fowler, and L. Nordheim, "Electron emission in intense electric field," *Proc. Royal Soc.,* vol. 119, p. 173, 1928.

[2.7] R.P. Little, and W.T. Whitney, "Electon emission preceding electrical breakdwon in vacuum," *J. Appl. Phys.,* vol. 36, pp. 2430-2434, 1963.

[2.8] P. Spolaore, G. Bisoffi, F. Cervellera, R. Pengo and F. Scarpa, "The large gap case for HV insulation in vacuum," *IEEE Transactions on Dielectrics and Electrical Insulation,* vol. 4, pp. 389-393, August 1997.

[2.9] R. Hackham, and L. Altcheh, "Ac and dc electric breakdown of vacuum gaps with variation of air pressure in the range 10^{-9} to 10^{-2} torr using OFHC copper, nickel and niobium parallel plane electrodes," *Journal of Applied Physics,* vol. 46, pp. 627-636, 1975.

[2.10] H. Hirose, "More accurate breakdown voltage estimation for the new step-up test method," *IEEE Transactions on Dielectrics and Electrical Insulation,* vol. 10, pp. 475-482, June 2003.

[2.11] G.A. Farrall, "Electrical breakdown in vacuum," *IEEE Transaction on Electrical Insulation,* vol. EI-20, pp. 815-841, October 1985.

[2.12] P. Chatterton, "Vacuum breakdown in Electrical Breakdown of Gases," *Wiley, New York,* pp. 129-208, 1978.

[2.13] D. Alpert, D. Lee, E. Lyman, and H. Tomaschke, "Initiation of electrical breakdown in ultra high vacuum," *Journal of Vacuum Science & Technology,* vol. 1, pp. 35-50, November/December 1964.

[2.14] D. K. Davies, and M.A. Biondi, "Vacuum electrical breakdown between plane—parallel copper plates," *Journal of Applied Physics,* vol. 37, pp. 2969-2977, July 1966.

[2.15] T. Kamikawaji, T. Shioiri, M. Okawa, E. Kaneko, and I. Ohshima, "Generation of micro-particles fromcopper–chromium contacts and their influence on insulating performance in vacuum," *Proceedings of the 23rd International Conference on Electrical Contact Phenomena (Nagoya, Japan),* pp. 895-902, July 1994.

[2.16] K. Ohira, A. Iwai, Y. Saito, and S. Kobayashi, "Changes of parameters influencing breakdown characteristics of vacuum gaps during spark conditioning," *Proceedings of the 10th International Symposium on Discharges and Electrical Insulation in Vacuum (Eindhoven, Holland),* pp. 105-108, September 1998.

[2.17] G. A. Farrall, "Recovery of dielectric strength after current interruption in vacuum," *IEEE Transacitons on Plasma Science,* vol. PS-6, pp. 360-369, Decenmber 1978.

[2.18] G. Lins, "Influence of electrode separation on ion density in the vacuum arc," *Plasma Science, IEEE Transactions on*, vol.19, no.5, pp.718,724, Oct 1991.

[2.19] J.G. Andrews, and R.H. Varey, "Sheath growth in a low pressure plasma," *Phys. Fluids,* vol. 14, pp. 339-343, 1971.

[2.20] S. E. Childs, and A.N. Greenwood, "A model for DC interruption in diffuse vacuum arcs," *IEEE Trans. Plasma Sci.,* vol. PS-8, pp. 289-294, Aug. 1980.

[2.21] E. Huber, K. Frohlich, and R. Grill, "Dielectric Recovery of Copper Chromium Vacuum Interrupter Contacts After Short-Circuit Interruption," *IEEE Transactions on plasma science,* vol. 25, pp. 642-646, August 1997.

[2.22] G. Duning, and M. Lindmayer, "Plasma Density Decay of Vacuum Discharges After Current Zero," *IEEE Trans. Plasma Sci.,* vol. 27, pp. 923-929, August 1999.

[2.23] P. Sarrailh, L. Garrigues, G.J.M. Hagelaar, J.-P. Boeuf, G. Sandolache, and S.W. Rowe, "Plasma decay modeling during the post-arc phase of a vacuum circuit breaker," *Discharges and Electrical Insulation in Vacuum, 2008.*

ISDEIV 2008. 23rd International Symposium on vol. 1.2, pp. 406-409, Sept. 2008.

[2.24] S. Rowe, P. Sarrailh, L. Garrigues, J-P Boeuf, S. Popov, A. Batrakov, and G. Sandolache, "Post-arc period of vacuum circuit breakers: New 2D simulation and experimental results," *Discharges and Electrical Insulation in Vacuum (ISDEIV), 2010 24th International Symposium on* pp. 423-426, Aug. 30 2010-Sept. 3 2010.

[2.25] E. van Lanen, R. Smeets, M. Popov, and L. van der Sluis, "Vacuum Circuit Breaker Postarc Current Modelling Based on the Theory of Langmuir Probes," *Plasma Science, IEEE Transactions on* vol. 35, pp. 925-932, Aug. 2007.

[2.26] Y. Niwa, J. Matsuzaki, and K. Yokokura, "The basic investigation of the high-speed VCB and its application for the DC power system," *Discharges and Electrical Insulation in Vacuum, 2008. ISDEIV 2008. 23rd International Symposium on,* vol. 1, pp. 107-112, 15-19 Sept. 2008.

[2.27] Y. Niwa, T. Funahashi, K. Yokokura, J. Matsuzaki, M. Homma and E. Kaneko, "Basic investigation of a high-speed vacuum circuit breaker and its vacuum arc characteristics," *Generation, Transmission and Distribution, IEE Proceedings-,* vol. 153, pp. 11-15, 12 Jan. 2006.

[2.28] H. Odaka, M, Yamada, R. Sakuma, C. Ding, E. Kaneko, and S. Yanabu, "DC interruption characteristic of vacuum circuit breaker," *Electrical Engineering in Japan,* vol. 161, pp. 17-25, 21 JUN 2007.

[2.29] W. J. Premerlani, "Forced Commutation Performance of Vacuum Switches for HVDC Breaker Application," *IEEE TRANS.,* vol. PAS-101, pp. 2721-2727, Aug. 1982.

[2.30] A.N. Greenwood, "Vacuum Switchgear," *the insitution of electrical engineers,* vol. 18, pp. 109-121, 1994.

[2.31] P. G. Slade, "The Vacuum Interrupter: Theory, Design, and Application," *CRC Press and Taylor & Francis Group,* pp. 177-249, 2008.

3 Vacuum circuit breaker mechanisms

3.1 Introduction

The objective of the operating mechanism of the vacuum circuit breaker (VCB) is to close and open the contacts when the appropriate operating signals are received. In order to achieve optimal VCB performance, many design mechanisms should be considered, such as control of impact velocity, along with detailed analysis of the contact dynamics, etc. [3.1]. Although the closed position, where energy is transmitted, occupies almost all of the VCB's useful life, the moment of separation is one of the most significant periods for the VCB. AC energising is widely employed in the solenoid operation of the VCB, but DC is also appropriate, avoiding the need for rectification. Thus DC energising is proposed to speed up mechanical activation.

Prior to separation of the internal VCB electrodes, there is an interesting phenomenon that a coil current 'peak' appears even after the coil current-zero. This phenomenon was first observed by Bauer and Sitar [3.2] who noted that after the plunger starts to move back to its original position due to the spring force, a transient increase in the solenoid coil current may be noticed due to the induced back EMF. The reason for this counter-electromotive force is discussed in detail and its occurrence is exploited for VCB adaptive control purposes.

A more interesting observation is that no matter how different factors affect the coil current, the occurrence of the peak is consistent in relation to the formation of the arc voltage. With analogue devices, the opening speed of the VCB is found to be approximately 1ms^{-1}. This means that the moment VCB interruption starts can be predicted by utilising the current peak, which provides the reference point for delaying triggering of the auxiliary circuit for current interruption. The delay depends on the gap distance required. Consequently, a control circuit is proposed to utilise the relationship between the occurrence of the current peak and the formation of arc voltage.

3.2 Solenoid operation

In this thesis, a VCB manufactured by AMPCONTROL company [3.3] is utilised (with three vacuum interrupters in one frame), which is primarily for direct on-line switching of squirrel cage induction motors and other applications, such as transformer and capacitor switching. The key element in the VCB is the vacuum interrupter, which carries the load current during normal operation. The internal mechanisms and model of the vacuum interrupter have been discussed in Chapter 2 and Appendix B.

Figure 3.1 illustrates the typical solenoid mechanism. Normally, the armature is held in an open position by the force from a spring which connects to two rectifier switches, which are in a closed state during the VCB off-state and are in opened when the VCB is on. Since the solenoid coil is energised by an electrical current passing through the coil, it acts as a permanent type magnet and the strength (H) of this magnetic field is proportional to the coil current magnitude. However, the VCB remains in the open position until the magnetic force produced by the solenoid coil exceeds the spring force. The rectifier switches remain closed until the electrodes have been in contacted for a while, which then compresses the spring. The purpose of rectifier switches is to retain full power for closing but to reduce the power for holding the vacuum interrupter. This delay action is possible because there is always a lag between the movement of the armature and the vacuum interrupter, due to the connection mechanism, i.e. the vacuum interrupter starts to travel after the armature has moved. In summary, since the magnetic force is proportional to the square of coil current, the contacts start to close/open when the solenoid coil current has increased/reduced to certain level, which means that the magnetic force produced by the current is bigger/smaller than the spring forces. During VCB separation, these compressed springs have enough force to open the contacts at short time after the coil power has been removed.
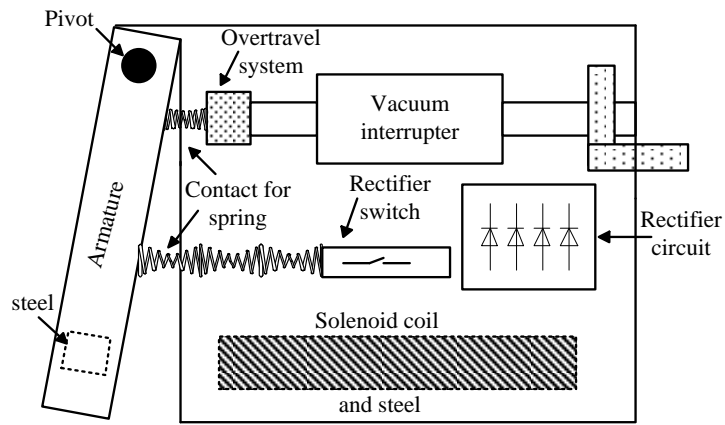
Figure 3.1 Schematic diagram of a solenoid operated VCB.

Figure 3.2 A VCB example. (Manufactured by AMPCONTROL) [3.3].

Table 3.1 Technical data on triple pole vacuum circuit breakers.

Contactor reference	CMV 15	CMV 30	CMV 40	CHV 30	CHV 40/50
Operating voltage, kV	1.2	1.2	1.2	3.6	3.6
Current rating, A	150	300	400	300	400
Max motor duty, kW	225	450	600	1350	1350
Max transformer duty, kVA	250	500	660	1500	1500
Closing coil- closing, W	250	340	340	220	220
110A ac hold in, W	12	55	55	85	85
Weight of contactor, kg	4	10	10	12.5	12.5
Thermal rating (1s), kA	4	6			
Mechanical life, cycles	5×10^6				

The objective of this thesis is to discuss how the VCB clears a fault, based on its vacuum characteristic. This means concentrating on the separating moment and the period after this. Figure 3.2 and

Table 3.1 illustrate the appearance of the VCB and the different voltage and current ratings. The experimental results in this thesis are based on the CMV 15 type.

3.2.1 Solenoid design

The basic operation of solenoid mechanism has been introduced in the previous section. Now its design will be introduced in terms of general principles, force and motion characteristics, etc.

Figure 3.3 is the VCB bottom view, where the basic elements of a typical solenoid include the solenoid coil and the steel core as well as the armature. The dashed line represents the magnetic flux Φ produced by the energised coil. The magnetic circuit consists of six portions, where 1, 3, 5 and 6 represent the magnetic flux through the steel and, 2 and 4 are the magnetic flux through the air gaps with length $g - x$ in terms of the coordinate position x. The cross sectional area of each portion is A. The armature is attracted towards the solenoid coil after the coil has been energised; where the attractive force between the two is a function of coil current and is dominated by the magnetic flux density B before the core material saturates.
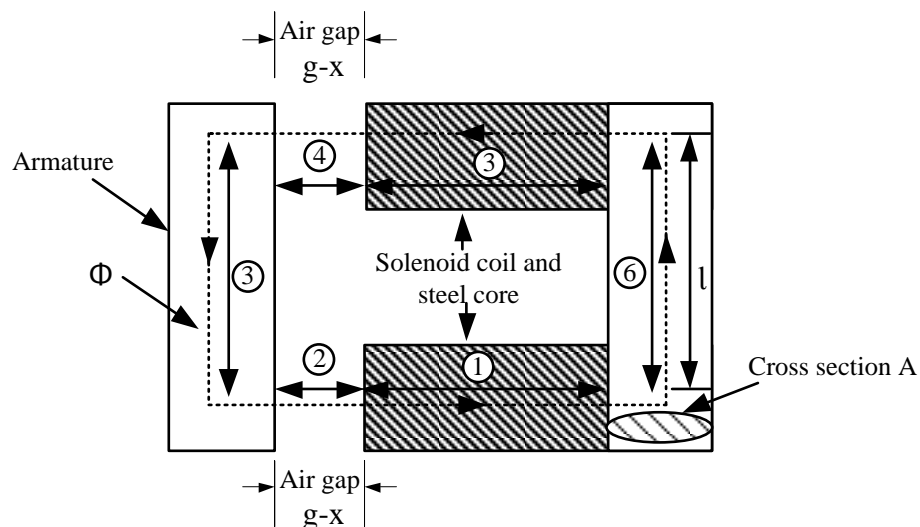
Figure 3.3 Rudimentary solenoid.

According to the Ampere's law, the magneto-motive force (MMF) produced by the energised coil is Ni if there are N turns in the solenoid coil and is equal to the line integral of the magnetic field strength H which is measured in ampere turns per metre (A/m):

$$\oint H \times l_s = \sum i = N \times i \tag{3.1}$$

For most practical topologies, this equation can be rewritten as:

$$\sum_k H_k \times l_{l_k} = \sum_m N_m \times i_m \tag{3.2}$$

and the flux density B is a function of H assuming linear operation:

$$B = \mu \times H \ \text{weber/m}^2 \tag{3.3}$$

$$\mu = \mu_r \times \mu_0$$

where μ represents the permeability of the medium; μ_r is the relative permeability; μ_0 is the permeability of air ($\mu_0 = 4 \times \pi \times 10^{-7}$).

The magnetic flux Φ is given by:

$$\Phi = B \times A = \frac{N \times i}{\Re} \tag{3.4}$$

$$\Re = \frac{l}{\mu \times A}$$

where $\Re$ represents the reluctance of the magnetic circuit.

Table 3.2 compilation of ampere-turns for series parts of magnetic circuit

Portion	Material	Area	$B = \Phi/A$	H	Length	$H \times l$	$\Re$
1	Steel	A_1	B_1	(curve) H_1	l_{l_1}	$H_1 \times l_{l_1}$	$\dfrac{l_1}{\mu \times A_1}$
2	Air	A_2	B_2	(B_0/μ_0) H_2	l_{d2}	$H_2 \times l_{d2}$	$\dfrac{l_2}{\mu_0 \times A_2}$
3	Steel	A_3	B_3	(curve) H_3	l_{l_3}	$H_3 \times l_{l_3}$	$\dfrac{l_3}{\mu \times A_3}$
4	Air	A_4	B_4	(B_0/μ_0) H_4	l_{d4}	$H_4 \times l_{d4}$	$\dfrac{l_4}{\mu_0 \times A_4}$
5	Steel	A_5	B_5	(curve) H_5	l_{l_5}	$H_5 \times l_{l_5}$	$\dfrac{l_5}{\mu \times A_5}$
6	Steel	A_6	B_6	(curve) H_6	l_{l_6}	$H_6 \times l_{l_6}$	$\dfrac{l_6}{\mu \times A_6}$

Thus, calculation of each series magnetic circuit section can be put in tabular form as in Table 3.2, which is hopefully self-explanatory.

The equations for this magnetic circuit can be simplified by assuming the cross sectional A of each portion is same. H_A and H_S represent the magnetic field intensity in the air-gap and steel respectively, which are constant for a given medium, if A is constant. Thus an 'electrical' equivalent circuit of the solenoid magnetic circuit is illustrated in Figure 3.4. (In the analogy between magnetic and electrical circuits: MMF≡voltage, flux≡current, and reluctances≡resistance.)
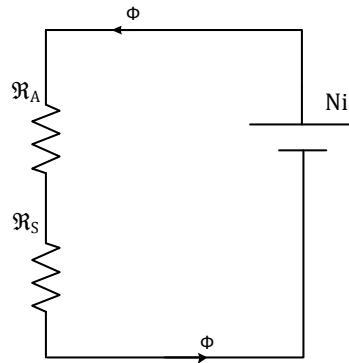
Figure 3.4 Equivalent magnetic circuit.

However, the property of magnetic reluctance is different from resistance, which is considered as an energy consumption component. Magnetically, reluctance is an energy storage element. The 'DC voltage' source represents the MMF produced by the coil amp-turns. $\Re_A$ and $\Re_S$ represent magnetic reluctance in the air-gap and steel respectively. Thus these magnetic reluctances are given by:

$$\Re_A = \frac{l_{d2} + l_{d4}}{\mu_0 \times A} = \frac{2 \times (g - x)}{\mu_0 \times A} \tag{3.5}$$

$$\Re_S = \frac{l_{l_1} + l_{l_3} + l_{l_5} + l_{l_6}}{\mu_r \times \mu_0 \times A} \tag{3.6}$$

Equation (3.2) becomes:

$$H_A \times (l_{d2} + l_{d4}) + H_S \times (l_{l_1} + l_{l_3} + l_{l_5} + l_{l_6}) = N \times i \tag{3.7}$$

Since the permeability in steel is higher than in air, most of the MMF is concentrated across the air-gaps. Thus the flux Φ is written as:

$$\Phi = \frac{N \times i}{\mathfrak{R}_A} = \frac{N \times i \times \mu_0 \times A}{2 \times (g - x)} \qquad (3.8)$$

The flux linkage Λ is defined as the flux that pass through all of the circuit, multiplied by the number of turns N:

$$\Lambda = N \times \Phi = \frac{N^2 \times i \times \mu_0 \times A}{2 \times (g - x)} \qquad (3.9)$$

The inductance of the solenoid, L, is defined as the ratio of flux linkages to the current through it:

$$L = \frac{\Lambda}{i} = \frac{N^2 \times \mu_0 \times A}{2 \times (g - x)} \qquad (3.10)$$

This equation is only valid for small solenoid current, since the steel cores will saturate and produce a nonlinear characteristic at high current. If the magnetising characteristic is linear, then the energy W_L stored in the solenoid coil is:

$$W_L = \frac{1}{2} \times L \times i^2 = \frac{1}{2} \times \frac{N^2 \times \mu_0 \times A}{2 \times (g - x)} \times i^2 \qquad (3.11)$$

As mentioned previously, all of the MMF is focused in the air-gaps, which means that all the energy will be applied within the air-gap to attain system movement $(g - x)$. Thus according to the conservation of energy, the magnetic force applying on an object is:

$$F_x = \frac{\partial W}{\partial x} \qquad (3.12)$$

and the energy density w_a in the air-gap is:

$$w_a = \frac{W_L}{2v_a} = \frac{\frac{1}{2} \times L \times i^2}{2 \times (g - x) \times A} = \frac{1}{2} \times \mu_0 \times \left(\frac{N \times i}{2 \times (g - x)}\right)^2$$
$$\approx \frac{1}{2} \times \mu_0 \times H^2 \qquad (3.13)$$

where v_a is the air-gap volume, namely $g \times A$ for each gap.

Assuming the current is allowed to change to maintain constant flux through the solenoid coil, a change in the system magnetic energy ΔW gives a change of energy stored in the air-gap. Therefore, if a mechanical force applied to the armature moves it an additional distance Δx, the work done is:

$$\Delta W_{magn} = 2 \times A \left[\frac{1}{2} \times \mu_0 \times H^2 \times (g - x + \Delta x) - \frac{1}{2} \times \mu_0 \times H^2 \right.$$
$$\left. \times (g - x) \right] \tag{3.14}$$
$$= \mu_0 \times H^2 \times \Delta x \times A$$

The energy balance between mechanical and magnetic must be equal, $\Delta W_{mech} = \Delta W_{magn}$, which gives the magnetic force:

$$F = \mu_0 \times H^2 \times A = \frac{B^2 \times A}{\mu_0} = \frac{\Phi^2}{\mu_0 \times A} \tag{3.15}$$

The magnetic force is inversely proportional to the cross sectional area A. This means that for a constant flux Φ, the magnetic force increases as the cross section area A reduces. However, there is a limit to how far the cross sectional area can be reduced before excessive fringing occurs, which effectively enlarges the cross sectional area A. Also, the magnetic circuit reluctance increases with excessive rounding of the solenoid core pole faces, where the magnetic material may saturate thereby decreasing the total flux Φ [3.4].

3.3 The AC energising coil circuit

3.3.1 Mathematical model

Solenoid operation was discussed in the previous section in term of magnetic force produced when energising the solenoid coil. Now the energising coil circuit is considered when meeting VCB requirements.

In

Table 3.1, the power required for closing the VCB contacts is far greater than the power required for holding them closed. Thus, a rectifier circuit with two switches is used to achieve these different power objectives, as shown in Figure 3.5. The rectifier switches are in a closed state when the VCB is off and are in an opened state once the VCB mechanical system moves. The step-down transformer is used to

achieve the required excitation voltage, $\sqrt{2}v\sin\omega t$. The uncontrolled rectifier circuit comprises the four diodes D_1 to D_4. R_L and R_S represent the load resistor and the solenoid coil resistance respectively, where R_L is introduced into the energising circuit to reduce the current once the VCB is closed and for dissipating the energy when the VCB has opened. No coil suppression is used, as this would slow down the rate of current fall at turn-off. The inductance of the solenoid coil is represented by L_S.
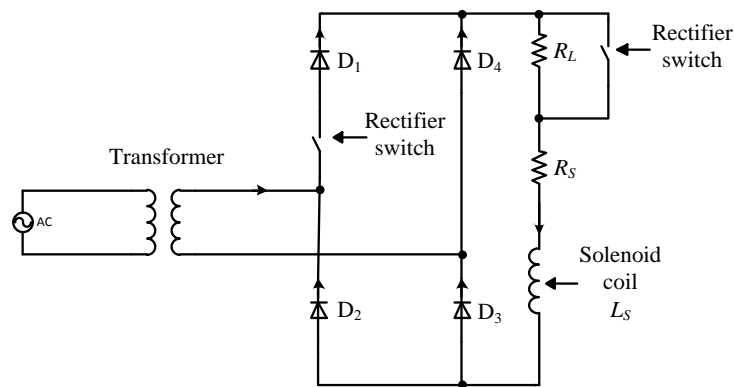
Figure 3.5 The AC energising circuit of the VCB

The solenoid is activated with a full-wave rectifier. Once the actuator has moved, both rectifier switches are opened, with the one switch reconfiguring the circuit as a half-wave rectifier, and the other switch adding series resistance to decrease the power to the solenoid, as per Table 3.1. Figure 3.6 illustrates the exciting and freewheeling circuits of the half-wave rectifier.
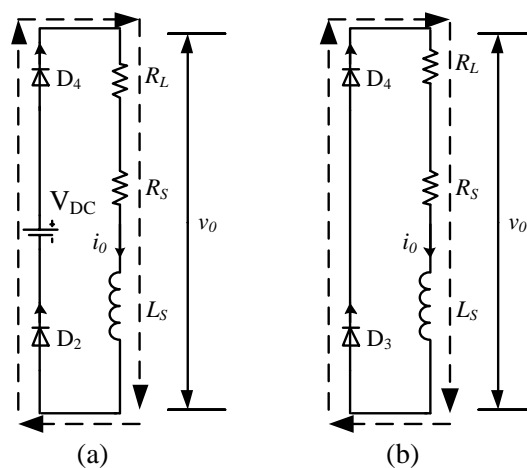
Figure 3.6 Half-wave rectifier during exciting and de-exciting circuit

The output voltage is half the secondary winding voltage of the transformer (sinusoidal input voltage). During the on state, the forward voltage applied across the power semiconductors (diodes) is small, so can be ignored in the analysis. Thus the mean output voltage v_0 (thence mean output current) is given by:

$$v_0 = \bar{I}_0 \times R_{L+S} = \frac{1}{2\pi} \times \int_0^\pi \sqrt{2}v \times \sin(\omega t) \times d\omega t$$

$$v_0 = \frac{\sqrt{2}v}{\pi} = 0.45 \times v = \bar{I}_0 \times R_{L+S} \qquad (3.16)$$

The RMS load circuit voltage v_{rms} is:

$$v_{rms} = \sqrt{\frac{1}{2\pi} \times \int_0^\pi (\sqrt{2}v \times \sin \omega t)^2 \times d\omega t}$$

$$v_{rms} = \frac{v}{\sqrt{2}} = 0.71 \times v \qquad (3.17)$$

According to the Kirchhoff's voltage law, the current through the solenoid coil must be continuous and above the minimum value required for the VCB to remain closed. The current during excitation is:

$$L_S \frac{di_0}{dt} + R_{L+S}i_0 = \sqrt{2}v \sin(\omega t) \qquad 0 \le \omega t \le \pi \qquad (3.18)$$

And the current during freewheeling is given by:

$$L_S \frac{di_0}{dt} + R_{L+S}i_0 = 0 \qquad \qquad \pi \le \omega t \le 2\pi \qquad (3.19)$$

During the period $0 \le \omega t \le \pi$, the supply current, through D_2 and D_4, is equal to the current through the solenoid coil:

$$i(\omega t) = i_0(\omega t)$$

$$= \frac{\sqrt{2}v}{Z} \sin(\omega t - \theta) + (I_{o2\pi} + \frac{\sqrt{2}v}{Z} \sin \theta) \times e^{-\omega t/\tan \theta} \qquad (3.20)$$

$$0 \le \omega t \le \pi$$

For

$$I_{o2\pi} = \frac{\sqrt{2}v}{Z} \sin(\theta) \times \frac{1 + e^{-\pi/\tan \theta}}{e^{\pi/\tan \theta} - e^{-\pi/\tan \theta}} \qquad (3.21)$$

$$\text{where } Z = \sqrt{(R_{L+S})^2 + (\omega L_S)^2}$$

$$\tan \theta = \omega L_S / R_{L+S}$$

During the period $\pi \leq \omega t \leq 2\pi$, when the supply current is zero, the coil current freewheels through the diodes D_3 and D_4:

$$i_0(\omega t) = i_{\text{D3+D4}}(\omega t) = I_{o1\pi} \times e^{-(\omega t - \pi)/\tan \theta} \qquad \pi \leq \omega t \leq 2\pi \qquad (3.22)$$

for

$$I_{o1\pi} = I_{o2\pi} \times e^{\pi/\tan \theta}$$

However, for VCB closing (before the two mechanical switches can operate), the energising circuit is a single-phase full-wave diode bridge circuit as in Figure 3.5. This means that the load resistor R_L is bypassed by one switch. Thus the current through the solenoid coil is:

$$i_0(\omega t) = \frac{\sqrt{2}v}{Z'} \sin (\omega t - \theta') + \frac{2 \sin \theta'}{1 - e^{-\pi/\tan \theta'}} \times e^{-\omega t/\tan \theta'} \qquad (3.23)$$
$$0 \leq \omega t \leq \pi$$

$$\text{where } Z' = \sqrt{(R_S)^2 + (\omega L_S)^2}$$

$$\tan \theta' = \omega L_S / R_S$$

The RMS current is derived by integration of this current equation (3.23) squared, and is given by:

$$I_{rms} = \frac{v}{Z'} [1 + 4 \sin^2 \theta' \tan \theta' \times (1 + e^{-\pi/\tan \theta'})]^{1/2} \qquad (3.24)$$

The solenoid coil withstands the transformer secondary rectified voltage and its mean voltage is:

$$v_0 = \bar{I}_0 \times R_L = \frac{1}{\pi} \times \int_0^\pi \sqrt{2}v \times \sin(\omega t) \times d\omega t \qquad (3.25)$$

$$v_0 = \frac{2\sqrt{2}v}{\pi} = 0.9 \times v = \bar{I}_0 \times R_L$$

At coil deactivation, the coil current freewheels to zero through diodes D_3 and D_4. Initially the load resistor R_L is in the decay path, before its parallel connected bypass switch has operated.

3.3.2 The simulation and experimental results

According to equation (3.15), when energising the solenoid coil, once the coil current increases to a certain level, the armature starts to close as the magnetic force is greater than the spring force. The rectifier switches open when the internal electrodes of the vacuum interrupter have closed. Hence, the full-wave rectifier circuit becomes a half-wave circuit, which produces less power, but enough to complete contact closure and contact holding. As the air gap decreases, the flux increases and coil current is reduced. However, the reduced coil current still maintains the flux above the necessary threshold level. When the VCB receives the signal to open, the armature circuit remains close until the solenoid coil current decreases to a certain level. As has been indicated, it is a bi-directionally electrically activated solenoid mechanism. Thus the electrodes of the VCB start to part after the armature has moved minimally. The simulation of the energising circuit utilises **PSPICE** software to analyse the voltage and current of the solenoid coil in terms of rated voltage of the UK.
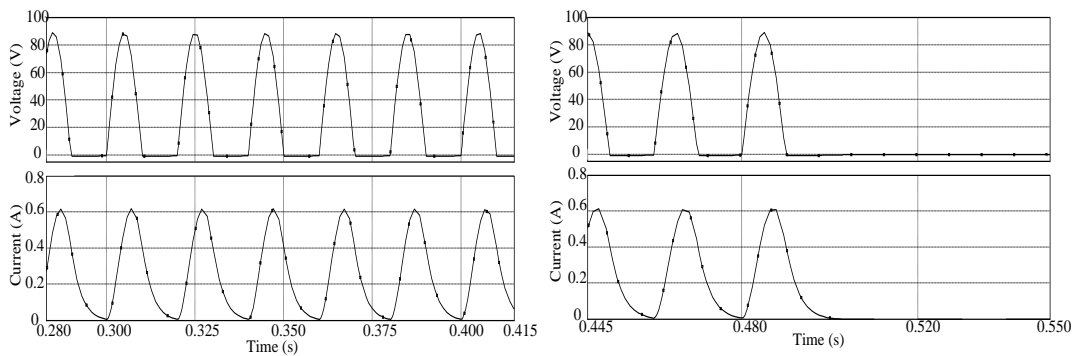
Figure 3.7 The simulation results of voltage and current during VCB holding and separation.
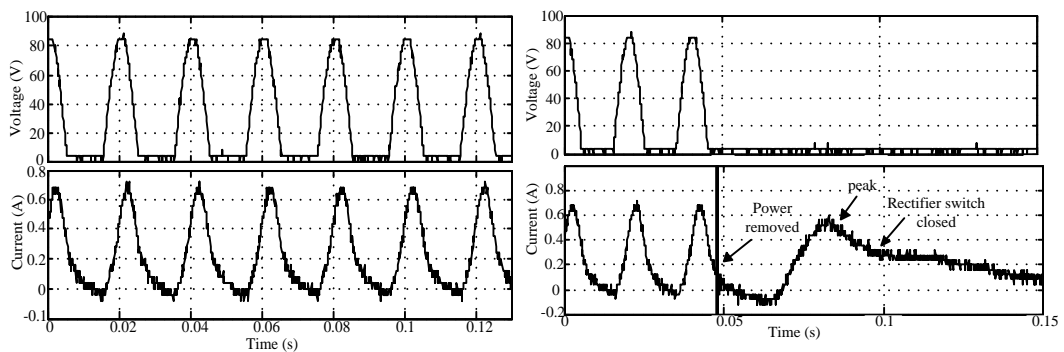
Figure 3.8 The experimental results of voltage and current during VCB holding and separation.

Figure 3.7 and Figure 3.8 show the simulation and experimental results respectively. It is apparent that both figures are basically the same during the steady-state but completely different during separation. This difference is a 'peak' in the practical coil current even if its external power is removed. This is due to the counter-electromotive force (counter-EMF), which is not included in the basic PSpice circuit model. This EMF feature will subsequently be exploited. The change of discharge rate of the coil current after the peak indicates the rectifier switches closing, one of which bypasses the load resistor R_L, hence increasing the time constant.

The VCB arc properties during the separating period, as shown in Figure 3.9 (a), were investigated with a test circuit comprising a DC source, the VCB, and a transmission line represented by a resistor and an inductance. As mentioned in Appendix B.1, the arc voltage indicates the separation of the internal electrodes, while the current magnitude through the VCB dominates the period of the arc voltage after electrode separation. For example, forgiven electrodes, the arc period is 0.9ms for 6kA interruption current but reduces to 0.1ms for 1kA. For a low test current, the arc voltage period can be considered as an indication of the electrode separating period.
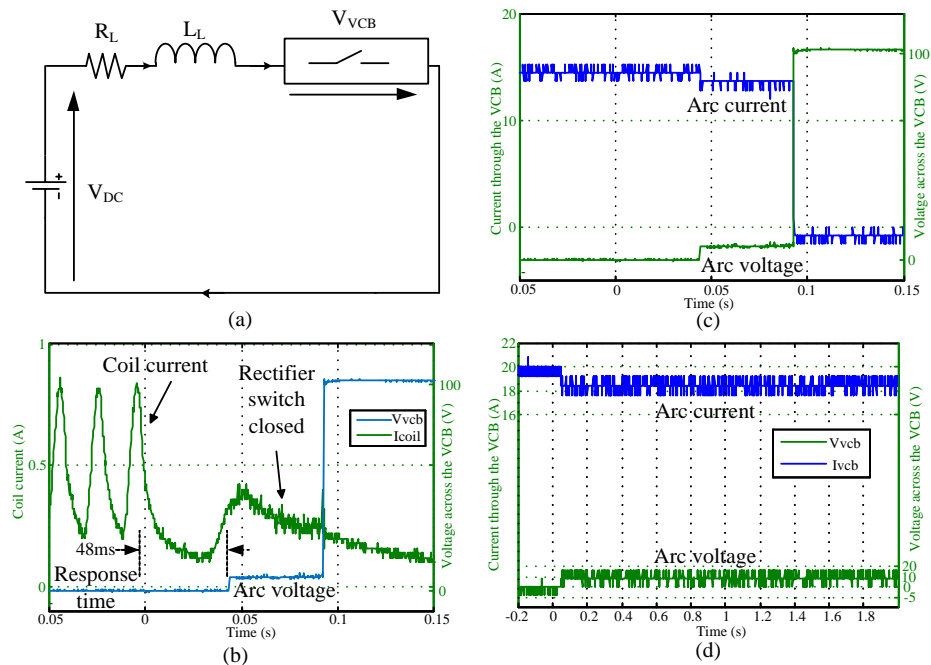
Figure 3.9 A test circuit and its experimental results (V_{DC}=120V I_{DC}=15A)

51

Figure 3.9 (b) shows that the response time, from receiving the off signal to internal electrode separation, is approximately 48-55ms (having repeated this operation at least 100 times). Figure 3.9 (c) illustrates that the arc voltage is 12V, provided the electrodes part. Having varied the DC source with other factors unchanged this is shown to be independent of the DC source (V_{DC}). Since V_{DC} is 120V, the arc current is reduced when the arc voltage (12V) occurs. The arc duration suffers random rupture at 15A but is stable at 18A. As shown in Figure 3.9 (d), the 18A arc current continues to flow until its source of energy is removed. This proves the existence of current chopping, i.e. the arc is unstable if the conducting current is below a certain value (18A) for a given vacuum interrupter (Cu). This current chopping level (<18A) establishes that the VCB electrode material is made of pure copper [3.5].

Since the VCB used in this thesis is designed for AC systems, which include inductive elements, fast separating and closing are not essential. The 48ms response time of the VCB is therefore adequate. However, in DC systems that lack passive components (and an AC supply) to constrain the magnitude of the fault current, a VCB with fast response and rapid separation is necessary. Thus, methods to accelerate the opening speed should be explored, without changing the mechanism, since exploitation of existing VCBs in DC environments is the subject of this thesis. That is, only the energising circuit should be changed, and not the mechanical parts.

The coil current is always reduced from the same value I_m, after removing its source of energy. For analysis the parameters of the coil and the load (R_L, R_S and L_S) are assumed constant, where the coil inductance L_S is assumed independent of air-gap changes. Reviewing Figure 3.6 (b) and considering the combined on-state voltage of the diodes to be V_S, the equation to describe the discharge loop is:

$$L_S \frac{di_0}{dt} + R_{s+L} i_o = -V_S$$

With the initial condition $i_o(t) = I_m$, this yields:

$$i_0(t) = \frac{-V_S}{R_{L+S}} \left(1 - e^{\frac{-t}{\tau}}\right) + I_m e^{\frac{-t}{\tau}} \tag{3.26}$$

where $\tau = \frac{L_S}{R_{S+L}}$, and V_S = voltage across the solenoid coil.

When $i_0(t) = 0$:

$$\frac{-V_S}{R_{L+S}}\left(1 - e^{\frac{-t}{\tau}}\right) = I_m e^{\frac{-t}{\tau}}$$

$$t = -\tau \times \ln\left(\frac{V_S}{V_S + I_m R_{L+S}}\right) \tag{3.27}$$
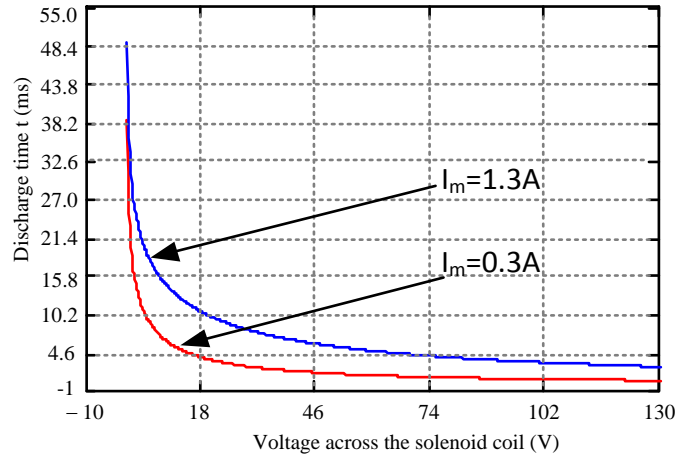
Figure 3.10 Relationship between discharge time and voltage across the solenoid coil

The plots in Figure 3.10 represent equation (3.27) for a range of voltages across the solenoid coil, based on coil currents (I_m) of 1.3A and 0.3A. It is apparent that the higher coil current needs more time to discharge. However the discharge time reduces as the voltage increases. Thus, in order to accelerate the discharge rate, to speed up the VCB separating period, an increase in voltage applied across the solenoid coil is proposed. However, there is a limit to how high the voltage can be before the occurrence of insulation breakdown.

3.4 The DC energising coil circuit

3.4.1 The mathematical model

In order to reduce the VCB response time, without changing the physical mechanism, a DC energising coil circuit is proposed with applies a high voltage across the

solenoid coil. Pulse width modulation (PWM) signals for solid state switches are produced by utilising closed-loop current control with a proportional plus integral (PI) regulator (as shown in Appendix A.2.3). The objective is to achieve a controllable coil current that retains a similar function as an AC energising circuit during the VCB closed state, but accelerates the discharge rate of the coil current once the off signal is received. Current control removes current variation due to resistance variation resulting from coil heating.
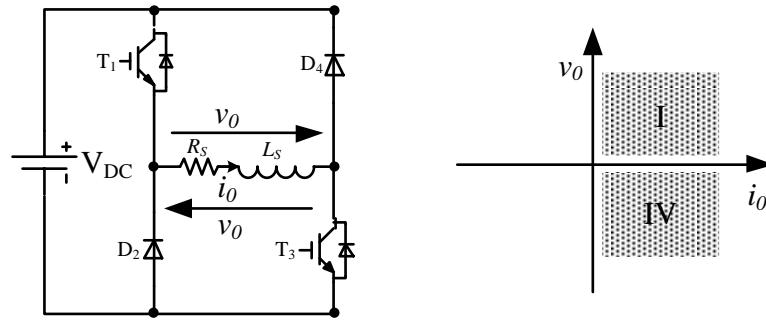
Figure 3.11 The DC energising circuit for the VCB.

The circuit in Figure 3.11 is termed an asymmetrical half H-bridge circuit, which includes insulated gate bipolar transistors (IGBT) represented by T_1 and T_3, a DC source V_{DC} and two complementary diodes D_2, and D_4. As for the load, the load resistor R_L is removed thus only the coil resistor and inductor remain, represented by R_S and L_S respectively. Bi-directional voltage output v_0 but unidirectional coil current i_0 are realised by controlling switches T_1 and T_3 to operate in the first and fourth quadrants. Therefore three different voltage states can be applied across the solenoid coil: $\pm V_{DC}$ and 0V, where there are two topologies for producing the zero output state, as shown in Figure 3.12 (b).

During the positive output voltage state, V_{DC} is impressed across the solenoid coil when both switches T_1 and T_3 are both on, as shown in Figure 3.12 (a). The equation describing this condition is:

$$L_S \frac{di_0}{dt} + R_s i_o = V_{DC}$$

which yields:
$$i_0(t) = \frac{V_{DC}}{R_S}\left(1 - e^{\frac{-t}{\tau}}\right) + \check{I}e^{\frac{-t}{\tau}} \qquad (3.28)$$

$$\text{where } \tau = \frac{L_S}{R_S}$$

For VCB closing, the coil current starts to increase from zero, so that $\check{I} = 0$. Otherwise $\check{I}$ is the value at the end of the previous cycle.
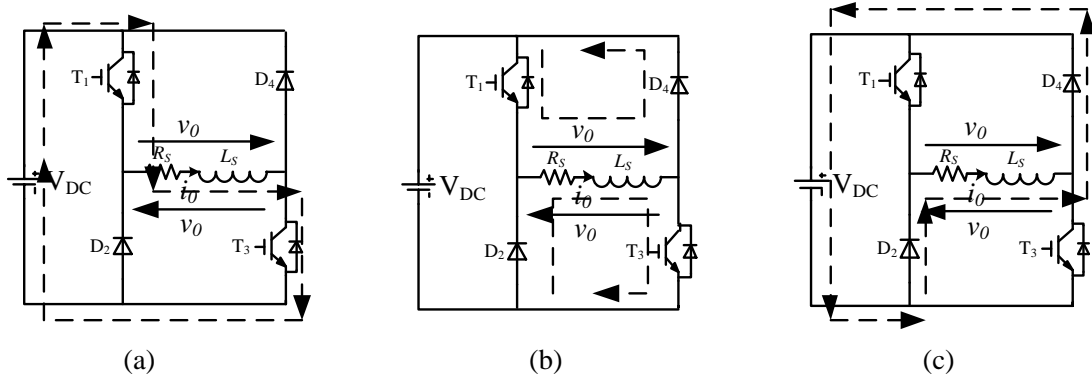
Figure 3.12 DC energising operational current paths: (a) T$_1$ and T$_3$ introducing a +V$_{DC}$ path; (b) T$_1$ and D$_4$ (or T$_3$ and D$_2$) introducing a 0V loop; and (c) D$_2$ and D$_4$ introducing a -V$_{DC}$ path.

In a zero voltage loop, the output voltage is zero, and T$_1$ and D$_4$ (or T$_3$ and D$_1$) are conducting, as shown in Figure 3.12 (b). Hence the circuit equation is:

$$L_S\frac{di_0}{dt} + R_s i_o = 0$$

which yields:
$$i_0(t) = \hat{I}e^{\frac{-t}{\tau}} \qquad (3.29)$$

$$\text{where } \tau = \frac{L_S}{R_S}$$

In a negative voltage loop, the circuit loop only involves the D$_2$ and D$_4$. A negative voltage is impressed across the solenoid coil to achieve a rapid current drop, as defined by:

$$L_S\frac{di_0}{dt} + R_s i_o = -V_{DC}$$

which yields:
$$i_0(t) = \frac{-V_{DC}}{R_S}\left(1 - e^{\frac{-t}{\tau}}\right) + \hat{I}e^{\frac{-t}{\tau}} \qquad (3.30)$$

55

where $\tau = \frac{L_S}{R_S}$

By alternating the zero volt loops, the load frequency is twice each IGBT switching frequency. Consequently the output ripple current is reduced for a given switching frequency. Decreasing the ripple current results in a more stable solenoid mechanism, as spring distortion and vibration will be less. Additionally, the semiconductor losses are evenly distributed [3.6].

3.4.2 Simulation and experimental results

In order to realise fast VCB response to on and off signals, auxiliary control circuitry is introduced to attain maximum efficiency from the DC energising circuit. As mentioned, there are two spring connected rectifier switches in the original AC energising circuit. The relationship between the rectifier switches and the state of the VCB is that they are off when the VCB on and on when the VCB off (but with some hysteresis delay). Thus these now redundant rectifier switches can be used in conjunction with high speed Optocouplers (6N137 shown in Appendix A.2.6) to observe the state of the VCB. Along with the logical control circuit shown in Figure 3.13, the control ON/OFF and PWM signals are fed to IGBT switches T_1 and T_3.
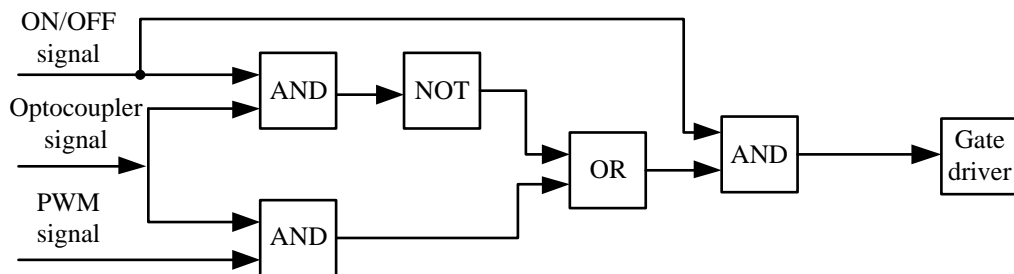
Figure 3.13 Logical control circuit

To attain maximum power quickly for VCB closing, a 'high' signal is produced by the ON/OFF control board (shown in Appendix A.2.1) and is transmitted to the gate driver by the logical control circuit. Then the PWM signal produced by the PI regulator replaces the previous 'high' signal, thereby reducing the power delivered to the holding level.
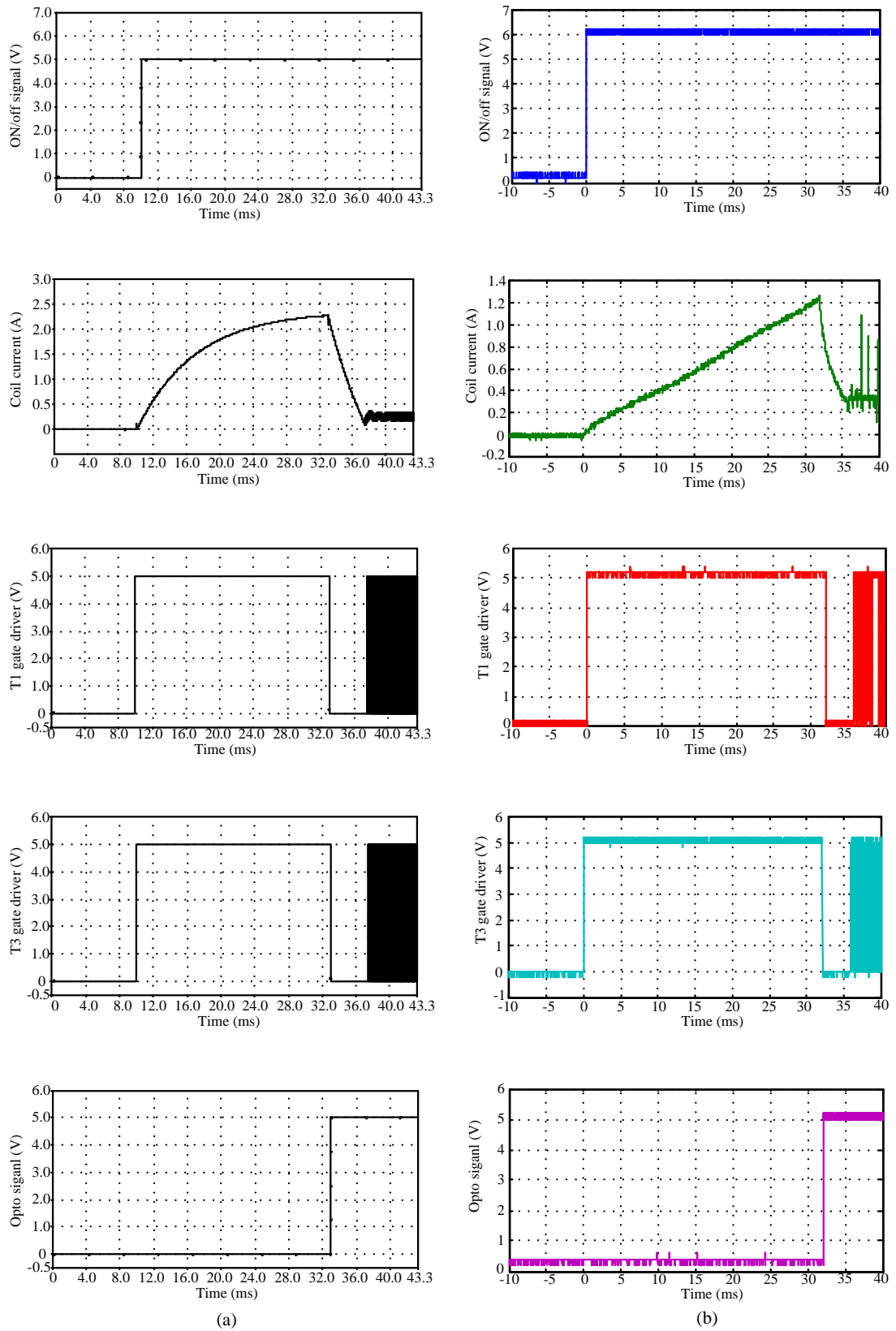
Figure 3.14 DC energising circuit during closing: (a) simulation results; (b) experimental results ($V_{DC}=108V$, $i_0=0.3A$).

The plots in Figure 3.14 illustrate the DC energising circuit. The simulation and experimental results are similar, except for the coil current. The simulations use a fixed inductor, while practically the air-gap dominates solenoid coil inductance which linearly increases with decreasing air-gap before saturating, according to equation (3.10). Consequently, the linear increase in the practical coil current results from the continuously changing time constant. However, both coil currents decrease to 0.3A, after Opto signal feedback, indicating the VCB is operating as designed.
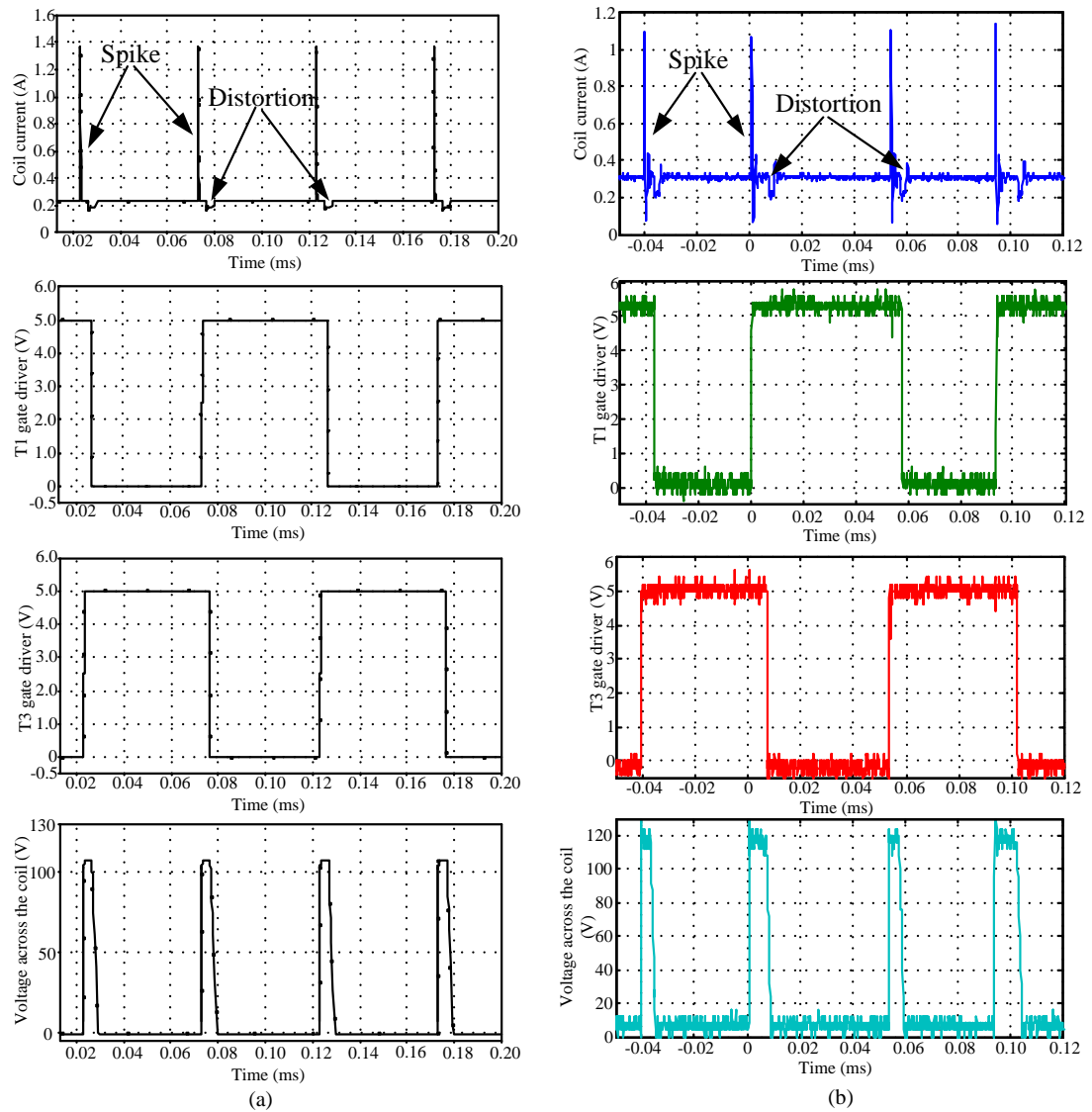
Figure 3.15 The DC energising circuit during steady-state: (a) simulation results; and (b) experimental results (V_{DC}=108v, i_0=0.3A).

From the simulation and experimental results in Figure 3.15, the 10kHz coil ripple current component can be ignored. This means the coil current is virtually DC. The stray (inter-winding and inter-turn) capacitance not only results in a coil current 'spike' each time T_1 and T_3 turn-on, exciting the solenoid coil, but also causes 'distortion' once a zero voltage loop occurs. Although the spikes and distortion do not affect the behaviour of the VCB mechanism, they do introduce control board noise. The isolation circuit shown in Appendix A.2.5 is utilised to alleviate noise problems.
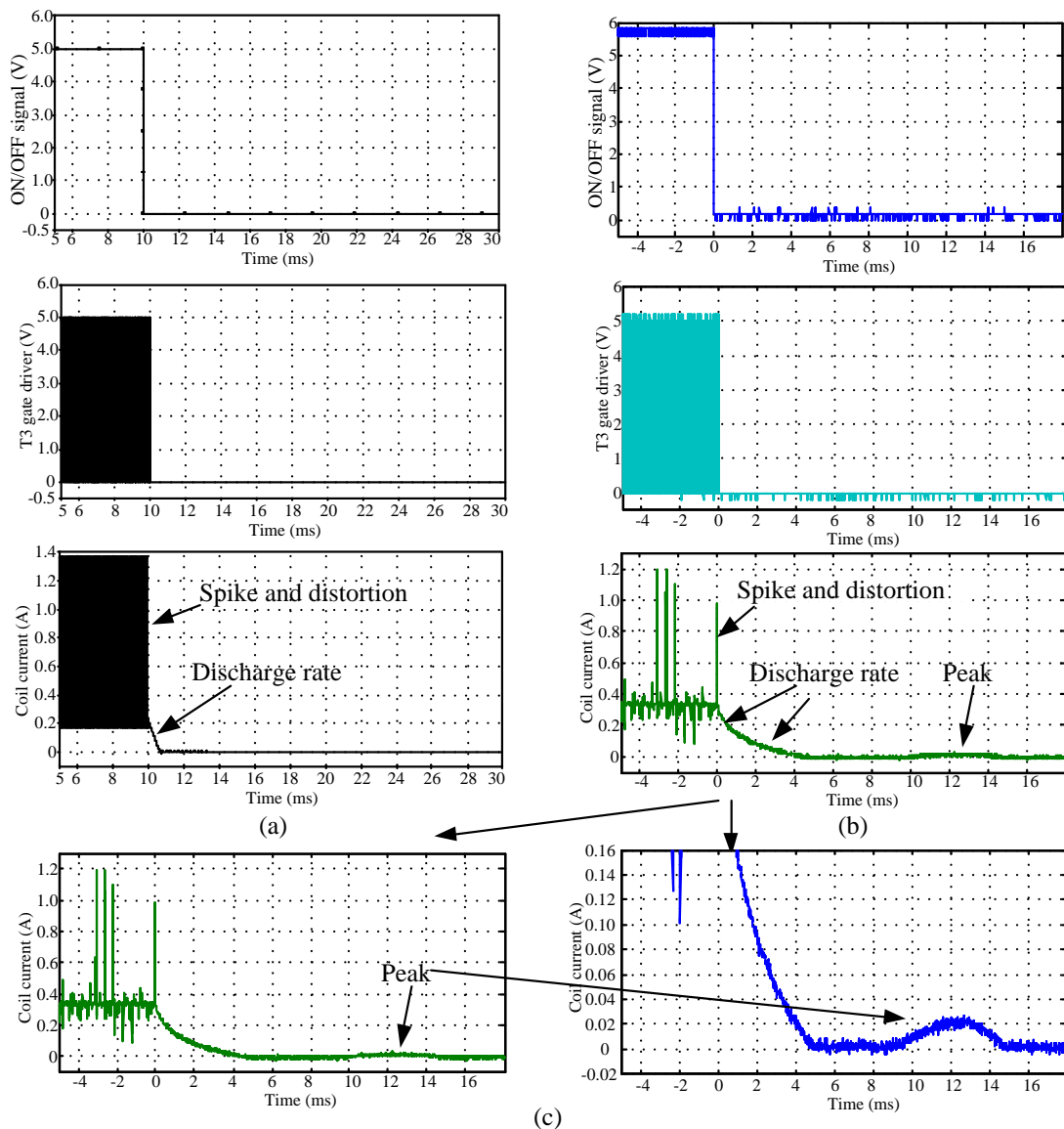
Figure 3.16 energising circuit during separating moment: (a) simulation results; (b) experimental results; and (c) expanded result for coil current (V_{DC}=108V, i_0=0.3A).

59

The results for the DC energising circuit during VCB contact separation are shown in Figure 3.16 including (a) simulation results, (b) experimental results, and (c) expanded view of the coil current. The logic control circuit providing the PWM signals to control the switches cease once the 'OFF' signal occurs. The simulation and experimental results are similar, except the coil current which, due to the coil inductance, is shown experimentally to vary linearly with VCB movement.

When the 'off' signal appears, the experimental coil current contains two distinct discharge regions. The first region is the same as the simulation results, i.e. a linear decrease at a fast rate. The second region is an exponential decrease when the armature starts to separate from the solenoid coil (this observation will be proved in Section 3.4.3). Finally, after reaching zero, a peak is then observed in the experimental waveform (but not the simulations), as seen in Figure 3.6 (c).

A fast VCB response, associated with using the DC energising circuit in Figure 3.9, is confirmed in Figure 3.17. By considering Figure 3.17 (a) and (c), the reponse time between the 'off' signal and arc voltage is 13 to 15ms, after repeating this operation at least 100 times. The PWM DC approach is faster than the AC energising method. The coil current peak occurs at around 8ms and lasts for approximately 6ms after coil power removal, as shown in Figure 3.17 (b). Comparing this result to the AC energising circuit results in Figure 3.8 and Figure 3.9, there are two observations. Regardless of whether or not an AC or DC energising circuit is used, the occurrence of an arc voltage is always accompanied by the coil current peak, and the rectifier switches are always switched on near the end of the peak. This gives information that the coil current peak occurrence is consistent with the formation of the arc voltage, consistently occuring within tens of microseconds of each other. In Figure 3.17 (d) the opto signal bounces at around 14ms, because the rectifier switches change is dominated by the action of the mechnical spring.

The solenoid coil voltage is shown in Figure 3.17 (e). The negative volatge is impressed across the solenoid coil to speed up the coil current discharge rate once the off signal occurs. Then after 5ms, the voltage rises and since the coil current is zero, (the discharge loop shown in Figure 3.12 (c) is no longer conducting) the voltage rise displays the coil counter-EMF (counter-electromotive force) due to the movement of

the armature causing a change of flux Φ in the solenoid magnetic circuit. (This will be discussed in Section 3.5.1). With the amature parting from the coil, the voltage potentially continues to increase until the counter-EMF is greater than the DC source. The coil voltage is eventually clamped by the bridge diodes to the DC source, and coil current rises.
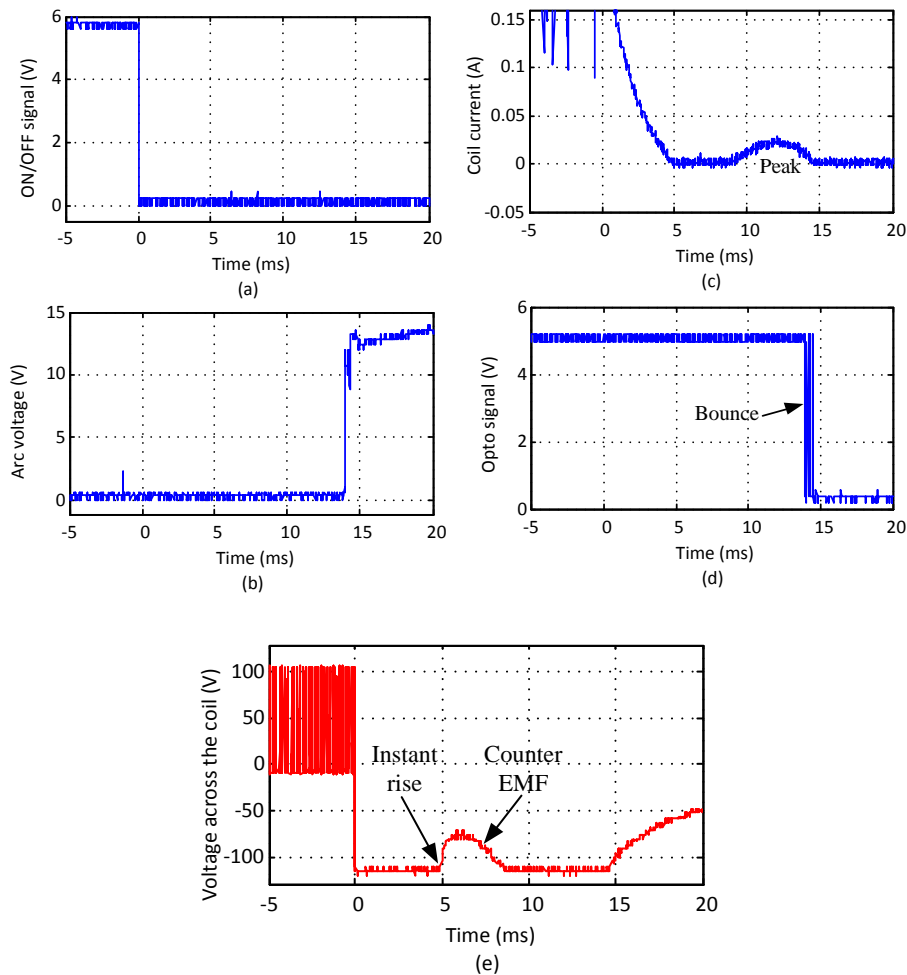
Figure 3.17 Experimental waveforms of the DC energising circuit and opto circuit (V_{DC}=108v, i_0=0.3A).

Since the separating moment is significant, experiments were performed to find the time difference between the coil current peak and the arc voltage, by varying the voltage applied across the solenoid coil (DC source), as shown in Figure 3.18. Although equation (3.27) is based on assumptions, such as fixed parameters, its practicability is supported by the experimental results in Figure 3.18 (a). A higher DC source voltage discharges the coil current faster, with an associated acceleration

in VCB movement. Figure 3.18 (b) shows that the peak current amplitude decreases as the DC source voltage is increased, and disappears at voltage higher than 128V. The timing of its formation is however consistent with respect to the arc voltage formation. Figure 3.18 (c) illustrates a contrary phenomenon, specifically that the counter-EMF disappears at low DC source voltages of 78V and 87V. The figure also shows that the time to the initiation of the counter-EMF reduces as the DC source voltage is increased.
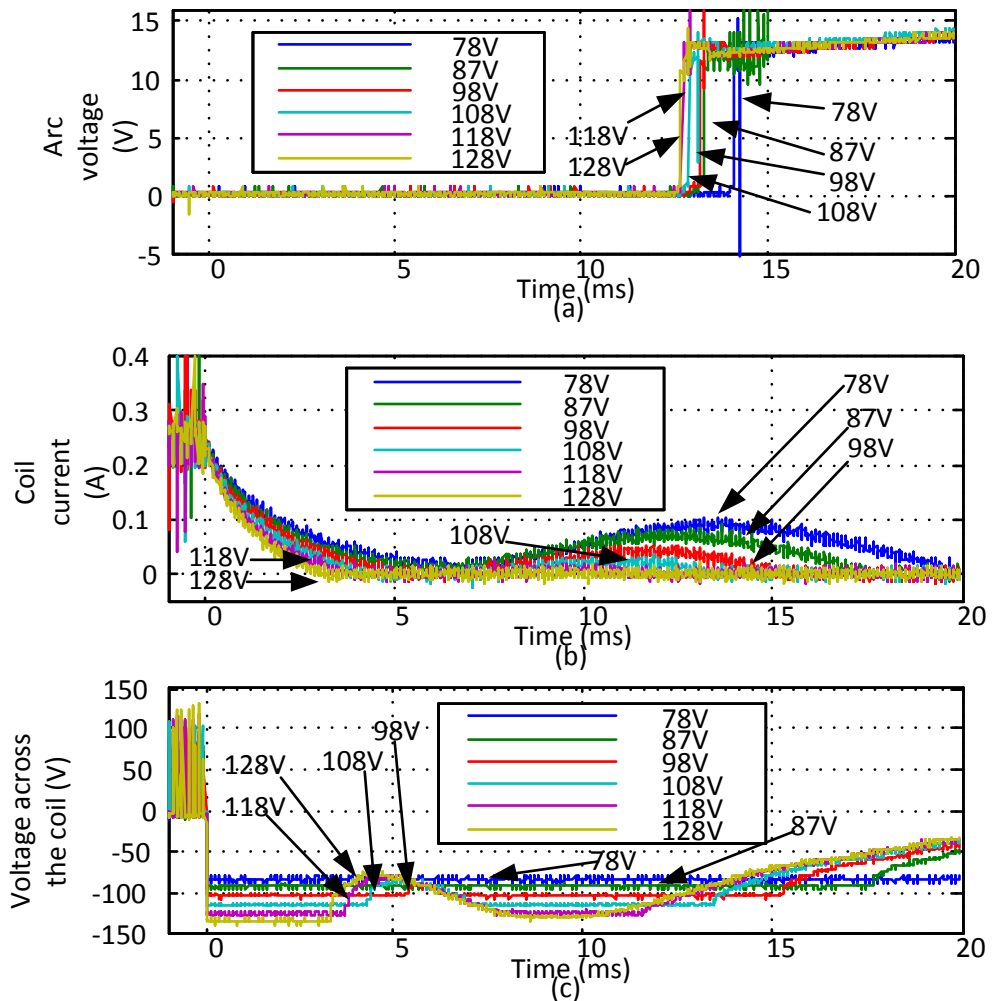
Figure 3.18 Waveforms demonstrate the relationship between the peak and the arc voltage based on a range of DC source (i_0=0.3A).

To explain the observations drawn from Figure 3.18, the armature movement principle is now discussed in detail. Equation (3.15) shows that the magnetic force is

directly proportional to magnetic flux Φ squared, which derives from the coil current. The VCB contacts stay closed because the magnetic force produced by the coil current is far greater than the minimum spring force required to force the armature away from the coil. Therefore the minimum spring force can be expressed as a threshold value in current terms. Since close-loop current control is employed in the DC energising circuit, the coil current always reaches to same value during the VCB closed state, no matter what voltage is applied across the solenoid coil. This means that once the off signal is received, the coil current starts to reduce from same value, independent of the source voltage. The time to the threshold current reduces if the DC source voltage is increased, because of the higher reducing *di/dt*. That is, the armature will start to separate earlier if a higher DC source is used. This means that the counter-EMF appears sooner if a higher DC source is used.

As coil current falls below the threshold level, the armature circuit starts to separate. The opening speed of the VCB is dominated by the difference between the net force produced by the spring force and the decreasing magnetic force. As for magnetic force, it presents an ever-decreasing trend because Φ reduces not only due to the decreasing coil current but also due to an increase of the magnetic reluctance (increasing air gaps), according to equation (3.4). Again the coil current (hence magnetic force) falls faster by increasing the DC source. The spring force decreases almost linearly due to the increasing air-gap. Thus, the initial opening speed of the VCB increases as the DC source is increased. The counter-EMF is influenced by the residual magnetisation and the opening speed of the VCB, which will be discussed in Section 3.5.1. As a consequence the counter-EMF increases as the DC source is increased.

When the coil current reduces to near zero, the net forces (spring and magnetic forces) produce a relatively stable movement, with the spring force dominating. The magnetic force reduces further, and is mainly produced by the residual magnetism that is relatively small compared to the ever-reducing flux density B. Thus, the counter-EMF finally disappears.

Whether the counter-EMF is observed or not, depends on the DC source magnitude. With a high voltage, it appears earlier if the coil current discharges to zero faster.

Although the counter-EMF finally disappears, the peak current amplitude produced by the voltage difference between the counter-EMF and the DC source increases as the DC source is reduced.

3.4.3 Auxiliary circuit for observing the instant of separation of the VCB

Coil current discharge in practice can be divided into two parts based on the movement of the armature and on the threshold value. Coil current starts to decrease at the same rate as shown in the simulation of Figure 3.16 (a), until reaching the threshold value. Then, as the coil current reduces below the threshold, it exponentially decreases to zero. The VCB separation movement can be observed in detail by utilising a slot sensor (Transmissive Opto Schmitt sensor HOA2001) that produces a 'high' output signal when its optical path is uninterrupted. The slot sensor is placed into a track that allows the sensor to be adjusted within a range of distances, and a blade is fixed to the armature, as shown in Figure 3..
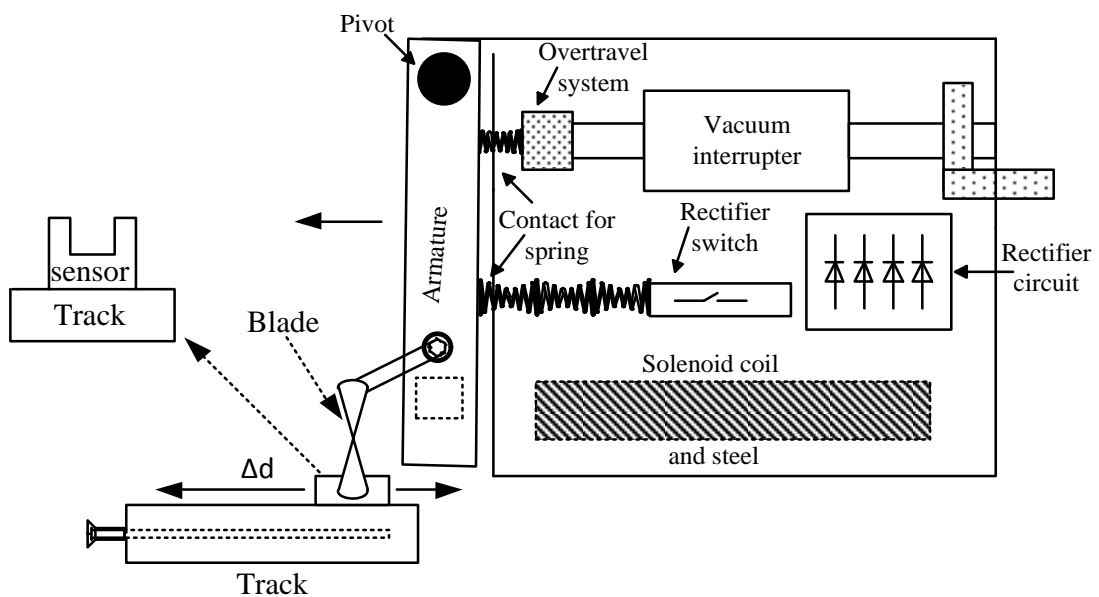
Figure 3.19 Schematic diagram of a solenoid operated VCB with a slot sensor

In order to attain accurate results, the slot sensor was placed mechanically close to the armature. With the slot sensor, the critical point to indicate the armature movement is illustrated in Figure 3.19. Any errors result from spring deflection,

deformation of the contact area, coil current spikes, etc. These factors cause uncertainty in net force production, resulting in a variable and relative displacement between the blade and the slot sensor during each operation. The instant of separation is also unpredictable because the net force is unpredictable, as previously mentioned. However, even with displacement errors, the signal from the slot sensor always occurs before the coil current reduces to zero.
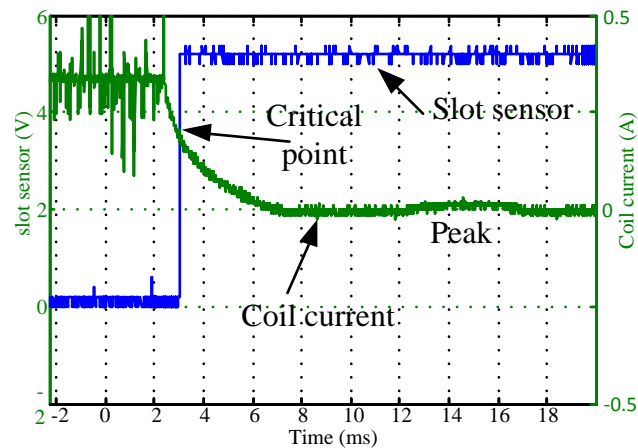
Figure 3.19 Experimental result for the slot sensor and coil current

Separation of the internal electrodes is of more interest and significance than armature separation, since it immediately precedes generation of the vacuum arc. Due to the small test current used, the occurrence of the arc voltage implies separation of the electrodes. Thus the slot sensor is adjusted along its mounting track until the slot sensor signal and the arc voltage occur at the same time as shown in Figure 3.20 (a) and (b). Based on this reference point, the displacement difference (Δd) and an associated time difference (Δt) are produced as the slot sensor moves away from the armature, as shown in Figure 3.20 (c) and (d). Thus, the movement of the VCB after the occurrence of the arc voltage can be studied by analysing the relationship between the time difference (Δt) and the displacement difference (Δd).

Figure 3.20 (e) illustrates that the armature linearly separates from the solenoid coil with a velocity of approximately 1m/s after the occurrence of the arc voltage. This means that the armature maintains stable movement, meaning the net force becomes stable. Also the plots in Figure 3.18 (c) show that the counter-EMF displays the same

trajectory, even if it operates over a range of DC sources voltages, because the spring force dominates the armature movement.
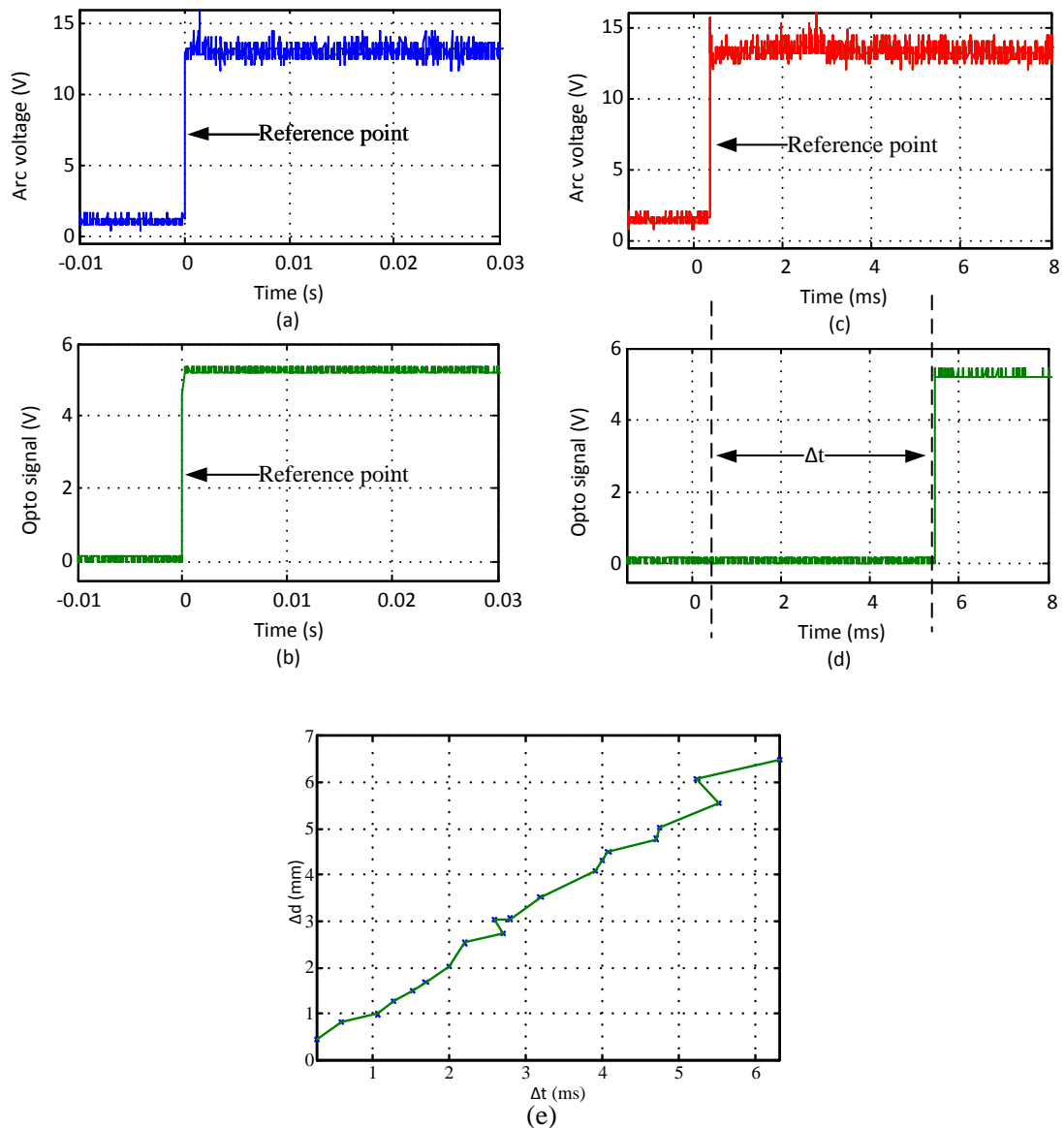
Figure 3.20 Experiment waveforms based on the arc voltage and slot sensor: (a) arc voltage; (b) opto signal; (c) arc voltage; (d) opto signal.

The DC energising circuit adopted a close-loop current controller to reduce the opening time of the VCB. Experimental results demonstrate that its separation time is improved from 48-55ms to 13-15ms by replacing the original AC energysing circuit. Both coil driving approaches illustrate that the occrrence of the EMF peak is consistent with the formation of the arc voltage. Generally, the VCB opening time is

required to decrease as the application power rating increases. This is because, in a DC network, the energy to be disspated is a function of fault current squared. The amount of stored energy required to produce a current-zero in the VCB is related to the separation time, that is, short separation time means a reduction in energy requriment. Therefore the incurred stresses reduce as the separation time decreases.

Since the employed VCB is only upgraed in its energising circuit, the opening time could be further improved if its mechanical topology were to be modified. Greenwood [3.7] stated that VCB separation time can be achieved within 5ms by intoducing a hydraulic breaker actuator. Holaus [3.8] proposed that the opening speed can achieve a velocity of 12m/s to 50m/s in terms of the moving mass, by utilising an opening coil for VCB separation (rather than only a spring). The same coil drive circuit as in Figure 3.11 could be applied to this second coil, giving the same performance improvement as achieved for the single coil VCB.

3.5 The back electromotive force after coil discharge

3.5.1 Why a counter-EMF occurs

The peak in the coil current is due to the counter-EMF induced by the magnetic flux change because of the relative movement between the armature and the solenoid coil.

In order to understand how the counter-EMF arises, the hysteresis loop in Figure 3.21 is interpreted. Initially, the steel core is an un-magnetised ferromagnet. As the coil is energised, the magnetisation M and the induced magnetic flux density Bincrease with an increase in the magnetic field strength H which is proportional to the coil current. As the coil is energised further, the increases obey the initial magnetisation curve until saturated, during which period:

$$B_s = \mu_0(H + M_s) \cong \mu_0 M_s \tag{3.31}$$

where μ_0 is permeability of a vacuum, M_s is saturation magnetisation, and B_s is saturation flux density.

However, B does not follow the initial curve to decrease if H (excitation current) is reduced. Instead, it decreases along another trajectory. When H is reduced to zero, it leaves a net magnetisation, denoted by B_r, in the core. B can only be reduced to zero when the H field is applied in the negative direction to a specific value H_C, called the *coercive force.* Since the steel is a 'soft' material, there is hysteresis loss during its magnetisation under ac operation. This is illustrated by a narrow but high hysteresis loop of small area, as shown in Figure 3.21. Ferromagnetic elements (iron, nickel, cobalt) always exhibit hysteresis where there is a lag or delay between B and H in an alternating field [3.4].
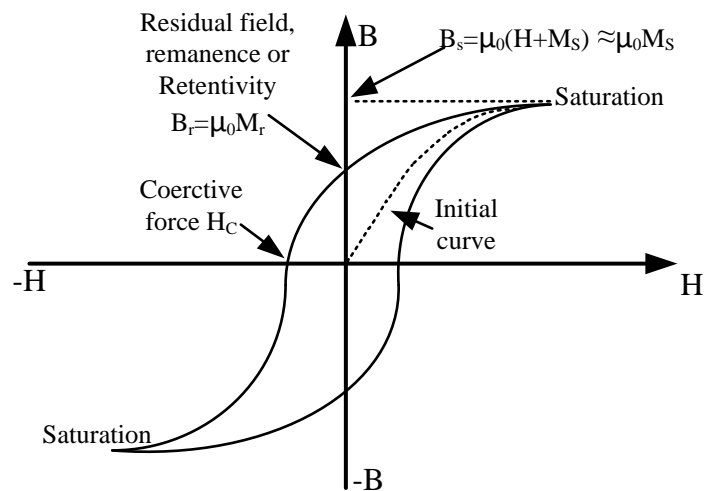
Figure 3.21 Hysteresis loop of soft magnetic materials which are readily magnetized and demagnetized.

With reference to the VCB magnetic circuit in the Figure 3.3, (assuming DC excitation) the residual magnetisation B_{r0} is permanent magnetisation which is the state that exists in permanent magnets. The magnetic circuit B_{r0} is not the saturation residual magnetisation B_r since there is always an air-gap even if the VCB has been closed. In other words, a permanent magnet is produced by increasing the coil current and then reducing it to zero in this experiment. The remaining magnetisation B_{r0} can be considered as the source for the B field in the solenoid magnetic circuit. As a consequence, the new magnetic circuit is shown in figure 3.23.
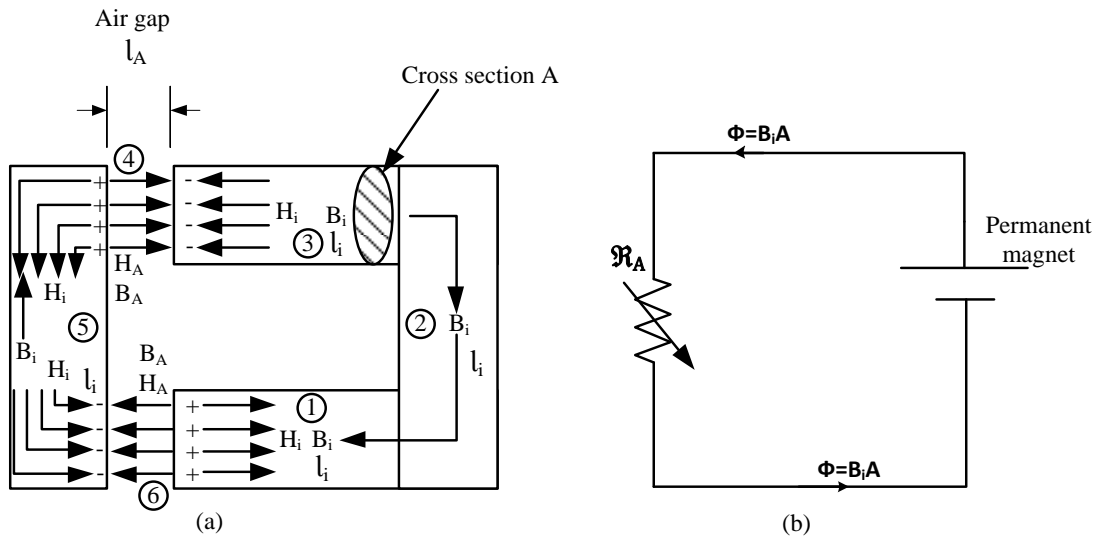
Figure 3.22 The magnetic circuit and its electrical equivalent of an electromagnet

During separation of the VCB, the air-gap is increased as the armature parts from the solenoid coil. This means that the reluctance of the solenoid magnetic circuit is increased causing a corresponding decrease in flux Φ and flux density B which were originally $B_{r0}A$ and B_{r0} respectively. To find the point on the hysteresis loop of Figure 3.21, equivalent to the new flux density through the steel (and therefore also in the air-gap, assuming $A_i = A_A$, then $B_i = B_A$), an equation in terms of H_i and B_i can be derived in terms of the coordinates in Figure 3.21. According to the Ampere's law $\oint Hd\mathrm{l} = NI$, with $NI = 0$, the equation to describe the circuit of Figure 3.22 (a) is:

$$H_A \mathrm{l}_A + H_i \mathrm{l}_i = 0 \qquad (3.32)$$

where H_i and H_A represent the magnetic field strength through the steel and air-gap respectively, l_i is the total length of steel including the armature, and l_A is gap distance. Due to the continuity of flux in the series circuit: $\Phi_i = \Phi_A$, so that the flux density ignoring fringing is:

$$B_i = B_A \qquad (3.33)$$

which can be rewritten as $H_A = B_i / \mu_0$. Substituting into equation (3.32), gives the straight line equation:

$$B_i = \frac{-l_i}{l_A}\mu_0 H_i \tag{3.34}$$

The relationship between B and H in the steel is obtained in term of the geometry of the circuit. This line is defined as the *shearing line* which intersects the BH curve in Figure 3.23. The solution to equation (3.34) is the point of intersection with the hysteresis loop. The reluctance of the air-gap $\mathfrak{R}_A$ increases as the gap distance increases, thus flux Φ and flux density B decrease and the intersecting point shifts farther down the BH curve.
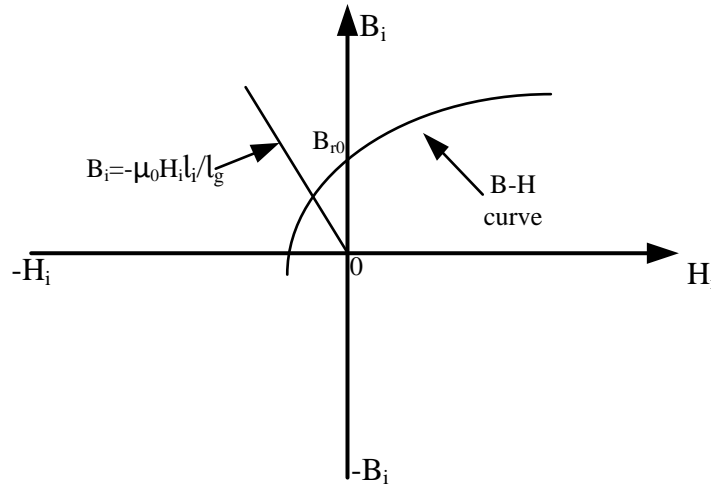
Figure 3.23 Intersection between the shearing line and the demagnetisation curve gives the magnetic field in the permanent magnet of Figure 3.22.

The shearing line equation implies that there is a H field in the opposite direction to B_i in the steel, as shown in Figure 3.22 (a). As described in reference [3.4], there is a magnetic surface charge density $\rho_{sm} = M \cdot \hat{n}$ on the gap faces, which is the source for the H field. Figure 3.22 (a) illustrates the surface charge density that can be calculated by first obtaining M as follows. Since B_i and H_i are determined by the intersection point in Figure 3.23, the equation to describe M is given by utilising the relation $B_i = \mu_0(H_i + M)$:

$$M = \frac{B_i}{\mu_0} - H_i \tag{3.35}$$

From Figure 3.23, the presence of the magnetic charges on the gap faces results in the negative H field through the steel which imposes a demagnetising effect on the

70

material. In other words, a permanent magnet produces a magnetic flux in free space, but the magnet itself induces a demagnetising field. Since steel is ferromagnetic, $\mu_r = 1 + \frac{M}{H} \approx \frac{M}{H}$, and substitution into (3.35), gives:

$$\mu_r H_i = \frac{B_i}{\mu_0} - H_i$$

$$H_i = \frac{B_i}{\mu_0 \mu_r} \tag{3.36}$$

The relation $B_i = \mu H_i$ is valid in a permanent magnet application: it provides a negative permeability μ, since the point of intersection on the BH curve is in the second quadrant, where H_i is negative. Assuming the steel and air-gap cross-sections are equal, due to flux continuity $\Phi = B_i A_i = B_A A_A$, and the equation to describe the flux through the gap and steel is:

$$\Phi = B_A A_A = \frac{-l_i}{l_A} \mu_0 H_i A_A \tag{3.37}$$

After substituting equation (3.36) into (3.37) and supposing the residual magnetisation B_{r0} is constant regardless of an increase in the air-gap, then $B_i = B_{r0}$, whence:

$$\Phi = B_A A_A = \frac{-l_i}{l_A} \frac{B_{r0}}{\mu_r} A_A \tag{3.38}$$

As indicated previously, there is still an air-gap distance l'_A during the VCB closed state. Reviewing Figure 3.20 (e), the armature has a linear movement when it reaches a stable state. This means that $l_A = l'_A + v_a t$. According to Faraday's law $\varepsilon = -N \frac{d\phi}{dt}$, then:

$$\varepsilon = \frac{N l_i B_{r0} A_A v}{\mu_r (l'_A + v_a t)^2} \tag{3.39}$$

where N represents the number of coil turns, l_i is the total length of steel including the attached armature, B_{r0} is the residual magnetisation, A_A is the cross section area, v_a represents the armature speed, μ_r is the relative permeability, and l'_A is the initial gap distance before armature separation.

In summary, the back EMF is determined by the residual magnetisation and the VCB opening speed for a given circuit geometry. Equation (3.39) is incomplete because of

two factors. Firstly, the residual magnetisation was assumed to decrease as the air-gap increased, whereas here it was considered as a constant. Secondly, the VCB opening speed is initially non-uniform, whilst here it is considered as immediately having stable motion following separation. The graphs in Figure 3.24 represent equation (3.39) in terms of different initial conditions, and show how the counter-EMF is affected by different factors.
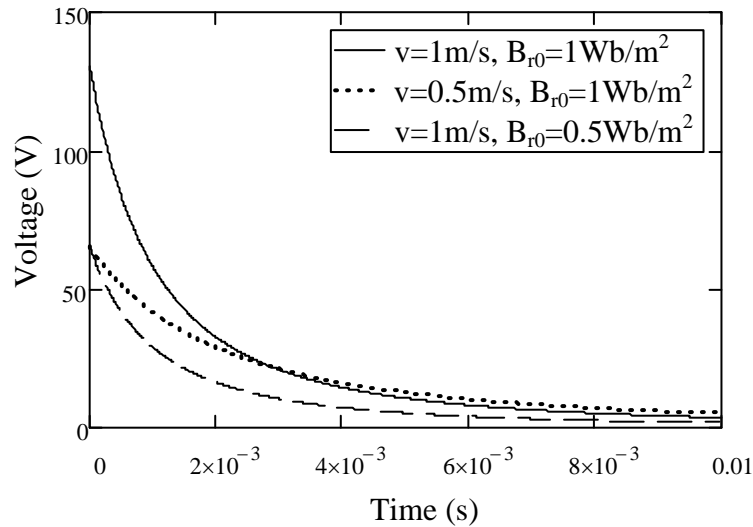
Figure 3.24 Waveforms based on equation (3.40) with initial conditions: $N = 1693$, $l_i = 0.386m$, $A_A = 8 \times 10^{-4}m^2$, $\mu_r = -1000$, $l_g' = 0.002m$.

3.5.2 Exploitation of the counter-EMF

Due to the absence of a natural current-zero (with DC), many auxiliary commutation circuits have been proposed to produce a zero current instant in the VCB. However, when to trigger the auxiliary circuit is a problem, since time is needed for the VCB gap to widen sufficiently to support voltage. The longer it takes for the electrodes to part, the greater the energy needed from the auxiliary circuit. The commutation energy can be minimised if delayed and applied at the instant when the gap is sufficiently wide enough to support the voltage after current-zero. As mentioned in Chapter 2, the *di/dt* of the VCB varies with the gap distance. Based on practical results, the counter-EMF is observed to occur after the armature has moved away from the solenoid coil. The occurrence of the counter-EMF is always earlier than the formation of the arc voltage, with the time between them constant. The transient

increase in the coil current, or the peak, is monitored and amplified by a current transducer (LA55-P as shown in Appendix A.2.3) and the instrumentation amplifier (LT1168 as shown in Appendix A.2.4), and then fed to a comparator circuit (LM311 as shown in Appendix A.2.3) to produce a 'high' signal as input to the microcontroller (dsPIC30F2020 as shown in Appendix A.2.5). The experimental results are shown as following:
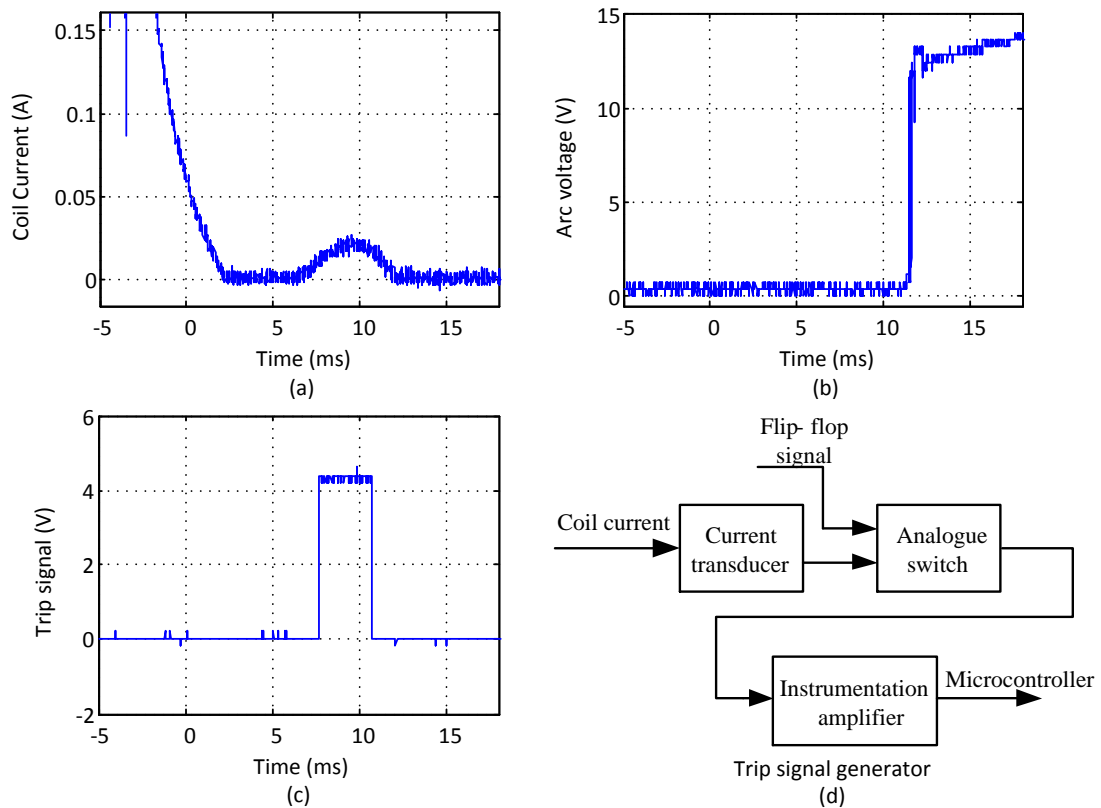
Figure 3.25 Waveforms based on the control circuit for producing the trip signal.

The experimental plots in Figure 3.25 (a) and (b) illustrate that the occurrence of the transient increase in coil current is consistent with the arc voltage formation. Figure 3.25 (c) demonstrates that the transient increase (or peak) in coil current is converted to a 'high' signal for input to the microcontroller. The duration of the high signal (trip signal) is adjustable and the microcontroller is triggered once the trip signal is received. There is approximately 5ms between the peak of coil current and the arc voltage occurring. This implies that the trip signal is ahead of the arc voltage, giving 5ms for the auxiliary circuit to prime to produce a current zero in the VCB. Since the

electrode separation speed after the arc voltage occurs is constant at 1m/s, triggering of the auxiliary commutation circuit is controlled by the microcontroller. Thus commutation for different gap widths (different HVDC withstand voltages) can be achieved.
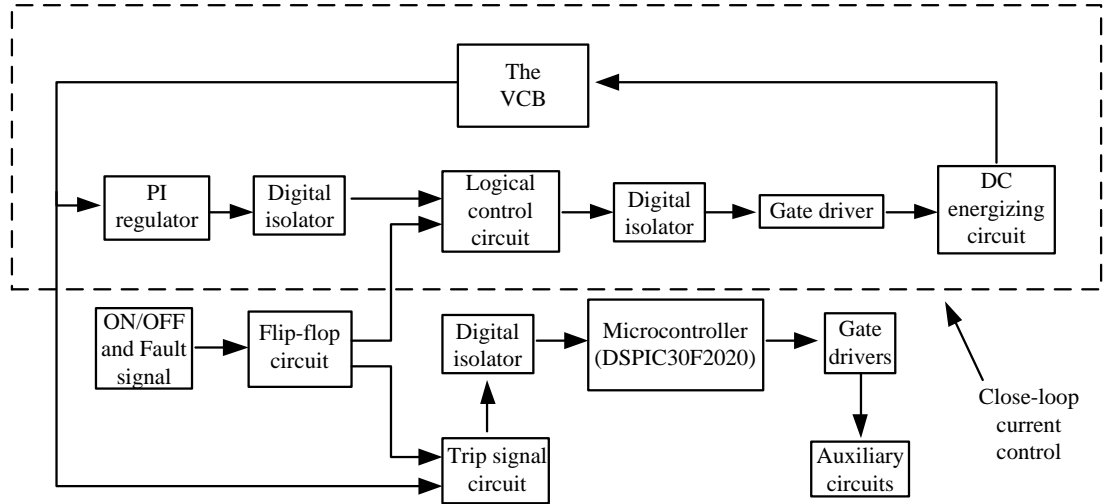
Figure 3.26 Schematic diagram of control for the VCB

Closed-loop current control of the coil was present in Section 3.4. The detailed circuits in the Figure 3.26 are shown in Appendix A.2.

- ➢ ON/OFF and Fault signal circuit: circuit with small mechanical switches to produce the ON/OFF and Fault signal.
- ➢ Flip-flop: dual D-type positive-edge-triggered flip-flop devices (SN5474) to recognise the oncoming signal is ON/OFF or Fault and then dispatch it to the correct channel. For example, the trip signal circuit is only activated in the fault situation. Otherwise, it is in the 'off' state.
- ➢ Trip signal circuit: consists of a current transducer, an instrumentation amplifier and an analogue switch (ADG201HS). The analogue switch is utilised so only the transient increase of coil current is amplified. Other parts of the coil current are under closed-loop current control.
- ➢ Microcontroller: input uses negative-edge-triggered or positive-edge triggered signals. This means that, as the trip signal changes from positive to zero or zero to positive, it delivers signals to activate the auxiliary circuit, to

produce a VCB zero current point. All the signals are controllable to investigate the VCB characteristics under various conditions, such as interruption of a fixed dc current at different gap distances.

3.6 Summary

This chapter presented a coil DC activation method that reduced VCB opening time from approximately 50ms to 13ms. The same circuit can be used on a dedicated opening coil, which would signifiantly dcrease the opening time. The coil counter-EMF was observed and utilised to optimally trigger the auxiliary commutation circuit; however, this method is only valid in such VCB with indirect mechanism.

A circuit will be proposed and illustrated in Chapter 4 to investigate VCB characteristic in terms of conditions such as range of interrupting current levels, different gap distances, variable di/dt and dv_{VCB}/dt, etc.

References

[3.1]   A.N. Greenwood, "Vacuum Switchgear," *The insitution of electrical engineers,* vol. 18, pp. 137-173, 1994.

[3.2]   P. Bauer, and J. Sitar, "Evaluation of electromagnetic actuator analysis," *Power Electronics Specialists Conference, 2006. PESC '06. 37th IEEE* pp. 1-6, 18-22 June 2006.

[3.3]   A. Wallacetown, "Vacuum contactors," pp. 1-6, AUGUST 2008.

[3.4]   M. A. Plonus, *Applied electromagnetics*. united states of america: McGraw-Hill, Inc, 1978.

[3.5]   E. Huber, K. Frohlich, and R. Grill "Dielectric Recovery of Copper Chromium Vacuum Interrupter Contacts After Short-Circuit Interruption," *IEEE Transactions on plasma science,* vol. 25, pp. 642-646, August 1997.

[3.6]   B. W. Williams, *Power Electronics: Devices, Drivers, Applications, and Passive components*: Barry W Willams, 2006.

[3.7]   A.N. Greenwood, P. Barkan, and W.C. Kracht, "HVDC Vacuum Circuit Breakers," *Power Apparatus and Systems, IEEE Transactions on* vol. PAS-91, pp. 1575-1588, July 1972.

[3.8]   W. Holaus, and K. Frohlich, "Ultra-fast switches- a new element for medium voltage fault current limiting switchgear," *Power Engineering Society Winter Meeting, 2002. IEEE* vol. 1, pp. 299-304, 2002.

4 Analysis of commutation circuits for hybrid breakers

4.1 Introduction

The main difficulty in DC interruption is the absence of natural current-zeros. The interruption methods considered in Chapter 1 were active and passive commutation. Therefore, with the aid of the control method proposed in Chapter 3, a circuit employing active commutation is proposed to investigate VCB characteristics during the internal electrodes opening period. The VCB is considered as a 'black box', and the detail of the mechanism discussed in Chapter 2 and Appendix is ignored.

Previously, a vacuum switch-triggered spark gap was used as a commutation switch for providing counter-current through the VCB [4.1, 2]. Here it is replaced by solid-state switches, which incur energy loss during the reset process of the commutation circuit. In order to mathematically analyse the commutation circuit, equations are derived which include the dimensions of commutation components, di/dt , dv_{VCB}/dt, etc.

The post-arc current plays a significant role in the VCB interruption process. Equations describing the post-arc are proposed by references [4.3, 4]. However here within, one initial condition, that the ion density is only determined by the arc's natural decay and the post-arc current, is questioned. Thus, the properties of the post-arc current are investigated by varying di/dt, dv_{VCB}/dt and interruption current level, as well as gap distance.

The VCB interruption properties in interrupting high power have been considered extensively [4.5-9], but low power interruption has been ignored. In addition, the VCB in this thesis is for a low power three phase AC network, hence has three vacuum interrupters. Experimental results presented show that each of the three interrupters has the same interruption properties but that their interruption performances differ. In order to explore these differences, the relationship between the VCB conduction resistance and interruption times is investigated in terms of fixed interruption current, di/dt, and arcing time.

4.2 Analysis of commutation circuits

4.2.1 Active and passive commutation modes

As mentioned in Chapter 1, a virtual current-zero is developed by utilising auxiliary means which include current oscillation and voltage commutation. Voltage commutation is where current commutation is achieved by introducing a voltage which exceeds the on-state voltage of the parallel commutation path.

A current oscillation requires auxiliary circuits connected in parallel to the main breaker [4.1]. The additional circuits inject a controlled counter-current into the circuit breaker. A forced current-zero arises if the counter-current is greater than the instantaneous fault current passing through the VCB. Hence, it is important to know the fault current level. With this method, contact erosion is decreased as the arcing time is reduced [4.10].
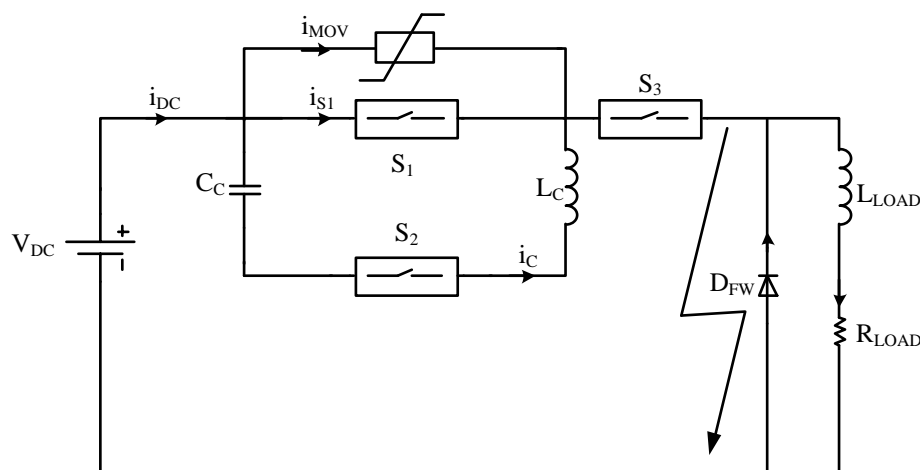
Figure 4.1 Basic uni-directional DC system with a commutation circuit: S₁: main breaker, S₂: auxiliary switch, S₃: load breaker, C_C and L_C: commutation capacitor and coil, and MOV: metal oxide varistor.

In Figure 4.1, the main breaker is located between a DC source V_{DC} and a load isolator S_3 followed by a load that includes resistance R_{LOAD} and inductance L_{LOAD}. The load resistance and inductance include wiring and connection components. The commutation circuit, consisting of capacitor C_C and coil inductance L_C, as well as auxiliary switch S_2, all placed across the main breaker S_1. The metal oxide varistor

(MOV) is connected in across S_1 to prevent device over-voltage during system current interruption. The commutation mode depends on whether C_C is pre-charged or not; it is active commutation if C_C is pre-charged, otherwise it is passive commutation. Since the load is normally inductive, the freewheel diode D_{FW} is parallel connected to the load side to maintain current continuity. The voltage across the commutation capacitor C_C is suppressed as the freewheel diode D_{FW} bypasses any energy being transferred from the downstream lines during the interruption. Effectively the conducting freewheel diode emulates the load condition during a DC load side short circuit fault. A freewheel diode cannot be used on the source side.

In the active mode, when an 'off' signal from the fault sensor is received, the main breaker S_1 opens and when the inter-electrodes reach certain gap distance, the auxiliary switch S_2 is closed and a current oscillation i_C starts, increasing to oppose the current i_{S1} through in the main breaker S_1. With the commutation capacitor C_C pre-charged, there will be at least one current-zero in the main breaker provided the L_C and C_C resonant circuit is designed properly. The polarity of capacitor C_C reverses, since the main current i_{DC} is commutated to the parallel path when the current i_{S1} is reduced to zero. Then another current-zero occurs in switch S_2, dominated by the upstream line and commutation parameters. Three factors determine the commutation capacitor C_C final charge, including its initial voltage, the system voltage, and a voltage related to the stored inductive energy in the upstream line. If the switch S_2 is bi-directional, the current i_C will continuously oscillate, dissipating energy in resistive components until it reduces zero. This means the voltage across the commutation capacitor C_C finally remains charged to the supply voltage. The switch S_2 and the rectifier station are uni-directional switches. So, the commutation capacitor C_C charges until the first current-zero in switch S_2. At this instant, current interruption is complete and isolation switch S_3 can be opened with zero current. For successful commutation, the main switch S_1 not only withstands the high di/dt but also maintain isolation between its electrodes at the current-zero. There are disadvantages with this method:

➢ A external voltage is required to maintain the initial charge of capacitor C_C;

- ➢ Large capacitance for commutation capacitor C_C is required to generate a large counter-current. Consequently, this results in a large size and a high price.
- ➢ The commutation circuit can only function once (if no reset is incorporated).

A passive mode of operation may be required in some applications. In the passive commutation mode, there is also a current oscillation in the main switch S_1, which results from the interaction between the arc voltage and the commutation parameters (a negative resistance characteristic means that the arc voltage decreases as arc current increases). It takes a longer time to introduce a current zero in the main switch S_1 owing to the lack of a pre-charge voltage across the commutation capacitor C_C. That is, as the uncharged capacitor C_C is repeatedly charged and discharged by the arc voltage, an oscillatory current will occur. With an increase in arc length and as the heat loss gives rise to an increasing arc voltage, the commutation current i_C oscillation will grow [4.11]. The current-zero in the main breaker S_1 is generated when the magnitude of commutation current equals the main current. Now the main current i_S is commutated into the parallel path, and the capacitor voltage increases to its highest value when the current i_C is reduced to zero. However, in this situation the auxiliary switch S_2 is bi-directional, and the capacitor voltage may charge to the supply voltage level due to the continuous oscillation.

4.3 The test circuit

As mentioned in Chapter 2 and Appendix B, the VCB model is complicated, since it involves many parameters including contact material, gap distance, electrodes dimensions, etc. A small change in any parameter can result in a significant performance change. There is no complete mathematic model describing all VCB properties in terms of its internal parameters. Here the VCB will be considered as a 'black box', ignoring all of the internal parameters, but the 'black box' will attempt to retain the features and regular pattern of successful VCB interruptions based on external conditions. There are two external parameters that possess this function [4.6, 8, 12]; they are di/dt and dv_{VCB}/dt, where the former represents the rate of

decrease of current through the VCB immediately before a current zero and the latter represents the rate of increase of voltage across the VCB immediately after a current zero. Thus, in order to investigate VCB characteristic, a test circuit, as shown in Figure 4.2, is proposed and established based on a hybrid circuit breaker with active mode commutation. The difference compared with the original circuit [4.13] is that the extra switch T_2 is employed to achieve a controllable reversal of commutation capacitor voltage in the test circuit. For the purpose of a more detailed description of circuit operation, the interrupting sequences are based on the control strategy described in Chapter 3, as shown in Figure 4.3. Photographs of the test rigs are shown in Appendix A.1.1. Snubber circuits have been omitted; for convenience inductors are assumed linear; the voltage drops across semiconductors and the VCB during the on state are zero; and the current through the VCB and the voltage drop across the capacitor bank C_{bank} are considered constant during separation of the VCB electrodes since the commutation time is shorter than the time constant of the inductive load. The auxiliary switches T_1 T_2 T_3 and T_4 each comprise a diode in series with an IGBT.

The detailed solution is achieved by solving the differential equations that correspond to each interval, where the end state of the previous interval is the initial state of the following interval. With reference to the circuit voltage and current waveforms in Figure 4.4, the operational sequence for the test circuit follows.

There are three stages to the operational cycle. These are resetting the commutation circuit, introduction of the fault current, and interruption of the commutation circuit. The sequential timing operations for the test circuit are given in Table 4.1.

Table 4.1 Switched timing regulations

stage	time	VCB	T_1	T_2	T_3	T_4
reset of test circuit (a) (b)	t_{nor}	On	On	Off	Off	Off
	t_{0-}	On	Off	On	Off	Off
introduction of fault current (c)	t_0	On	Off	Off	Off	On
interruption of commutation the circuit (d) (e) (f)	t_1	Off	Off	Off	Off	On
	$t_2 - t_6$	Off	Off	Off	On	On
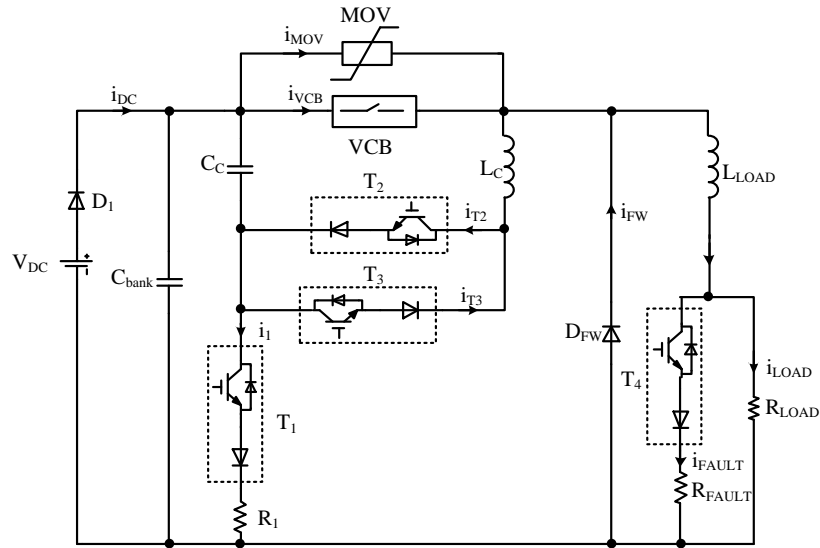
Figure 4.2 The test circuit; VCB: vacuum circuit breaker, $T_{1,2,3,4}$: a diode and a series IGBT.
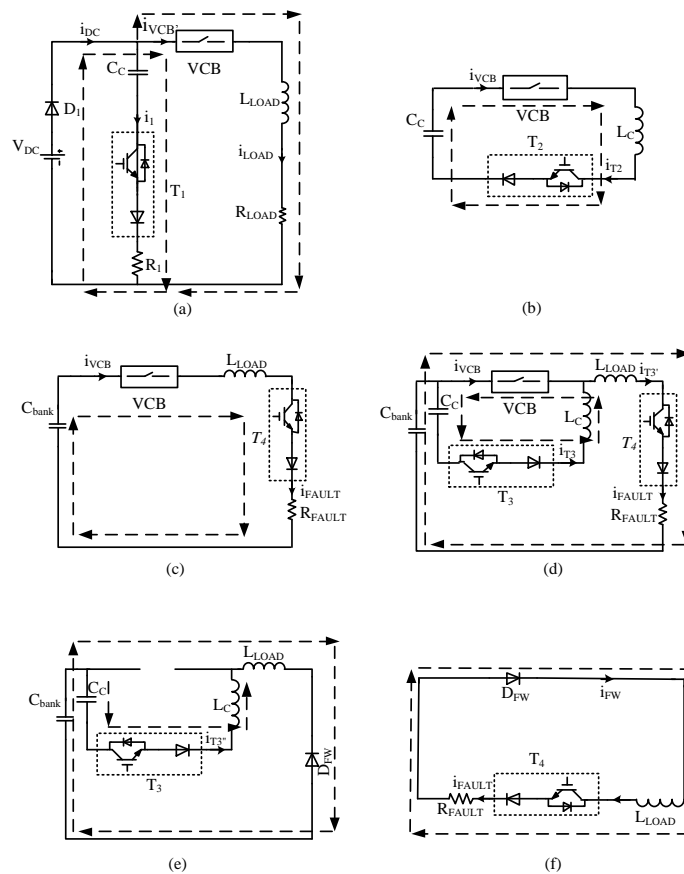
Figure 4.3 Test interruption sequences; VCB: vacuum circuit breaker, $T_{1,2,3,4}$: a diode plus series IGBT.

82
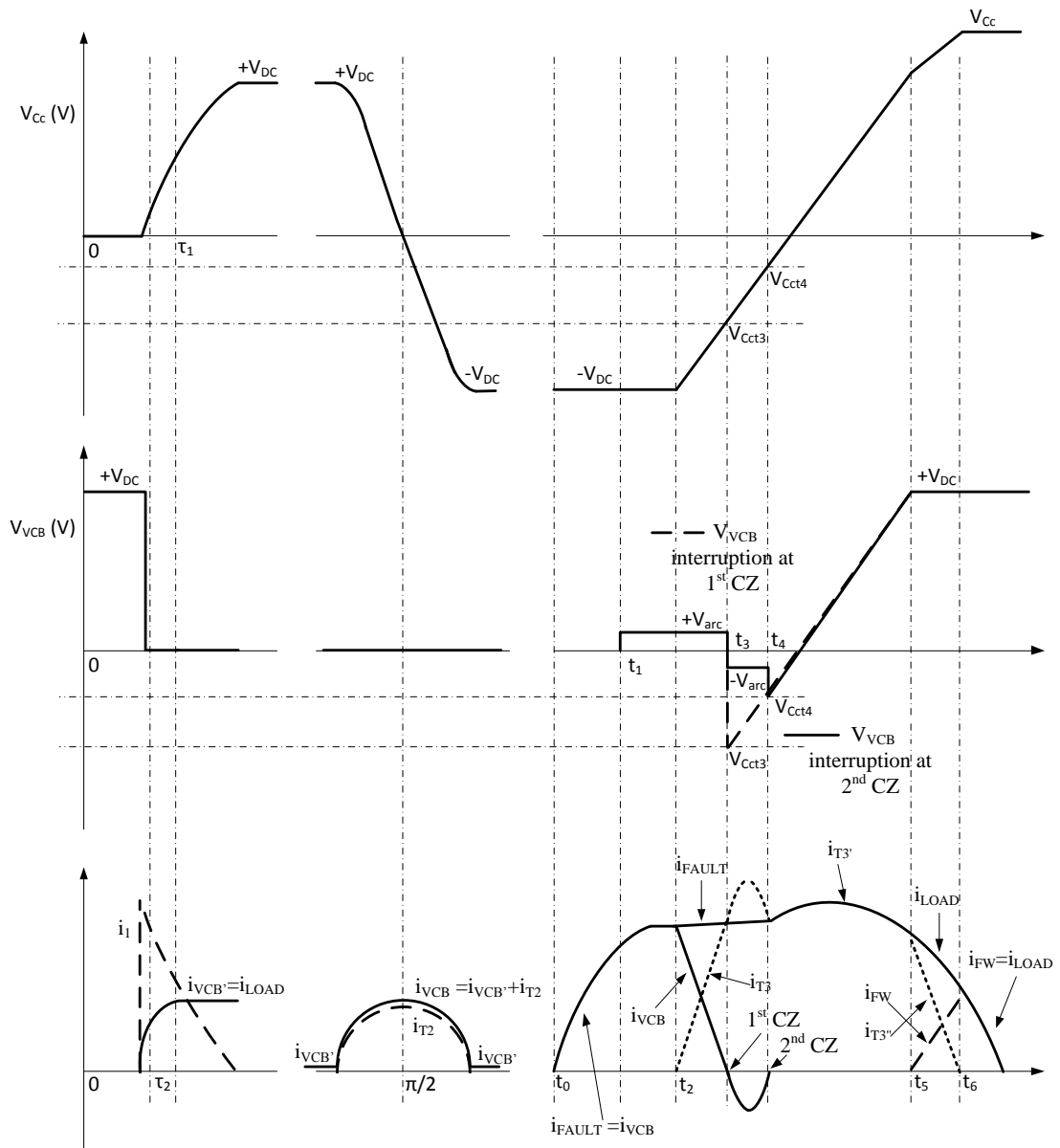
Figure 4.4 Operational sequence of the test circuit; CZ current-zero crossing in the VCB

Figure 4.3 (a) illustrates how the test circuit operates normally t_{nor}. The DC source (V_{DC}) used during testing can provide voltage up to 600V but current is limited to 10A. To investigate VCB properties in high current situations, the capacitor bank (C_{bank}) is charged to the DC source voltage in order to supply a fault current determined by fault resistor R_{FAULT}, which is connected in parallel with the load resistor R_{LOAD} by T₄. When the VCB is in the 'on' state, a low current (V_{DC}/R_{LOAD}) is supplied by the DC source V_{DC} through the VCB to the load that consists of

inductance L_{LOAD} and resistance R_{LOAD}. The switches T_2, T_3 and T_4 are off but T_1 is on, charging the commutation capacitor to the DC source voltage with an exponential profile via resistor R_1. In this interval, the equation relating currents i_{DC}, $i_{VCB'}$ and i_1 is:

$$i_{DC} = i_{VCB'} + i_1 \tag{4.1}$$

where the circuit loop comprising V_{DC}, D_1, C_C, T_1, and R_1 obeys the following differential equation:

$$\frac{1}{C_C} \int i_1 dt + i_1 R_1 = V_{DC} \tag{4.2}$$

with the initial conditions:

$$V_{C_C} = 0 \text{ (V)}$$

which yields:

$$i_1(t) = \frac{V_{DC}}{R_1} e^{\frac{-t}{\tau_1}} \quad \text{(A)} \tag{4.3}$$

and $$V_{C_C}(t) = V_{DC}(1 - e^{\frac{-t}{\tau_1}}) \text{ (V)} \tag{4.4}$$

where $\tau_1 = R_1 C_C$

Since the maximum current supplied by the DC source is 10A, R_1 is 200Ω to limit capacitor C_C charging current. Thus diode D_1 has a low current rating. When the current i_1 reduces to zero, the voltage across the commutation capacitor C_C reaches V_{DC}, remaining at this voltage provided T_1 is 'on'.

The circuit loop comprising V_{DC}, D_1, VCB, L_{LOAD}, and R_{LOAD} gives:

$$L_{LOAD} \frac{di_{VCB'}}{dt} + i_{VCB'} R_{LOAD} = V_{DC} \tag{4.5}$$

with the initial conditions:

$$i_{VCB'} = 0 \quad \text{(A)}$$

which yields:

$$i_{VCB'}(t) = i_{LOAD}(t) = \frac{V_{DC}}{R_{LOAD}} \left(1 - e^{\frac{-t}{\tau_2}}\right) \quad \text{(A)} \tag{4.6}$$

where $\tau_2 = \frac{L_{LOAD}}{R_{LOAD}}$

When equation (4.6) stabilises, the current i_{VCB}, flowing through the VCB equals the source current i_{DC}. However, due to the large load resistance ($R_{LOAD} = 600\Omega$), the current is small (1A) in this interval so can be ignored in the following analysis.

In Figure 4.3 (b), although the voltage V_{C_C} across the commutation capacitor C_C is equal to the DC source voltage, it is not ready to commutate the VCB due to its voltage polarity, V_{C_C}. However, there is approximately 5ms between the peak produced by the counter-EMF and the separation of inside electrodes. This means once the trip signal that corresponds to the occurrence of the current peak is received at t_{0-}, the voltage polarity of the commutation capacitor has to be reversed within a short time, 5ms, with the microcontroller signalling the T$_1$ off but T$_2$ on for a short period. The circuit loop equation for C_C, VCB, L_C and T_2 is:

$$\frac{1}{C_C} \int i_{T_2} dt + L_C \frac{di_{T_2}}{dt} = 0 \tag{4.7}$$

with the initial conditions
$$i_{T_2} = 0 \text{ (A) and } V_{C_C} = -V_{DC} \text{ (V)}$$

which yield:
$$i_{T_2}(t) = \frac{V_{DC}}{Z} \sin \omega_0 t \text{ (A)} \tag{4.8}$$

and
$$V_{C_C}(t) = -V_{DC} \cos \omega_0 t \text{ (V)} \tag{4.9}$$

$$0 \leq \omega_0 t \leq \pi \quad \text{(rad)}$$

where $\omega_0 = 1/\sqrt{L_C C_C}$ (rad/s) and $Z = \sqrt{L_C/C_C}$ (Ω)

At $\omega_0 t = \pi$ the current i_{T_2} cannot reverse because the diode in the T$_2$ blocks and the voltage V_{C_C} across the commutation capacitor retains a charge of $-V_{DC}$.

The Figure 4.3 (c) illustrates how the fault current arises. It is that when only T$_4$ is switched on at t_0 (with the others switches off), the energy stored in the capacitor bank C_{bank} will be released through the load inductor L_C and fault resistor R_{FAULT} to produce a high current through the VCB before the electrodes separate. The commutation circuit is a second order L-C-R circuit with a capacitor initial charged to V_{DC}. The load resistor R_{LOAD} is ignored due to its large resistance compared with

the   fault   resistor R_{FAULT}.   The   circuit   loop   comprising C_{bank}, VCB, L_{LOAD}, T_4 and R_{FAULT} is expressed by:

$$\frac{1}{C_{bank}} \int i_{FAULT} dt + L_{LOAD} \frac{di_{FAULT}}{dt} + i_{FAULT} R_{FAULT} = 0 \tag{4.10}$$

with the initial conditions

$$i_{FAULT} = i_{VCB}, \approx 0 \text{ (A)}; V_{C_{bank}} = -V_{DC} \text{ (V)}$$

Equation (4.10) can be divided into three different models in term of the relationship

between R_{FAULT} and $2\sqrt{\frac{L_{LOAD}}{C_{bank}}}$.

When $R_{FAULT} > 2\sqrt{\frac{L_{LOAD}}{C_{bank}}}$, it is an over-damped circuit. There are two unequally

negative real numbers in its root. Thus, it yields:

$$i_{FAULT}(t) = -\frac{V_{DC}}{L_{LOAD}(P_2 - P_1)}(e^{P_1 t} - e^{P_2 t}) \quad \text{(A)} \tag{4.11}$$

and $$V_{C_{bank}}(t) = \frac{V_{DC}}{(P_2 - P_1)}(P_2 e^{P_1 t} - P_1 e^{P_2 t}) \quad \text{(V)} \tag{4.12}$$

where $$P_1 = -\frac{R_{FAULT}}{2L_{LOAD}} + \sqrt{(\frac{R_{FAULT}}{2L_{LOAD}})^2 - \frac{1}{L_{LOAD}C_{bank}}}$$

$$P_2 = -\frac{R_{FAULT}}{2L_{LOAD}} - \sqrt{(\frac{R_{FAULT}}{2L_{LOAD}})^2 - \frac{1}{L_{LOAD}C_{bank}}}$$

The capacitor bank C_{bank} always discharges its stored energy into the fault, as shown
in Figure 4.5 (a). When $t = 0_+$, $i_{FAULT}(0_+) = 0$, and as $t \to \infty$, $i_{FAULT}(\infty) = 0$.
Thus, the fault current must firstly ascend from zero and then descend to zero. The
time t_m to reach maximum current is determined from $\frac{di_{FAULT}}{dt} = 0$, and is given by:

$$t_m = \frac{\ln(P_2/P_1)}{P_1 - P_2} \tag{4.13}$$

When $R_{FAULT} < 2\sqrt{\frac{L_{LOAD}}{C_{bank}}}$, the circuit is under-damped, so there is a pair of complex

conjugate roots. Equation (4.10) therefore yields:

$$i_{FAULT}(t) = \frac{V_{DC}}{\omega_1 L_{LOAD}} e^{-\delta_1 t} \sin(\omega_1 t) \quad \text{(A)} \tag{4.14}$$

and
$$V_{C_{bank}}(t) = \frac{V_{DC}\omega_2}{\omega_1} e^{-\delta_1 t} \sin(\omega_1 t - \beta_1) \quad \text{(V)} \tag{4.15}$$

where $\delta_1 = \frac{R_{FAULT}}{2L_{LOAD}}$, $\omega_1^2 = \frac{1}{L_{LOAD}C_{bank}} - \left(\frac{R_{FAULT}}{2L_{LOAD}}\right)^2$, $\omega_2 = \sqrt{\delta_1^2 + \omega_1^2}$, and $\beta_1 = \tan^{-1}\frac{\omega_1}{\delta_1}$

The voltage and current resonate with an ever-decreasing amplitude if bi-directional switches are employed, as shown in Figure 4.5 (b). During the process, they change direction within each period while the capacitor and inductor storage elements exchange energy in each period. However, the uni-directional switches can prevent continuous resonance. When $\omega_1 t = \beta_1$, the fault current increases to its maximum value.

When $R_{FAULT} = 2\sqrt{\frac{L_{LOAD}}{C_{bank}}}$, its latent root contains a multiple root. Thus equation 4.10 yields:

$$i_{FAULT}(t) = \frac{V_{DC}}{L_{LOAD}} t e^{-\delta_1 t} \quad \text{(A)} \tag{4.16}$$

and
$$V_{C_{bank}}(t) = V_{DC} e^{-\delta_1 t}(1 - \delta_1 t) \quad \text{(V)} \tag{4.17}$$

In Figure 4.5 (c), the voltage and current are not resonating but keep a similar trajectory to (a), where the voltage and current both continue to reduce until zero.

Since VCB opening speed after electrode separation is 1m/s, the time difference between t_1 and t_2 determines how far the internal electrodes have separated. Independent of the discharge mode, the commutation circuit current (having triggered T₃) has to rise to (or exceed) the fault current $i_{FAULT}(t)$ level at t_2, in order to be able to investigate VCB interruption properties. When the electrodes start to open at t_1, the VCB experiences an arc voltage, the polarity of which depends on the direction of the VCB current, until a successful commutation is achieved.

(a)

(b)

(c)
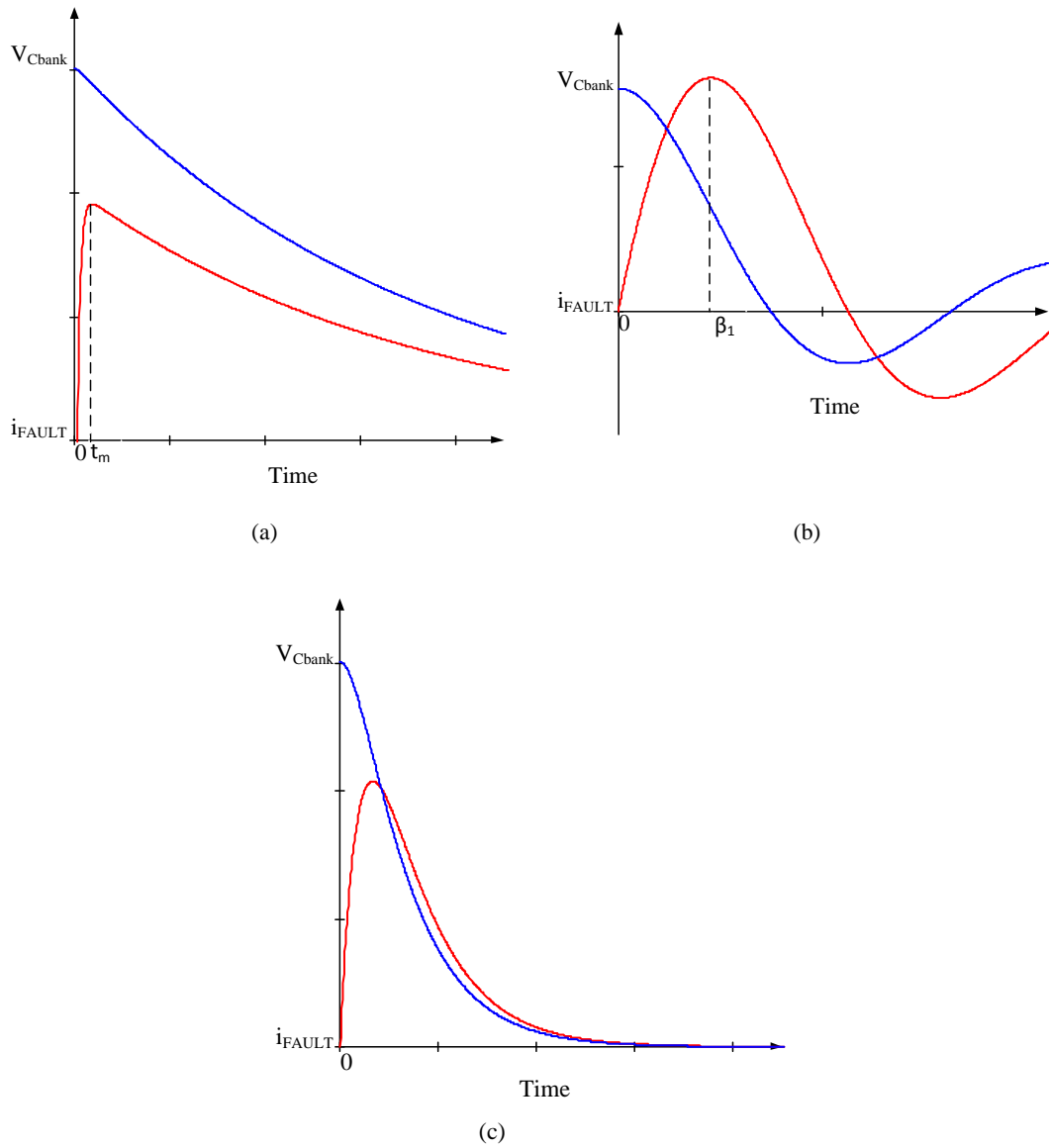
Figure 4.5 Fault circuit voltage and current waveforms: (a) $R_{FAULT} > 2\sqrt{\frac{L_{LOAD}}{C_{bank}}}$**; (b)** $R_{FAULT} < 2\sqrt{\frac{L_{LOAD}}{C_{bank}}}$**; and**

(c) $R_{FAULT} = 2\sqrt{\frac{L_{LOAD}}{C_{bank}}}$

In Figure 4.3 (d), for analysis, since the commutation period $t_2 - t_3$ is far shorter than the fault path time constant, it is assumed that the fault current $i_{FAULT}(t)$ is constant within this period. During experimentation, most commutation times are within the range of tens to hundreds of microseconds and the maximum is 1ms, while the fault current last for at least 20ms. Switch T_3 is fired to introduce the counter-current flow through the VCB, forcing the fault current through the VCB to zero,

once the electrodes have separated a specific distance. As a consequence, in this interval, the relationships between i_{FAULT}, i_{VCB} and i_{T3} are given by:

$$i_{FAULT} = i_{VCB} + i_{T3} \text{ (A)} \qquad (4.18)$$

where the differential equation for i_{T3} is the same but with opposite direction to i_{T2} during commutation and is given by:

$$\frac{1}{C_C}\int i_{T_3}dt + L_C\frac{di_{T_3}}{dt} = 0 \qquad (4.19)$$

with the initial conditions

$$i_{T_3} = 0 \text{ (A) and } V_{C_C} = V_{DC} \quad \text{(V)}$$

which yields:

$$i_{T_3}(t) = \frac{V_{DC}}{Z}\sin\omega_0 t \text{ (A)} \qquad (4.20)$$

and
$$V_{C_C}(t) = V_{DC}\cos\omega_0 t \text{ (V)} \qquad (4.21)$$

$$0 \le \omega_0 t \le \pi \quad \text{(rad)}$$

where $\omega_0 = 1/\sqrt{L_C C_C}$ (rad/s) and $Z = \sqrt{L_C/C_C}$ (Ω)

With the appropriate choice of L_C and C_C, that is, with an appropriate selection of di/dt, a successful interruption should occur as a result of the first current-zero. If commutation failures, then the second current-zero can be utilised. Because the auxiliary switches (T₁ T₂ T₃ and T₄) are uni-directional, the counter-current introduced by the resonant $L_C C_C$ circuit can produce at least two current-zeros, thus providing two opportunities for an interruption. The interruption process is considered to have failed if the VCB current continues after the second current-zero. (This is similar to AC breakers which can be specified based on two mains cycles for commutation.) It is assumed that interruption is achieved at first current-zero, which means $i_{T_3}(t_3) = i_{FAULT}(t_2, t_3)$. The time t_{CZ1} to the first VCB current-zero is:

$$t_{CZ1} = \frac{-\sin^{-1}\frac{i_{FAULT}(t_2)Z}{V_{DC}}}{\omega_0} \qquad (4.22)$$

The time t_{CZ2} to the second VCB current zero is:

$$t_{CZ2} = \frac{\pi + \sin^{-1}\frac{i_{FAULT}(t_2)Z}{V_{DC}}}{\omega_0}$$

The VCB voltage falls to the residual voltage of the commutation capacitor and follows its change. Thus the fault current passing through the VCB is commutated into the $L_C - C_C$ path. Current $i_{T_3'}$ in the circuit loop C_{bank}, C_C, T_3, L_C, L_{LOAD}, T_4 and R_{FAULT} is defined by:

$$\frac{1}{C_C}\int i_{T_3'}dt + L_C \frac{di_{T_3'}}{dt} + L_{LOAD}\frac{di_{T_3'}}{dt} + i_{T_3'}R_{FAULT} = V_{DC} \tag{4.23}$$

where the voltage across C_{bank} can be considered a DC source due to a large C_{bank}. Initial conditions are

$$i_{T_3'} = i_{T_3}(t_3) \text{ (A) and } V_{C_{C'}} = V_{C_C}(t_3) \text{ (V)}$$

$R_{FAULT} < 2\sqrt{\frac{L_{LOAD}}{C_C}}$. Thus equation 4.23 yields:

$$i_{T_3'}(t) = 2K_1 e^{-\delta_2 t}\cos(\omega_3 t - \theta) \quad \text{(A)} \tag{4.24}$$

$$V_{C_{C'}}(t) = \frac{2K_1}{C_C\omega_4}[\cos(\beta_2 - \theta) - e^{-\delta_2 t}\cos(\omega_3 t - \theta + \beta_2)] + V_{C_C}(t_3) \quad \text{(V)} \tag{4.25}$$

where $\delta_2 = \frac{R_{FAULT}}{2(L_{LOAD}+L_C)}$, $\omega_3^2 = \frac{1}{(L_{LOAD}+L_C)C_C} - \left(\frac{R_{FAULT}}{2(L_{LOAD}+L_C)}\right)^2$, $\omega_4 = \sqrt{\delta_2^2 + \omega_3^2}$,

and $\beta_2 = \tan^{-1}\frac{\omega_3}{\delta_2}$

$$K_1 = \sqrt{\left(\frac{i_{T_3}(t_3)}{2}\right)^2 + \left(\frac{\frac{V_{DC}-V_{C_C}(t_3)}{L_{LOAD}+L_C} - \delta_2 i_{T_3}(t_3)}{2\omega_3}\right)^2}$$

$$\theta = \tan^{-1}\frac{\frac{V_{DC}-V_{C_C}(t_3)}{L_{LOAD}+L_C} - \delta_2 i_{T_3}(t_3)}{\omega_3 i_{T_3}(t_3)}$$

During the interval $t_3 - t_5$, current $i_{T_3'}$ initially increases since residual voltage remains on capacitor C_C. Then it starts to reduce, allowing diode D_{FW} to conduct, whence the voltage across the VCB reaches its maximum voltage, V_{DC}.

In the Figure 4.3 (e), with diode D_{FW} conducting, the load (the fault) is bypassed, effectively decoupling the fault from the commutation circuit. Current $i_{T_3'} = i_{T_3''} + i_{FW}$, where $i_{T_3''}$ discharges through the circuit loop C_{bank}, C_C, T_3, L_C and D_{FW}, transferring magnetic energy to an electric field, causing V_{C_C} to increase according to:

$$\frac{1}{C_C} \int i_{T_3''} dt + L_C \frac{di_{T_3''}}{dt} = V_{DC} \tag{4.26}$$

with initial conditions

$$i_{T_3''} = i_{T_3'}(t_5) \text{ (A) and } V_{C_{C''}} = V_{C_{C'}}(t_5) \text{ (V)}$$

which yields

$$i_{T_3''}(t) = \frac{V_{DC} - V_{C_{C'}}(t_5)}{Z} \sin(\omega_0 t) + i_{T_3'}(t_5) \cos(\omega_0 t) \text{ (A)} \tag{4.27}$$

$$V_{C_C''}(t) = [V_{DC} \cos(\omega_0 t) - V_{C_{C'}}(t_5)(\cos(\omega_0 t) - 1) \tag{4.28}$$

$$+ Z i_{T_3'}(t_5) \sin(\omega_0 t)]$$

where $\omega_0 = 1/\sqrt{L_C C_C}$ (rad/s) and $Z = \sqrt{L_C/C_C}$ (Ω)

The voltage V_{C_C} across the commutation capacitor terminates with the opposite polarity, when current $i_{T_3''}$ reduces to zero. The transfer of the stored magnetic energy in L_C causes this voltage rise. The time t_d, t_5 to t_6, is:

$$t_d = \frac{1}{\omega_0} \tan^{-1} \frac{i_{T_3'}(t_5) Z}{V_{DC} - V_{C_{C'}}(t_5)} \tag{4.29}$$

In the Figure 4.3 (f), as the current $i_{T_3''}$ reduces to zero at t_6, the current i_{FW} passes through the circuit loop L_{LOAD}, T_4, R_{FAULT} and D_{FW} to dissipate the magnetic energy stored in load (fault) inductor L_{LOAD}, which obeys the following differential equation:

$$L_{LOAD} \frac{di_{FW}}{dt} + R_{FAULT} i_{FW} = 0 \text{ (A)} \tag{4.30}$$

with initial conditions

$$i_{FW}(t_6) = i_{T_3'}(t_6)$$

which yields

$$i_{FW}(t) = i_{T_3'}(t_6) e^{\frac{-t}{\tau_3}}$$

where $\tau_3 = \frac{L_{LOAD}}{R_{FAULT}}$

The analytical equations corresponding to each interval of the test circuit have now been derived. They can be used to calculate the required peak voltage, peak currents, the current-zero time, etc., when the component values and special conditions, such

as the time when the commutation circuit is triggered to achieve a current-zero, are known.

In summary, under the influence of the DC energising circuit, the mechanical response time of the VCB from receiving an 'off' signal to the electrodes separating is approximately 13ms. The time interval from the occurrence of the coil current peak to electrode separation is approximately 5ms. During this 5ms interval, the requirements for this test circuit are not only to establish a specifiable fault current passing through the VCB, but also to ready the commutation circuit to generate a VCB current-zero. The commutation circuit is activated when the electrodes have separated a specific distance. Current interruption is complete provided there is a current-zero in the commutation circuit.

4.3.1 Commutation circuit calculations

Since there is a limitation on the energy storage capability of the commutation capacitor, which needs significant energy to produce a successful current-zero, the maximum fault current should be identified by applying equations (4.10-17). Then the commutation capacitance is calculated in terms of the commutation frequency, system voltage, and current ratings. From equation (4.20), the maximum counter-current is:

$$I_{peak} = i_{T_3}(\frac{\pi}{2\omega_0}) = \frac{V_{DC}}{Z}\sin(\omega_0 \frac{\pi}{2\omega_0}) \text{ (A)} \tag{4.31}$$

Since $\omega_0 = 2\pi f = 1/\sqrt{L_C C_C}$ (rad/s) and $Z = \sqrt{L_C/C_C}$ (Ω), then

$$L_C = (\tfrac{1}{2}\pi f/C_C)^2 \quad \text{(H)} \tag{4.32}$$
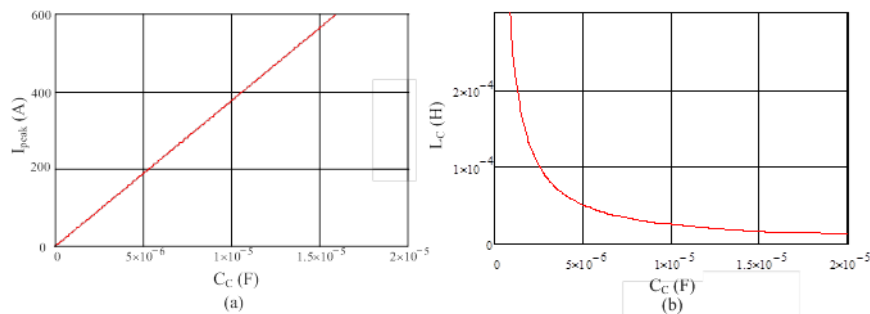
Figure 4.6 (a) The maximum peak current with commutation frequency 10kHz and (b) the required commutation coil.

92

Figure 4.6 (a) shows the relationship of capacitance and the maximum counter-current produced with initial voltage -600V for a 10kHz commutation frequency (50 μs half period) and part (b) illustrates the commutation inductance required for the counter-current with a 10kHz commutation frequency. In addition, Greenwood [4.1] found that a current magnitude design margin is needed for commutation circuits, which means the maximum counter-current is always larger than the interrupting current.

As mentioned, di/dt is defined as the net rate of change of the VCB current between the moment commutation commences and the moment that the current decreases to zero, once the electrodes have parted a specific distance. Based on equation (4.20) and (4.22):

$$\frac{di}{dt} = \frac{i_{FAULT}(t_2)}{t_{CZ1}} = \frac{i_{FAULT}(t_2)}{\sqrt{L_C C_C}\,\sin^{-1}(\frac{i_{FAULT}(t_2)Z}{V_{DC}})} \tag{4.33}$$

where $t_{CZ1} = t_2 - t_3$ and $Z = \sqrt{\frac{L_C}{C_C}}$

The di/dt is determined by four parameters namely the interrupting current $i_{FAULT}(t_2)$, the initial capacitor voltage V_{DC}, the commutation capacitance C_C, and the commutation inductance L_C. The effect of each parameter on di/dt, is illustrated in the Figure 4.7; where the plots represent equation (4.33) for different parameters with parameter values listed in each legend.
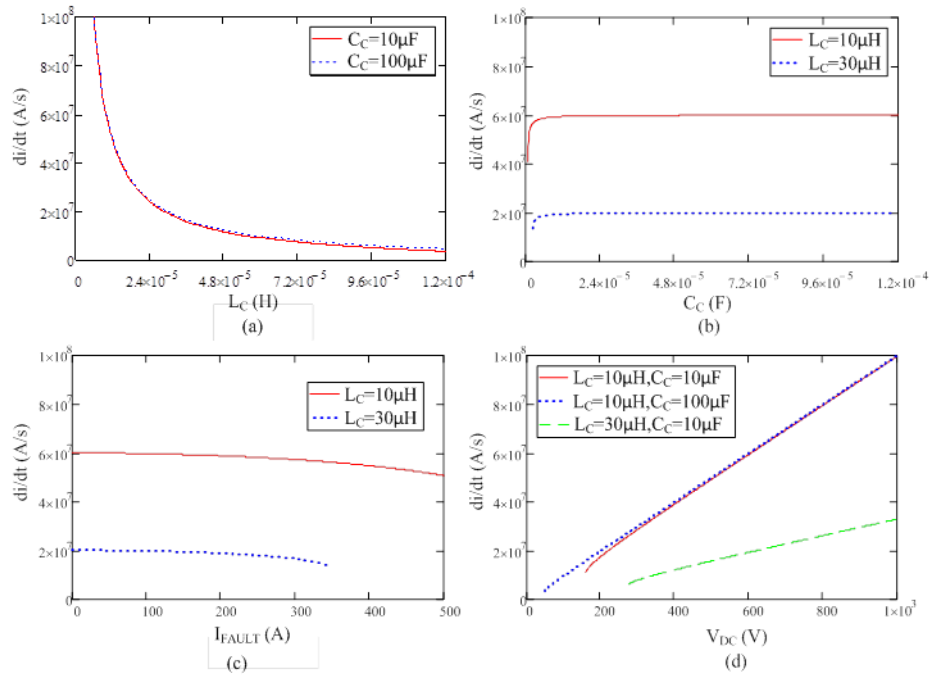
Figure 4.7 The maximum di/dt as function of: (a) commutation inductance; (b) commutation capacitance; (c) interrupting current; and (d) initial capacitor voltage.

In Figure 4.7 (a), with a fixed interrupting current of 160A and initial capacitor voltage of 600V, the value of di/dt experiences a continuously decreasing trend as L_C increases. This trend is independent of C_C, based on commutation capacitances of 10μF and 100μF. Figure 4.7 (b), with the same conditions except two different inductances, 10μH and 30μH, confirm that di/dt remains unchanged once C_C reached a certain value. di/dt starts to increase after C_C increases above a minimum value in order to produce a counter-current the same level as i_{FAULT}. This increase is very steep. It is difficult for this situation to occur because normally the maximum counter-current is designed to be large compared to i_{FAULT}, therefore small C_C causing an increase in di/dt is eliminated. Figure 4.7 (c) shows the relationship between di/dt and i_{FAULT} in terms of a 600V initial capacitor voltage and 10μF commutation capacitance. When the commutation inductance L_C is fixed, di/dt almost remains unchanged until i_{FAULT} exceeds the maximum counter-current produced by the commutation circuit. However, for different commutation inductances, 10μH and 30μH, the di/dt produced by the smaller inductance is large compared to that associated with the higher inductance. The relationship between

di/dt and initial capacitor voltage is shown in figure (d) with a fixed 160A interrupting current but varied commutation parameters. Regardless of the varied commutation parameters, the di/dt exhibits an ever-increasing trend with an increase in the initial capacitor voltage. Based on a fixed commutation inductance, 10μH, but varied capacitance, 10μF and 100μF, once the initial capacitor voltage was increased to produce a counter-current with the same level as the interrupting current, the trend of di/dt is the same, a continual increase. With the same commutation capacitance, 10μF, but different inductances, 10μH and 30μH, the di/dt difference introduced by the larger inductance not only has a larger value than that associated with the smaller inductance, but also possesses faster rise rate. In summary, the di/dt trend is dominated by the commutation inductance and the initial voltage across C_C ($V_{Cc}=L_C di/dt$), but independent of commutation capacitance and interrupting current.

Odaka [4.6] established that the dv_{VCB}/dt variation across the VCB after current interruption can be found from the interrupting current $i_{VCB} = i_{FAULT}$ (t_2) (current at the beginning of commutation) and a simplified equivalent circuit comprising the commutation capacitor C_C and inductor L_C, and the snubber capacitor C_s connected in parallel to the VCB, as shown in Figure 4.8.
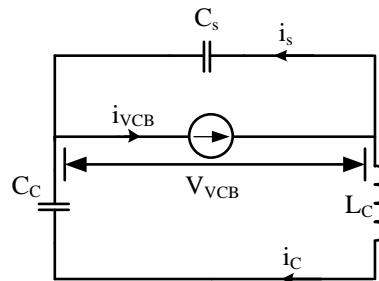
Figure 4.8 Equivalent circuit

From the equivalent circuit in figure 4.8, after taking Laplace transforms, dv_{VCB}/dt can be determined from:

$$\frac{i_{VCB}}{s} = \frac{i_C}{s} + \frac{i_s}{s} \tag{4.34}$$

95

$$V_{VCB} = \frac{i_C}{s}\left(sL_C + \frac{1}{sC_C}\right) \qquad (4.35)$$

$$V_{VCB} = \frac{i_C}{s}\frac{1}{sC_s} \qquad (4.36)$$

thus, V_{VCB} is:

$$V_{VCB} = \frac{i_{VCB}}{s^2(C_s+C_C)} + \frac{i_{VCB}C_C}{C_s(C_s+C_C)}\frac{1}{s^2 + \sqrt{\frac{C_s+C_C}{C_sC_CL_C}}} \qquad (4.37)$$

which, after taking the inverse Laplace transform, yields:

$$V_{VCB}(t) = \frac{i_{VCB}t}{C_s+C_C} + \frac{i_{VCB}C_C}{C_s(C_s+C_C)}\sqrt{\frac{C_sC_CL_C}{C_s+C_C}}\sin\sqrt{\frac{C_s+C_C}{C_sC_CL_C}}t \qquad (4.38)$$

dv_{VCB}/dt at current zero is given by differentiating (4.38):

$$\frac{dv_{VCB}}{dt} = \frac{i_{VCB}}{C_s+C_C} + \frac{i_{VCB}C_C}{C_s(C_s+C_C)} \qquad (4.39)$$

Three parameters determine the dv_{VCB}/dt trend, namely interrupting current i_{VCB}, commutation capacitance C_C, and the snubber capacitance C_s. dv_{VCB}/dt characteristics in terms of these parameters are shown in Figure 4.9, for a fixed commutation inductance, 10µH. In Figure 4.9 (a), based on an interrupting current i_{VCB} =160A, dv_{VCB}/dt reduces as C_s increases. However, it is unchanged if C_C is increased from 10µF to 100µF. To confirm this, the same conditions, including $C_C = 10$µF, are utilised in Figure 4.9 (b) which shows that dv_{VCB}/dt is increased when C_s is between 5µF and 10µF. dv_{VCB}/dt remains unchanged with increasing C_C, which indicates their independence. With $C_C = 10$µF, the increasing trend of dv_{VCB}/dt with increasing i_{VCB} is seen in Figure 4.9 (c). However, the increase of dv_{VCB}/dt is reduced when C_s is increased from 5µF to 10µF. In conclusion, dv_{VCB}/dt is determined by i_{VCB} and C_s, ($i_{VCB}=C_sdv_{VCB}/dt$), rather than C_C which has little effect.
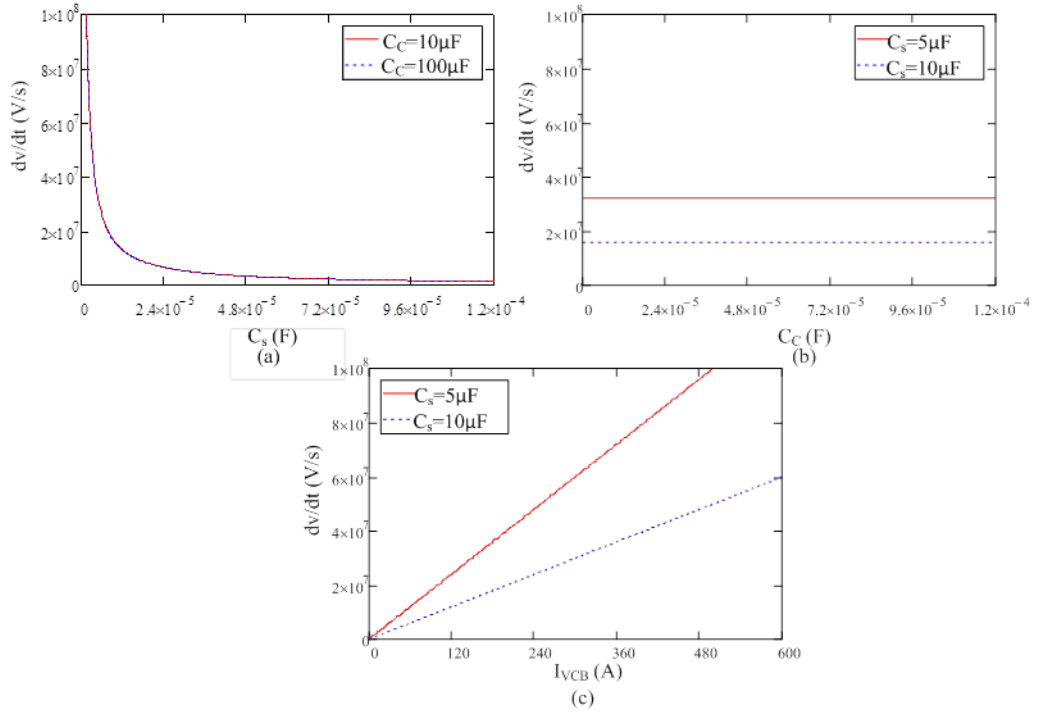
Figure 4.9 Maximum dv/dt as function of: (a) snubber capacitance; (b) commutation capacitance; and (c) interrupting current.

From [4.13], the cross-sectional views of single-layer and multi-layer cylindrical inductors are shown in Figure 4.10 (a) and (b). The inductance of a single-layer cylindrical inductor, is given by (dimensions are in mm):

$$L = \frac{\mu_{eff} r^2 N^2}{228.6r + 254l} \quad (\mu H) \tag{4.40}$$

by considering insulation spacing between the single layer turns:

$$L = \frac{\frac{2}{3}\mu_{eff} N^{1.3}(d+d_w)^{1.7}}{(d_w+S)^{0.7}} \quad (\mu H) \tag{4.41}$$

where d_w is the bare wire diameter and S is the spacing between turns.

The equation for a multi-layer cylindrical inductor is given by:

$$L = \frac{\mu_{eff} r^2 N^2}{152.4r + 228.6l + 254b} \quad (\mu H) \tag{4.42}$$

The plots in Figure 4.10 (c) represent the effective permeability based on the former l/d ratio and the core material permeability. These values of effective permeability

are utilised in the design of the single-layer inductor. The winding is considered closely wound over 95 percent of the core length.
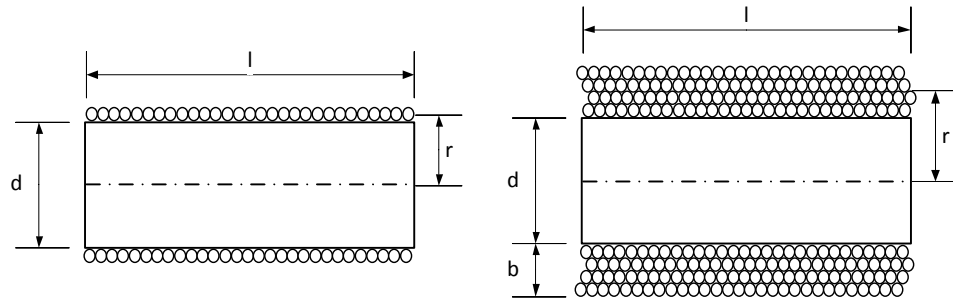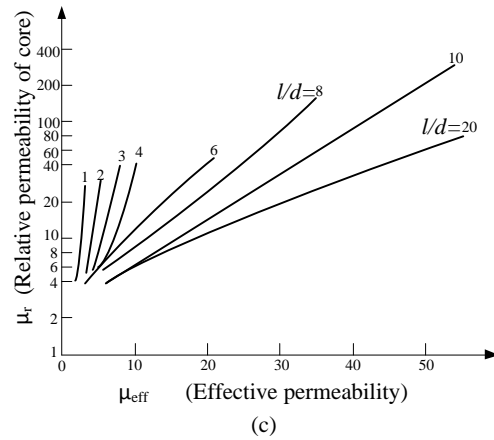
Figure 4.10 Cylindrical inductors: (a) single-layer coil; (b) multi-layer coil; (c) effective permeability for different aspect ratios, l/d.

4.3.2 Precautions for the commutation circuit components

To prime the commutation circuit, ready to produce a high counter-current through the VCB, the commutation capacitor voltage should be reversed by triggering switch T_2. Resonant circuit losses and leakage mean the capacitor does not retain the full dc voltage (reversed).

Energy losses can be expressed as:

$$E_{nor} = \int_0^t v(t) \cdot i(t) dt \tag{4.43}$$

$$= \sum_{m=1}^{k} v(m) \cdot i(m) \Delta t \tag{4.44}$$

where v and i represent the voltage drop across a device and the current passing through it, respectively. Equation (4.43) can be used for continuous functions, while for discontinuous or discrete cases, equation (4.44) may be applicable.

The energy losses in the resonant loop are due to resistance in the inductor, solid-state switches, and capacitor.

Solid-State Switches Losses

Solid-state switch energy losses comprise conduction losses (E_{cond}), and switching on E_{SON} and off E_{SOFF} losses, with the conduction losses dominating in the test circuit. Switching losses E_{SON} and E_{SOFF} can be ignored since turn-on and off are soft switching action due to the initial and final inductor current being zero in this LC resonant circuit.

The conduction voltage of a solid-state switch, can be determine from [4.14-16]:

$$v_{CE} = v_{CE0} + r_c i_{ce} \tag{4.45}$$

where v_{CE0} is the IGBT on-state collector-emitter voltage with zero-current; r_c is collector-emitter on-state resistance, and i_{ce} is the current passing through IGBT.

The same approximation can be utilised for the diode conduction voltage, namely:

$$v_D = v_{D0} + r_D i_D \tag{4.46}$$

where v_{D0} represents diode on-state anode-cathode voltage with zero-current, r_D is anode-cathode on-state resistance, and i_D is the current passing through the diode, where $i_{ce} = i_D$ here due to series connection of the IGBT and diode.

The necessary parameters can be obtained directly from the solid-state device datasheets shown in Figure 4.11. In order to produce accurate calculations, parameter variation has to be considered. This means the v_{CE0} and v_{D0} values from the plots have to be scaled by (v_{CEmax}/v_{CEtyp}) or (v_{Dmax}/v_{Dtyp}). Although the datasheet tables provide values, for an engineering calculation a safety margin should be adopted [4.15].
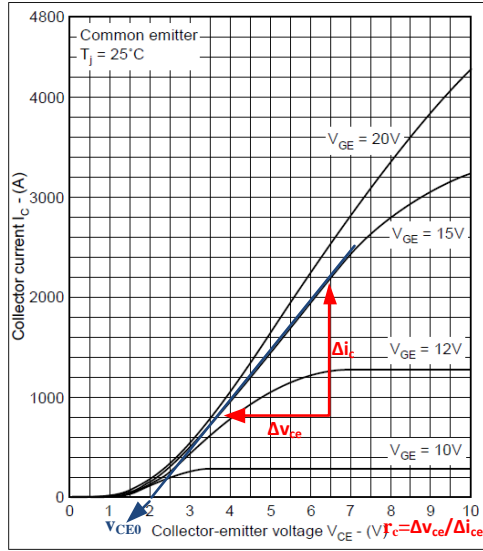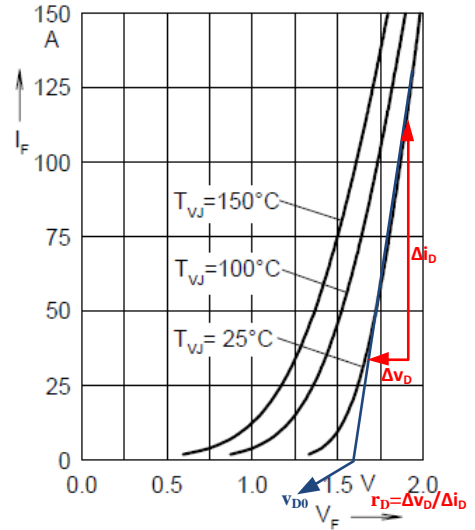
(a)   (b)

Figure 4.11 Reading the v_{CE0}, v_{D0} and r_c, r_D from the data-sheet diagram: (a) IGBT (GP600DHB16S) and (b) Diode (DSEI 2×101).

The resonance output current can be assumed to be half-wave sinusoidal:

$$i_c(t) = I_0 \sin(\omega t)\, 0 \leq \omega t \leq \pi \quad (rad) \tag{4.47}$$

where I_0 represents the peak resonant output current and $\omega \cong 1/\sqrt{L_C C_C}$.

Thus, the IGBT conduction loss energy is:

$$E_{CE} = \int_0^{\pi\sqrt{L_C C_C}} v_{CE} \cdot i_c(t)dt = \int_0^{\pi\sqrt{L_C C_C}} (v_{CE0} + r_c i_c) \cdot i_c(t)dt \tag{4.48}$$

$$= \int_0^{\pi\sqrt{L_C C_C}} v_{CE0} \cdot i_c(t)dt + \int_0^{\pi\sqrt{L_C C_C}} r_c i_c \cdot i_c(t)dt$$

$$= (v_{CE0} \cdot \bar{I}_0 + r_c \cdot I_{rms}^2) \cdot \frac{\pi}{\omega}$$

where $\bar{I}_0$ and I_{rms}^2 are the average and RMS currents i_c, respectively.

A similar expression results for the diode conduction loss:

$$E_D = (v_D \cdot \bar{I}_0 + r_D \cdot I_{rms}^2) \cdot \frac{\pi}{\omega} \tag{4.49}$$

100

Line Resistance Losses

Since the inductance and capacitance are varied during experimentation, the resistance R_C of the commutation circuit varies.

The expression for the energy losses in the line resistance can be approximated as:

$$E_L = \int_0^{\pi\sqrt{L_C C_C}} R_C i_c(t)^2 dt \tag{4.50}$$

$$= R_C \cdot I_{rms}^2 \cdot \frac{\pi}{\omega}$$

Table 4.2 shows the requirements for these semiconductor switches. The voltage rating of T1 may be problematic since it is twice that of the other switches.

<div align="center">

Table 4.2 Solid-state switches voltage ratings

</div>

	T_1		T_2		T_3		T_4	
	IGBT	Diode	IGBT	Diode	IGBT	Diode	IGBT	Diode
Voltage rating	at least $2\times V_{DC}$	at least $1\times V_{DC}$	at least the max V_{C_C}	at least the max V_{C_C}	at least the max V_{C_C}	at least the max V_{C_C}	at least $1\times V_{DC}$	at least $1\times V_{DC}$
Current rating	depends on R_1	depends on R_1	rated fault current	rated fault current	rated fault current	rated fault current	rated fault current	rated fault current

4.4 Test circuit simulation using PSPICE

In general, MATLAB software is used in one specific case but, generally, PSPICE [4.17, 18] is used since the simulation will closer approach the laboratory setup conditions since device characteristics are important. PSPICE simulation results are redrawn with MATLAB.

Test circuit behaviour can be accurately explored if the basic device specifications and characteristics are detailed, such as, the current through and voltage across each component. An accurate detailed model may give rise to long simulation times. It is difficult to simulate the test circuit since no PSPICE VCB model exist. Fortunately,

the thyristor, or specifically the silicon-controlled rectifier (SCR) shown in Figure 4.12, can be utilised as an alternative for the VCB during simulation due to their similar electrical behaviour. The SCR has three features which mirror the VCB. Firstly, switching to the on state requires a gate signal (positive V_{GK} or I_G) and a positive voltage V_{AK} from the anode to cathode; secondly, to remain in the on state requires a continual anode-cathode (holding) current I_{AK}; and finally, switching to the off state requires reversal of the polarity of V_{AK} and the current I_{AK} must reduce to zero. Turn-off cannot, however, be achieved with low power gate conditions.
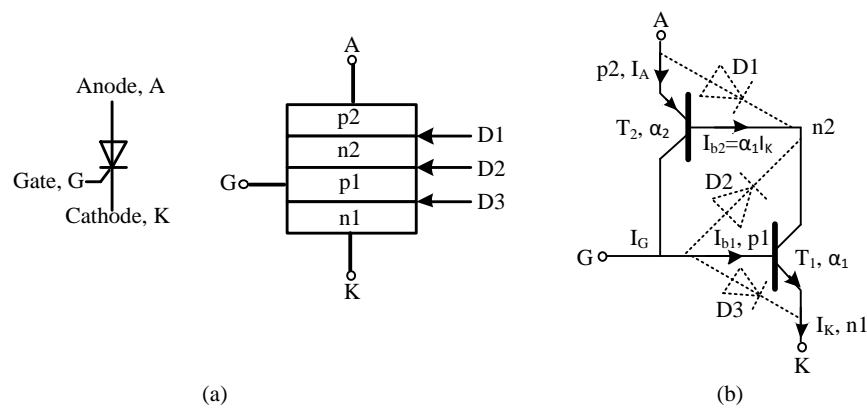
Figure 4.12 Cross-section of the SCR showing its model derivation: (a) schematic of the SCR cross-section and (b) the npn-pnp two transistor model of the basic SCR.

Several SCR models exist [4.19-21], but the choice is dominated by the behaviour of devices and the computation time. Here, the PSPICE SCR model is employed, after modifying a few parameters to better approach VCB electrical behaviour. These parameters are listed in Table 4.3. V_{DRM}, V_{RRM} and $I_{T(RMS)}$ are set with the same rating as the VCB. V_{TM} in a real SCR is not acceptable, since VCB contact resistance is of the order $\mu\Omega$ rather than $m\Omega$ as in the SCR. By adjusting I_H and T_{off}, a failed interruption could be simulated effectively and utilised to forecast how the VCB transient behaved with too high a dv_{VCB}/dt and di/dt. However, due to the limitations in setting I_H and conditions for switching the SCR to the off state, some VCB conditions cannot be achieved in simulation, such as a successful interruption at the second current-zero and current chopping.

Table 4.3 SCR parameters

Characteristic	Symbol	Unit
Peak Repetitive Off-State Voltage	$V_{DRM},$ V_{RRM}	V
On-State RMS Current	$I_{T(RMS)}$	A
Peak Forward On-State Voltage	V_{TM}	V
Holding Current	I_H	mA
Turn-Off Time	T_{off}	Ms

4.4.1 Simulation of deliberately unsuccessful interruption

A typical interruption failure occurs when the counter-current produced by the commutation circuit is less than the fault current due to slow detection and triggering of the solid-state switches. That is, there is no current-zero in the VCB. The commutation parameters are deliberately designed to result in an unsuccessful interruption. Figure 4.13 gives an overall view, and Figure 4.14 and Figure 4.15 depict the detailed simulation of the preparation and interruption of the test circuit, respectively. The figures on the left describe the voltage across capacitor bank $V_{C_{bank}}$, the commutation capacitor V_{C_C}, and the main switch (SCR) V_{VCB}. The figures on the right plot the current passing through the main switch i_{VCB}, the fault path i_{FAULT}, the resistor R_1 path i_1, the commutation T$_2$ path i_{T2} and T$_3$ path i_{T3}.
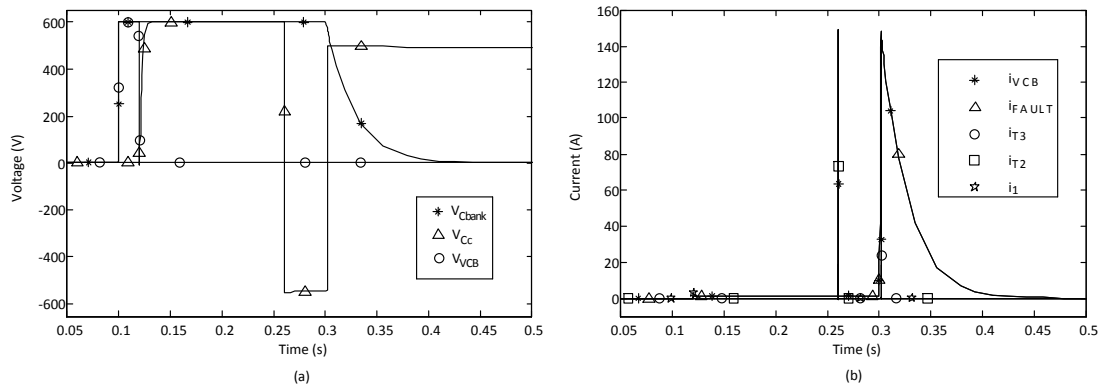
Figure 4.13 The overall view of test circuit voltage and current waveforms during an unsuccessful interruption; $(V_{DC} = 600V, C_{bank} = 7mF, C_C = 10\mu F, R_1 = 200\Omega, L_C = 150\mu F, L_{LOAD} = 1.7mH, R_{LOAD} = 600\Omega, R_{FAULT} = 4\Omega)$.
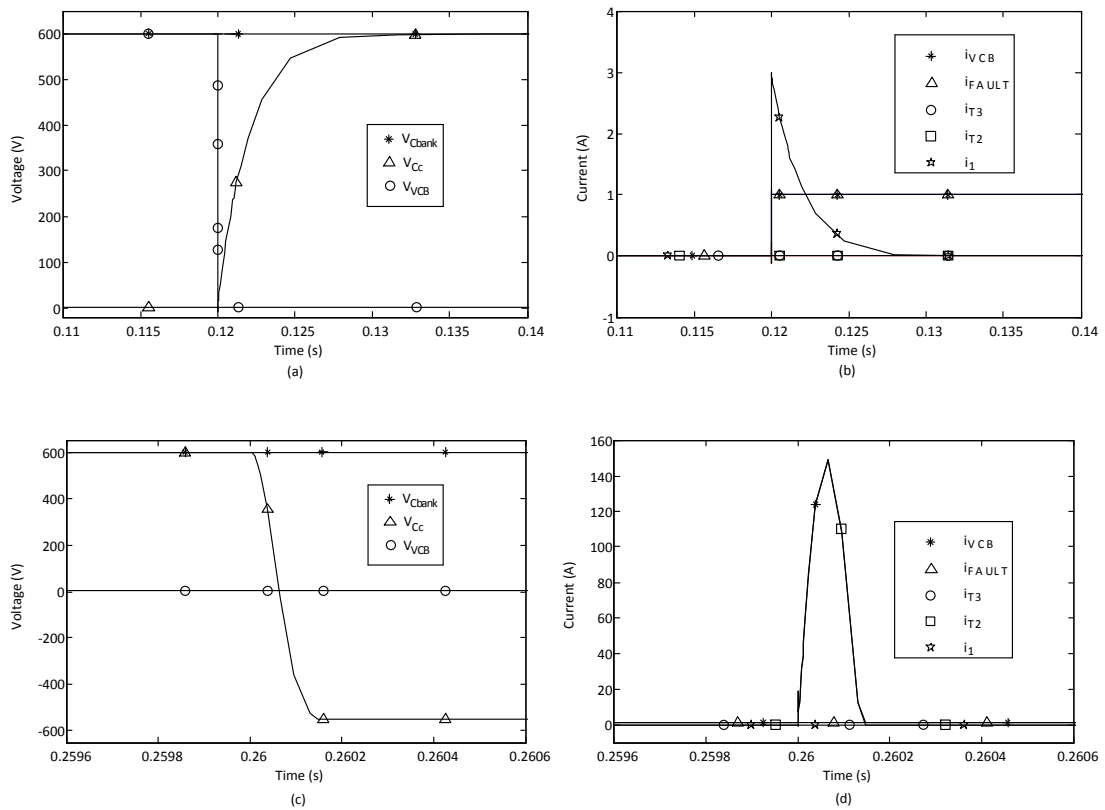
Figure 4.14 Test circuit simulation waveforms during preparation; $V_{DC} = 600V, C_{bank} = 7mF, C_C = 10\mu F, R_1 = 200\Omega, L_C = 150\mu F, L_{LOAD} = 1.7mH, R_{LOAD} = 600\Omega, R_{FAULT} = 4\Omega.$

Although the graphs are consistent with what is expected, the expanded plots of Figure 4.14 (d) and Figure 4.15 (e) highlight some discrepancies in the commutation process. For example, the capacitor is reverse charged to approximately 500V where, by lossless LC resonance, 600V is expected as shown in Figure 4.14 (c). In this case,

the discrepancy is due to the IGBT and diode PSPICE model resistances being too large. None of the discrepancies, however, impact on the analysis.
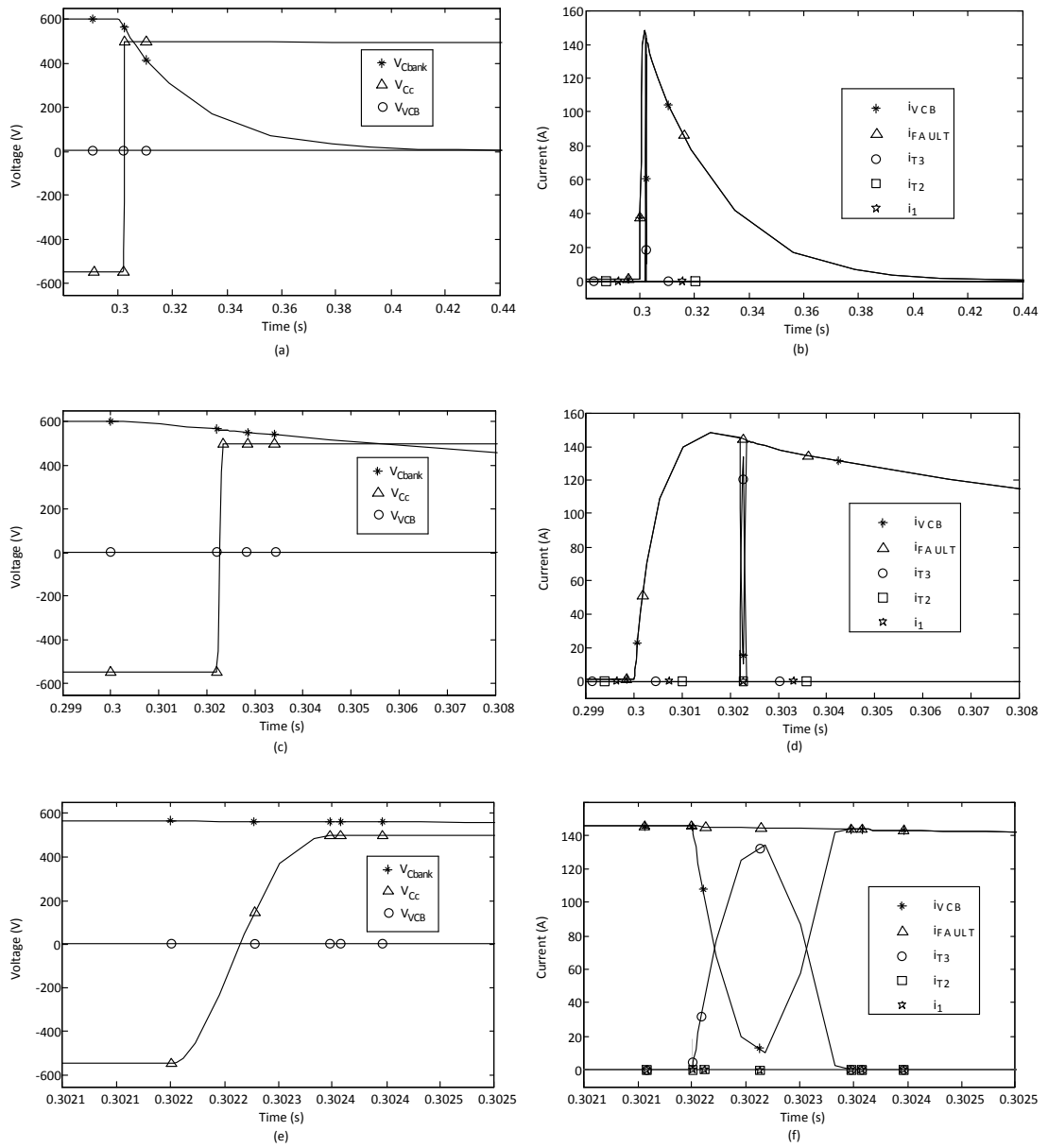
Figure 4.15 Windows enlargement of the occurrence of fault current and the test circuit interruption;
$V_{DC} = 600\text{V}, C_{bank} = 7\text{mF}, \ C_C = 10\text{μF}, \ R_1 = 200\text{Ω}, \ L_C = 150\text{μF}, \ L_{LOAD} = 1.7\text{mH}, R_{LOAD} = 600\text{Ω},$
$R_{FAULT} = 4\text{Ω}.$

105

4.4.2 Simulation of a successful interruption at the first current-zero with and without a snubber capacitor

Test circuit performance during a successful interruption at the first current-zero is shown in Figure 4.16 to Figure 4.18. The waveforms on the left are voltage and current is on the right.
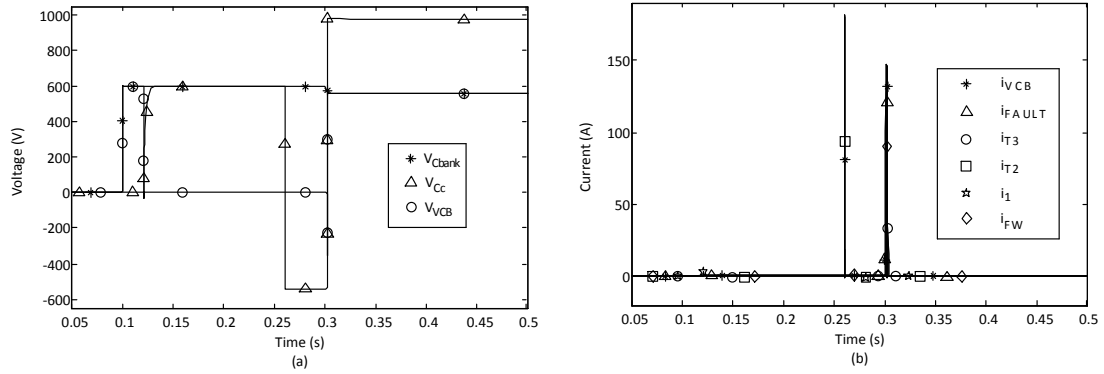
Figure 4.16 The test circuit voltage and current during a hybrid interruption; $V_{DC} = 600V, C_{bank} = 7mF$, $C_C = 10\mu F$, $R_1 = 200\Omega$, $L_C = 100\mu F$, $L_{LOAD} = 1.7mH, R_{LOAD} = 1\Omega$, $R_{FAULT} = 4\Omega$
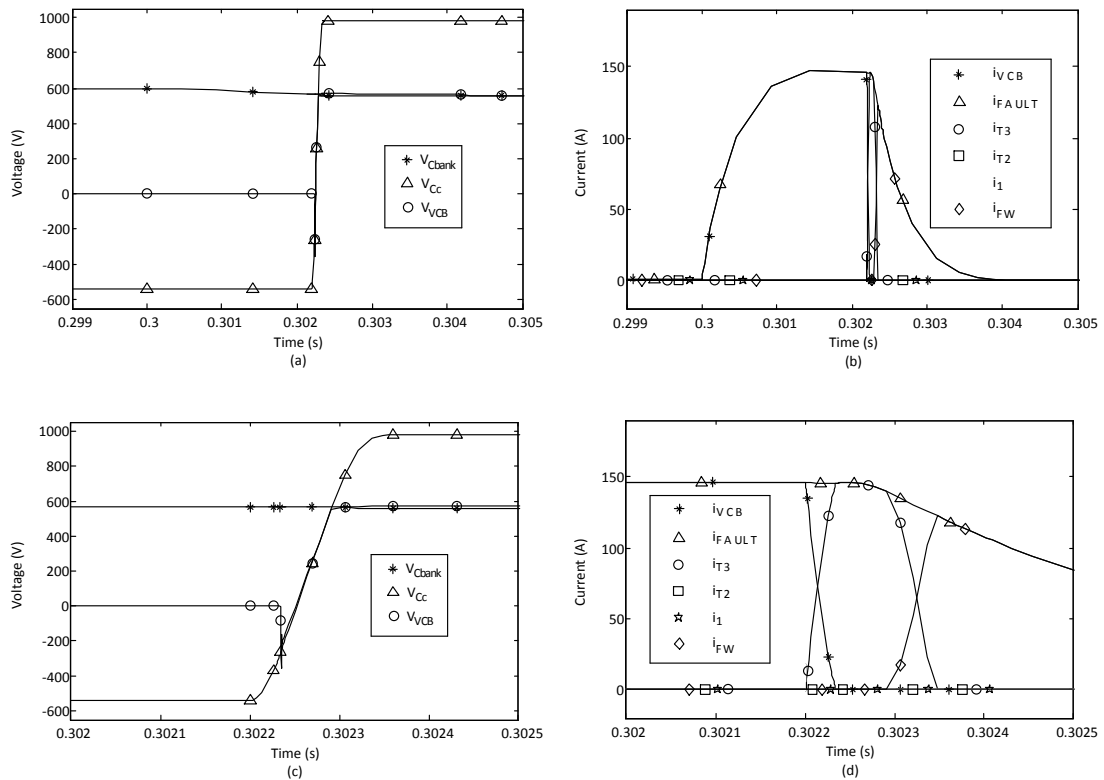
Figure 4.17 Enlargement of fault current and the interruption of the test circuit without a snubber capacitor; $V_{DC} = 600V, C_{bank} = 7mF$, $C_C = 10\mu F$, $R_1 = 200\Omega$, $L_C = 100\mu F$, $L_{LOAD} = 1.7mH, R_{LOAD} = 1\Omega$, $R_{FAULT} = 4\Omega$.

106
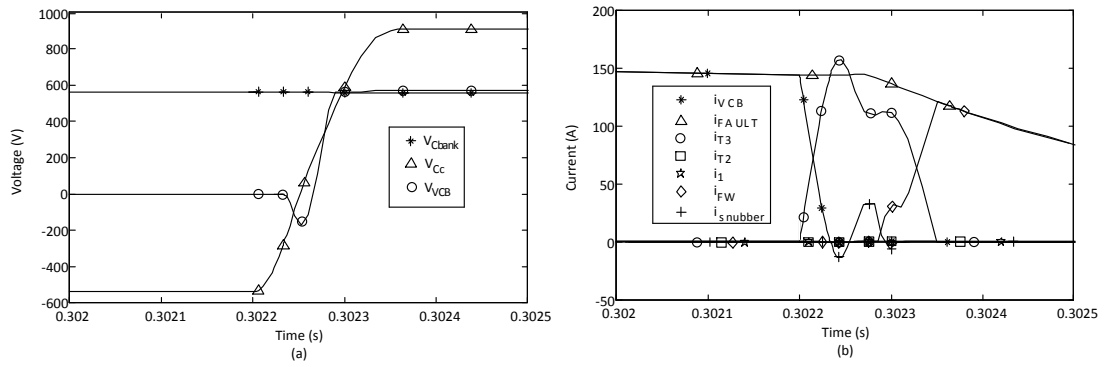
Figure 4.18 Enlargement of the test circuit interruption with a snubber capacitor; $V_{DC} = 600V, C_{bank} = 7mF, \ C_C = 10\mu F, \ R_1 = 200\Omega, \ L_C = 100\mu F, \ L_{LOAD} = 1.7mH, R_{LOAD} = 600\Omega, \ R_{FAULT} = 4\Omega, C_s = 1\mu F.$

There is no difference between Figure 4.16 and Figure 4.13 except V_{C_C} and i_{T2} both rise to a higher level. The decreased L_C decreases commutation circuit impedance $(Z = \sqrt{L_C/C_C})$, causing i_{T2} to increase, according to equation (4.8). Due to successful interruption, the energy stored in the inductance is transferred so as to contribute to the V_{C_C} increase. The preparation stage of the test circuit for introducing counter-current maintains the same basic current and voltage trajectories, except for peak values and duration of the half sinewave, for all simulations. In Figure 4.17, V_{VCB} immediately equals V_{C_C} when the first current-zero occurs and then tracks its change until the freewheel diode D_{FW} conducts. This sudden change in V_{VCB} causes the large dv_{VCB}/dt that can be slowed by introducing snubber capacitor C_s that diverts the current from the VCB after the current-zero appears, as shown in Figure 4.18.

4.4.3 Simulation of an unsuccessful interruption due to high *di/dt*
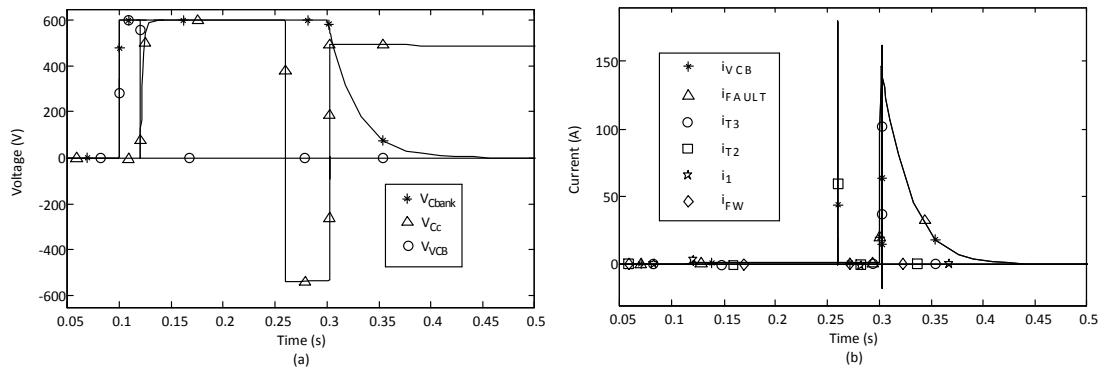
Figure 4.19 The test circuit voltage and current in a hybrid interruption; $V_{DC} = 600V$, $C_{bank} = 7mF$, $C_C = 10\mu F$, $R_1 = 200\Omega$, $L_C = 100\mu F$, $L_{LOAD} = 1.7mH$, $R_{LOAD} = 600\Omega$, $R_{FAULT} = 4\Omega$

The circuit parameters and conditions are similar to the previous case except T_{off} of the SCR model is changed to a large value. Now a failed interruption induced by large di/dt and dv_{VCB}/dt can be simulated, as shown in Figure 4.19. As the literature highlights, with high di/dt and dv_{VCB}/dt, the VCB still conducts even if current-zero points occur. The VCB is seen as a short circuit in this situation [4.6, 8, 9].

Figure 4.20 illustrates a more detailed view during interruption in terms of enlargement step by step. The current i_{VCB} is complementary to i_{T3} which exhibits continual conduction after two current-zero points. Although an SCR is a unidirectional conducting device, PSPICE lumped element model can conduct bidirectionally (like the triac), with the correct parameter settings.
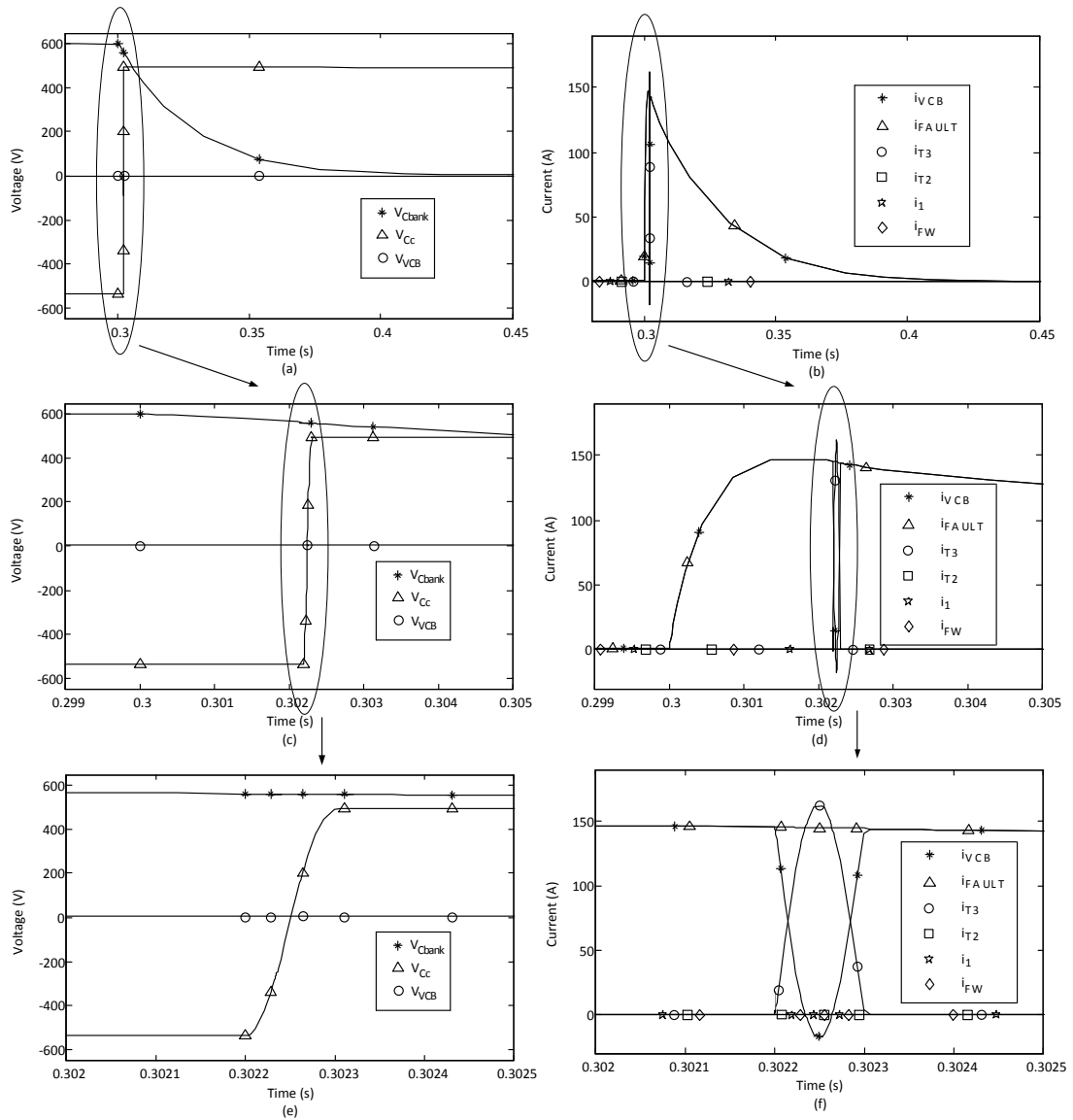
Figure 4.20 Enlargement during interruption of the test circuit; $V_{DC} = 600V$, $C_{bank} = 7mF$, $C_C = 10\mu F$, $R_1 = 200\Omega$, $L_C = 100\mu F$, $L_{LOAD} = 1.7mH$, $R_{LOAD} = 600\Omega$, $R_{FAULT} = 4$.

4.5 Experimental validation

Test circuit experimentation is necessary to validate the analysis and simulation results, and also to explore VCB interruption in terms of external conditions, including di/dt and dv_{VCB}/dt. As mentioned in Chapter 3, the control signals for the test circuit are produced by a microcontroller (dsPIC30F2020, as in Appendix A.2.5). This means VCB properties when interrupting the same current level for

different gap distances can be investigated. Interruption probability is based on the successful interruption at least one of first two current-zero points. To avoid system damage due to the effects of excessive currents, an MOV was connected across the VCB and a series diode was located before the capacitor bank ($C_{bank} = 7$mF) to block currents flowing back into low power 600V DC source. 600Ω load resistance was utilised in all the experiments. The SH5Y AC VCB was used. Parameters for this device are given in Table 3.1.

4.5.1 The preparation stage of the commutation circuit

Figure 4.21 shows the parameter dependant performance of the commutation circuit during capacitor voltage reversal, which includes the voltage across the commutation capacitor V_{C_C}, the IGBT V_{igbt}, and diode V_{diode}. The series current through these components is given by i_{T2}.

The overall- performance of the commutation circuit is shown in Figure 4.21 (a). Before switch T$_2$ is triggered, V_{igbt} withstands voltage V_{C_C}. Then V_{diode} blocks V_{C_C} after the reversal, having experienced controlled *di/dt* reverse recovery. V_{C_C}, initially 100V does not reverse to -100V, but to -80V as a result of LC circuit losses. Figure 4.21 (b) presents the accurate voltage drops of solid-state switches during conduction.
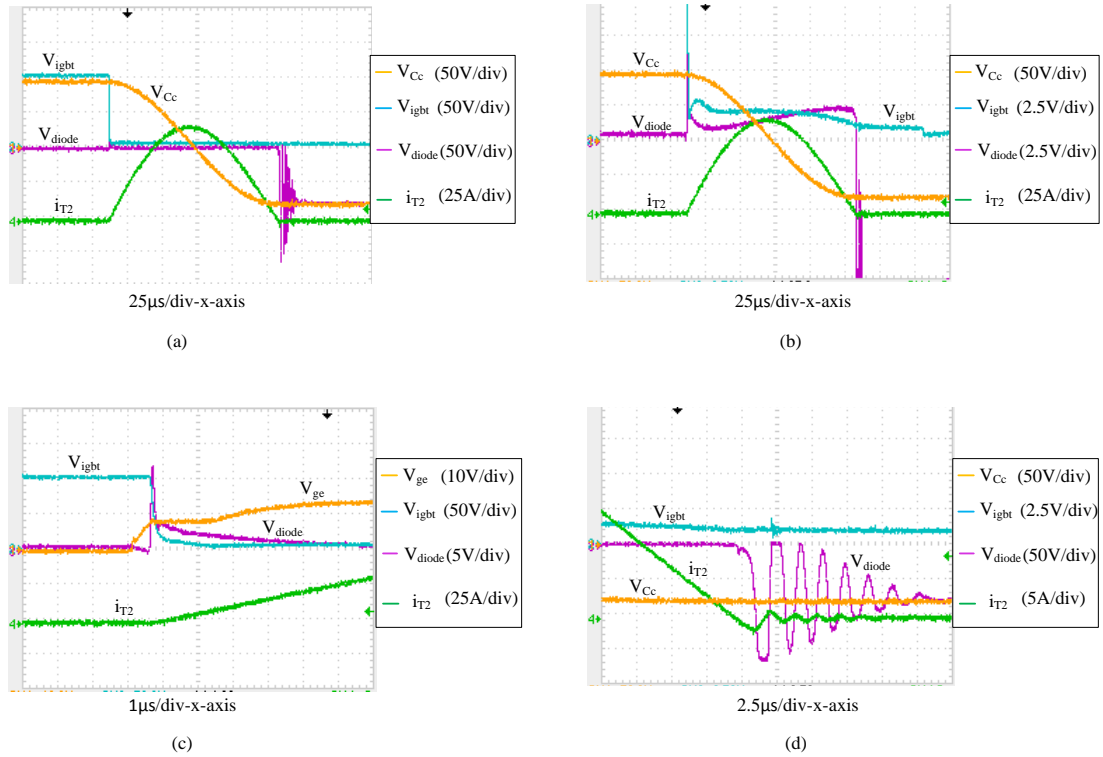
Figure 4.21 Waveforms illustrate the performance of commutation circuit with initial 100V across commutation capacitor ($C_C = 29\mu F$, $L_C = 50\mu H$): (a) overall-view; (b) conduction; (c) switch-on; and (d) switch-off.

Detailed performance during switch turn-on is seen in Figure 4.21 (c). The commutation circuit is a soft switch-on circuit, since the current starts from zero. Figure 4.21 (d) displays the diode characteristics during switch-off, where oscillation due to reverse recovery is observed [4.22].

Oscilloscope recorded data can be used for accurate power loss calculation during the commutation circuit reversal of V_{C_C} from its original 100V (V_{ori}). Putting the data into equation (4.44), the practical energy loss caused by the solid-state switches is calculated and tabulated in Table 4.4.

Table 4.4 Energy losses based on practical data

	Switch-on (mJ)	Conduction (mJ)	Switch-off (mJ)
IGBT energy losses	0.03	10.4	0.00046
Diode energy losses	0.004	8.9	0.045
Total energy losses	0.034	19.3	0.04546

The total loss is 19.38mJ, while the conduction energy loss (19.3mJ) dominates. Energy dissipation during switch-on and off (0.08mJ) can be assumed as zero.

The 29µF capacitor and 50µH inductor have measured resistances of 50mΩ and 62mΩ respectively. The energy stored in the capacitor electric field at 100V is 145mJ from $\frac{1}{2}C_C V^2$. After reversal, there is approximately -80V (V_{aft}) across the commutation capacitor, as shown in Figure 4.21 (a). Thus, the energy loss E_{loss} during reversal is:

$$E_{loss} = \frac{1}{2}C_C\left(V_{ori}^2 - V_{aft}^2\right) = \frac{1}{2} \cdot 29 \cdot 10^{-6} \cdot (100^2 - 80^2) \cong 50 \text{ mJ} \quad (4.51)$$

In terms of equation (4.47), the resonant output current is:

$$i_c(t) = I_0 \sin(\frac{1}{\sqrt{L_C C_C}}t) = i_{T2}(t) = 68\sin(26{,}261t) \quad (4.52)$$

From in Section 4.3.2, the semiconductor on-state parameters can be obtained from the datasheets, specifically: $v_{CE0} = 2V$ and $r_c = 2\Omega$, and $v_{D0} = 1.55$ and $r_D = 1.9\Omega$ for IGBT and diode respectively. Hence, employing equations (4.48) and (4.49), the calculated semiconductor conduction power losses are 19.5mJ, where the energy loss in the IGBT is 11mJ and is 8.5mJ in the diode. The energy loss due to inductor and capacitor resistances is 28mJ, from equation (4.50). Thus calculated losses are 47.7mJ while measured losses are 50mJ.

It is observed that with fixed capacitance, the capacitor voltage V_{Ccaft} after reversal increases as the commutation inductance L_C increases. For fixed inductance, V_{Ccaft} decreases as the commutation capacitance C_C increases. It is mathematically convenient to explain this if the solid-stated switches are considered purely resistive.

By assuming total resistance R_C in the commutation path, equation (4.7) for the circuit loop C_C, VCB, L_C and T_2 becomes

$$\frac{1}{C_C}\int i_{T_2}dt + R_C i_{T_2} + L_C\frac{di_{T_2}}{dt} = 0 \tag{4.53}$$

with the initial conditions

$$i_{T_2} = 0 \text{ (A) and } V_{C_C} = -V_{DC} \text{ (V)}$$

for resonance, $R_C < 2\sqrt{\frac{L_C}{C_C}}$ which yields

$$i_C(t) = \frac{V_{DC}}{\omega_5 L_C}e^{-\delta_3 t}\sin(\omega_5 t) \text{ (A)} \tag{4.54}$$

and

$$V_{C_C}(t) = \frac{V_{DC}\omega_6}{\omega_5}e^{-\delta_3 t}\sin(\omega_5 t - \beta_3) \text{ (V)} \tag{4.55}$$

where $\delta_3 = \frac{R_C}{2L_C}$; $\omega_5^2 = \frac{1}{L_C C_C} - \left(\frac{R_C}{2L_C}\right)^2$; $\omega_6 = \sqrt{\delta_3^2 + \omega_5^2}$ and $\beta_3 = \tan^{-1}\frac{\omega_5}{\delta_3}$.
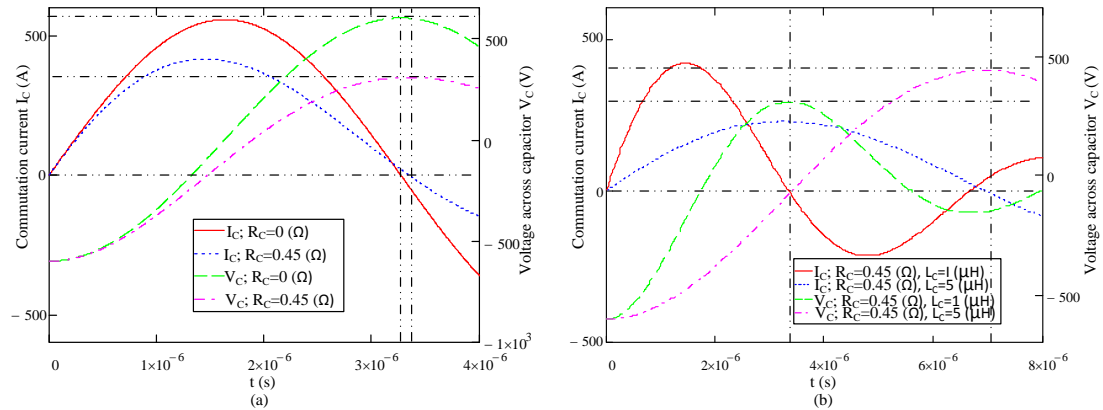
Figure 4.22 Current and voltage waveforms across the capacitor with specific parameters

The plots in Figure 4.22 (a) represent equations (4.54) and (4.55) for two different R_C values. A small difference of approximately 0.5Ω causes a significant difference in the peak voltage and current, as well as in the time delay between them. Therefore,

the commutation circuit needs careful design. Wiring resistance (AC and DC) should be minimised and V) the commutation inductor winding optimised. In this study, IGBTs were used in preference to MOSFETs, since MOSFET voltage rating is limited to approximately 1kV.

Figure 4.22 (b) shows the capacitor voltage is increased by using larger inductor. Increasing inductance will also affect the commutation current into the VCB in the next stage of operation. Also the L_C and C_C half period must be less 5ms. A new commutation circuit configuration is therefore proposed as shown in Figure 4.23. In this new configuration, one inductor can be optimised for reversing the capacitor voltage, whilst the other is optimised for producing the counter-current.
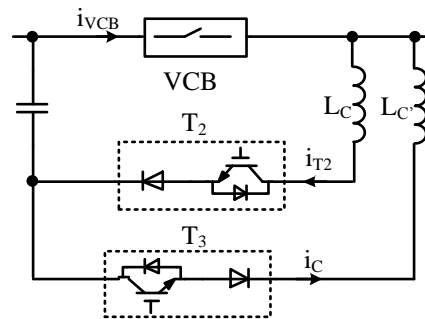
Figure 4.23 The commutation circuit with auxiliary inductor L$_{C'}$

4.5.2 Successful interruption at first or second current-zero without a snubber

The performance of the test circuit interrupting a 330A fault current at the first current-zero is shown in Figure 4.24. Figure 4.24 (a) depicts an overall view and Figure 4.24 (b) shows the commutation duration in detail. After the voltage V_{C_C} across the commutation capacitor was reversed and retained, the fault current i_{FAULT} produced by the capacitor bank voltage $V_{C_{bank}}$ is actuated and flows through the VCB before electrode separation, so that $i_{FAULT} = i_{VCB}$. Then the fault current through the VCB is sinusoidally displaced by the commutation circuit current i_{T3}, until the VCB current is zero, when $i_{FAULT} = i_{T3}$ and $i_{VCB} = 0$. During this period, the voltage across the VCB (V_{VCB}) is initially zero because the electrodes were closed, and then when the electrodes separate a constant 12V arc forms as i_{FAULT} rises. Next the gap voltage clamps to the capacitor residual voltage V_{C_C}, until i_{T3} starts to

decrease (D_{FW} conduction). Then V_{VCB} has been charged to V_{DC} but V_{C_C} continues to increase due to energy stored in commutation inductor L_C, due to it conducting the fault current.
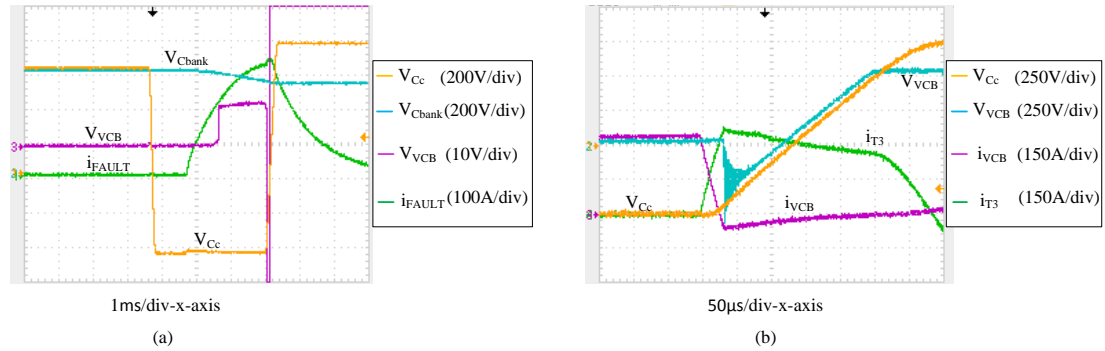
Figure 4.24 Experimental waveforms for the interruption of the test circuit at the first current-zero.
($I_{FAULT} = 330\text{A}, V_{DC} = 600\text{V}, L_C = 49.4\mu\text{H}, C_C = 76.67\mu\text{F}, L_{LOAD} = 1.7\text{mH}, R_{FAULT} = 1.7\Omega$)
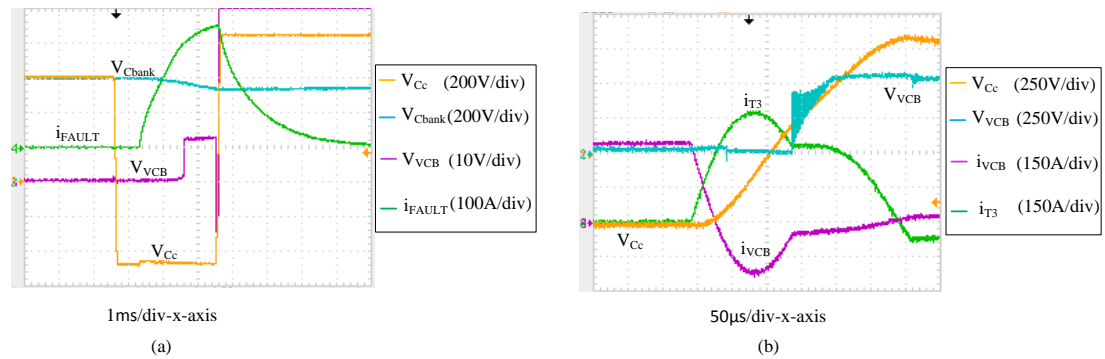
Figure 4.25 Test circuit experimental waveforms for the interruption at the second current-zero.
($I_{FAULT} = 330\text{A}, V_{DC} = 600\text{V}, L_C = 36.87\mu\text{H}, C_C = 32.05\mu\text{F}, L_{LOAD} = 1.7\text{mF}, R_{FAULT} = 1.7\Omega$)

The corresponding parts of Figure 4.25 show interruption at the second current-zero with same interrupting current level, which are similar to those for interruption at first current-zero. In this case i_{VCB} continues to flow through the VCB in the opposite direction. The arc voltage V_{VCB}=12V is reverse. Finally, the interruption is successful at the second current-zero.

With successive interruption attempts the resonance voltage V_{VCB} progressively decays, since resistance is introduced as the plasma starts to recover. Oscillation with the commutation inductor occurs after successful interruption because of the VCB gap capacitive effect [4.4].

4.5.3 With and without snubber circuit
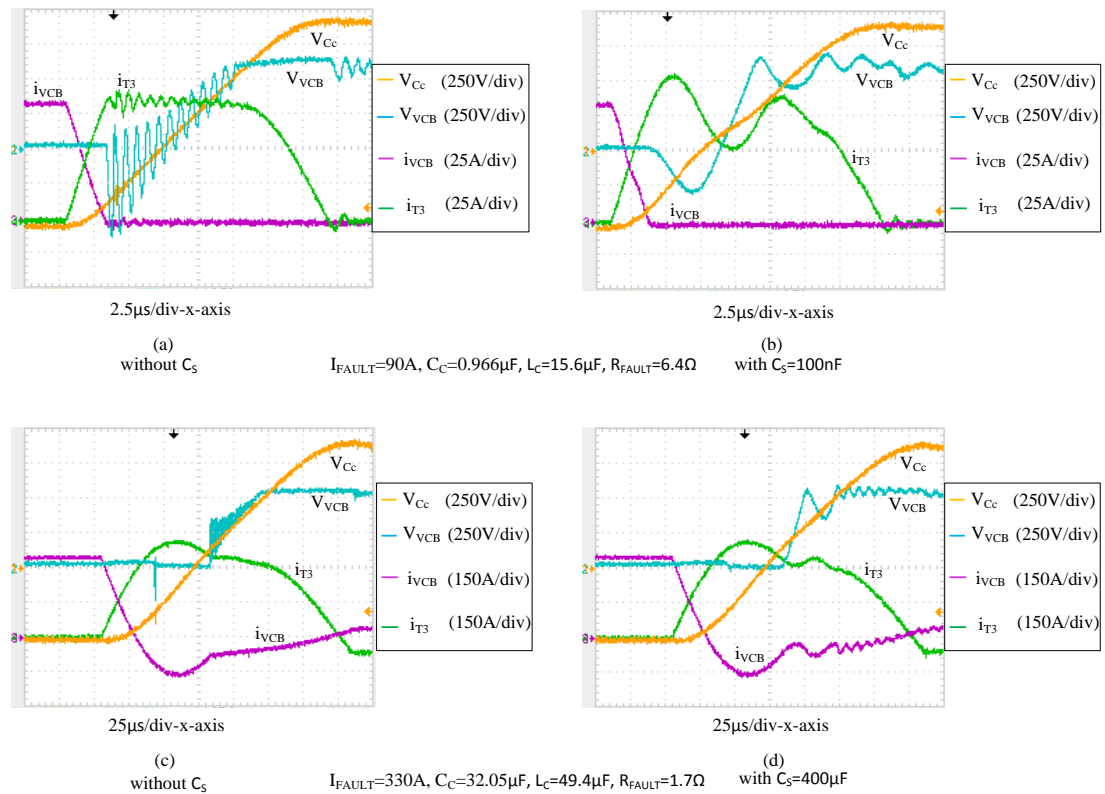
Figure 4.26 Experimental waveforms for interruptions of the test circuit at first and second current-zero with and without snubber circuit.($V_{DC} = 600V, L_{LOAD} = 1.7mF$)

Figure 4.26 (a) provide more detail of the interruption process. The di/dt in this case is 32.3A/µs, which means the commutation time of i_{VCB} is 2.78µs, from 90A to zero. V_{VCB} sharply drops to the residual voltage V_{C_C} causing a higher dv_{VCB}/dt provided i_{VCB} reached zero and no longer flows. The performance can be improved by introducing a snubber circuit as shown by Figure 4.26 (b), where dv_{VCB}/dt is 900V/µs. The interruption performance at the second current-zero without and with a snubber circuit is shown in Figure 4.26 (c) and (d) respectively, where the value of dv_{VCB}/dt in figure (d) is 82.5V/µs. The relationship between di/dt and dv_{VCB}/dt will be described in Section 4.6.4.

116

4.5.4 Unsuccessful interruption

Interruption failure means that i_{FAULT} continues to flow through the VCB (as given in equations (4.10) to (4.17)) as shown in Figure 4.27. Although i_{T3} produces two VCB current-zeros, i_{VCB} returns to the pre-commutation fault condition of i_{FAULT} and an arc voltage V_{VCB} is re-established. Since V_{C_C} has been charged positive, the test circuit is unable to interrupt a fault.

1ms/div-x-axis

(a)

50µs/div-x-axis

(b)
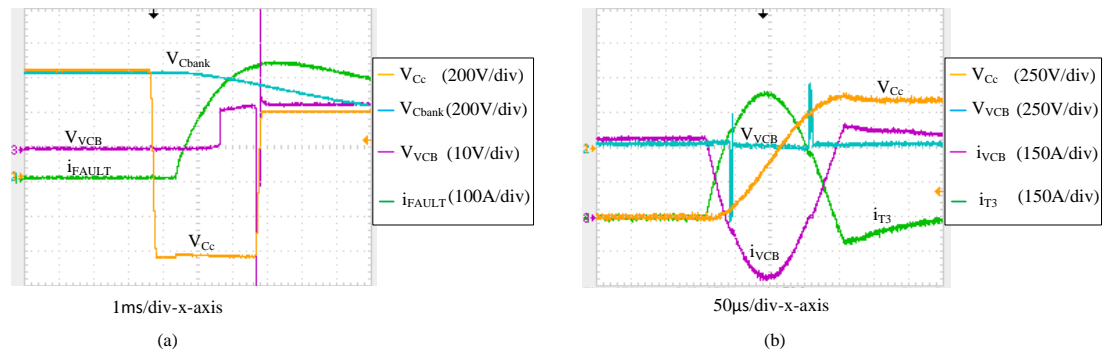
Figure 4.27 Experimental waveforms for unsuccessful interruption at both current-zeros. ($I_{FAULT} = 330A, V_{DC} = 600V, L_C = 49.4µH, C_C = 76.67µF, L_{LOAD} = 1.7mF, R_{FAULT} = 1.7Ω$)
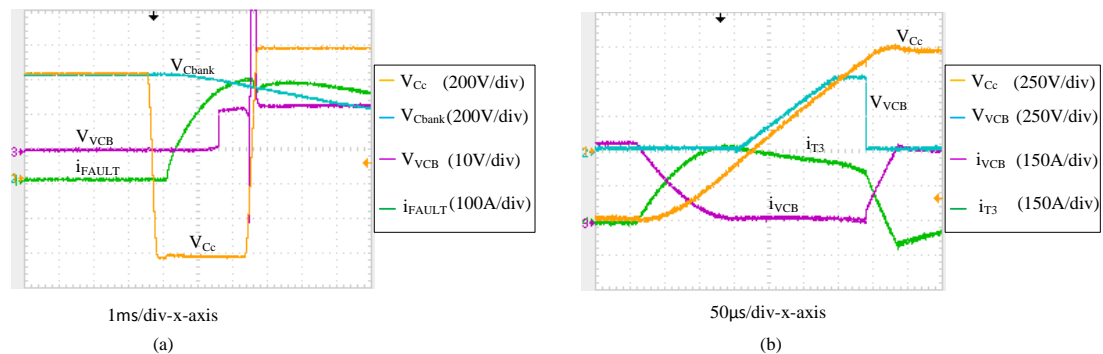
1ms/div-x-axis

(a)

50µs/div-x-axis

(b)

$I_{FAULT}=330A, C_C=76.67µF, L_C=131.96µF, R_{FAULT}=1.7Ω$

25µs/div-x-axis

(c)

25µs/div-x-axis

(d)
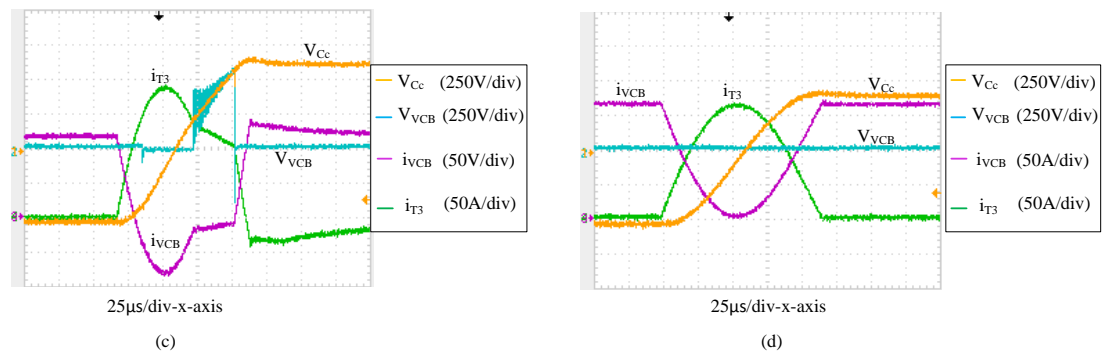
$I_{FAULT}=170A, C_C=12.8µF, L_C=99µF, R_{FAULT}=3.4Ω$

Figure 4.28 Experimental waveforms for unsuccessful interruption at first and second current-zero, with too large a fault current.($V_{DC} = 600V, L_{LOAD} = 1.7mF$)

Voltage performance during unsuccessful interruption is shown in Figure 4.28 (a), with the corresponding current waveforms in Figure 4.28 (b). Interruption failure occurrence is random; sometimes, even with successful interruption at the first or second current-zero, failure occurs without any electrical visual indication, as shown in Figure 4.28 (b) and (c). Failed interruption due to a peak i_{T3} that does not realise a current-zero in i_{VCB} is shown in Figure 4.28 (d).

As described in Appendix B, the reason for arc re-ignition is that there is no vacuum state in the vacuum interrupter after a current zero or that parts of the contacts may still be able to emit vapour because of a hot spot on electrode surface after experiencing the arc. Although interruption failure is random, the probability of successful interruption obeys a principle which will be presented in Section 4.6.4.

4.5.5 Interruption with different gap distance but same interrupting current

1ms/div-x-axis   1ms/div-x-axis

(a)   (b)
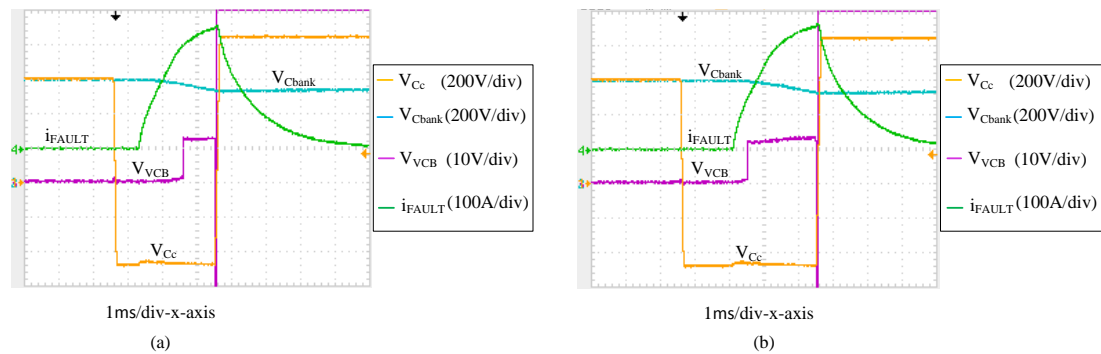
Figure 4.29 Experimental waveforms for interruptions with same interrupting current but different gap distance: (a) gap distance 1mm and (b) gap distance 2mm. ($I_{FAULT} = 330A, V_{DC} = 600V, L_C = 36.87\mu H, C_C = 32.05\mu F, L_{LOAD} = 1.7mF, R_{FAULT} = 1.7\Omega$)

As mentioned in Chapter 3, after electrode separation the VCB maintains stable movement with an opening speed of approximately 1m/s. As indicated in Appendix B, the occurrence of arc voltage could be considered as the separation point of the VCB internal electrodes if the interruption current is low for a given VCB. This means the period of the arc voltage is related to the how far the electrodes have parted. Also, the time difference between the occurrence of counter-EMF induced current peak and separation of VCB electrodes is fixed, reaching a maximum 5ms.

Thus, the VCB can interrupt the same current level for different gap distances by calculated adjustment of the control signals, as shown in Figure 4.29. In this figure the time between V_{Cc} being reversed and the occurrence of arc voltage is a fixed 2ms, but the time to trigger i_{FAULT} is variable. Hence, interruption at gap distances of 1mm and 2mm are shown in Figure 4.29 (a) and (b) respectively.

The interruption properties of the VCB at a range of gap distances were investigated and will be illustrated in Section 4.6.4.

4.6 VCB properties based on practical results

4.6.1 Arc voltage
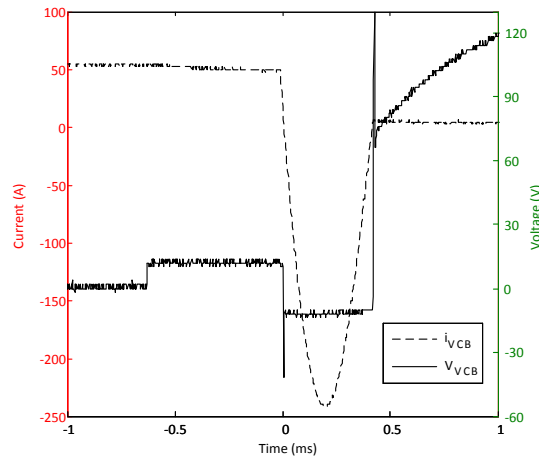
Figure 4.30 Experimental waveforms for the performance of the arc voltage based on its current.
($I_{FAULT} = 50A, V_{DC} = 150V, L_C = 49.4\mu H, C_C = 400\mu F, L_{LOAD} = 0.5mF, R_{FAULT} = 3\Omega$)

Figure 4.30 shows arc voltage performance in term of current i_{VCB} through the VCB. During all the experiments, once the electrodes separated, the arc voltage attained a constant 12V within tens of µs, for all current levels. The 12V arc voltage reverses polarity if i_{VCB} flows in the opposite direction. A 12V arc voltage indicates pure copper electrodes according to Davies and Miller [4.22]. Due to the stability of the

119

arc voltage, based on information in Appendix B, there can be no plasma overlap region above the cathode electrode, the occurrence of which would introduce an arc voltage increase. The arc is always in diffuse mode, since the constricted mode causes an arc voltage decrease. Thus all experimental results were obtained with a diffuse arc.

4.6.2 Current chopping

The characteristics of current chopping are shown in Figure 4.31. When i_{VCB} is reduced, especially to a few amperes, the voltage V_{VCB} produced by the arc becomes unstable resulting in i_{VCB} dropping to zero abruptly and prematurely. The reasons for current chopping have been presented in Appendix B. Briefly, due to lack of conducting components such as electrons and ions, i_{VCB} cannot self-sustaining, hence rapidly extinguishes, and the rapid *di/dt* in conjunction with circuit inductance produces an over-voltage across the VCB. Mathematically, the residual plasma (current) does not comply with equation (B.3).
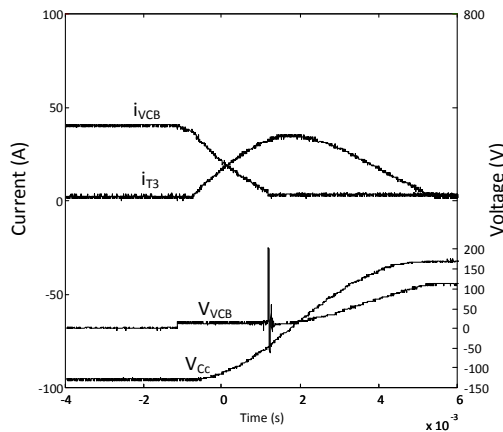
Figure 4.31 Experimental waveforms for current chopping. ($I_{FAULT} = 40A, V_{DC} = 100V, V_{Cc} = 150V,$
$L_C = 1.67mH, C_C = 400\mu F, L_{LOAD} = 0.5mF, R_{FAULT} = 2.5\Omega$)

However, after extensive experimentation, the phenomenon of current chopping vanishes when one of two conditions occurs in relation to the VCB used in this thesis. The first condition is to make *di/dt* larger than 1A/μs if i_{VCB} is less than 50A. The second condition is to ensure i_{VCB} is more than 50A if the *di/dt* is less than 1A/μs.

The arc starts to recover as the current passing through it is reduced, but there is a recovery rate to determine how it recovers. Although the quantity of conduction components, including ions and electrons as well as metal particles, is dominated by the interrupting current level (i_{VCB}), the electrode material, and the VCB electrode dimensions [4.23, 24], the recovery rate determines how much conduction components remains after experiencing an ever-reducing current with fixed di/dt. Thus, for small i_{VCB}, the quantity of residual conductive components is not enough to keep the current smoothly reducing to zero, except if the di/dt is faster than the plasma recovery rate. However, for large i_{VCB}, the phenomenon of current chopping never occurs even if di/dt is less than 1A/μs. A di/dt less than 1A/μs ensured 100% interruption probability in all experiments.

4.6.3 Post-arc current

The post-arc duration is critical in a vacuum interrupter, since it involves the remaining inter-contact ions and electrons, after the circuit current zero. In order to maintain the internal vacuum, interrupters are permanently sealed in ceramic, so the arc cannot be observed. The characteristics of post-arc current were investigated indirectly, based on external electrical behaviour including di/dt, dv_{VCB}/dt, and interruption current level, and gap distance (arcing time).

In order to observe post-interruption performance, i_{VCB} and V_{VCB} are redrawn on a different time-base by utilising MATLAB, as shown in Figure 4.32, where i_{VCB} is presented on a small scale. Current passing through the VCB after i_{VCB} has reduced to zero is interpreted as post-arc current. The delay described in Section 2.4 is observed where the post-arc current appears even if V_{VCB} is zero or equal to the arc voltage (12V), as shown in Figure 4.32 (a). This has been explained by accounting for the thermal velocity of the particles [4.4]. In order to answer the question proposed by the author, that the ion density immediately after current-zero is only determined by its natural decay and the post-arc current, the post-arc current i_{pc} peak after zero crossing is defined. Its performance is investigated by varying di/dt, dv_{VCB}/dt, interruption current level, and gap distance; and will be discussed in end of this section.

There is resonance in Figure 4.32 (b) caused by diode recovery as i_{T3} reaches zero, as shown in Figure 4.26 (a). Based on the sheath theory described in Section 2.4, the post-arc current increases provided an ever-increasing V_{VCB} is maintained. The post-arc current suddenly falls to zero once the sheath reaches the new anode electrode. However, Figure 4.32 (b) and (c) illustrate that the post-arc current rises with an increase in V_{VCB} at first, but slowly reduces as V_{VCB} reaches the DC supply voltage level, 600V. The 600V test voltage is insufficient to ensure the sheath spreads to the new anode electrode, as shown in Figure 4.33 (a). The VCB internal model is shown as a sheath capacitance C_{VCB} across the opening contacts. According to equation (2.5), C_{VCB} is fixed at the instant of sheath contact, so becomes a first-order discharge circuit. The duration t_{dur}, from the post-arc current start to extinction, as presented in Figure 4.32 (d), was investigated by varying interruption current, di/dt, dv_{VCB}/dt and arcing time. However, the results show that it is only sensitive to the test voltage (V_{VCB} in here) as shown in Figure 4.33 (b). The experiment conditions were di/dt=20.73A/μs for interrupting fixed fault current 50A, at voltages 300V, 400V and 600V.
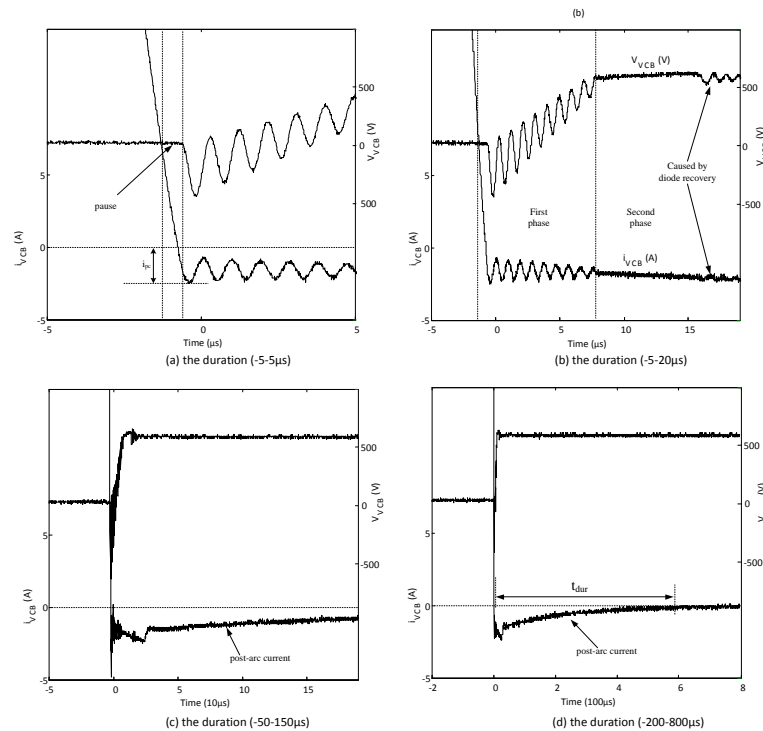
Figure 4.32 Experimental waveforms for the post-arc current.($I_{FAULT} = 90A, V_{DC} = 600V, L_C = 21.45\mu H, C_C = 0.966\mu F, L_{LOAD} = 0.5mF, R_{FAULT} = 6.7\Omega$)

122
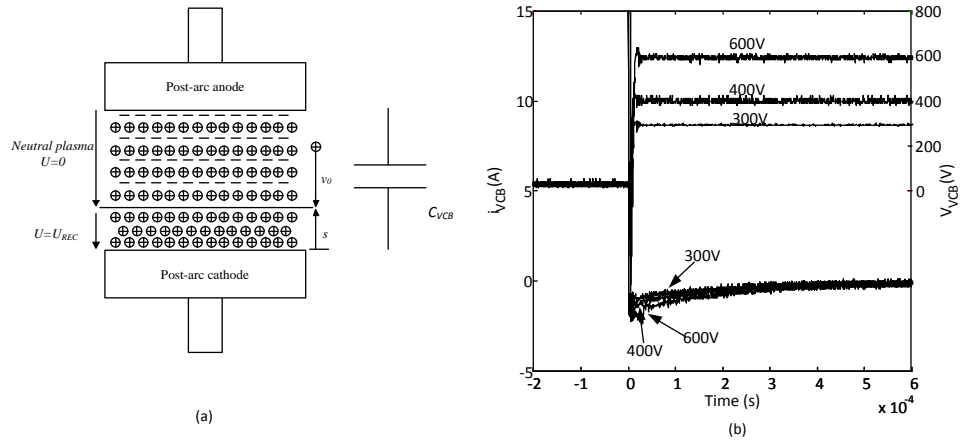
Figure 4.33 (a) Model of sheath with $V_{VCB} = 600V$ and (b) experimental waveforms of post-arc current at different test voltages (V_{VCB}).

In order to accurately examine i_{pc} after the current-zero, the interruption current i_{FAULT} was set to 90A and 45A, both being within the current probe measurement range, and the arcing time (gap distance) was selected at 1.5mm and 2.5mm to reduce the error produced by VCB movement. The experimental conditions were: di/dt =126A/µs, 69.64A/µs, 33.71A/µs, and 20.73A/µs with dv_{VCB}/dt=3kV/µs and 1kV/µs. Each experiment was repeated at least 20 times, always yielding similar results, typically as shown in Figure 4.34. Figure 4.34 (a) is an example of the relationship between i_{pc} and di/dt in terms of a fixed i_{FAULT}, arcing time, and dv_{VCB}/dt. Figure 4.34 (b) illustrates that i_{pc} is insensitive to arcing time (gap distance) based on a fixed di/dt, dv_{VCB}/dt, and i_{FAULT}. Figure 4.34 (c) displays the performance of i_{pc} in terms of varied i_{FAULT} but fixed arcing time, di/dt, and dv_{VCB}/dt. Figure 4.34 (d) presents the change in i_{pc} if dv_{VCB}/dt is varied, with the other three parameters fixed.

The properties of i_{pc} are shown in Figure 4.34 (e). With an increase in di/dt, i_{pc} is increased. i_{pc} is proportional to the interruption current (i_{FAULT} here) that increases as i_{FAULT} is increased. However, i_{pc} decreases when dv_{VCB}/dt decreases. In conclusion, there is a linear relationship between ion density and the interruption current. The ion density at the moment immediately following interruption is impacted by di/dt and dv_{VCB}/dt. However, an interesting phenomenon is observed:

123

no matter how di/dt and dv_{VCB}/dt change, the post-arc current reaches the same final value (2A for $V_{VCB} = 600V$) after approximately 10µs. The post-arc current is dominated by di/dt and dv_{VCB}/dt only at the moment of interruption, thence it is determined by the transient recovery voltage. Hence, the post-arc current can be divided into two phases, as shown in Figure 4.32 (b).
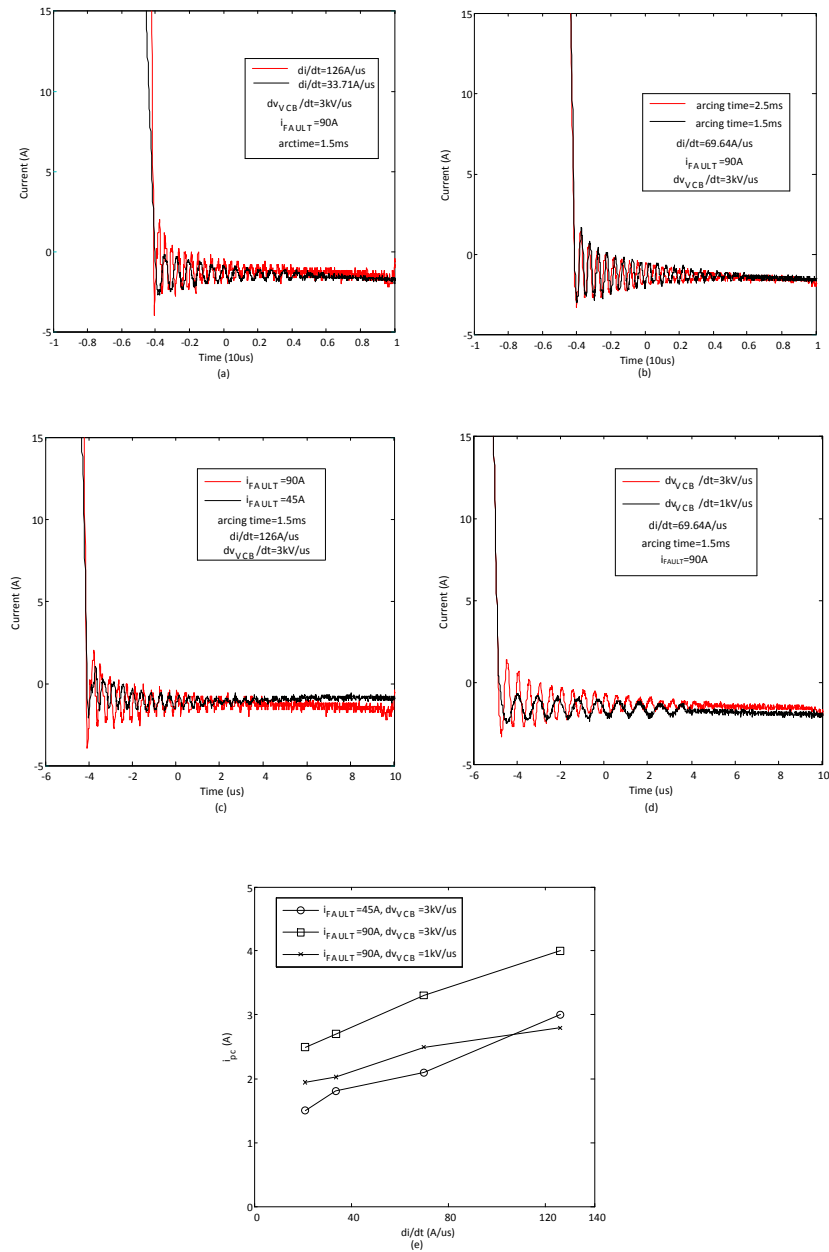
Figure 4.34 Experimental waveforms for the post-arc current in terms of interrupting current level (i_{FAULT}), arcing time (gap distance), dv_{VCB}/dt, and di/dt.

4.6.4 VCB Interruption characteristics

di/dt-dv_{VCB}/dt characteristic

The VCB characteristics in terms of the relationship between di/dt and dv_{VCB}/dt were investigated with interruption currents of 90A and 330A at an arcing time of 1ms and 2ms. Figure 4.35 (a) illustrates the results with interruption currents of 90A and 330A at gap distance of 1mm. The results for interruption at gap distances of 1mm and 2mm with interruption current 90A are shown in Figure 4.35 (b). Interruption success and failure are represented by circle and cross symbols, respectively. The lines indicate the boundary between successful and failed interruption. The experimental conditions are shown in Table 4.5. The experiments were repeated at least 30 times for every value.

Table 4.5 Experimental conditions for di/dt -dv_{VCB}/dt characteristic

i_{FAULT} (A)	g (mm)	di/dt (A/μs)	dv_{VCB}/dt (V/μs)
90	1	73.18	187.5
		40.68	692.3
	2	398.6	300
		201.4	500
330	1	70	47.14
		41.92	194.1
		36.39	300

Note: i_{FAULT} is interruption current; g is gap length; di/dt is rate of change of the VCB current before current-zero; and dv_{VCB}/dt is the VCB voltage immediately after current-zero.
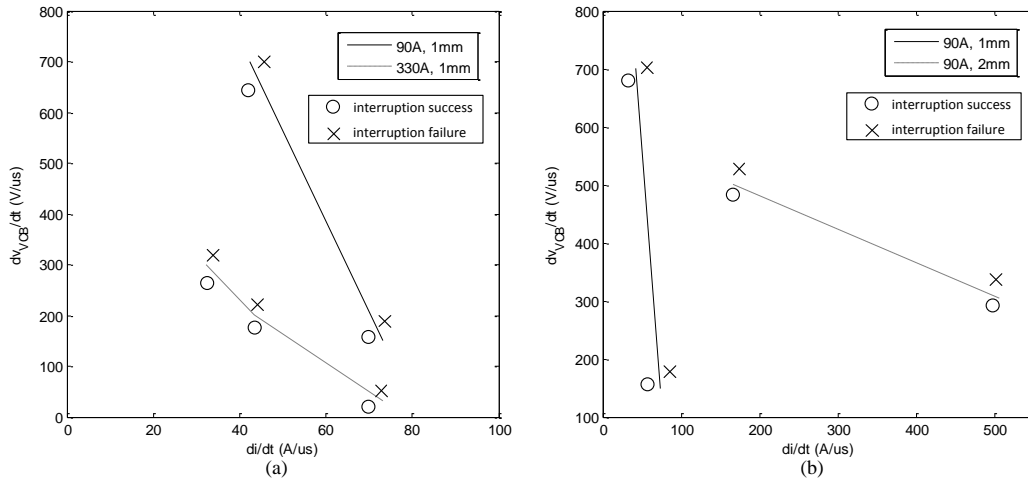
Figure 4.35 Relationship between di/dt and dv_{VCB}/dt.

With the same di/dt, dv_{VCB}/dt when interrupting 330A is smaller than when interrupting 90A. At an arcing time of 1ms, although some dv_{VCB}/dt are large compared to those at 2ms, the di/dt generally presents a small value. Regardless of interrupting 90A and 330A or with a gap distance of 1mm and 2mm, in obtaining 100% interruption probability, an increase in di/dt requires a decrease in dv_{VCB}/dt. The reason is that there is a relationship between successful interruption rate and the post-arc current at the first phase, namely interruption probability rises as i_{pc} decreases. However, di/dt cannot increase even if it is aided by a decrease in dv_{VCB}/dt. The snubber capacitance will lose its function if large di/dt is selected. A decrease in dv_{VCB}/dt means more snubber capacitance is required. The snubber circuit topology needed in a real power system may not be simple like in Figure 4.8. It must comply with the needs of the power system, such as inclusion of an auxiliary switch to discharge the energy stored in a capacitor after interruption.

An experiment, interrupting 330A at an arcing time of 1ms without snubber capacitance, was carried out. The result indicated that the interruption probability can reach 100% when di/dt is reduced to 2.53A/μs. By comparing to the maximum di/dt (73.18A/μs) with snubber capacitance, the difference is the commutation time, which is approximately 5μs with snubber capacitance and approximately 131μs without snubber capacitance, based on successful interruption at the first current-zero.

126

Since this test circuit is microcontroller controlled, the time difference can be compensated by triggering the commutation circuit (T₃) early. With the snubber capacitance removed, retesting gave the experimental results that follow.

VCB characteristics without snubber capacitance

The VCB interruption characteristics without snubber capacitance were investigated with varying interruption current, di/dt, and arcing time, with results as shown in Figure 4.36. The interruption success and failure are indicated by circle and cross symbols respectively. The boundary between successful and failed interruption is denoted by solid lines. The experimental conditions are tabulated in Table 4.6 and the experiments were repeated at least 32 times for each test.

Table 4.6 Experimental conditions for interruption characteristics without snubber capacitance

i_{FAULT} (A)	di/dt (A/μs) g (mm)				
	0.5	1	1.5	2	2.5
90	-	20.5	73.27	150.5	302.5
110	1.69	5.86	21.97	47.62	61.34
170	1.29	3.85	12.5	24.93	42.03
220	1.19	3.29	5.05	12.3	22.78
330	0.89	2.53	4.08	15.55	21.41

Note: i_{FAULT} is the interruption current; g is gap length; and di/dt is rate of change of VCB current before current-zero.
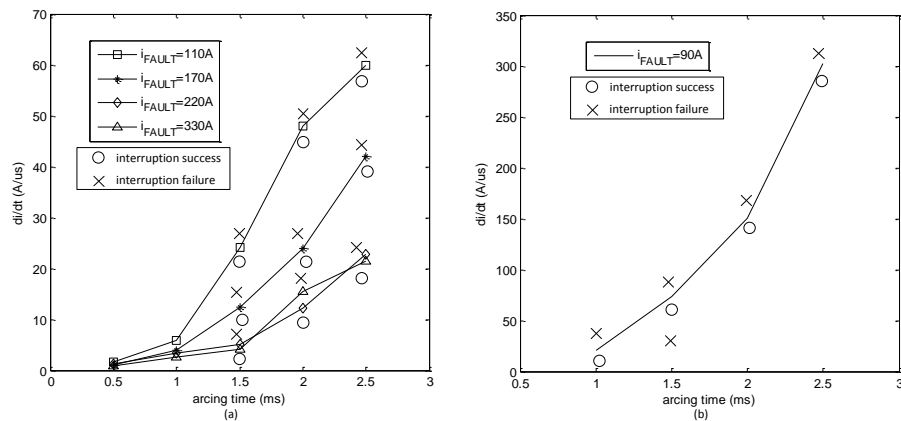
Figure 4.36 VCB interruption characteristic without snubber capacitance in terms of varied interruption current, di/dt and arcing time.

As shown in Figure 4.36 (a), with small arcing time, di/dt is almost same regardless of the interruption current level. For a large arcing time, the interruption limit current

increases with decreasing di/dt. The reason is that the post-arc current at first phase i_{pc} decreases as di/dt is reduced. It is not valid to say that the VCB has better interruption properties at large gaps than at small gaps, i.e., di/dt increases with an increased arcing time, since i_{pc} performs the same at different gap distances. The dielectric strength increases as the gap volume is increased. Figure 4.36 (b) shows that a failed interruption could occur with a low probability (about 1 in 32 times) even if the di/dt is low.
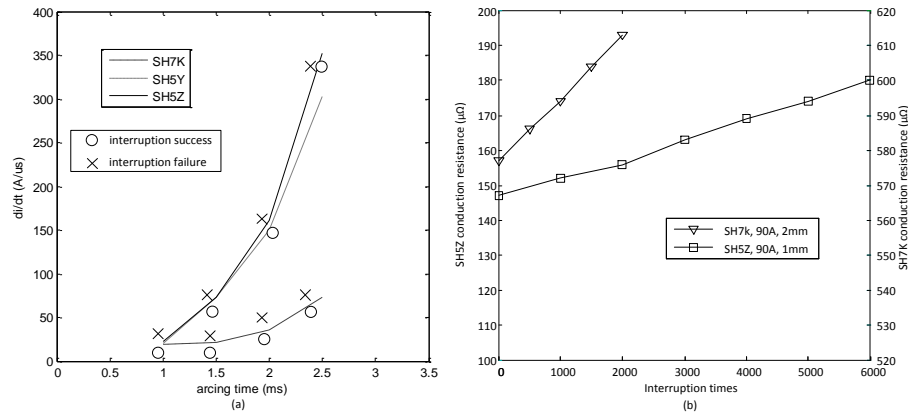
Figure 4.37 Interruption properties: (a) SH7K, SH5Y and SH5Z; (b) relationship between conduction resistance and interruption times for the SH5Z at arcing time 1ms, for SH7K at arcing time 2ms.

Table 4.7 Experimental conditions for testing SH7K, SH5Y and SH5Z

Vacuum interrupter	di/dt (A/µs)			
	g (mm)			
	1	1.5	2	2.5
SH7k	18.75	21.75	36.24	73.27
SH5Y	20.5	73.27	150.5	302.5
SH5Z	22.5	73.27	160.5	350

Note: g is gap length and di/dt is rate of change of VCB current before current-zero.

As mentioned previously, there are three vacuum interrupters in this VCB series; SH7K, SH5Y and SH5Z. Their interruption properties, without snubber capacitance, were investigated with 90A interruption current, by varying di/dt and arcing time, with performance as shown in Figure 4.37 (a). Above each line represents the failed interruption zone. The experimental conditions are shown in Table 4.7, and the experiments were repeated at least 32 times for each value.

All three vacuum interrupters display the same interruption property trends. However, SH5Y and SH5Z have a similar interruption performance, with large values of di/dt compared to those of SH7K. The reason is because of the conduction resistance, which are 167μΩ for SH5Y, 147μΩ for SH5Z, and 577μΩ for SH7K. These are the mean of ten values, when measured with a precision ohm-meter (model number BS407). Consequently, the lower conduction resistance contributes to better interruption performance.

As mentioned previously, after repeated operation, the electrode surface will have many overlapping craters, due to electrode surface erosion, uniformly distributed due to the retrograde motion of multiple cathode spots. Thus, in time, the conduction resistance will increases with an increase in interruption times for a given interruption current. This increase in conduction resistance will be aggravated by having to interrupt longer arcing times. Figure 4.37 (b) shows the relationship between conduction resistance and interruption times, based on a fixed 90A interruption current and a di/dt of 20.5A/μs, for arcing times of 1ms for SH5Z, and 2ms for SH5Y. Each resistance is the mean of ten measured values. The increased conduction resistance in the SH5Y after 2000 interruptions reaches the same value as SH5Y at 6000 interruptions, due to the difference in arcing time. Consequently, the test circuit in Figure 4.3 under microcontroller control not only speeds up the interruption time, but also reduces cathode surface erosion.

4.7 Summary

This chapter describes active and passive commutation circuits in detail. An active commutation test circuit was proposed, and in simulation and experimentally, the VCB interruption properties were investigated in terms of varied interruption current, di/dt, dv_{VCB}/dt, and arcing time. The low power VCB interruption experimental results exhibit the same trend as for high power interruption. For example, in order to obtain a 100% successful interruption rate with fast commutation, an increase in di/dt introduces a decrease in dv_{VCB}/dt. For fixed di/dt, dv_{VCB}/dt, and arcing

time, the interruption probability reduces as the interruption current is increases. The di/dt and dv_{VCB}/dt for successful interruption reduce with decreasing electrode spacing [4.1, 2, 6-9, 12]. However, the key parameter determining interruption probability is di/dt, where even if dv_{VCB}/dt is low, successful interruption become impossible if di/dt is above certain level [4.5]. The arc starts to recover as its current is reduced, but recovery speed is determined by a recovery rate. For a given gap, if di/dt is slightly more than the recovery rate, interruption is possible with a snubber capacitor connected. However, if di/dt significantly exceeds the recovery rate, interruption becomes impossible, snubber or no snubber.

The post-arc current was analysed by measuring its electrical behaviour. The post-arc current can be divided into two phases in terms of duration: the first phase was defined as being between the current-zero the instant when V_{VCB} rises to the supply voltage, and the remainder is considered as the second phase. Experimental results showed that i_{pc} in the first phase is influenced by di/dt and dv_{VCB}/dt, which increases i_{pc} with an increase in di/dt or decreases it as dv_{VCB}/dt is decreased, for a given interruption current. This explains why the di/dt and dv_{VCB}/dt dominate successful interruption probability. The second phase is dominated by the test voltage. The interruption properties of all three vacuum interrupters in this VCB series were investigated with a 90A interrupting current, and varied di/dt and gap distances. The experimental results show they have same interruption trend but different interruption performance, where lower conduction resistance contributes to better interruption performance.

By utilising the relationship between the peak current produced by the counter-EMF and the separation of the VCB electrodes, the performance of the active commutation mode based test circuit was improved, and offered the following features:

➢ There is no need for a continuous external voltage to charge the commutation capacitor C_C: it is charged from the system voltage;

➢ There is no need for large capacitance C_C, since the interruption time is reduced.

> ➤ With an optimally designed commutation circuit, the interruption probability is improved and the extra time for commutation can be compensated by early triggering. Electrode surface erosion is reduced, thus the useful life of the VCB is extended.

The total VCB opening time is approximately 13ms based on the DC energising circuit. This means this test circuit may be applicable to low power rating application, but a 13ms delay will be unacceptable in high power rating application. Operation speed will be the downfall of any DCCB involving a mechanical breaker, since sub-millisecond performance may be necessary.

References

[4.1]   A.N. Greenwood, and T.H. Lee, "Theory and Application of the Commutation Principle for HVDC Circuit Breakers," *Power Apparatus and Systems, IEEE Transactions on,* vol. PAS-91, pp. 1570-1574, July 1972.

[4.2]   A.N. Greenwood, P. Barkan, and W.C. Kracht, "HVDC Vacuum Circuit Breakers," *Power Apparatus and Systems, IEEE Transactions on* vol. PAS-91, pp. 1575-1588, July 1972.

[4.3]   G. Duning, and M. Lindmayer, "Plasma Density Decay of Vacuum Discharges After Current Zero," *IEEE TRANSACTIONS ON PLASMA SCIENCE,* vol. 27, pp. 923-929, AUGUST 1999.

[4.4]   E. van Lanen, R. Smeets, M. Popov, and L. van der Sluis, "Vacuum Circuit Breaker Postarc Current Modelling Based on the Theory of Langmuir Probes," *Plasma Science, IEEE Transactions on* vol. 35, pp. 925-932, Aug. 2007.

[4.5]   W.J. Premerlani, "Forced Commutation Performance of Vacuum Switches for HVDC Breaker Application," *IEEE TRANS.,* vol. PAS-101, pp. 2721-2727, Aug. 1982.

[4.6]   H. Odaka, M, Yamada, R. Sakuma, C. Ding, E. Kaneko, and S. Yanabu, "DC interruption characteristic of vacuum circuit breaker," *Electrical Engineering in Japan,* vol. 161, pp. 17-25, 21 JUN 2007.

[4.7]   Y. Niwa, T. Funahashi, K. Yokokura, J. Matsuzaki, M. Homma and E. Kaneko, "Basic investigation of a high-speed vacuum circuit breaker and its vacuum arc characteristics," *Generation, Transmission and Distribution, IEE Proceedings,* vol. 153, pp. 11-15, 12 Jan. 2006.

[4.8]   Y. Niwa, J. Matsuzaki, and K. Yokokura, "The basic investigation of the high-speed VCB and its application for the DC power system," *Discharges and Electrical Insulation in Vacuum, 2008. ISDEIV 2008. 23rd International Symposium on,* vol. 1, pp. 107-112, 15-19 Sept. 2008.

[4.9]   K. Arimatsu, Y. Yoshioka, S. Tokuyama, Y. Kato, and K. Hirata, "Development and Interrupting Tests on 250KV 8KA HVDC Circuit

Breaker," *Power Apparatus and Systems, IEEE Transactions on,* vol. PAS-104, pp. 2452-2459, Sept. 1985.

[4.10] S. Greitzke, and M. Lindmayer, "Commutation and Erosion in Hybrid Contactor Systems," *Components, Hybrids, and Manufacturing Technology, IEEE Transactions on ,,* vol. 8, pp. 34-39, Mar 1985.

[4.11] A. Lee, P.G. Slade, K.H. Yoon, J. Porter, and J. Vithayathil, "The Development of a HVDC SF6 Breaker," *IEEE Trans. Power App. Syst.,* vol. 104, pp. 2721-2729, Oct. 1985.

[4.12] Y. Niwa, T. Funahashi, K. Yokokura, J. Matsuzaki, M. Homma and E. Kaneko, "Basic investigation of a high-speed vacuum circuit breaker and its vacuum arc characteristics," *Generation, Transmission and Distribution, IEE Proceedings-,* vol. 153, pp. 11-15, 12 Jan. 2006.

[4.13] B.W. Williams, "POWER ELECTRONICS: Devices, Drivers, Applications, and Passive components," pp. 1241-1284, 2006.

[4.14] M.H. Bierhoff, and F.W. Fuchs, "Semiconductor losses in voltage source and current source IGBT converters based on analytical derivation," *Power Electronics Specialists Conference, 2004. PESC 04. 2004 IEEE 35th Annual,* vol. 4, pp. 2836-2842, 2004.

[4.15] M. Ghasem Hosseini Aghdam, S. Hamid Fathi, and Azadeh Ghasemi, "The Analysis of Conduction and Switching Losses in Three-Phase OHSW Multilevel Inverter Using Switching Functions," *Power Electronics and Drives Systems, 2005. PEDS 2005. International Conference on* vol. 1, pp. 209-218, 2005.

[4.16] Dr. Dušan Graovac, and Marco Purschel, "IGBT Power Losses Calculation Using the Data-Sheet Parameters," *Infineon Technologies AG Application Note,* vol. 1.1, January 2009.

[4.17] L.W. Nagel, "SPICE2: A computer program to simulate semiconductor circuits: Electronics Research Laboratory," *Univ. California of Berkeley, Moemorandum ERL-M520,* May 1975.

[4.18] E. Ramshaw, and D.C. Schuurman, "Pspice simulation of power electronics circuit: an introductory," *London: Chapman & Hall,* 1997.

[4.19] J. McGhee, "A transient model of a three terminal p-n-p-n switch and its use in predicting the gate turn-on process," *Int. J. Electronics,* vol. 35, pp. 73-9, 1973.

[4.20] N.A. Losic, "Computer-aided analysis and design of commutating, di/dt and dv/dt circuits for thyristors," *IEEE Industry Applications Society Annual Meeting,* vol. 2, pp. 1196-201, 1990.

[4.21] B.W. Williams, "State-space thyristor computer model," *Proc. IEE,* vol. 124, September 1977.

[4.22] Davis, D. William, and H.C. Miller, "Analysis of the electode products emitted by DC arcs in a vacuum ambient," *J. Appl. Phys.,,* vol. 40, pp. 2212-2221, 1969.

[4.23] J.G. Andrews, and R.H. Varey, "Sheath growth in a low pressure plasma," *Phys. Fluids,* vol. 14, pp. 339-343, 1971.

[4.24] E. Huber, K. Frohlich, and R. Grill, "Dielectric Recovery of Copper Chromium Vacuum Interrupter Contacts After Short-Circuit Interruption," *IEEE Transactions on plasma science,* vol. 25, pp. 642-646, August 1997.

5 Cascaded commutation circuit for a hybrid breaker

5.1 Introduction

With the control method proposed in Chapter 3, a test circuit using active commutation without a snubber circuit was used in Chapter 4 to investigate VCB properties. For interruption with fixed current and gap distance, the interruption probability in the circuit with or without a snubber was the same, except for the commutation time. The circuit with a snubber has a short commutation time since di/dt could be set to a larger value than in the circuit without a snubber. When interrupting lower currents, the extra commutation time without a snubber could be compensated by advancing the triggering of the commutation circuit. However, the advantage of early triggering becomes uncertain at high interrupted current. For example, from Table 4.5, for an interruption current of 90A and gap of 1mm, the interruption probability without a snubber circuit reached 100% when di/dt was 20.5A/µs. This means that the commutation time from 90A down to zero is approximately 5µs. However, when the interruption current is increased to 330A, the di/dt decreased to 2.53A/µs. And the commutation time is approximately 130µs. Hence based on previous results, when the interruption current increases 1000A the di/dt will reduce more, perhaps to 1A/µs or less, in which case the commutation time increases to 1ms. Consequently, it is difficult to interrupt high current commutation with a relatively short gap, without a snubber circuit. Thus, the problem reverts back to the trade-off between di/dt and dv_{VCB}/dt.

However di/dt and dv_{VCB}/dt will be fixed once the commutation circuit (L and C) components are selected. This means the interruption probability is undefined according to the experimental results presented. Thus, in order to increase the interruption probability, steps must be taken to adjust the di/dt and dv_{VCB}/dt values. To this end, Greenwood [5.1] introduced components into the breaker circuit as shown in Figure 5.1 (a). By comparing this topology with that in Figure 4.1, a saturable reactor L_S in added in series with the circuit breaker and a series $R_S C_S$ snubber circuit is added in parallel with the circuit breaker.
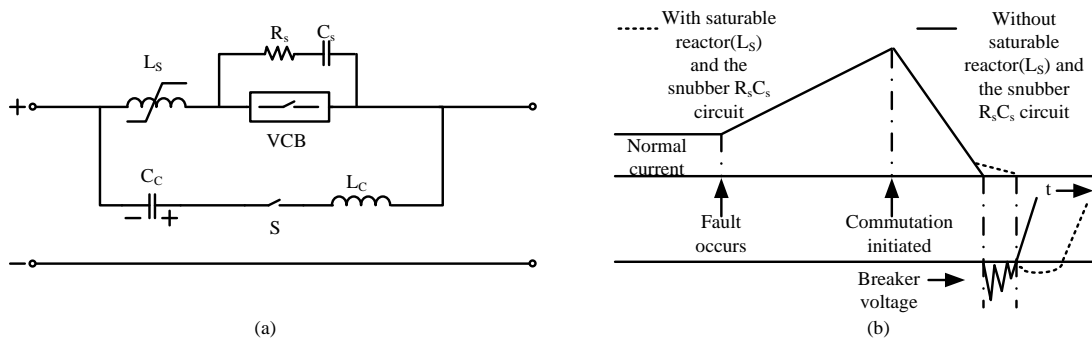
Figure 5.1 (a) Components added to the breaker circuit to profile the di/dt and dv_{VCB}/dt and (b) corresponding current and voltage during interruption.

Figure 5.1 (b) shows the performance of current and voltage, with and without the added components, during interruption. In steady-state operation, L_S is saturated and has a low inductance due to it carrying the load current. When commutation is triggered and the current through this reactor is reduced, L_S presents a larger inductance when it comes out of saturation. Then the current smoothly decreases to zero with a much lower di/dt. After the current-zero, the dv_{VCB}/dt is reduced for two reasons. Firstly, the capacitance of the VCB is increased due to parallel connection of C_s. Secondly, the voltage to charge the VCB appears across L_S, which always starts in its unsaturated state. Also, if properly designed, a low amplitude, short voltage pulse with duration of 20 to 30µs is introduced across the VCB following interruption.

Although the saturable reactor improves commutation performance, it is not prevalent in hybrid breaker applications. According to Premerlani [5.2], the significant limitation is that the saturable reactor must be connected in-line and must be sized for full load current. Also the time to saturate is voltage dependant, i.e. a short time to saturate is required in high voltage applications. However, ways to achieve a similar effect are possible. Thus a cascaded commutation circuit shown in Figure 5.2 is proposed. It utilises more solid-state switches to reduce the current prior to current-zero and to reduce the voltage after current-zero. A snubber circuit is not necessary.

136

5.2 Basic principles of the cascaded commutation circuit

As mentioned in Section 4.3, the test circuit provides three processes, namely the preparation (or reset) of the commutation circuit, the introduction of fault current, and the triggering of the commutation circuit. The proposed cascaded commutation circuit is a modification of the interruption of commutation circuit, meaning it is a quantifiable extension of the original circuit, and inherits most of test circuit features and properties.

Figure 5.2 The cascaded commutation circuit of hybrid breaker; VCB: vacuum circuit breaker, $T_{1,2,3,4,5,6}$: series diode and IGBT combination.

Figure 5.2 shows the cascaded commutation circuit. Simulation and experimental results follow the analysis of this topology. Photographs of the test rigs are shown in

Appendix A.1.1. The circuit is the same as the test circuit proposed in Chapter 4, except for the addition of two further commutation paths, involving capacitors $C_{C1} = C_{C2} = C_{C2}$ that are connected using solid-state switches T$_4$-T$_5$-T$_6$, as shown. The three solid-state switches are controlled by gating signals applied as a series of sequential time intervals, overlapping for 1μs to ensure commutation continuity, as shown in Figure 5.4 (b). Under normal load conditions, only the VCB and T$_1$ are closed, to transmit power to load and to charge the commutation capacitors C_{C1}, C_{C2} and C_{C2} with an initial voltage totalling V_{DC}, while the other switches, T$_2$ to T$_6$, are open. The DC fault is introduced by turning on T$_3$, so that the energy stored in the capacitor bank C_{bank} is released through the load inductor L_C into the fault resistor R_{FAULT}, to produce a high current through the VCB before the electrodes open. For commutation preparation, the commutation capacitors $C_{C1,2,3}$ are reversed charged by turning on T$_2$ after receiving the trip signal. Since $C_{C1} = C_{C2} = C_{C2}$ the voltage cross each capacitor is same, i.e. $V_{C_{C1}} = V_{C_{C2}} = V_{C_{C3}}$. The fault clearance interruption procedure is shown in Figure 5.3. For analysis convenience, the VCB arc voltage is ignored due to its low value.

At time t_1, the electrodes start to open introducing an arc voltage across the VCB. When a specific gap distance had been reached, at $t_2 = t_{c0}$ the solid-state switch T$_4$ is closed. Then, the counter-current $i_{L_C} = i_{C3}$ produced by $L_C C_{C1,2,3}$ rises and forces the current $i_{VCB} = i_{FAULT}$ through the VCB to decrease: see loop $C_{C1,2,3}$, VCB, L_C and T$_4$ as shown in Figure 5.5 (a). At t_{c1}, as shown in Figure 5.5 (b), the counter-current $i_{L_C} = i_{C2}$ is switched into the loop $C_{C1,2}$, VCB, L_C and T_5 by turning on switch T$_5$, then T$_4$ off. After obtaining energy from $L_C C_{C1,2}$ the current continues to rise until t_{c2}. Then the counter-current transfers into the next loop C_{C1}, VCB, L_C and T_6, as shown in Figure 5.5 (c), after the solid-state switch T$_6$ is fired and T$_5$ is turned off, such that $i_{L_C} = i_{C1}$ is produced by $L_C C_{C1}$. When the counter-current reaches the fault current i_{FAULT} level (after a specifiable commutation time from t_{c0} to t_{c3}), the first VCB current-zero occurs at t_{c3} and i_{FAULT} is commutated into the loop C_{bank}, C_{C1}, T_6, L_C, L_{LOAD}, T_3 and R_{FAULT}, as shown in Figure 5.5 (d). Since only capacitor C_{C1} is in the circuit, the voltage V_{VCB} across the VCB is forced to equal and track the residual capacitor voltage of $V_{C_{C1}}$ until voltage $V_{C_{C1}}$ approaches

zero at t_{c4}. Then i_{FAULT} is switched into the loop C_{bank}, $C_{C1,2}$, T_5, L_C, L_{LOAD}, T_3 and R_{FAULT} by turning on solid-state switch T_5, then T_6 off, as shown in Figure 5.5 (e). V_{VCB} follows the residual voltage of $V_{C_{C1}}$ plus $V_{C_{C2}}$ until t_{c5} when the residual voltage $V_{C_{C1}} + V_{C_{C2}}$ approaches zero. Then the solid-state switch T_4 is fired and T_5 is turned off, and i_{FAULT} enters the loop C_{bank}, $C_{C1,2,3}$, T_4, L_C, L_{LOAD}, T_3 and R_{FAULT}, as shown in Figure 5.5 (f). The VCB voltage starts to increase following the residual voltage $V_{C_{C1}} + V_{C_{C2}} + V_{C_{C3}}$. Now the cascaded circuit has the same topology as the test circuit and follows the same interruption process, as described in Chapter 4. For a failed interruption at the first current-zero, i_{VCB} would repeat the timing sequence to produce a second current-zero. A second commutation failure would constitute interruption failure. The equations describing the sequential time intervals are presented later in this chapter.
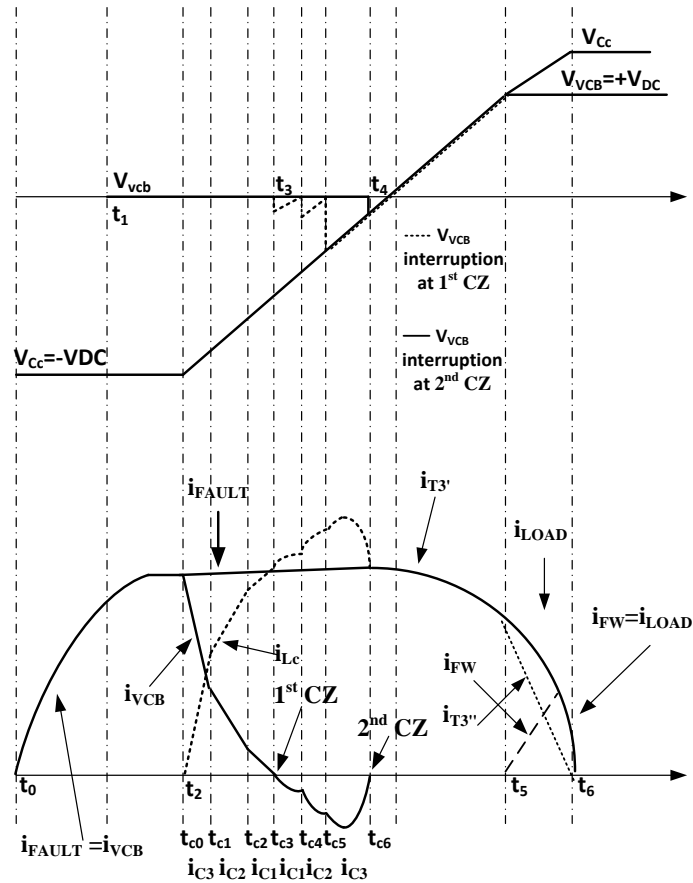
Figure 5.3 Operational sequence for the cascaded circuit; CZ current-zero crossing in the VCB

The initial conditions including the commutation capacitance and initial capacitor voltage vary from one test condition to the next. According to equation (4.34), although the di/dt is independent of commutation capacitance, it is sensitive to the initial capacitor voltage, i.e. it decreases as the initial capacitor voltage reduces. Additionally, a short small-amplitude voltage pause is introduced after the interruption, because the residual capacitor voltages are charged step by step. Thus an increase in the VCB interruption probability is expected due to a decrease in di/dt and dv_{VCB}/dt.

In order to explain the operation of the cascaded circuit, the mathematical description of the interruption sequences during commutation is based on the timing diagram in Figure 5.4 (b). Section 4.3 provides an introduction to resonant commutation and background to fault current aspects.
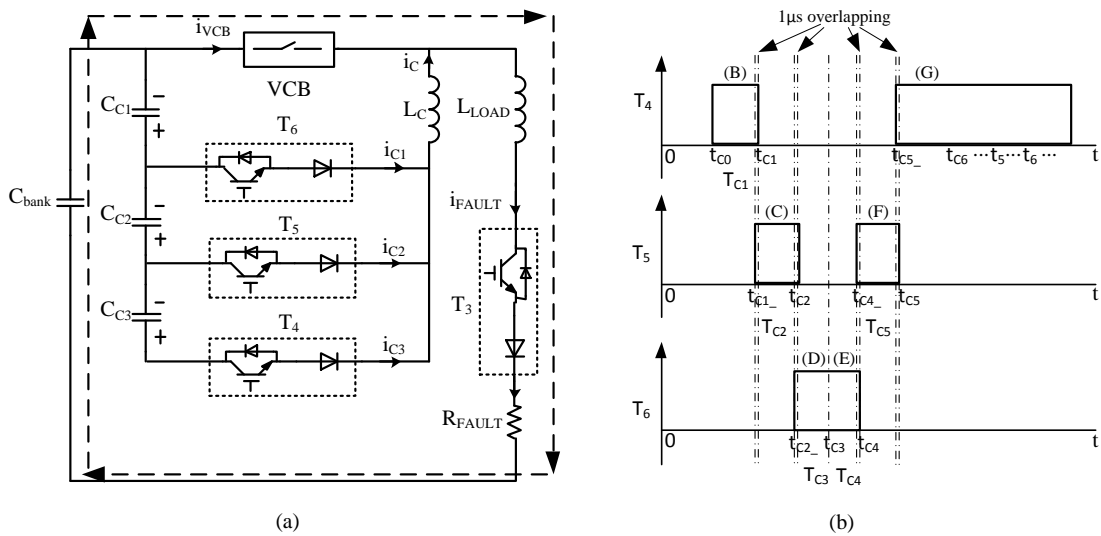
Figure 5.4 (a) the cascaded commutation circuit and (b) the timing diagram
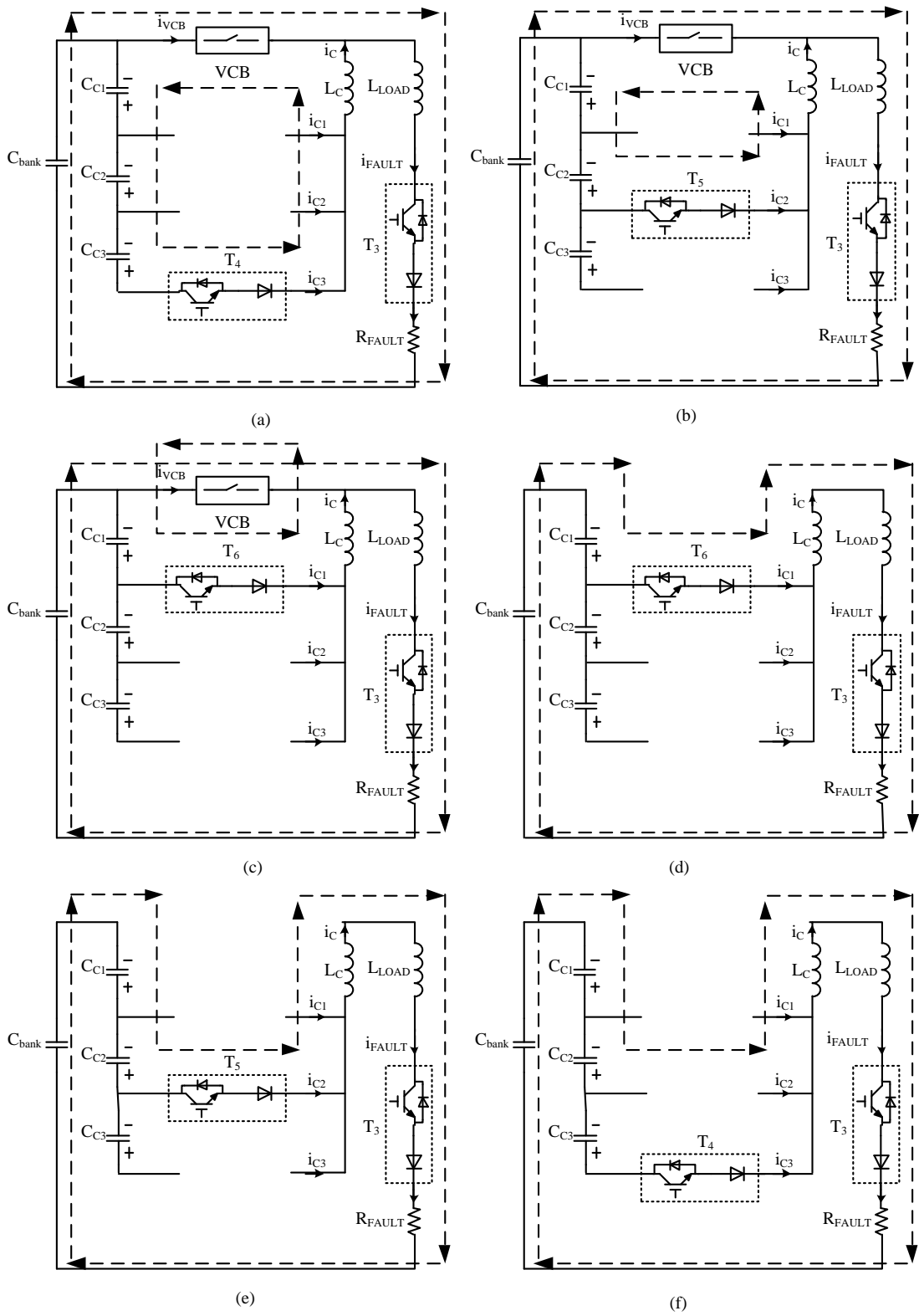
Figure 5.5 Interruption sequence of the cascaded commutation circuit.

141

Analytical solutions

For analysis the inductors are assumed linear, and the voltage drops across all solid-state switches and the VCB are zero during the on-state. Due to large bank capacitance C_{bank}, its voltage is considered constant, and equal to V_{DC}. The commutation capacitors have no circuit leakage paths when inactive, and the VCB fault current i_{FAULT} is unchanged during the commutation process, since the commutation time is shorter than the fault path time constant. The detailed solution is obtained by solving the differential equations correspond to each interval, with the end state of a given interval being the initial state of the following interval, thereby maintaining continuity between successive intervals.

Cascaded commutation circuit: pre-activation and post-activation timing

Figure 5.4 (a) depicts the cascaded circuit when the VCB fault current has reached its expected value according to equations (4.10) to (4.17). The VCB electrodes have separated a specific distance. The commutation capacitor $C_{C1,2,3}$ has been reversed charging, so that the commutation circuit is ready to produce a counter-current through the VCB. In the Figure 5.4 (b), in order to maintain cascaded commutation circuit continuity, solid-state switches T_4-T_5-T_6 are controlled through a sequence of six time intervals with 1μs overlap (intervals T_{C1}-T_{C2}-T_{C3}-T_{C4}-T_{C5}-T_{C6}) Intervals T_{C3} and T_{C4} use the same signal. The overlap ensures continuity, that is $t_{c1} = t_{c1\_}$, $t_{c2} = t_{c2\_}$, $t_{c4} = t_{c4\_}$, and $t_{c5} = t_{c5\_}$.

(a) first interval $t_{c0} \leq t \leq t_{c1}$

At time $t_2 = t_{c0}$, switch T_4 is turned on to introduce counter-current i_{L_C} through the VCB, forcing the current i_{VCB} through the VCB to decrease. The relationship between i_{FAULT}, i_{VCB} and i_C is:

$$i_{FAULT} = i_{VCB} + i_{L_C} \qquad (A) \qquad\qquad (5.1)$$

where $i_{L_C} = i_{C3}$ and $C_{C1} = C_{C2} = C_{C2}$, thus the current i_{C3} through circuit loop $C_{C1,2,3}$, VCB, L_C and T_4 is defined by:

$$\frac{1}{C_{C1,2,3}} \int i_{C3} dt + L_C \frac{di_{C3}}{dt} = 0 \tag{5.2}$$

with the initial conditions

$$i_{C3}(t_{c0}) = 0 \text{ (A) and } V_{C_C}(t_{c0}) = -V_{DC} \qquad \text{(V)}$$

which yields:

$$i_{C3}(t) = \frac{V_{DC}}{Z} \sin \omega_0 t \quad \text{(A)} \tag{5.3}$$

and
$$V_{C_{C1,2,3}}(t) = -V_{DC} \cos \omega_0 t \quad \text{(V)} \tag{5.4}$$

$$0 \le \omega_0 t \le \pi \quad \text{(rad)}$$

where $\omega_0 = 1/\sqrt{L_C C_{C1,2,3}}$ (rad/s)

$$Z = \sqrt{L_C / C_{C1,2,3}} \quad \text{(Ω)}$$

$$C_{C1,2,3} = \tfrac{1}{3} C_{C1} = \tfrac{1}{3} C_{C2} = \tfrac{1}{3} C_{C3} \quad \text{(F)}$$

At the end of this interval, the voltage across the commutation capacitors $C_{C1,2,3}$ is $V_{C_{C1,2,3}} = V_{C_{C1,2,3}}(t_{c1})$, i.e. $V_{C_{C1}} = V_{C_{C2}} = V_{C_{C3}} = \tfrac{1}{3} V_{C_{C1,2,3}}(t_{c1})$, and the commutation current is $i_C = i_{C3}(t_{c1})$. Thus the equation describing this interval T_{C1} is:

$$T_{C1} = t_{c1} - t_{c0} = \frac{-\sin^{-1} \frac{i_{C3}(t_{c1})Z}{V_{DC}}}{\omega_0} \tag{5.5}$$

(b) second interval $t_{c1} \le t \le t_{c2}$

T₅ is turned on and T₄ off at t_{c1}, then the commutation current i_{L_C} switches into the loop $C_{C1,2}$, VCB, L_C and T₅, and is equal to the current i_{C2} which can be expressed by the differential equation:

$$\frac{1}{C_{C1,2}} \int i_{C2} dt + L_C \frac{di_{C2}}{dt} = 0 \tag{5.6}$$

with initial conditions

$$i_{C2}(t_{c1}) = i_{C3}(t_{c1}) \text{ (A) and } V_{C_{C1,2}}(t_{c1}) = \tfrac{2}{3} V_{C_{C1,2,3}}(t_{c1}) \quad \text{(V)}$$

which yields:

$$i_{C2}(t) = i_{C3}(t_{c1}) \cos \omega_{0'} t - \frac{2V_{C_{C1,2,3}}(t_{c1})}{3Z'} \sin \omega_{0'} t \quad \text{(A)} \tag{5.7}$$

143

and
$$V_{CC_{1,2,}}(t) = Z''^{i_{C3}}(t_{c1})\sin\omega_{0'}t + \tfrac{2}{3}V_{CC_{1,2,3}}(t_{c1})\cos\omega_0 t \quad \text{(V)} \qquad (5.8)$$

$$0 \le \omega_0 t \le \pi \quad \text{(rad)}$$

where $\omega_{0'} = 1/\sqrt{L_C C_{C1,2}}$ (rad/s)

$$Z' = \sqrt{L_C / C_{C1,2}} \quad (\Omega)$$

$$C_{C1,2} = \tfrac{1}{2}C_{C1} = \tfrac{1}{2}C_{C2} = \tfrac{1}{2}C_{C3} \quad \text{(F)}$$

At the end of this interval, the voltage across the commutation capacitor $C_{C1,2}$ is $V_{CC_{1,2}} = V_{CC_{1,2,}}(t_{c2})$, where $V_{CC_1} = V_{CC_2} = \tfrac{1}{2}V_{CC_{1,2}}(t_{c2})$, and $V_{CC_3} = \tfrac{1}{3}V_{CC_{1,2,3}}(t_{c1})$, and the commutation current is $i_{L_C} = i_{C2}(t_{c2})$. Thus the equation describing this interval T_{C2} is:

$$T_{C2} = t_{c2} - t_{c1} = \frac{-\sin^{-1}\dfrac{V_{CC_{1,2}}(t_{c1}) \times i_{C2}(t_{c2}) + L_C \times i_{C2}(t_{c1}) \times \omega_{0'} \times A}{\left(C_{C1,2} \times \left(V_{CC_{1,2}}(t_{c1})\right)^2 + L_C \times \left(i_{C2}(t_{c1})\right)^2\right) \times \omega_{0'}}}{\omega_{0'}} \qquad (5.9)$$

where $A = \sqrt{\dfrac{C_{C1,2} \times (V_{CC_{1,2}}(t_{c1}))^2 + L_C \times (i_{C2}(t_{c1}))^2 - L_{Cx}(i_{C2}(t_{c2}))^2}{L_C}}$

(c) third interval $t_{c2} \le t \le t_{c3}$

Solid-state switch T_6 is fired and T_5 is turned off at time t_{c2}. Commutation current i_{L_C} enters the loop C_{C1}, VCB, L_C and T_6. The resulting current i_{C1} is defined by:

$$\frac{1}{C_{C1}} \int i_{C1} dt + L_C \frac{di_{C1}}{dt} = 0 \qquad (5.10)$$

with the initial conditions

$$i_{C1}(t_{c2}) = i_{C2}(t_{c2}) \text{ (A) and } V_{CC_1}(t_{c2}) = \frac{V_{CC_{1,2}}(t_{c2})}{2} \quad \text{(V)}$$

which yields:

$$i_{C1}(t) = i_{C2}(t_{c2})\cos\omega_{0''}t - \frac{V_{CC_{1,2}}(t_{c2})}{2\,Z''}\sin\omega_{0''}t \quad \text{(A)} \qquad (5.11)$$

and
$$V_{CC_1}(t) = Z'' i_{C2}(t_{c2})\sin\omega_{0''}t + \frac{V_{CC_{1,2}}(t_{c2})}{2}\cos\omega_{0''}t \quad \text{(V)} \qquad (5.12)$$

$$0 \le \omega_0 t \le \pi \quad \text{(rad)}$$

where $\omega_{0''} = 1/\sqrt{L_C C_{C1}}$ (rad/s)

$$Z'' = \sqrt{L_C / C_{C1}} \quad (\Omega)$$

$$C_{C1} = C_{C2} = C_{C3} \quad \text{(F)}$$

When the commutation current i_{C1} rises to equal the fault current, in the commutation period t_{c0} to t_{c3}, this is sufficient time for vacuum recovery, having introduced a VCB current-zero. Since the period of each interval has been calculated, it is possible to achieve the first current-zero at time t_{c3}. This means $i_{C1}(t_{c3}) = i_{FAULT}(t_{c3})$ and the commutation capacitor C_{C1} voltage is $V_{C_{C1}} = V_{C_{C1}}(t_{c3})$. Other capacitor voltages are $V_{C_{C2}} = \frac{1}{2}V_{C_{C1,2}}(t_{c2})$ and $V_{C_{C3}} = \frac{1}{3}V_{C_{C1,2,3}}(t_{c1})$. The period of this interval T_{C3} is:

$$T_{C3} = t_{c3} - t_{c2} = \frac{-\sin^{-1}\dfrac{V_{C_{C1}}(t_{c1}) \times i_{FAULT}(t_{c3}) + L_C \times i_{C1}(t_{c2}) \times \omega_{0''} \times A'}{(C_{C1} \times \left(V_{C_{C1}}(t_{c2})\right)^2 + L_C \times (i_{C1}(t_{c2}))^2) \times \omega_{0''}}}{\omega_{0''}} \tag{5.13}$$

where $A' = \sqrt{\dfrac{C_{C1} \times (V_{C_{C1}}(t_{c1}))^2 + L_C \times (i_{C1}(t_{c2}))^2 - L_{Cx} \times (i_{FAULT}(t_{c3}))^2}{L_C}}$

In summary, the commutation current i_{L_C}, before current-zero, can be described by the piecewise linear function:

$$i_C = \begin{cases} i_{C3}(t)i_{C3}(t) = \dfrac{V_{DC}}{Z}\sin\omega_0 t & (t_{c0} \le t \le t_{c1}) \\[2mm] i_{C2}(t) = i_{C3}(t_{c1})\cos\omega_{0'} t - \dfrac{2V_{C_{C1,2,3}}(t_{c1})}{3Z'}\sin\omega_{0'} t & (t_{c1} \le t \le t_{c2}) \\[2mm] i_{C1}(t) = i_{C2}(t_{c2})\cos\omega_{0''} t - \dfrac{V_{C_{C1,2}}(t_{c2})}{2Z''}\sin\omega_{0''} t & (t_{c2} \le t \le t_{c3}) \end{cases} \tag{5.14}$$

(d) fourth interval $t_{c3} \le t \le t_{c4}$

i_{FAULT} is commutated into the loop C_{bank}, C_{C1}, T_6, L_C, L_{LOAD}, T_3 and R_{FAULT}, but is still equal to i_{C1} and can be expressed by the differential equation:

$$\frac{1}{C_{C1}} \int i_{C1} dt + L_C \frac{di_{C1}}{dt} + L_{LOAD} \frac{di_{C1}}{dt} + i_{C1} R_{FAULT} = V_{DC} \tag{5.15}$$

where the voltage across C_{bank} can be considered as a DC source due to large C_{bank}.,
The initial conditions are

$$i_{C1}(t_{c3}) = i_{FAULT}(t_{c3}) \text{ (A) and } V_{C_{C1}}(t_{c3}) = V_{C_{C1}}(t_{c3}) \quad \text{(V)}$$

In practically $R_{FAULT} < 2\sqrt{\dfrac{L_{LOAD}}{C_{C1}}}$ which yields:

$$i_{C1}(t) = 2K_{1\prime}e^{-\delta_2 t}\cos(\omega_{3\prime}t - \theta') \quad \text{(A)} \tag{5.16}$$

$$V_{C_{C1}}(t) = \frac{2K_{1\prime}}{C_{C1}\omega_{4\prime}}[\cos(\beta_{2\prime} - \theta') - e^{-\delta_2 t}\cos(\omega_{3\prime}t - \theta' + \beta_{2\prime})] + V_{C_{C1}}(t_{c3}) \quad \text{(V)} \tag{5.17}$$

where $\delta_2 = \frac{R_{FAULT}}{2(L_{LOAD}+L_C)}$; $\omega_{3\prime}^2 = \frac{1}{(L_{LOAD}+L_C)C_{C1}} - \left(\frac{R_{FAULT}}{2(L_{LOAD}+L_C)}\right)^2$

$$\omega_{4\prime} = \sqrt{\delta_2^2 + \omega_{3\prime}^2}; \beta_{2\prime} = \tan^{-1}\frac{\omega_{3\prime}}{\delta_2}$$

$$K_{1\prime} = \sqrt{(\frac{i_{FAULT}(t_{c3})}{2})^2 + (\frac{\frac{V_{DC}-V_{C_{C1}}(t_{c3})}{L_{LOAD}+L_C}-\delta_2 i_{FAULT}(t_{c3})}{2\omega_{3\prime}})^2}$$

$$\theta' = \tan^{-1}\frac{\frac{V_{DC}-V_{C_{C1}}(t_{c3})}{L_{LOAD}+L_C}-\delta_2 i_{FAULT}(t_{c3})}{\omega_{3\prime}i_{FAULT}(t_{c3})}$$

Only capacitor C_{C1} is introduced into this circuit, and the VCB voltage V_{VCB} is clamped to the residual voltage $V_{C_{C1}}$ until the end of this interval, t_{c4}.

(e) fifth interval $t_{c4} \leq t \leq t_{c5}$

After turning switch T_5 on and T_6 off, the fault current i_{FAULT} diverts into the loop C_{bank}, $C_{C1,2}$, T_5, L_C, L_{LOAD}, T_3 and R_{FAULT}. This means i_{C2} offers energy for fault current continuity, and is defined by:

$$\frac{1}{C_{C1,2}}\int i_{C2}dt + L_C\frac{di_{C2}}{dt} + L_{LOAD}\frac{di_{C2}}{dt} + i_{C2}R_{FAULT} = V_{DC} \tag{5.18}$$

where the voltage across C_{bank} can be considered as a constant DC source due to the value of large C_{bank}. Initial conditions are

$$i_{C2}(t_{c4}) = i_{FAULT}(t_{c4}) \quad \text{(A)}$$

$$V_{C_{C1,2}}(t_{c4}) = V_{C_{C1}}(t_{c4}) + V_{C_{C2}}(t_{c4}) \quad \text{(V)}$$

where $V_{C_{C2}}(t_{c4}) = \frac{1}{2}V_{C_{C1,2}}(t_{c2})$, which yields

$$V_{C_{C1,2}}(t_{c4}) = V_{C_{C1}}(t_{c4}) + \frac{1}{2}V_{C_{C1,2}}(t_{c2}) \quad \text{(V)}$$

As before, $R_{FAULT} < 2\sqrt{\frac{L_{LOAD}}{C_{C1,2}}}$, thus:

$$i_{C1,2}(t) = 2K_{1\prime\prime}e^{-\delta_2 t}\cos(\omega_{3\prime\prime}t - \theta'') \quad \text{(A)} \tag{5.19}$$

$$V_{C_{C1,2}}(t) = \frac{2K_{1\prime\prime}}{C_{C1,2}\omega_{4\prime\prime}}[\cos(\beta_{2\prime\prime} - \theta'') - e^{-\delta_2 t}\cos(\omega_{3\prime\prime}t - \theta'' + \beta_{2\prime\prime})]$$

$$+V_{C_{C1,2}}(t_{c4}) \text{ (V)} \qquad (5.20)$$

where $\delta_2 = \dfrac{R_{FAULT}}{2(L_{LOAD}+L_C)}$; $\omega_{3''}^2 = \dfrac{1}{(L_{LOAD}+L_C)C_{C1,2}} - \left(\dfrac{R_{FAULT}}{2(L_{LOAD}+L_C)}\right)^2$

$$\omega_{4''} = \sqrt{{\delta_2}^2 + \omega_{3''}^2}; \quad \beta_{2''} = \tan^{-1}\dfrac{\omega_{3''}}{\delta_2}$$

$$K_{1''} = \sqrt{\left(\dfrac{i_{FAULT}(t_{c4})}{2}\right)^2 + \left(\dfrac{\frac{V_{DC}-V_{C_{C1,2}}(t_{c4})}{L_{LOAD}+L_C}-\delta_2 i_{FAULT}(t_{c4})}{2\omega_{3''}}\right)^2}$$

$$\theta'' = \tan^{-1}\dfrac{\frac{V_{DC}-V_{C_{C1,2}}(t_{c4})}{L_{LOAD}+L_C}-\delta_2 i_{FAULT}(t_{c4})}{\omega_{3''}i_{FAULT}(t_{c4})}$$

Now, V_{VCB} tracks the residual voltage $V_{C_{C1}}$ plus $V_{C_{C2}}$ until time t_{c5}.

(f) sixth interval $t_{c5} \leq t \leq t_{c6}$

In this interval, i_{FAULT} enters into the loop C_{bank}, $C_{C1,2,3}$, T_4, L_C, L_{LOAD}, T_3 and R_{FAULT} by switching the T_4 on and T_5 off. By considering $C_{C1,2,3}$ as one capacitor the circuit of Figure 5.5 (f) becomes the same topology as the test circuit shown in Figure 4.3 (e). This means that it will present same interruption process discussed in Section 4.3. The current i_{C3} describing the fault current can be expressed by the differential equation:

$$\frac{1}{C_{C1,2,3}} \int i_{C3}dt + L_C \frac{di_{C3}}{dt} + L_{LOAD} \frac{di_{C3}}{dt} + i_{C3}R_{FAULT} = V_{DC} \qquad (5.21)$$

where the voltage across C_{bank} is considered as a DC source due to the large value of C_{bank}. Initial conditions are

$$i_{C3}(t_{c5}) = i_{FAULT}(t_{c5}) \text{ (A)}$$

$$V_{C_{C1,2,3}}(t_{c5}) = V_{C_{C1,2}}(t_{c5}) + V_{C_{C3}}(t_{c5}) \qquad \text{(V)}$$

where $V_{C_{C3}}(t_{c5}) = \frac{1}{3}V_{C_{C1,2,3}}(t_{c1})$, which yields

$$V_{C_{C1,2,3}}(t_{c5}) = V_{C_{C1,2}}(t_{c5}) + \frac{1}{3}V_{C_{C1,2,3}}(t_{c1}) \qquad \text{(V)}$$

for $R_{FAULT} < 2\sqrt{\dfrac{L_{LOAD}}{C_{C1,2,3}}}$:

$$i_{C3}(t) = 2K_{1'''}e^{-\delta_2 t}\cos(\omega_{3'''}t - \theta''') \qquad \text{(A)} \qquad (5.22)$$

$$V_{C_{C1,2,3}}(t) = \frac{2K_{1'''}}{C_{C1,2,3}\omega_{4'''}}\cos(\beta_{2'''} - \theta''')$$

$$-\frac{2K_{1'''}}{C_{C1,2,3}\omega_{4'''}}e^{-\delta_2 t}\cos(\omega_{3'''}t - \theta''' + \beta_{2'''})] + V_{C_{C1,2,3}}(t_{c5}) \text{ (V)} \quad (5.23)$$

where $\delta_2 = \frac{R_{FAULT}}{2(L_{LOAD}+L_C)}$; $\omega_{3'''}^2 = \frac{1}{(L_{LOAD}+L_C)C_{C1,2,3}} - \left(\frac{R_{FAULT}}{2(L_{LOAD}+L_C)}\right)^2$

$$\omega_{4'''} = \sqrt{\delta_2{}^2 + \omega_{3'''}^2}; \beta_{2'''} = \tan^{-1}\frac{\omega_{3'''}}{\delta_2}$$

$$K_{1'''} = \sqrt{\left(\frac{i_{FAULT}(t_{c5})}{2}\right)^2 + \left(\frac{\frac{V_{DC}-V_{C_{C1,2,3}}(t_{c5})}{L_{LOAD}+L_C}-\delta_2 i_{FAULT}(t_{c5})}{2\omega_{3'''}}\right)^2}$$

$$\theta''' = \tan^{-1}\frac{\frac{V_{DC}-V_{C_{C1,2,3}}(t_{c5})}{L_{LOAD}+L_C}-\delta_2 i_{FAULT}(t_{c5})}{\omega_{3'''}i_{FAULT}(t_{c5})}$$

The VCB voltage tracks the residual voltage of $V_{C_{C1}} + V_{C_{C2}} + V_{C_{C3}}$ until the interruption finishes. Then the commutation capacitors are reset, ready for the next interruption. The VCB voltage is dominated by the commutation capacitor voltage, thus it can be expressed by the following piecewise linear function:

V_{VCB}

$$= \begin{cases} V_{C_{C1}}(t) = \frac{2K_{1'}}{C_{C1}\omega_{4'}}[\cos(\beta_{2'} - \theta') - e^{-\delta_2 t}\cos(\omega_{3'}t - \theta' + \beta_{2'})] + V_{C_{C1}}(t_{c3}) & (t_{c3} \le t \le t_{c4}) \\ V_{C_{C1,2}}(t) = \frac{2K_{1''}}{C_{C1,2}\omega_{4''}}[\cos(\beta_{2''} - \theta'') - e^{-\delta_2 t}\cos(\omega_{3''}t - \theta'' + \beta_{2''})] + V_{C_{C1,2}}(t_{c4}) & (t_{c4} \le t \le t_{c5}) \\ V_{C_{C1,2,3}}(t) = \frac{2K_{1'''}}{C_{C1,2,3}\omega_{4'''}}[\cos(\beta_{2'''} - \theta''') - e^{-\delta_2 t}\cos(\omega_{3'''}t - \theta''' + \beta_{2'''})] + V_{C_{C1,2,3}}(t_{c5}) & (t_{c5} \le t \le t_{c6}) \end{cases} \quad (5.24)$$

The fault current can also be represented by a piecewise linear function:

$$i_{FAULT} = \begin{cases} i_{C1}(t) = 2K_{1'}e^{-\delta_2 t}\cos(\omega_{3'}t - \theta') & (t_{c3} \le t \le t_{c4}) \\ i_{C1,2}(t) = 2K_{1''}e^{-\delta_2 t}\cos(\omega_{3''}t - \theta'') & (t_{c4} \le t \le t_{c5}) \\ i_{C3}(t) = 2K_{1'''}e^{-\delta_2 t}\cos(\omega_{3'''}t - \theta''') & (t_{c5} \le t \le t_{c6}) \end{cases} \quad (5.25)$$

In order to define the time intervals after the VCB current zero, the commutation capacitor voltage and current are investigated further. Comparison of equations (5.24) to (5.25) shows that they are similar except for the initial conditions which include i_{FAULT}, commutation capacitance C_C, and initial capacitor voltage V_C. Since the fault path has a large time constant compared to the commutation circuit, the fault current i_{FAULT} can be considered constant during the whole commutation period.

Figure 5.6 (a) shows the commutation capacitor voltage and current. The current i_{L_C} through the commutation capacitor equals the fault current i_{FAULT}. Due to the stored magnetic energy transfer and the residual voltage on the commutation capacitor,

there is an initial increase in i_C after the current-zero. Since the solid-state switches offer uni-directional conduction, the commutation capacitor is fully charged when i_C is reduced to zero. Note that Figure 5.6 (a) is intentionally un-scaled since it is presented mainly to demonstrated the general characteristic defined by equations (5.24) and (5.25). The scale of the figure will vary depending upon the parameter values used.
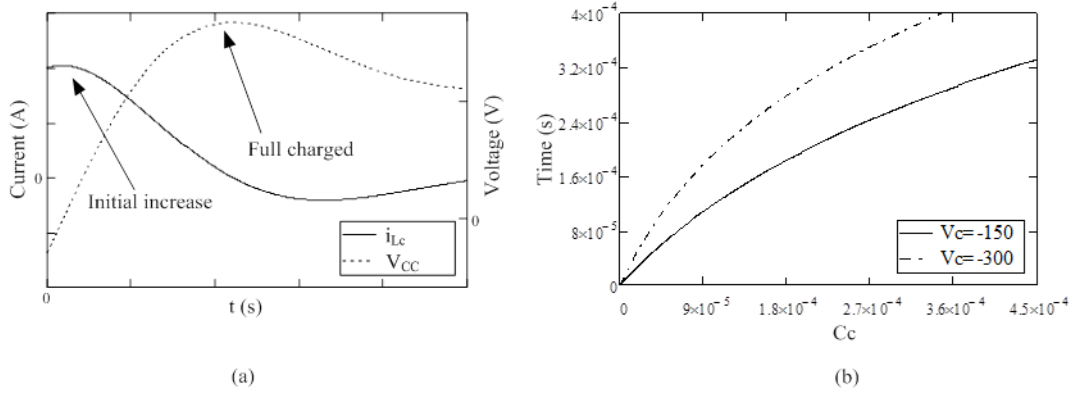
Figure 5.6 (a) The performance of commutation capacitor current and voltage after current-zero and (b) maximum discharge time with two initial commutation capacitor voltages as a function of commutation capacitance ($I_{FAULT} = 100A, V_{DC} = 600V, L_C = 49.4\mu H, L_{LOAD} = 1.7mF, R_{FAULT} = 6\Omega$).

The most significant design aspect is the period immediately following the current-zero in the VCB. Thus it is convenience to specify the duration from the initial residual capacitor voltage to when it retains zero charge. Due to the complexity of the commutation capacitor voltage equation, it is difficult to directly define a time interval equation. Capacitor voltage V_C approaches zero when i_C increases to its maximum. The approximate equation for the time interval after current-zero is obtained by equating the current differential equation with zero, which gives:

$$T_C = -\frac{\ln(-\frac{e^{2j\theta}(\delta_2+\omega_3 j)}{\delta_2-\omega_3 j})j}{2\omega_3} \qquad (5.26)$$

where $j = \sqrt{-1}$

Hence

$$T_{C4}=t_{c4}-t_{c3} = -\frac{\ln(-\frac{e^{2j\theta'}(\delta_2+\omega_3\prime j)}{\delta_2-\omega_3\prime j})j}{2\omega_3\prime} \qquad (5.27)$$

149

$$T_{C5}=t_{c5} - t_{c4} = -\frac{\ln(-\frac{e^{2j\theta''}(\delta_2+\omega_3,,j)}{\delta_2-\omega_3,,j})j}{2\omega_3,,}$$ (5.28)

The plots in Figure 5.6 (b) are for equation (5.26) with two initial residual capacitor voltages. The time interval increases with an increase in commutation capacitance and its initial residual voltage.

Since these time intervals are based on maximum discharge ability for each commutation capacitor voltage, this ensures i_{VCB} produces a second current-zero if interruption failure occurs at the first current-zero.

5.3 Calculating the time interval

The values of $C_{C1,2,3}$ and L_C can be calculated by utilising the procedures described in Section 4.3.1. The maximum counter-current $\hat{i_C}$ must larger than the fault current i_{FAULT}, and include a safety margin. But a high $\hat{i_C}$ results in larger capacitance however, meaning higher cost. Because $C_{C1} = C_{C2} = C_{C3} = 3C_{C1,2,3}$, each capacitor voltage is $V_{C_{C1}} = V_{C_{C2}} = V_{C_{C3}} = \frac{1}{3}V_{DC}$.

There are six time intervals, T_{C1} to T_{C6}, in the operation cycle of the cascaded commutation circuit. T_{C3} and T_{C4} are from the same signal impulse, which trigger switches T_3, T_4 and T_5 in the correct sequence. The first three time intervals T_{C1}, T_{C2} and T_{C3}, involve di/dt reduction while the remainder are for improving dv_{VCB}/dt. The equations for describing these time intervals have been presented in Section 5.2. Calculating these values are a problematic, especially the first three time intervals. Once the first three time intervals are specified the remainder are obtained from the proposed equations.

Since T_{C3} and T_{C4} are derived from the same signal, they can be considered 'joined', linking the reducing current before current-zero and the increasing voltage after current-zero. They maintain continuity during commutation. This means commutation current i_{L_C} has to rise to i_{FAULT} in the first two time intervals. Assuming the fault current is commutated into the VCB at the end of the first interval,

the interruption process is as for the test circuit discussed in Chapter 4, so equation (5.5) is the same as (4.22) and can be expressed as follows:

$$T_{C10}=t_{c1} - t_{c0} = \frac{-\sin^{-1}\frac{i_{FAULT}(t_{c1})Z}{V_{DC}}}{\omega_0} \tag{5.29}$$

where $\omega_0 = 1/\sqrt{L_C C_{C1,2,3}}$ (rad/s)

If i_{FAULT} is commutated at t_{c2}, equation (5.9) for describing time interval T_{C2} can be rewritten as:

$$T_{C20}=t_{c2} - t_{c1} = \frac{-\sin^{-1}\frac{V_{C_{C1,2}}(t_{c1})\times i_{FAULT}(t_{c2})+L_C\times i_{FAULT}(t_{c2})\times\omega_{0'}\times A}{\left(C_{C1,2}\times\left(V_{C_{C1,2}}(t_{c1})\right)^2+L_C\times\left(i_{FAULT}(t_{c2})\right)^2\right)\times\omega_{0'}}}{\omega_{0'}} \tag{5.30}$$

where $A = \sqrt{\frac{C_{C1,2}\times(V_{C_{C1,2}}(t_{c1}))^2+L_C\times(i_{FAULT}(t_{c2}))^2-L_{c\times}(i_{FAULT}(t_{c2}))^2}{L_C}}$

$V_{C_{C1,2}}(t_{c1}) = -\tfrac{2}{3}V_{DC}\cos\omega_0 t_{c1}$

$i_{FAULT}(t_{c1}) = i_{FAULT}(t_{c2})$ due to the large time constant of the fault path. Now considering t_{c0} as a starting point, $T_{C1} = t_{c1} - t_{c0} = t$. The total duration can be defined as:

$$T_{C1,2}=t_{c2} - t_{c0} = T_{C2} + T_{C1} = T_{C20} + t \tag{5.31}$$

To specify time interval values becomes a trade-off between T_{C1} and T_{C2}.

The graphs in Figure 5.7 represent equations (5.29) to (5.31) for the different conditions but a fixed 600V DC source. Based on the fixed fault current of 100A and commutation parameters including $L_C = 49.4\mu H$ and $C_{C1} = 40\mu F$, Figure 5.7 (a) compares the total duration $T_{C1,2}$ and the second time interval T_{C20}, as well as the first current-zero time T_{C10} of the test circuit. The figure shows how di/dt is reduced by the cascaded circuit, compared to the test circuit. The horizontal axis represents the first time interval, $T_{C1} = t_{c1} - t_{c0} = t$. The second time interval reduces as the first time interval increases, meaning a longer first time interval will result in less time for the second interval, thereby reducing $T_{C1,2}$. To maximise the cascaded circuit commutation time (compared to that of the test circuit), the second time interval should dominate commutation until current-zero. This means the switch T_5 turns on before T_4. However, since there is energy loss during capacitor voltage reversal, it is

prudent to initialise the commutation current with maximum energy, then switch into the second path.
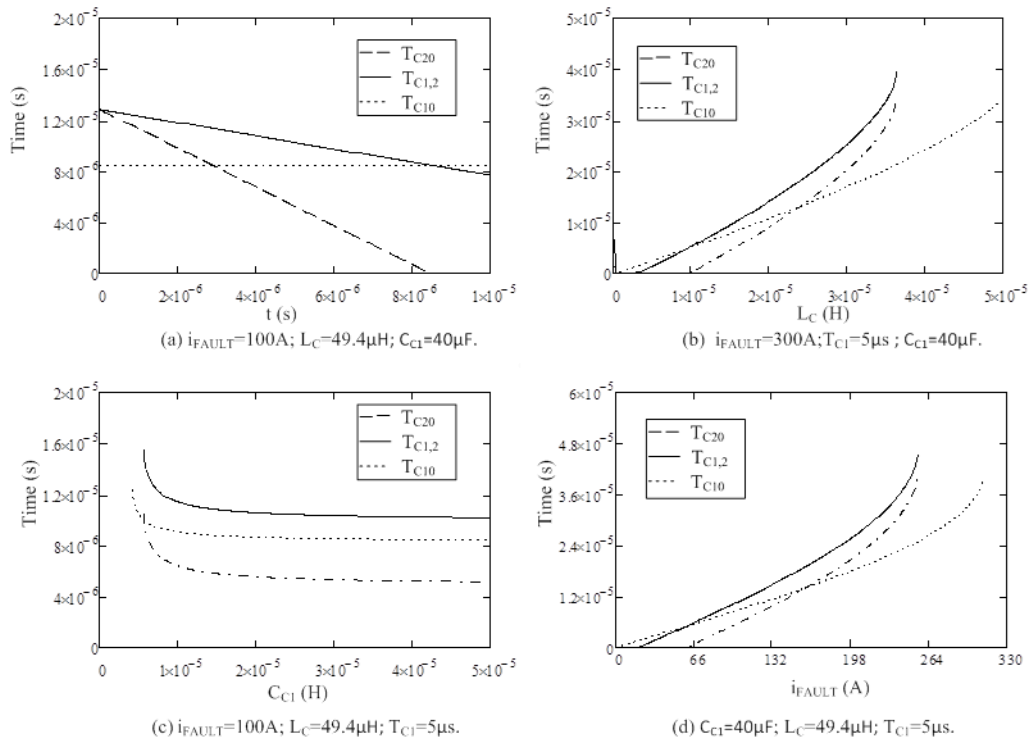
Figure 5.7 Time interval maximum values as a function of circuit parameters, with a 600V DC source: (a) first time interval; (b) commutation inductance; (c) commutation capacitance; and (d) interruption current.

With fixed 300A fault current, $C_{C1} = 40\mu F$ and first time interval $T_{C1} = 5\mu s$, Figure 5.7 (b) shows the relationship between the time intervals and the commutation inductance L_C. With an increase in L_C the time intervals are increased. At low inductance, the time intervals have similar values, meaning there is no commutation time difference between the cascade circuit and test circuit. At higher inductance, the commutation time differences become tens of μs, which is significant with respect to the VCB, since the vacuum arc has a fast recovery rate [5.3]. However, as the commutation inductance increases further, the test circuit can offer a VCB current-zero but the cascaded circuit cannot. The reason is that the energy stored in the capacitors is utilised differently. It is not possible for interruption with low inductance, which corresponds to large di/dt. The objective of the cascaded circuit

is to increase the interruption probability with relatively small commutation inductance at a short gap distance.

After utilising a fixed fault current of 100A, $L_C = 49.4\mu H$, and a first time interval $T_{C1} = 5\mu s$, Figure 5.7 (c) allows the conclusion to be drawn for the test circuit that the commutation capacitance has little effect on the commutation time and thereby does not influence di/dt.

With a first time interval of 5μs and commutation parameters $L_C = 49.4\mu H$ and $C_{C1} = 40\mu F$, the relationship between the time intervals and the fault current is shown in Figure 5.7 (d). The time intervals display an ever-increasing trend with an increase in the fault current, but are similar at low i_{FAULT}. The time interval increase in the cascaded circuit is however, large compared to the test circuit once the fault current has increased to certain value. Additionally, the ability to interrupt higher fault currents in the test circuit is better than in the cascaded circuit.

In summary, although there are six time intervals, T_{C1} to $T_{C6,}$ in the cascaded circuit, only T_{C1} to T_{C5} need to be specified because T_{C6} is a long signal impulse lasting until the end of the interruption. T_{C3} and T_{C4} are derived from the same signal, thus only four signals need to be processed. In order to specify these time intervals, the first two intervals should be defined first by utilising equations (5.29) and (5.30). The remaining two can be obtained from equation (5.26) in terms of different initial conditions. However, due to energy losses during commutation, a design safety margin is required, i.e. if the time interval is calculated 10μs, then 8μs is acceptable.

5.4 Simulation and experimental results

The cascaded hybrid circuit was simulated using PSPICE based on the model discussed in Section 4.4, with the results post processed in MATLAB. Since the cascaded circuit uses the same commutation preparation circuit and fault current introduction method as the test circuit, the associated features are not reconsidered

here. For convenience of comparison, the simulation and experimental results are presented side by side.

Figure 5.8 and Figure 5.9 show successful interruption at the first current-zero with 110A and 330A fault currents respectively. The general form and shape of the waveforms are the same in both cases. VCB current i_{VCB} is reduced as the counter-current i_C rises, then the decline rate of i_{VCB} is modified when the commutation path is switched. After the current-zero the VCB experiences a stepped-shaped pulse, since the residual voltages across each commutation capacitor, $V_{C_{C1}}$, $V_{C_{C2}}$ and $V_{C_{C3}}$, are charged step by step. The equations for describing this charging assume they are initially charged to zero. In addition, a little over-charging is acceptable because arc recovery is sensitive to the TRV amplitude rather than polarity.

A successful interruption at the second current-zero with a 110A fault current is shown in Figure 5.10. i_{VCB} reaches the second current-zero with a lower amplitude than in the test circuit case due to the commutation capacitors progressively discharging. Figure 5.11 illustrates an unsuccessful 100A fault current interruption. The differences between the simulation and experimental results are due to limitations of the model, a thyristor is employed in this simulation rather than the model of the VCB.
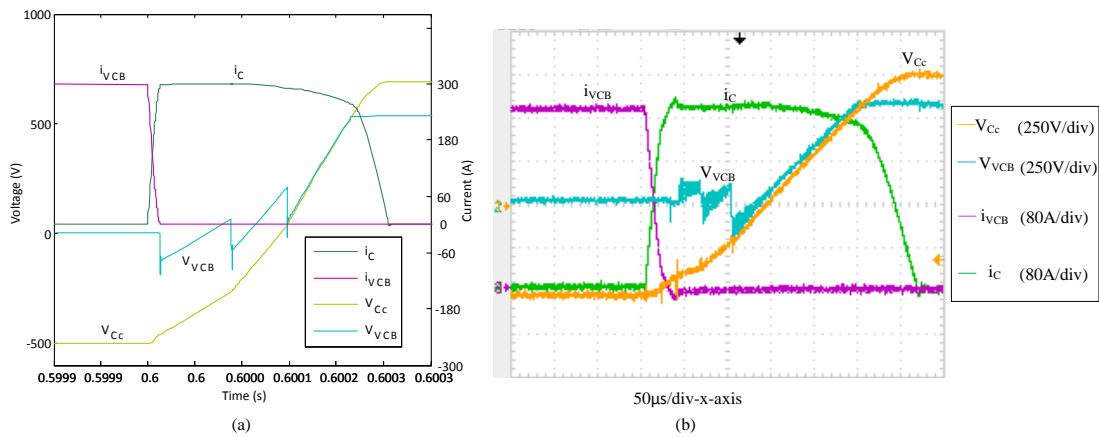
Figure 5.8 Cascaded commutation circuit voltage and current at first current-zero interruption: (a) simulation results and (b) experimental results. ($V_{DC} = 600$V, $C_{bank} = 7$mF, $C_{C1,2,3} = 120$μF, $R_1 = 200$Ω, $L_C = 49.4$μF, $L_{LOAD} = 1.7$mH, $R_{LOAD} = 600$Ω, $R_{FAULT} = 1.7$Ω)
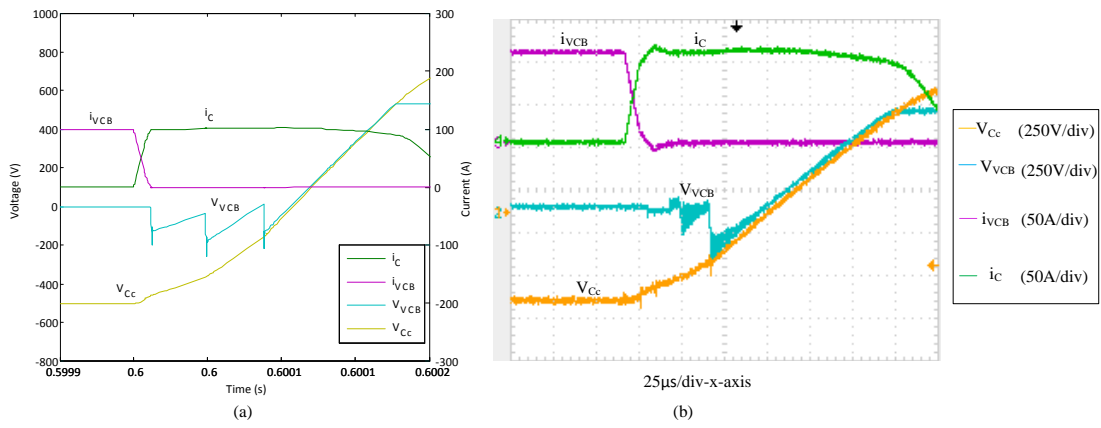
Figure 5.9 Cascaded commutation circuit voltage and current at first current-zero interruption: (a) simulation results and (b) experimental results. ($V_{DC} = 600V, C_{bank} = 7mF, C_{C1,2,3} = 12.81\mu F, R_1 = 200\Omega, L_C = 49.4\mu F, L_{LOAD} = 1.7mH, R_{LOAD} = 600\Omega, R_{FAULT} = 5.5\Omega$)
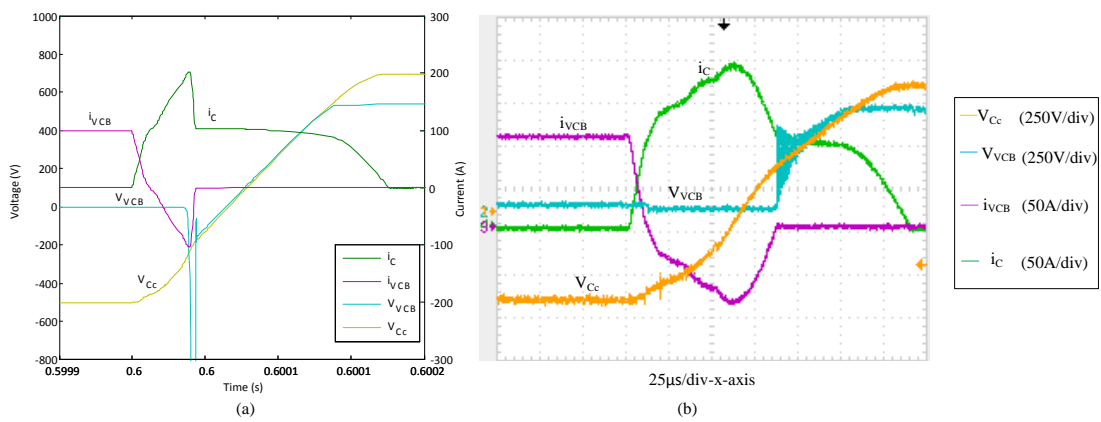
Figure 5.10 Cascaded commutation circuit voltage and current at second current-zero interruption: (a) simulation results; (b) experimental results. ($V_{DC} = 600V, C_{bank} = 7mF, C_{C1,2,3} = 12.81\mu F, R_1 = 200\Omega, L_C = 49.4\mu F, L_{LOAD} = 1.7mH, R_{LOAD} = 600\Omega, R_{FAULT} = 5.5\Omega$)
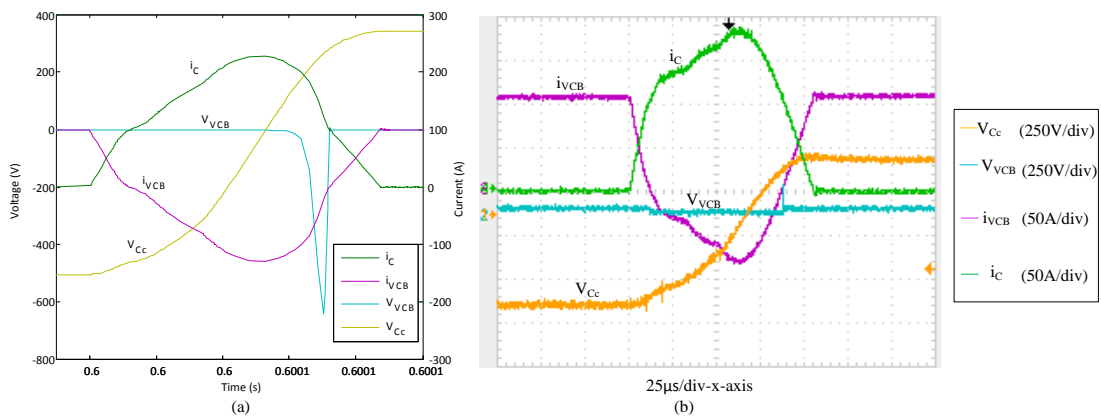
Figure 5.11 Cascaded commutation circuit voltage and current in an unsuccessful interruption: (a) simulation results and (b) experimental results. ($V_{DC} = 600V, C_{bank} = 7mF, C_{C1,2,3} = 12.81\mu F, R_1 = 200\Omega, L_C = 49.4\mu F, L_{LOAD} = 1.7mH, R_{LOAD} = 600\Omega, R_{FAULT} = 5.5\Omega$)

155

5.5 Cascaded commutation circuit performance

The experimental cascaded commutation circuit tests are based on the vacuum interrupter SH5Y. As with the test circuit, to avoid system damage due to excessive overcurrent, an MOV is connected in parallel with the VCB, a series blocking diode is located before capacitor bank ($C_{bank} = 7$mF) to protect the 600V DC source, and a load resistance of 600Ω were utilised.

Comparison between cascaded and test circuits

The comparison between the cascaded and test circuit investigates VCB interruption probability with a 1mm electrode spacing. The first and second current-zero interruption performances were analysed, based on successful interruption probability. Figure 5.12 and Figure 5.13 show the interruption performance results with 110A and 330A interruption currents respectively. The relationships between the successful interruption times and interruption at the first and second current-zero in terms of varied commutation parameters are shown in parts (a), (b) and (c) of each figure. The conclusion is that interruption probability increases with increased commutation inductance, as shown in part (d). The experimental conditions are tabulated in Table 5.1. The experiments were repeated 32 times for every value. The interruption probability in both commutation circuits increases as the commutation inductance is increased, creating a long commutation time. Since the cascaded circuit performance is better than that of the test circuit in terms of interruption success at the second current-zero, the interruption probability in the former circuit is larger than in the test circuit. For a given the DC voltage source, 600V, the commutation capacitance has to be increased with an increase in commutation inductance to produce adequate counter-current ($I = V/\sqrt{L/C}$). Both topologies exhibit similar performance for interruption at the first current-zero, due to having almost the same commutation time. The test circuit interruption probability tends to that of the cascaded circuit when the commutation inductance is increased.

Table 5.1 Experimental conditions for comparing the cascaded and test circuit

i_{FAULT} (A)	C_{C1} (µF)	L_C (µH)	Test circuit		Cascaded circuit			
			di/dt (A/µs)	T_{C10} (µs)	T_{C1} (µs)	T_{C2} (µs)	T_{C3}-T_{C4} (µs)	T_{C5} (µs)
110	40	14.6	33.11	3.5	2	1	30	30
		24.31	19.76	5.6	3	3	30	30
		49.4	9.55	11.5	6	8	30	30
330	40	14.6	30.09	11	7	6	5	5
	120	49.4	8.73	38	26	18	25	25
	150	70.12	6.01	55	40	24	25	25

Note: i_{FAULT} is interruption current; C_{C1} is commutation capacitance; L_C is the commutation inductance; di/dt is the rate of change of the VCB before current-zero; T_{C10} is the time to the first current-zero in the test circuit; and T_{C1}-T_{C5} is the time intervals in the cascaded circuit.
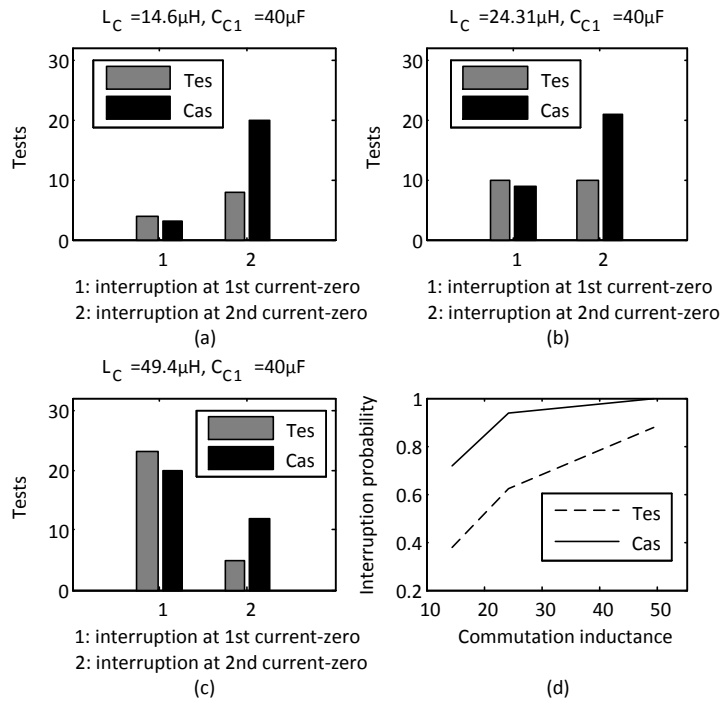
Figure 5.12 Experimental results for comparison between the cascaded and test circuit with fault current of 110A; where Tes and Cas are the abbreviation for 'test' and 'cascaded'; Tests repeated 32 times for each value.
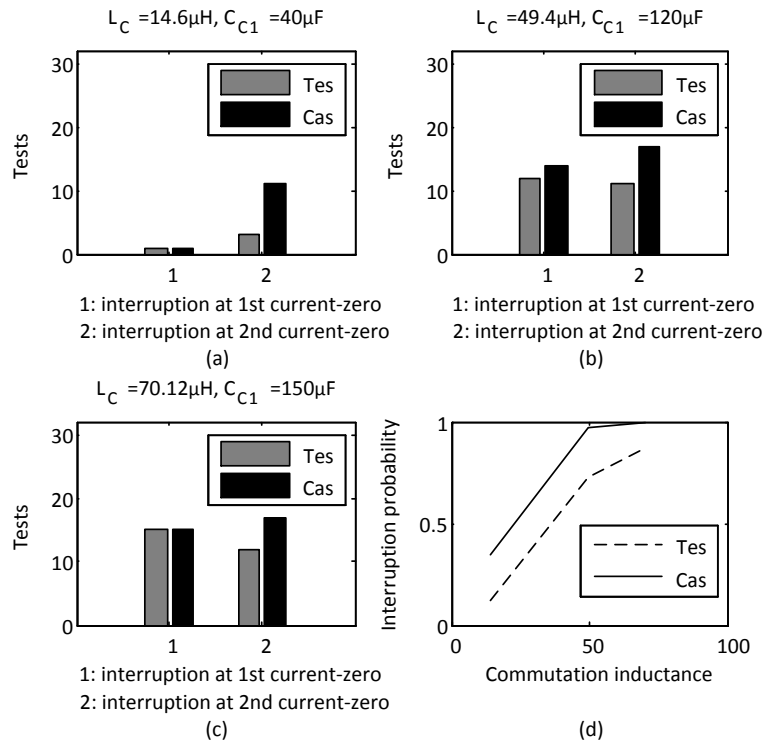
Figure 5.13 Experimental results for comparison between the cascaded and test circuit with fault current of 330A; where 'Tes' and 'Cas' are the abbreviation for test and cascaded; Tests repeated 32 times for each value.

A summary of the relationship between interruption probability and commutation inductance is shown in Figure 5.14. For each circuit, the figure is based on two commutation attempts, 110A and 330A faults, at a 1mm electrode spacing. Interruption probability increases as inductance increases (as *di/dt* decreases), while the interruption probability increases as the interruption current is decreased. This confirms that the interruption probability is sensitive to commutation time and interruption current level.
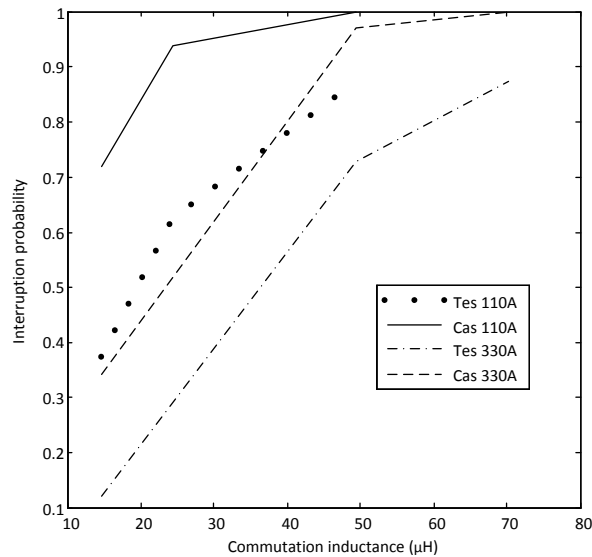
Figure 5.14 The relationship between the interruption probability and commutation inductance

The performance of the cascaded commutation circuit in reducing the dv_{VCB}/dt has been verified, where the interruption probability is increased by introducing a small amplitude pulse across the VCB. According to the equation (5.26) these pulse durations (T_{C3} to T_{C6}) are dominated by the residual commutation composite capacitor voltage and its capacitance (note that the value of composite capacitance varies as its three constituent capacitors, each having the same value, are connected in sequence, as shown in Figure 5.2. However, Table 5.1 exposes an interesting fact; where for interrupting currents 110A and 330A, and the same commutation parameters $C_{C1} = 40\mu F$ and $L_C = 14.6\mu H$, the pulse duration for 110A can be larger than for 330A. A higher fault current results in a lower capacitor residual voltage, and a significantly shorter pulse duration. Consequently, in order to produce a large pulse (long duration) after interrupting a high current, with fixed DC source, the commutation capacitance has to be increased.

Cascaded circuit performance at the first current-zero

Another objective for the cascaded circuit is to improve the di/dt by increasing the commutation time, thereby increasing the interruption probability at the first current-zero. As mentioned in Section 5.3, with fixed commutation parameters, the

159

commutation time to the first current-zero can be adjusted by the cascaded circuit (but not with the test circuit).

In order to analyse cascaded circuit performance at the first current-zero, the interruption probability calculation was based on a successful interruption at the first current-zero, with a 1mm fixed gap and a 330A interruption current, while varying commutation parameters and commutation time. The experimental conditions are shown in Table 5.2 and the experiment was repeated 32 times for each condition.

Figure 5.15 (a), (b) and (c) illustrate the relationship between successful interruption and the commutation time at the first current-zero, in terms of specific commutation parameters. Figure 5.15 (d) summarises the relationship between interruption probability and commutation time at the first current-zero. Although with a commutation time increase the interruption probability is increased, for each commutation parameter set, an increase in successful interruption is not obvious. For example, in Figure 5.15 (c) the commutation time has increased from 84μs to 106μs but interruption success still does not reach 100%. As discussed in Section 4.6.3, the post-arc current will stabilise 10μs after the current-zero. This indicates that the recovery rate before the current-zero is different to that after the current-zero.

Table 5.2 Experimental conditions for cascaded circuit performance at the first current-zero

i_{FAULT} (A)	C_{C1} (μF)	L_C (μH)	Cascaded circuit			
			T_{C1} (μs)	T_{C2} (μs)	T_{C3}-T_{C4} (μs)	T_{C5} (μs)
330	120	49.4	26	18	25	25
			11	45	15	15
	150	70.12	40	24	25	25
			30	42	15	15
	200	93.4	55	29	30	30
			40	56	20	20
			30	76	15	15

Note: i_{FAULT} is the interruption current; C_{C1} is the commutation capacitance; L_C is the commutation inductance; and T_{C1} to T_{C5} are the time intervals in the cascaded circuit.
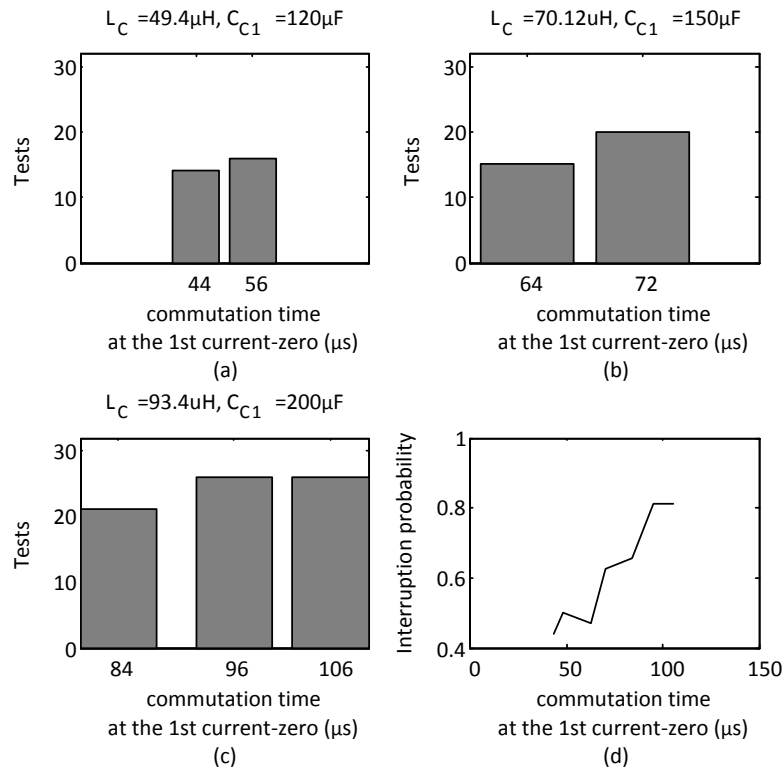
Figure 5.15 Experimental performance results of the cascaded circuit at first current-zero; Tests repeated 32 times for each value.

5.6 Summary

This chapter proposes a cascaded commutation circuit, without a snubber circuit, inspired by a breaker circuit topology containing a saturable reactor which slowed the *di/dt* prior to current-zero and then produced a low amplitude voltage pulse after current-zero. The validity of the cascaded commutation principle was confirmed by simulation and experimentally. The experiments showed that the interruption probability was better when using the cascaded commutation circuit rather than the test circuit introduced in Chapter 4, even with small inductance. The application of the cascaded commutation circuit was expected to increase interruption success at the first and second current-zero due to decreased di/dt and dv_{VCB}/dt. Interruption improvement was more apparent at the second current-zero, than the first. The reason is that the recovery rate of the residual arc after current-zero is faster than that before

161

the current-zero. In other words, the successful interruption probability is sensitive to the interruption current and the time taken to zero rather the di/dt value.

The analysis of the cascaded commutation circuit is not complete. For example the maximum counter-current produced by this cascaded circuit could be approximated by:

$$\hat{\imath}_C = V_{DC}\sqrt{\frac{C_{C1,2,3}}{L_C}} \tag{5.32}$$

where due to $C_{C1,2,3} = \frac{1}{3}C_{C1} = \frac{1}{3}C_{C2} = \frac{1}{3}C_{C3}$, Each capacitor voltage is $V_{C_{C1}} = V_{C_{C2}} = V_{C_{C3}} = \frac{1}{3}V_{DC}$, and each commutation current can be express as:

$$\widehat{\imath_{C1}} = \widehat{\imath_{C2}} = \widehat{\imath_{C3}} = V_{C_{C1}}\sqrt{\frac{C_{C1}}{L_C}} = V_{C_{C2}}\sqrt{\frac{C_{C2}}{L_C}} = V_{C_{C3}}\sqrt{\frac{C_{C3}}{L_C}} \tag{5.33}$$

The maximum counter-current can be rewritten as

$$\hat{\imath}_C = \frac{V_{DC}}{\sqrt{3}}\sqrt{\frac{C_{C1}}{L_C}} = 3V_{C_{C1}}\sqrt{\frac{C_{C1,2,3}}{L_C}} \tag{5.34}$$

The values of $C_{C1,2,3}$ and L_C can be calculated by the procedures described in Section 4.3.1. $\hat{\imath}_C$ is larger than the fault current i_{FAULT}, so if $\hat{\imath}_C$ is twice i_{FAULT}:

$$i_{FAULT} = \frac{1}{2}\hat{\imath}_C = \frac{V_{DC}}{2\sqrt{3}}\sqrt{\frac{C_{C1}}{L_C}} \tag{5.35}$$

This means that any of commutation currents $\widehat{\imath_{C1}} - \widehat{\imath_{C2}} - \widehat{\imath_{C3}}$ produced by corresponding capacitor voltage $V_{C_{C1}} = V_{C_{C2}} = V_{C_{C3}}$ is larger than i_{FAULT} due to $\frac{1}{3}V_{DC}\sqrt{\frac{C_{C1}}{L_C}} > \frac{V_{DC}}{2\sqrt{3}}\sqrt{\frac{C_{C1}}{L_C}}$. As a consequence, the commutation time to the first current-zero could be significantly increased once the third time interval is initiated. The equation describing the third time interval is however, complicated. The third-order cascaded circuit can be extended to an *N*-order cascaded circuit with *N* solid-state switches and capacitors. Then, although the capacitor number increases, each capacitor voltage rating is decreased. Interruption becomes more flexible and feasible under the closed-loop current control based on monitoring the VCB current.

References

[5.1]   A.N. Greenwood, and T.H. Lee, "Theory and Application of the Commutation Principle for HVDC Circuit Breakers," *Power Apparatus and Systems, IEEE Transactions on,* vol. PAS-91, pp. 1570-1574, July 1972.

[5.2]   W.J. Premerlani, "Forced Commutation Performance of Vacuum Switches for HVDC Breaker Application," *IEEE TRANS.,* vol. PAS-101, pp. 2721-2727, Aug. 1982.

[5.3]   G. A. Farrall, "Recovery of dielectric strength after current interruption in vacuum," *IEEE Transacitons on Plasma Science,* vol. PS-6, pp. 360-369, Decenmber 1978.

6 Conclusions

There are two DC hybrid switching techniques for the VCB. The first is arc interruption based on conventional current oscillation, and the second is interruption without an arc as in the voltage commutation approach proposed by ABB. The main difference is whether the interruption manages the arc or not. In order to highlight the advantage of the ABB approach of interruption without an arc (or the difficulties of the current oscillation approach), this thesis reports the use of a VCB as the main breaker and investigation the arc effects on the interruption performance when using the forced current commutation method. The experimental results showed the VCB offered large values of di/dt and dv/dt, but that there were limits to their values which varied from VCB to VCB. If these limits are approached, the interruption capability is reduced. Cost aside, the hybrid switching technology proposed by ABB would fulfil HVDC grid needs, provided its operating speed can be improve. The development direction of the hybrid switching technology should be based on interruption without an arc.

Based on the DC approach, which uses an asymmetrical half H-bridge circuit, the VCB opening time was reduced from approximately 50ms to approximately 13ms. The same circuit can be used on a coil where the opening action results from application of current, and would signifiantly increase the opening speed. The observation of coil counter-EMF offers great convenience to optimally trigger the auxiliary commutation circuit therefore reducing the stress on commutation capacitor. This, however, can only be applied to this kind of VCB with an indirect mechanism.

6.1 General conclusion

Chapter 1 gave an overview of present electric current limitation and interruption techniques for DC breaker designs, and proposed some features for high-speed

current limiting vacuum circuit breaker development based on the hybrid current commutation concept.

In Chapter 2, the basic characteristics of the vacuum arc were illustrated by utilising experimental evidence. The vacuum arc can be classified into two modes: namely the diffuse mode and the constricted mode. Since the diffuse mode not only causes less erosion on the electrode surface but also introduces easy interruption compared to the constricted mode, some proposed methods for maintaining a diffuse arc were presented. Examples of these methods are the use of magnetic fields and advanced electrode designs. In order to understand the residual arc, the post-arc mode was discussed, where the main elements are ions and electrons.

In Chapter 3, the VCB drive mechanism was described in detail. Solenoid operation was upgraded from a rectified AC energising circuit to a DC approach which uses an asymmetrical half H-bridge circuit. The VCB opening time was reduced from approximately 50ms to approximately 13ms. Using analogue devices, the VCB contact opening speed was measured to be approximately 1m/s. A detailed explanation for the occurrence of the counter-EMF was discussed. The counter-EMF appears to cause a peak in the coil current, where the occurrence of the peak is consistent in relation to arc voltage formation, regardless of external conditions. Consequently, a control circuit was assesses based on this relationship, to enable optimal synchronised triggering of the commutation circuit.

In Chapter 4, active and passive commutation circuits were discussed. Mathematical analysis was presented to aid understanding of the active commutation circuit, and simulation models were developed in order to calculate and select the values of commutation parameters, including the capacitor and inductor. Based on active current commutation circuit, a test circuit was used to investigate arc effects on the interruption performance by testing with varied interruption current, di/dt and dv_{VCB}/dt, and arcing time. The vacuum switch-triggered spark gap used as a commutation switch for providing the counter-current through the VCB was replaced by solid-state switches. An increase in the power losses during the preparation of the commutation circuit caused a decrease in the initial commutation capacitor voltage, thereby lowering the counter-current range.

Experimental results confirmed VCB interruption performance at low power rating is similar to that at high power rating. A decrease in di/dt or dv_{VCB}/dt introduces an increase in the interruption probability. Based on fixed di/dt, dv_{VCB}/dt and arcing time, the interruption probability was inversely proportional to the interruption current. With a fixed interruption current, the di/dt and dv_{VCB}/dt for maintaining successful interruption, increased once the arcing time was increased. However, with a large di/dt successful interruption became impossible even if the dv_{VCB}/dt was low. That is, with large di/dt, the VCB acted as a short circuit and the shape of the prospective recovery voltage was insignificant. di/dt is the key factor in determining the interruption probability. Also there is a voltage recovery rate which dominates how the vacuum arc recovers from a conduction state with a decrease in the interruption current. Consequently, successful interruption is based on the combined effects of di/dt and recovery rate. Recovery becomes impossible when the di/dt is large compared to the recovery rate even with a shunt snubber circuit connected.

After the post-arc was investigated by measuring its electrical behaviour, the ion density immediately after current-zero was not only determined by its natural decay and the post-arc current, but also dominated by the values of di/dt and dv_{VCB}/dt. The post-arc current increased as di/dt increased, and decreased with a decrease in dv_{VCB}/dt . This is why di/dt and dv_{VCB}/dt impact successful interruption probability. The relationship between VCB conduction resistance and interruption performance is: less conduction resistance better interruption performance.

In Chapter 5, a cascaded commutation circuit for the hybrid breaker was designed, analysed, simulated and experimentally compared with a test commutation circuit. A decreased *di/dt* prior to the current-zero followed by a relatively low amplitude voltage pulse after the current-zero increased the interruption probability, even with low values of commutation parameters, such as a low value inductor and a large value capacitor but with a low voltage rating. However, this interruption probability increase was mainly attributable to any successful interruptions at the second current-zero after the short pulse voltage with low amplitude was applied. As for interruption at the first current-zero, interruption probability increase was not apparent even if the

166

commutation time was increased from 84μs to 106μs. In summary, the interruption probability is based on the interruption current and the commutation time. The di/dt at the first current-zero is not significant.

6.2 Author's contribution

The thesis contributions can be summarised as follows:

- The general design requirements of a hybrid breaker were outlined, which target development of a current limiting vacuum circuit breaker based on a hybrid current commutation concept, allowing high-speed operation and high-current interruption capability.
- Without a change in the physical mechanism, VCB opening time was reduced by using a DC energising circuit.
- A mathematical equation was proposed to explain the occurrence of the counter-EMF associated with armature movement. The stress on the commutation capacitor is reduced by using the proposed adaptive control circuit.
- VCB interruption performance at low power rating was investigated by assessing a test circuit based on the active current commutation concept. Specification of the commutation circuit components using solid-state semiconductor devices as the commutation switch was presented. Equations to calculate the power losses associated with the test circuit were presented.
- The relationships between the gap distance, di/dt , dv_{VCB}/dt and interruption current were obtained. Consequently, the interruption time was reduced by triggering the commutation circuit to produce counter-current through the VCB at an optimal gap distance rather over the full gap distance. The erosion on the contact surface was reduced due to short arcing time, thus the useful VCB life is extended.

- The relationship between the post-arc and di/dt and dv_{VCB}/dt were established. This explains how di/dt and dv_{VCB}/dt impact on successful interruption probability.

- The relationship between VCB conduction resistance and interruption performance established that lower conduction resistance gives better interruption performance.

- The realisation of a cascaded commutation circuit adopting the hybrid active current commutation concept improves the interruption probability compared to test circuit based commutation, for the same conditions. Also it optimises commutation parameter sizes including the capacitor and inductor. It was established that successful interruption probability is sensitive to interruption current and the time taken to drive it to zero, rather than di/dt near current-zero.

6.3 Suggestions for future research

The research undertaken in this thesis emphasised the arc effects on VCB interruption performance by utilising forced current commutation technology. Suggestions for future research are:

- In order to create a cascaded commutation circuit that is more flexible and viable, a better closed-loop current control method should be developed.

- In order to prevent the fault current from increasing significantly, further research should concentrate on fault current limiters, fast mechanical switches or disconnectors with excellent insulating properties after the current-zero, and pure solid-state switches with minimal on-state losses, with fast and intelligent monitoring systems.

- In order to optimise the existing hybrid current commutation scheme, a better mathematical model to predict the arc characteristics should be sought.

- The development direction of hybrid switching technology for HVDC applications should focus on interruption without an arc.

Appendices

The appendices give a detailed description of the practical implementation, which includes the test rigs and control circuits, as well as program codes. Additionally, this appendix presents detailed background information on various arc aspects referred to in Chapter 2. Meanwhile, the lists of tables and figures are presented.

Appendix A
Experimental setup

A.1 Test Rig structure

In order to investigate interruption performance of the vacuum circuit breaker (VCB), two test rigs were constructed for practical implementation.

A.1.1 The test and cascaded commutation circuit

Since the proposed cascaded commutation circuit inherits most of test circuit features and properties, one experimental rig represents the needs of both circuits, which are based on different control signals. The circuits use the following components:

- 600V 10A DC voltage source
- 7mF capacitor bank
- Commutation capacitors and inductors both with a range of values
- A vacuum circuit breaker with three vacuum interrupters in one frame
- A few of solid-state switches each includes a diode (DSEI 2x101) in series with an IGBT (5SND 0800M170100)
- Control circuit including analogous circuits and digital circuits
- Gate drives
- Current transducer

- Load resistor 600Ω and inductor 1.7mH as well as fault resistor with a range of value
- Freewheel diode
- metal oxide varistor (MOV)

Figure A.1 illustrates the practical system photo. The commutation rig is shown in Figure A.2.
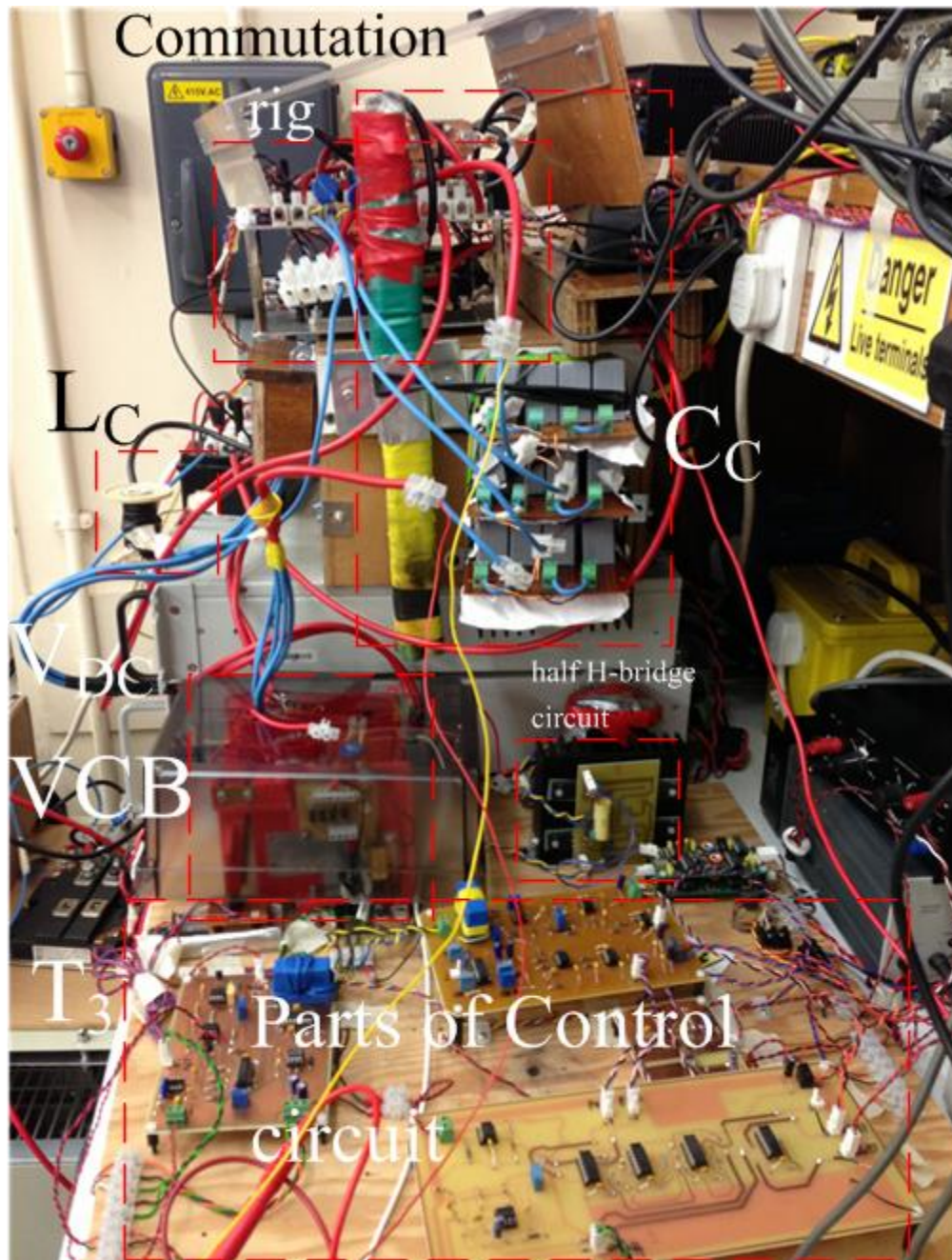
Figure A.1 System photo of the test rigs
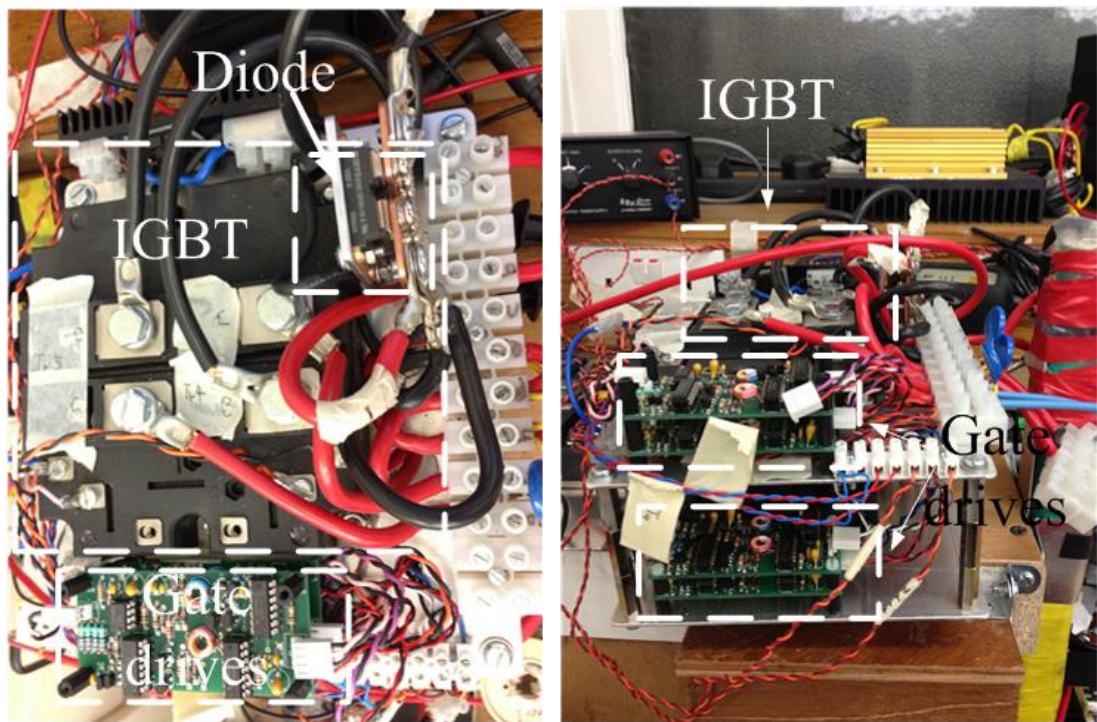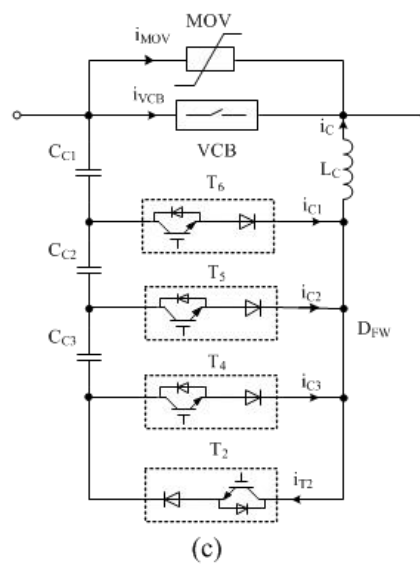
Figure A.2 Commutation rig: (a) top view; (b) side view; and (c) schematic diagram.

A.2 Control circuits

The control circuits can be divided into two groups in terms of device types. The first group are the analogous circuits, the second group are the digital circuits. The signals

for vacuum circuit breaker (VCB) mechanisms are based on the analogue circuits, for investigating the VCB interruption performance are produced by the digital circuits.

A.2.1 ON/OFF and Fault signal circuit

The ON/OFF and fault signal circuit described in Chapter 3 contains the following components:

- 5V voltage source
- mechanical switches
- Schmitt-Trigger inverters (CD74ACT14)
- Resistors and capacitors as well as diodes

The electrical circuit diagram and practical photo are shown in Figure A.3.
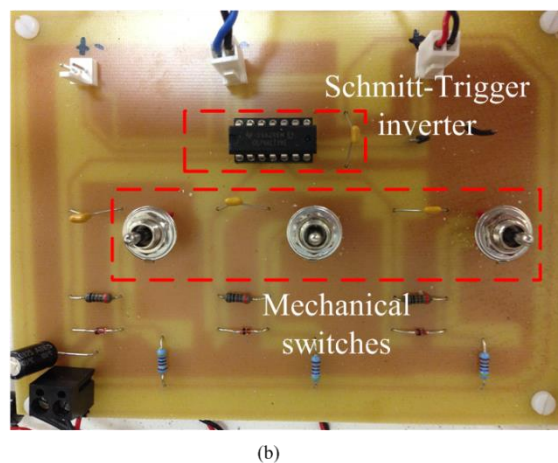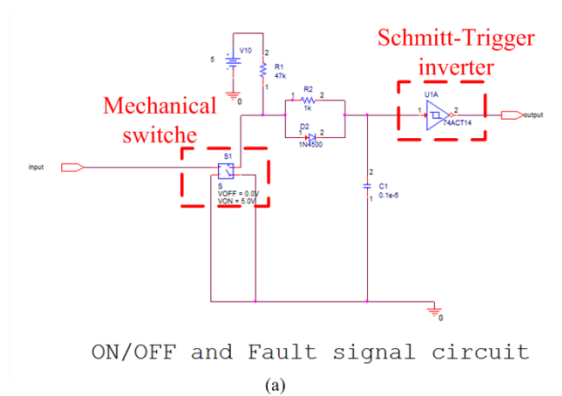
Figure A.3 ON/OFF and fault signal circuit: (a) one of three schematic diagram and (b) photograph.

A.2.2 Flip-flop circuit

The flip-flop circuit recognizes the incoming signal as ON/OFF or Fault and then dispatches it to the correct channel. The photo of the flip-flop circuit is shown in Figure A.4, with the circuit schematics shown in Figure A.5. It includes the following components:

- 5V voltage source
- flip-flop devices (SN5474)
- Timer devices (NE555)
- Resistor and capacitor as well as diode
- logic devices including NAND gate (MC74ACT00), NOT gate (74ACT04), XNOR gate (CD74HC7266)
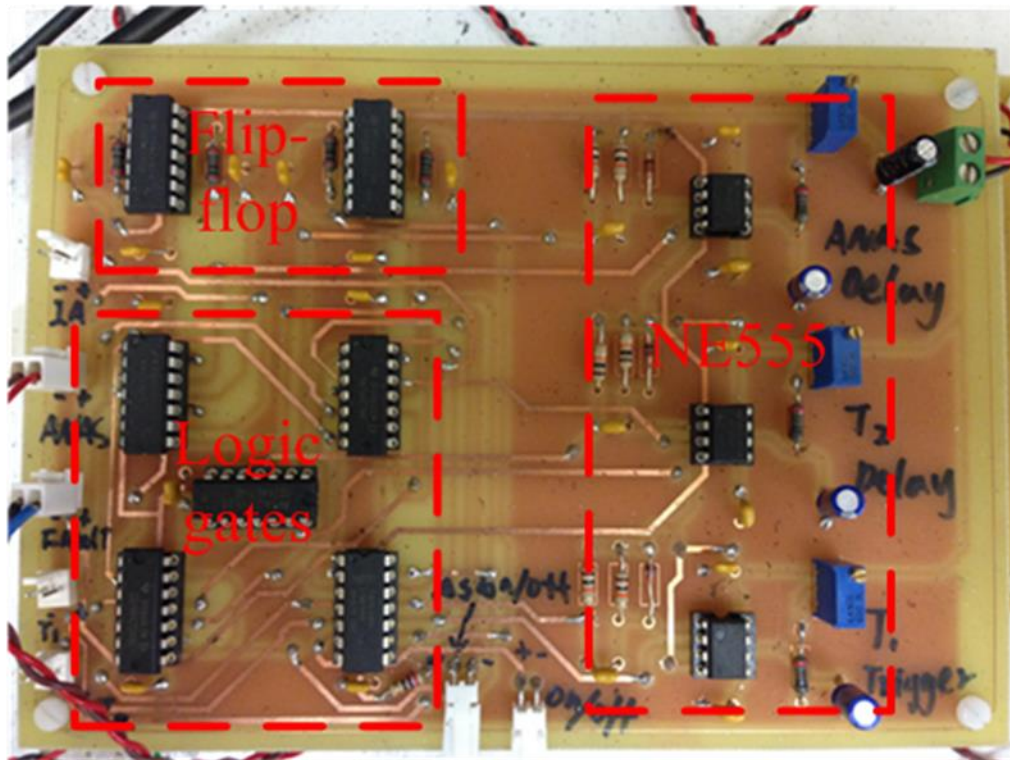
Figure A.4 Photo of the flip-flop circuit

Figure A.5 Circuit schematics of the flip-flop circuit.

174

A.2.3 PI regulator

The DC energising coil circuit described in Chapter 3, used to speeding up the VCB opening time, is based on close-loop current control with a proportional plus integral (PI) regulator which consists of the following components:

- 5V and ±15V voltage sources
- Current transducer (LEM LA 55-P)
- Monolithic wave generator (XR2206)
- Analogous devices, including operational amplifier (NE5534) and comparator (LM311)
- Potentiometer, resistor and capacitor as well as diode

Figure A.6illustrates the practical circuit photo. The circuit schematic is shown Figure A.7.
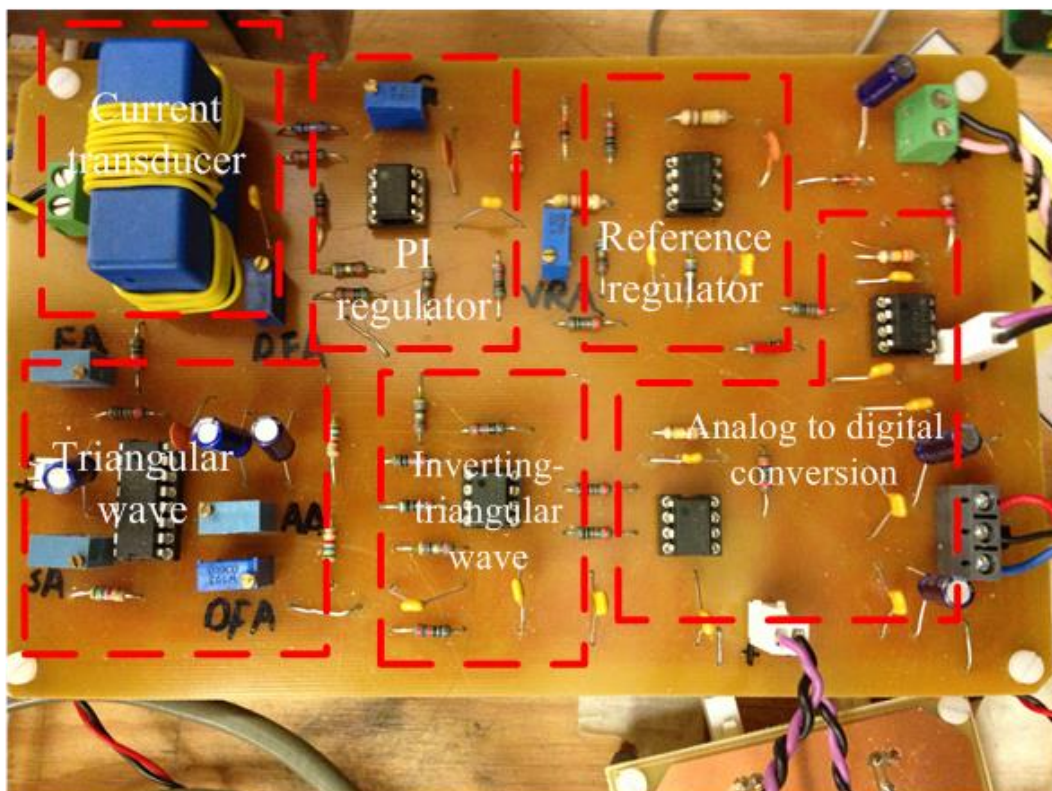
Figure A.6 Photo of the PI regulator circuit
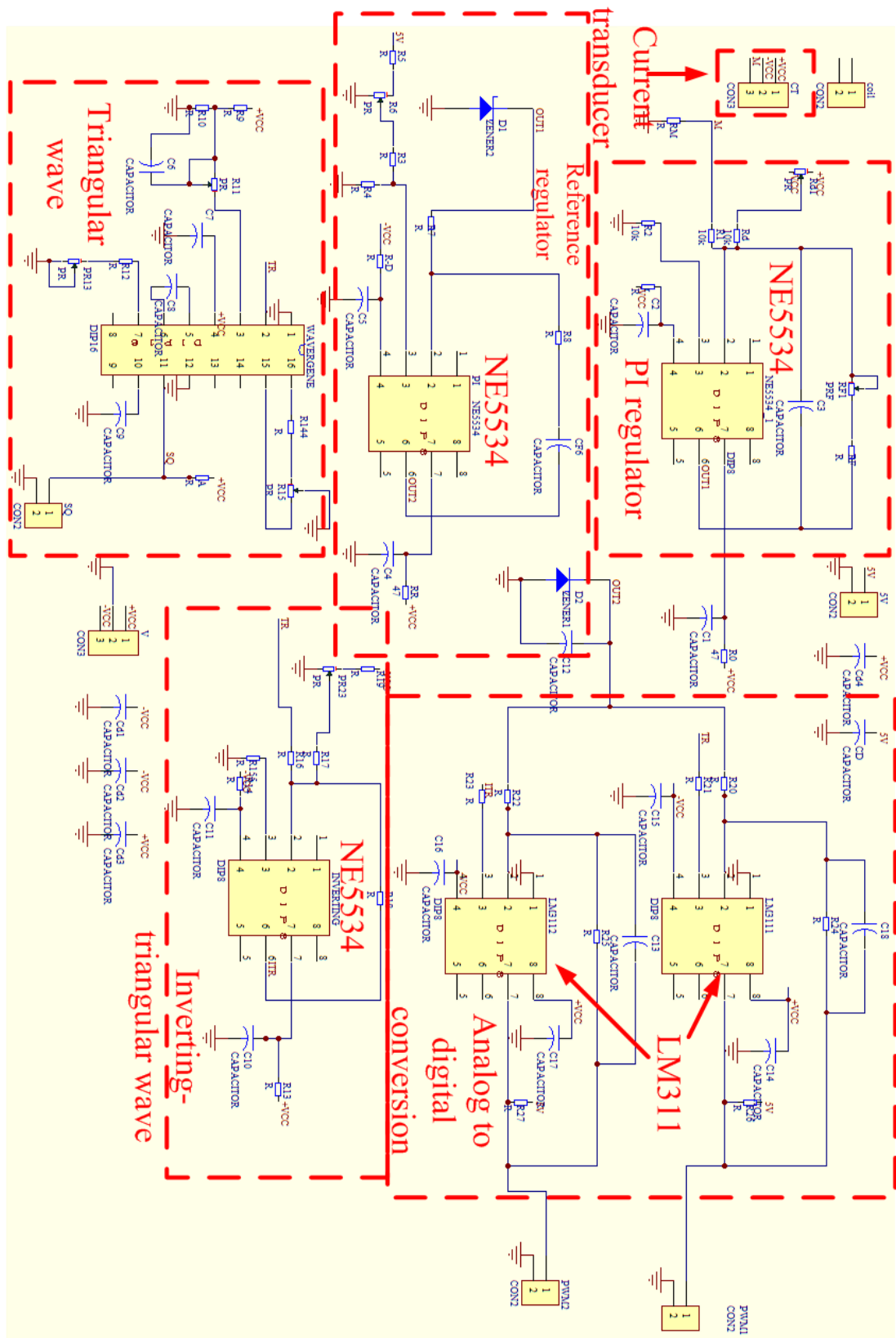
Figure A.7 Circuit schematics of the PI regulator

A.2.4 Trip signal circuit

The trip signal circuit selectively amplifies the transient increase of coil current; where the photo of the trip signal circuit is shown in Figure A.8, with the circuit schematics shown in Figure A.9. It contains the following components:

- 5V and ±15 voltage sources
- Current transducer
- Instrumentation amplifier (LT1168) and analogue switch (ADG201HS)
- Analogous devices, including operational amplifier (NE5534) and comparator (LM311) as well as timer device (NE555)
- Logic NOT Gate (74ACT04)
- Potentiometer, resistor and capacitor as well as diodes
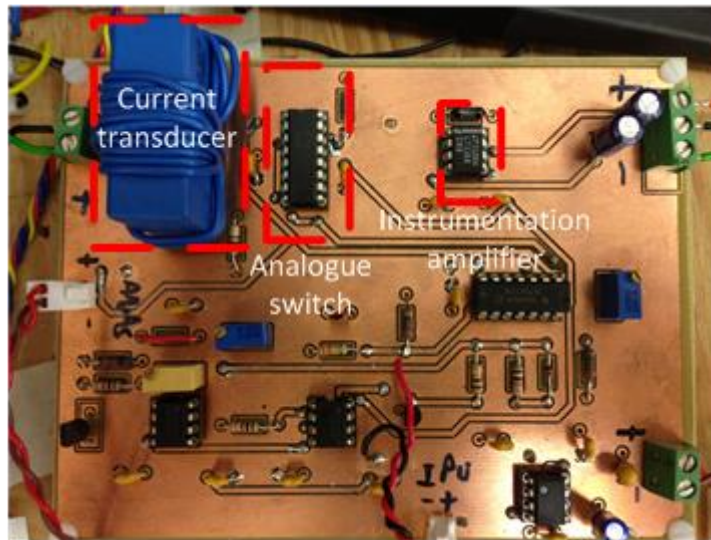
Figure A.8 Photo of the trip signal circuit
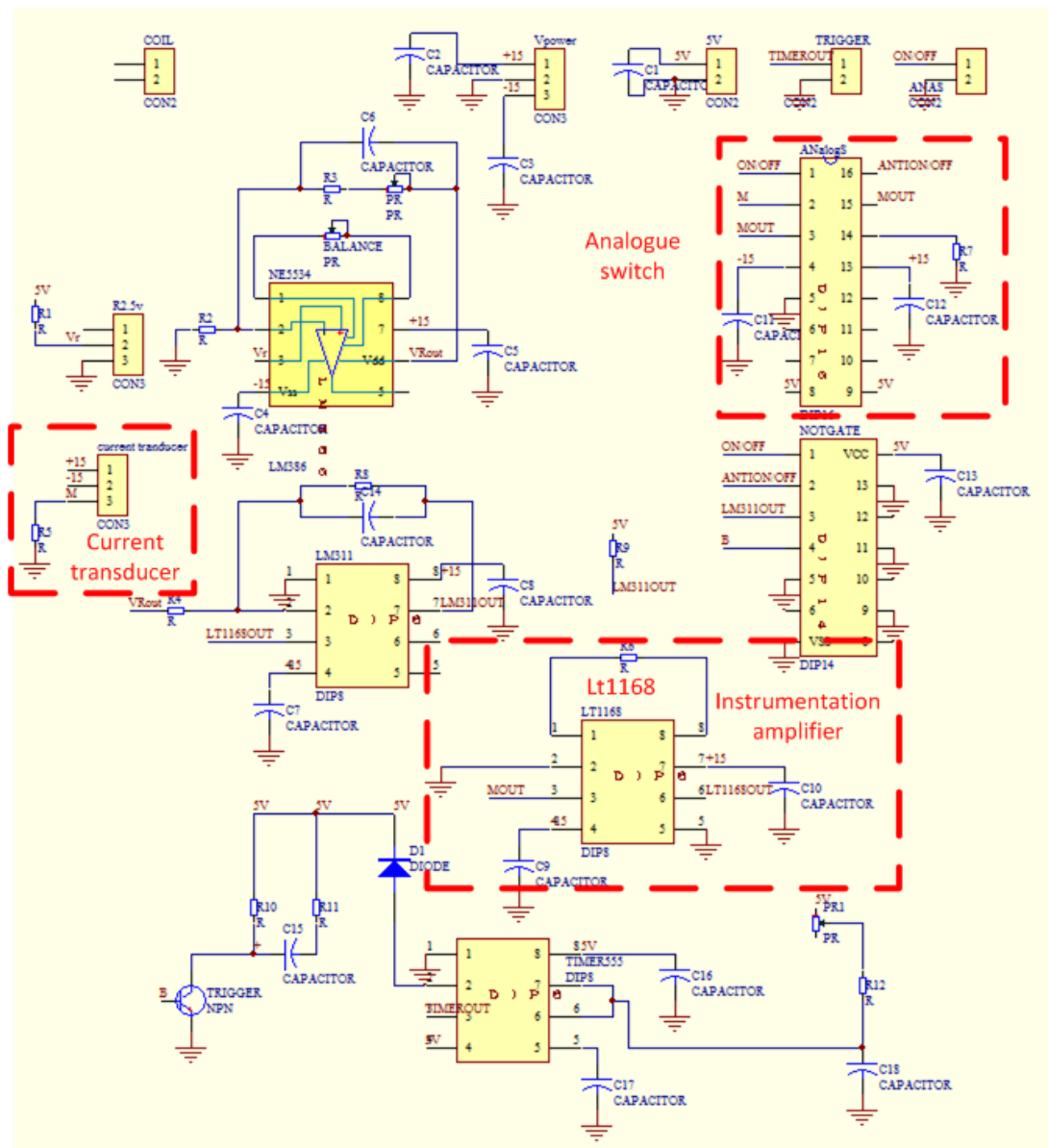
Figure A.9 Circuit schematics of the trip signal

A.2.5 Microchip controller

The main function of the PIC controller is to observe trip signal circuit changes and to produce signals to delay activate the commutation circuit. The dsPIC30F2020 controller provides the controllable signals to investigate VCB characteristics.

In order to connect analogue input signals to output a series of sequential time intervals, which are isolated using Optocoupler (ADuM1200-EP), an interface circuit

is introduced. The photo of the interface circuit is illustrated in Figure A.11, with the circuit schematics shown in Figure A.10.
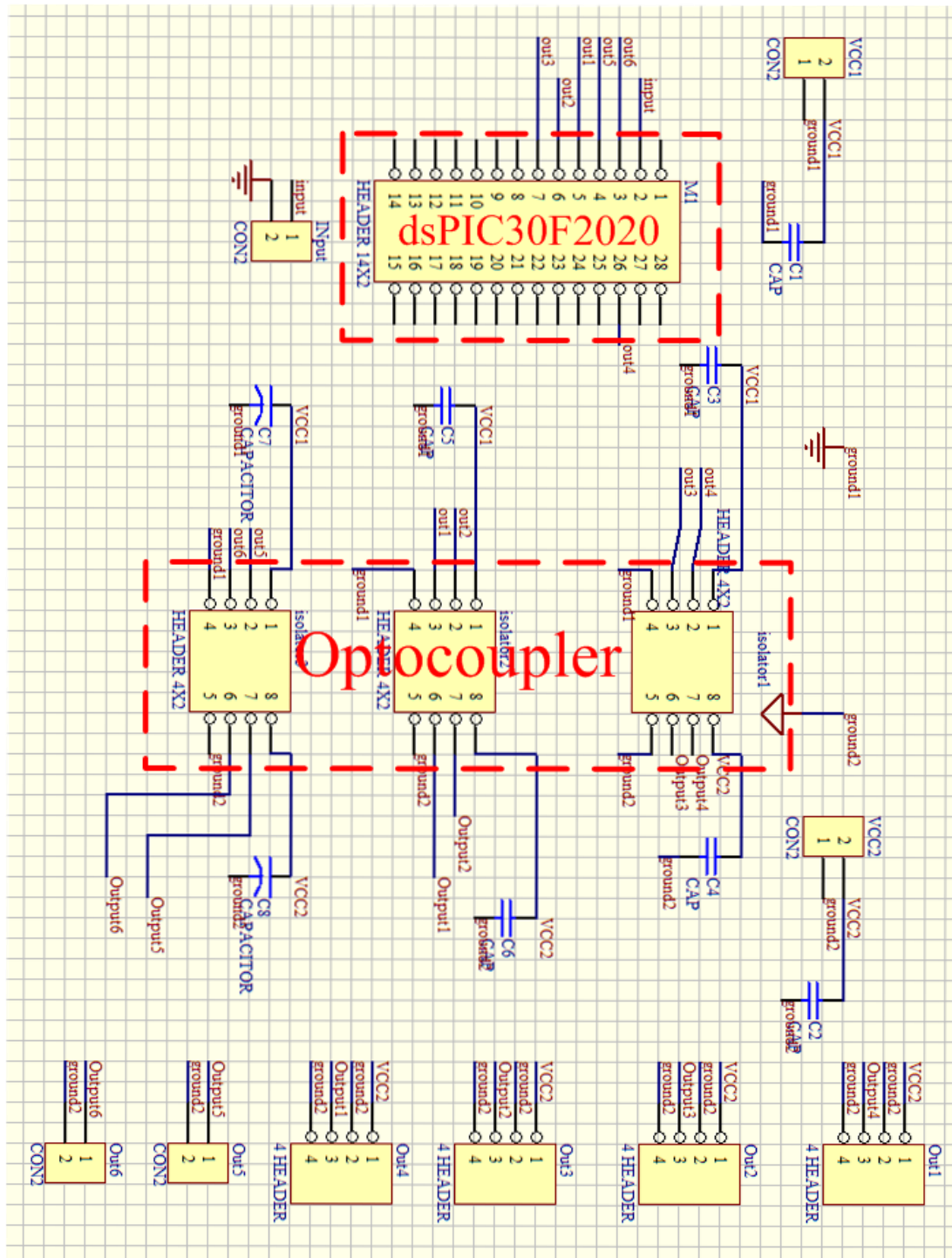
Figure A.10 Circuit schematics of the interface.
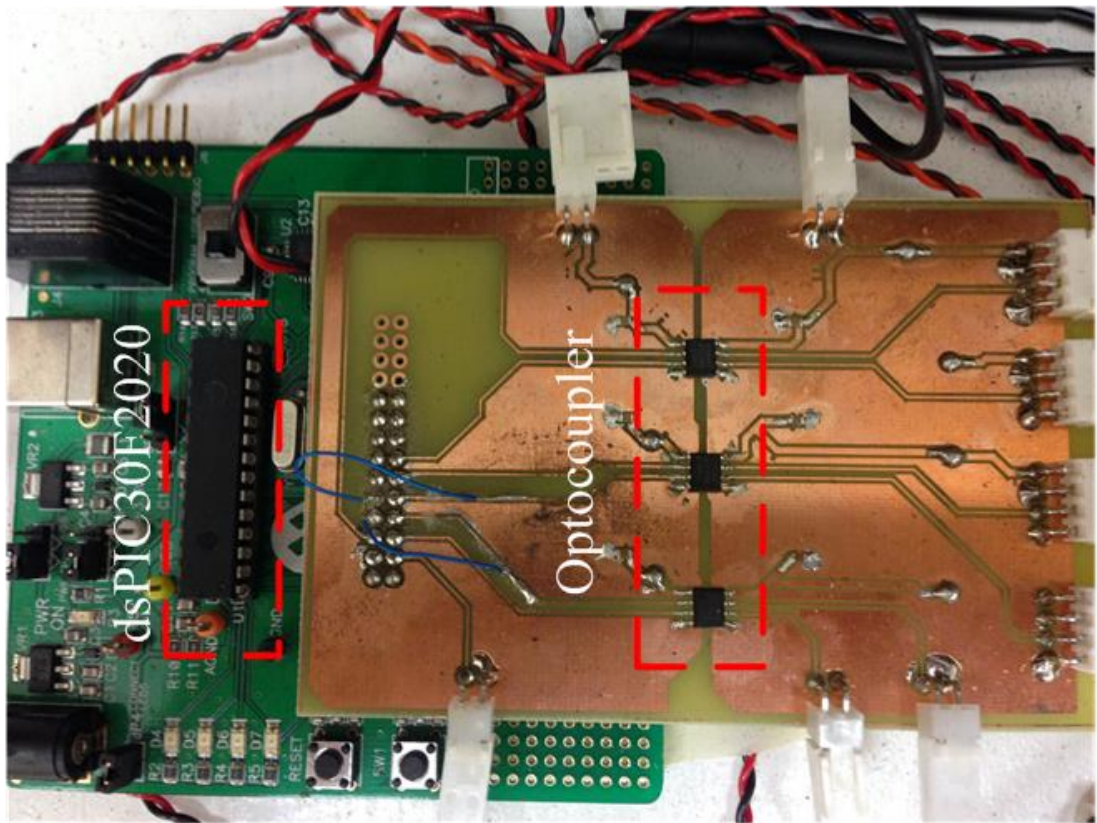
Figure A.11 Photo of the interface circuit.

A.2.6 Logic control circuit

(a)
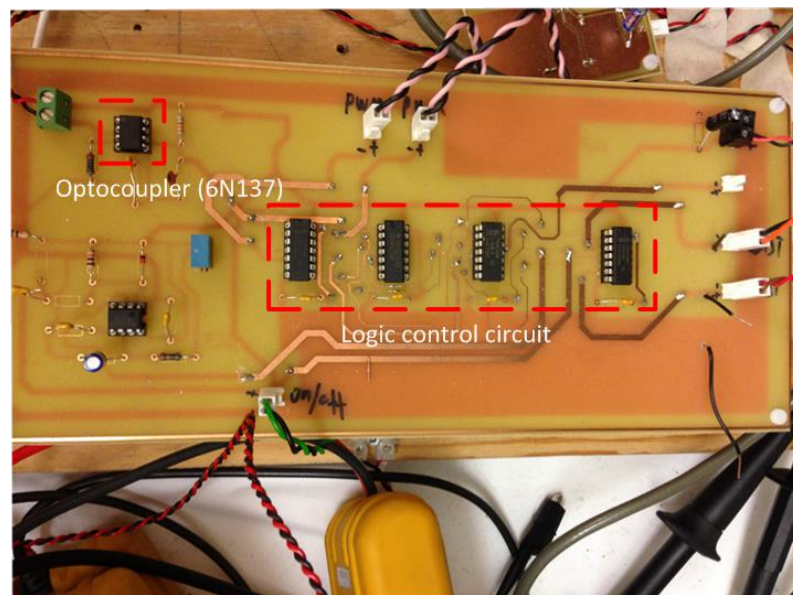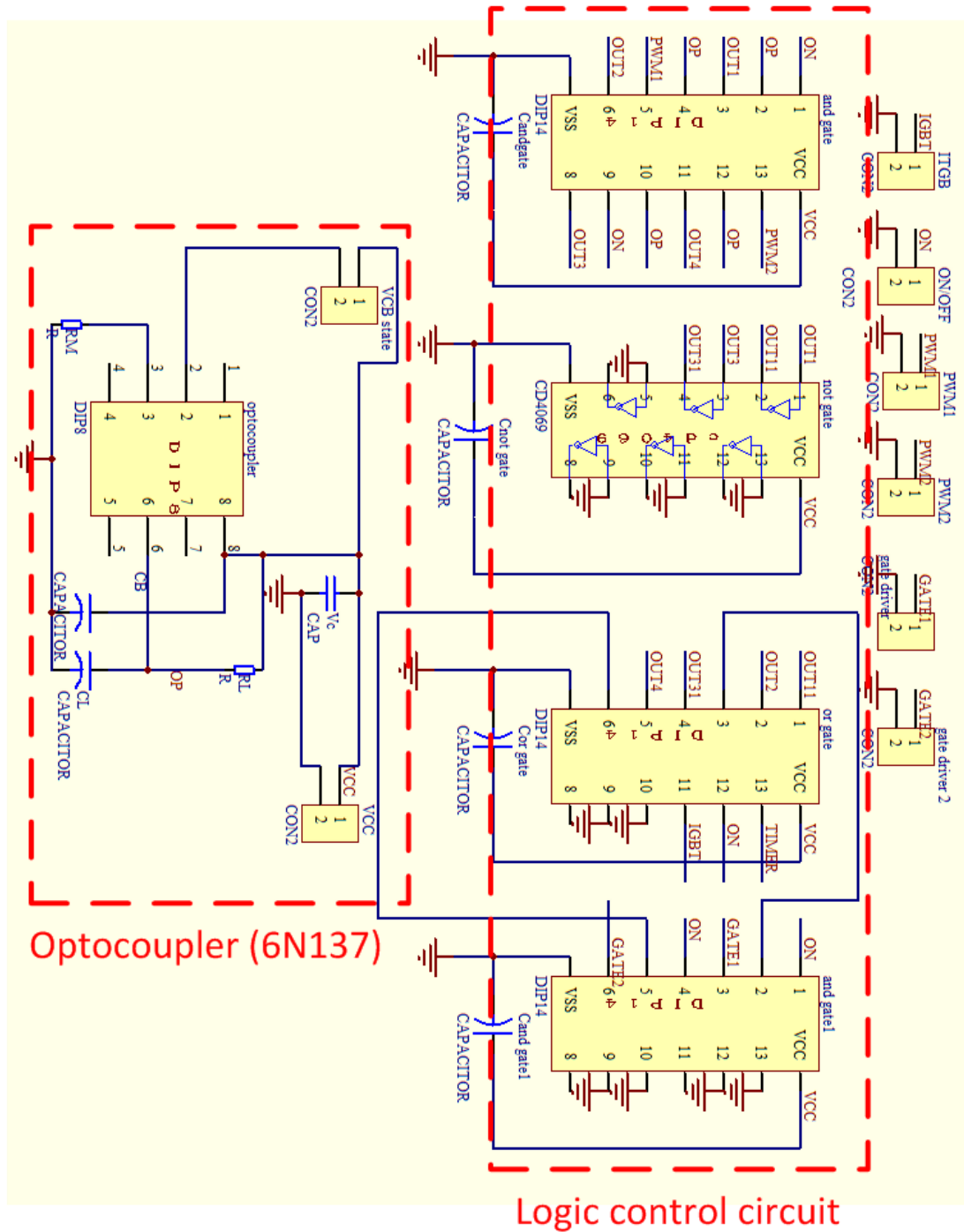
Figure A.12 (a) Photo of logic control circuit and (b) and its schematics.

As described in Chapter 3, these rectifier switches are used in conjunction with high speed Optocouplers (6N137) to observe the VCB state. With the logic control circuit shown in Figure A.12, the control ON/OFF and PWM signals are delivered to the correct channels.

A.3 Program codes

A.3.1 The test circuit code

```
#include        "delay.h"
voidDelayMs(unsigned intcnt)
{
        unsigned char i;
        while (cnt--) {
                i=4;
                while(i--) {
                        DelayUs(250);
                } ;
        } ;
}
int main()
{
        init();
        for(;;)
        {
        if(Input==0) pulse_gen();


        }
}

voidinit()
{
        INTCON1=0x0000;
        INTCON2=0x0000;
        ADPCFG=0x0FFF;
TRIS_Input=IN;
        TRIS_out1=OUT;
```

```c
        TRIS_out2=OUT;
        TRIS_out3=OUT;
    TRIS_out4=OUT;
}


voidpulse_gen()
{
    out1=1;
        DelayUs(1000);
    out2=1;
        out3=1;
    out1=0;
DelayMs(1);
    out3=0;
    out2=0;
        DelayMs(1000);
}
#include "p30f2020.h"
#include "pulse.h"
#include "typedefs.h"
voidtoppic_init(void)
{    INTCON1=0x0000;
    INTCON2=0x0000;
    ADPCFG=0x0FFF;
    TRIS_IN=IN;
    TRIS_out1=OUT;
    TRIS_out2=OUT;
    TRIS_out3=OUT;}
voidpulse_gene(void)
{
while(1){
```

```
if(Input==1){
        out1=1;
for(i=0;i<100;i++){}
        out2=1;
for(i=0;i<2;i++){}
        out1=0;
for(i=0;i<98;i++){}
        out3=1;
for(i=0;i<2;i++){}
        out2=0;
for(i=0;i<98;i++){}
        out2=1;
for(i=0;i<2;i++){}
        out3=0;
for(i=0;i<50;i++){}
        out1=1;
for(i=0;i<2;i++){}
        out2=0;
for(i=0;i<150;i++){}
        out1=0; }
else while (1)}}
```

A.3.2 The cascaded circuit code

```
#include        "delay.h"
voidDelayMs(unsigned intcnt)
{
        unsigned char i;
        while (cnt--) {
                i=4;
                while(i--) {
                        DelayUs(250);
                } ;
```

```c
        } ;
}
#include "p30f2020.h"
#include "delay.h"
#include "main.h"
int main()
{
        init();
   out4=1;
for(;;)  {        if(Input==0) {
DelayUs(100);
if (Input==0) pulse_gen();
                }


        }
}

voidinit()
{
        INTCON1=0x0000;
        INTCON2=0x0000;
        ADPCFG=0x0FFF;
TRIS_Input=IN;
        TRIS_out1=OUT;
        TRIS_out2=OUT;
        TRIS_out3=OUT;
        TRIS_out4=OUT;
        TRIS_out5=OUT;
        TRIS_out6=OUT;
}
voidpulse_gen()
{
```

```
   out4=0;
DelayUs(100);
   out1=1;
        DelayUs(200);
   out1=0;
DelayMs(0);
DelayUs(2500);
        out3=1;
DelayMs(0);//define delay time//
DelayUs(2420);
   out2=1;
   //DelayUs(2);
   //out6=1;
DelayUs(1);
   //out2=0;
DelayUs(19);
   //out5=1;
DelayUs(1);
   //out6=0;
DelayUs(19);
   //out6=1;
DelayUs(1);
   //out5=0;
   //DelayUs(20);
   //out2=1;
   //DelayUs(1);
  //out6=0;
DelayMs(300);
   //out1=0;
   out2=0;
   out3=0;
        DelayMs(1000);
```

```c
    out4=1;
}
#include "p30f2020.h"
#include "pulse.h"
#include "typedefs.h"

voidtoppic_init(void)
{    INTCON1=0x0000;
    INTCON2=0x0000;
    ADPCFG=0x0FFF;
    TRIS_IN=IN;
    TRIS_out1=OUT;
    TRIS_out2=OUT;
    TRIS_out3=OUT;}
voidpulse_gene(void)
{
while(1){
if(Input==1){
    out1=1;
for(i=0;i<100;i++){}
    out2=1;
for(i=0;i<2;i++){}
    out1=0;
for(i=0;i<98;i++){}
    out3=1;
for(i=0;i<2;i++){}
    out2=0;
for(i=0;i<98;i++){}
    out2=1;
for(i=0;i<2;i++){}
    out3=0;
for(i=0;i<50;i++){}
```

```
        out1=1;
for(i=0;i<2;i++){ }
        out2=0;
for(i=0;i<150;i++){ }
        out1=0; }
else while (1)}}
```

Appendix B

Arc characteristics

B.1 Formation of the vacuum arc during electrode separation
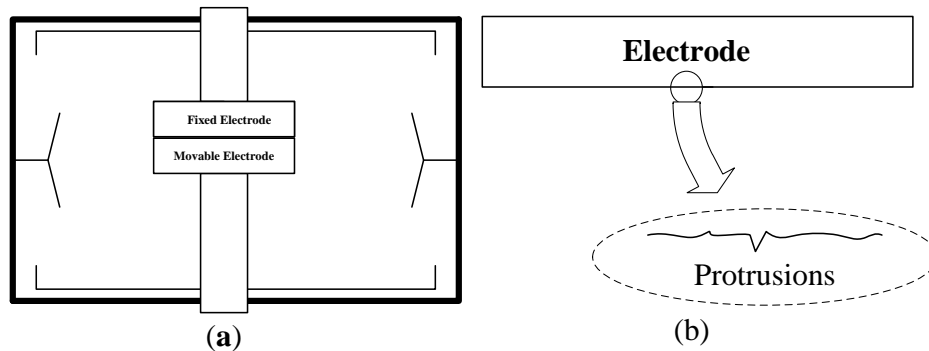
Figure B.1 The formation of the vacuum arc during electrodes opening:

(a) internal model and (b) protrusions.

Although since its introduction in the 1950s, improvements have been made to achieve reliable current interruption with minimum maintenance, the internal model of the vacuum circuit breaker (VCB) remains unchanged and can be considered as the simple model shown as Figure B.1 (a). There are two VCB electrodes: one fixed and the other moveable, and both are surrounded by a vacuum. They start to separate with current flowing, based on external conditions (the detailed external conditions and trigger signal is discussed in Chapter 3). Figure B.1 (b) shows that despite each electrode being carefully manufactured and highly polished before mounting into vacuum interrupter, microscopically the faces are rough, with protrusions on the electrode surface.

Paul G. Slade [1] stated that an arc will always form provided basic conditions are satisfied, namely the current and voltage are both greater than minimum values. The properties of the electrode material dominate arc formation and it always starts to burn in metal vapour from the actual electrodes. The inter-electrode resistance increases as the electrodes separate, which also causes an increase in the voltage

across the electrodes. Thus, the temperature of the contact spot T_{con} will also increases according to:

$$T_{con}^2 = T_0^2 + U_e^2 \times 10^7 K \qquad (\text{B.1})$$

where T_{con} represents the temperature of the electrode, T_0 is the original temperature of the electrode, and U_e is the voltage across the electrodes.

The temperature on the surface of the electrodes increases as the electrodes continue to part, especially at the protrusions. This is because the protrusions are subject to large electrical fields as the conduction area decreases, causing electrical field enhancement. Consequently, one of these protrusions melts, drawing a molten metal bridge between the electrodes, even across a vacuum (the number of protrusions drawing the molten metal bridge depends on the interruption current level) [2, 3] as illustrated in Figure B.2 (a). The inter-electrode region is stable when the *molten metal bridge* is initially created.

| (a) | (b) |
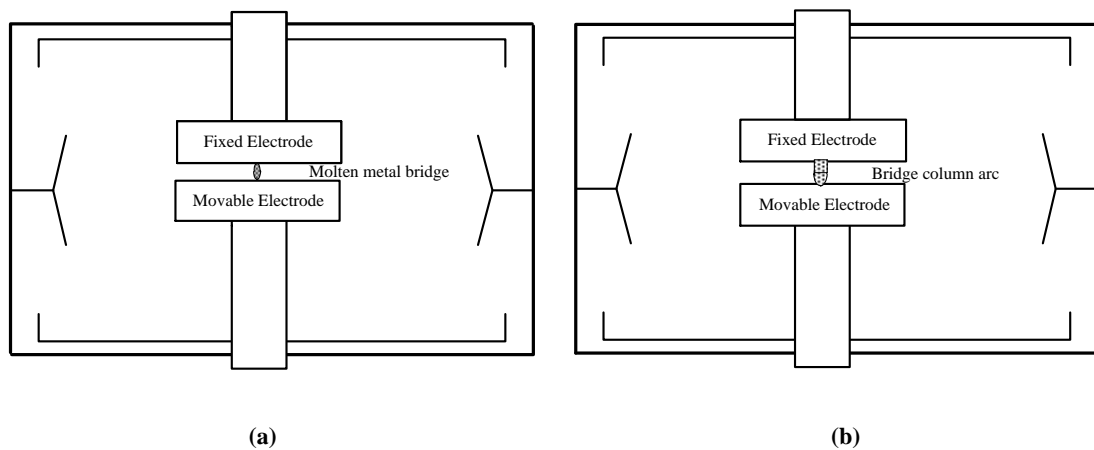
Figure B.2 Formation of the vacuum arc: (a) molten metal bridge; (b) bridge column arc.

However, as the electrodes continue to separate, maybe for a few hundred nanoseconds to a few microseconds, the molten metal bridge lengthens and finally ruptures due to physical reasons including surface tension effects, boiling of the highest temperature region, convective flows of the molten metal, and evaporation of the metal bridge's hot surface [4]. When the bridge ruptures, the area from the protrusion releases metal vapour, delivering metal particles into the electrode gap. Thus, a confined region of metal vapour exists in the gap between the electrodes, and this high vapour dense, high temperature and high pressure region is termed *the*

bridge column arc, as shown in Figure B.2 (b). This bridge column arc continues for up to a few hundred μs, depending on the interruption current level for a given pair of electrodes. At high densities/pressures, the ionisation state of the plasma increases sharply, since the coulomb interaction of the outer bound electrons of the neutral and ionised metal vapour with the surrounding charged particles gives rise to substantial energy level shifts and lowering of the electron binding energy [5]. The electrons that maintain current flow are not only released from the cathode, but also are produced by ion impact above the cathode (near the protrusions). Consequently, as the metal vapour region enlarges due to electrodes continued separation, a normal arc is formed, meaning current can flow between the electrodes.
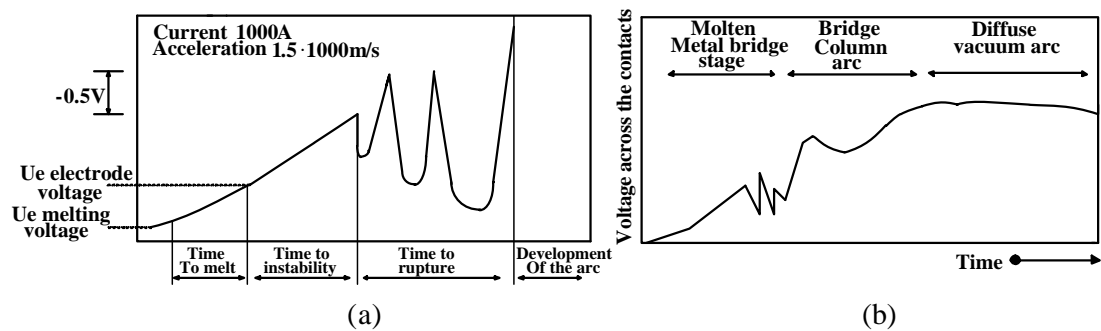
Figure B.3 Voltage drop across an opening electrodes showing [1]: (a) formation and rupture of the molten metal bridge; and (b) rupture of the molten metal bridge and the vacuum arc formation.

Figure B.3 (a) shows the voltage drop across an opening electrodes during the molten metal bridge transition from start to rupture. It is initially small, and slowly increases during the stable period of the molten metal bridge. Then voltage instability across the electrodes indicates rupture onset of the molten metal bridge. At bridge rupture, there is rapid voltage rise across the electrodes as shown in Figure B.2 (b), which is slightly higher than the expected minimum arcing voltage [6] and lasts for a tens of nanoseconds to microseconds depending on conduction current level and electrode material. Then the voltage decreases to the metal's minimum arcing voltage.
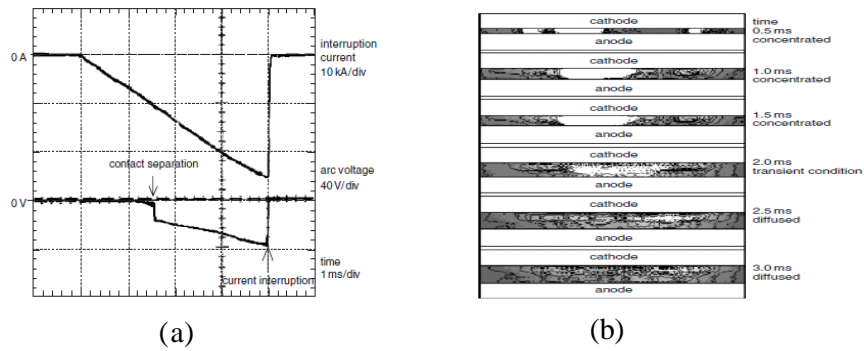
Figure B.4 (a) Interruption current and arc voltage; (b) arc appearance (interruption current 25kA) [2].

Niwa and Funahashi [2] observed experimentally arc behaviour of electrodes opening in a vacuum. Figure B.4 shows the arc behaviour of CuCr electrodes carrying 25kA. The molten metal bridge was observed immediately after electrode separation. Figure B.4 (a) shows that the electrodes are opened as current is increasing towards 10kA. At this moment, the voltage across the electrodes remains low for a few hundred μs and then sharply increases to approximately 18V as high-pressure, non-ideal plasma is formed. The voltage then reduces to 17V after a few hundred ns. Thus, the bridge column arc with a pressure of approximately one atmosphere is established to sustain current flow. It is concentrated and maintained around the ignited point (protrusions) for approximately 2ms before the transition to a diffuse arc under the axial magnetic field (AMF) applied.

Slade [6] stated that no matter the interruption in any media, such as air, SF6, oil, and vacuum, the bridge column is always the first stage of arcing between all opening electrodes, and the transition time from the bridge column to a diffuse arc is proportional to the interruption current, (e.g. 0.9ms for 6kA interruption current reduces to 0.1ms for 1kA for given electrodes). It appears that as electrodes continue to part, the volume of the column arc increases. Thus the bridge column arc is no longer sustainable, due to the metal vapour pressure decrease. It finally becomes a true 'vacuum arc'. However, if the current through the ever-parting electrodes is high enough, the high-pressure column arc will be maintained, independent of the gap distance.

B.2 **Diffuse vacuum arc**
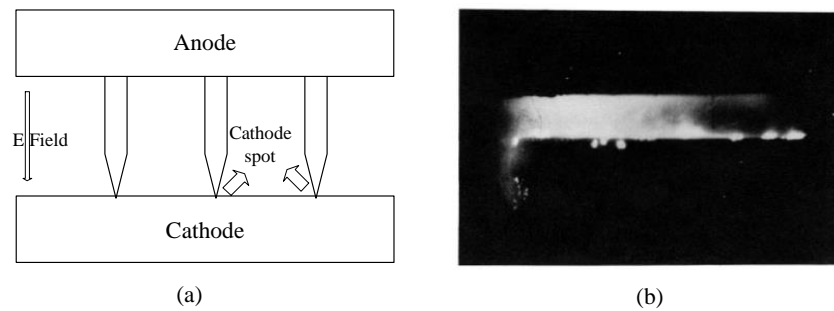
Figure B.5 Diffuse vacuum arc: (a) multiple cathode-spot arcs; and (b) a multiple cathode-spot arc (interruption current 8kA) [7].

If the interruption current is low enough, for a given electrode diameter, the bridge column arc will quickly transition to a diffuse arc. Figure B.5 describes the general appearance of the diffuse vacuum arc. The protrusions, that release electrons, positive-ions, and metal particles which permit circuit current flow, become a number of bright regions named *cathode spots*. They are in random motion over the cathode surface, and repel each other and even try to move down the edge of the electrode. The voltage across the electrodes reaches a stable small value due to the diffuse neutral plasma. The anode electrode plays a passive role, collecting electrons over its entire surface.

B.2.1 Cathode spots

The magnitude of the current flowing through opening electrodes determines the number of cathode spots, where experimental results shown in [8] illustrate that each copper spot can sustain the order of 100A. This means for a half-cycle of AC current, the number of spots increases as current reaches its peak and then decreases as the current approaches zero, when only one spot is left. It has been established that there is a mean diameter from 20μm to 100μm for each cathode spot after the arc is extinguished. The diameter provides a current density of the order of $10^{10} - 10^{11} \text{A/m}^2$ for a cathode spot sustaining 100A. These cathode spots have a finite lifetime; as one spot extinguishes, a new one is created by the splitting of an existing

spot or is formed directly on the cathode surface. Each cathode spot has a few sub-components or cells, in which the current density can reach high $1\text{-}10\times10^{12}\text{A/m}^2$. The speed of these sub-components is up to 60m/s over a short distance [9]. However, an individual cathode spot moves randomly over the electrode surface with a speed of about 1ms^{-1} [10]. Due to the speed difference between individual cathode spots and the subcomponent, the movement and reformation of cathode spots occurs, causing the release of more metal particles from the cathode electrode.

In a vacuum interrupter, as in Figure B.1 (a), the anode and cathode electrodes have the same dimensions, that is, have same shape and diameter. For such contact pairs, the cathode spots have been observed to move around the cathode surface, reach the edge, then extinguish. Then new cathode surface spots are created on the surface to maintain the current flow. However, current chopping could occur when there is a discontinuity in cathode spot reformation. To prevent most spots from moving to the cathode contact edge, the anode electrode has a smaller diameter than the cathode. experimental it has been established [11] that cathode spots repel each other, but continued to move along around a circle when they reach to edge, if the cathode electrode has a diameter appreciably larger than that of the anode. There is no reason to explain why the cathode spots move with a retrograde motion. However, Daalder [12] describes a picture of the contact surface after arcing that it is full of tracks, which contain overlapping craters over the whole cathode surface. Contacts surface erosion is typically uniform due to the retrograde motion of multiple cathode spots.

As mentioned in Section 2.2, there are two methods for pulling electrons out of a metal, one is thermionic emission, and the other is field emission, and both only occur when electrons gain enough energy to exceed the work function. Until 1961, Lee and Greenwood [13] proposed the active emission mechanism in a cathode spot of a vacuum arc by combining both methods, called T-F emission (T represents (thermal) temperature, F represents field). As a consequence, the behaviour of the cathode spot can be predicted by considering T-F emission and the physical property, thermal conductivity, evaporation constants, work function, etc. A good cathode spot model is not only consistent with all of what is observed, but also predicts what will happen if a parameter is changed.

Figure B.6 illustrates the cathode spot model. The cathode electrode is located on the left, opposite the anode, and plasma passes through the electrodes. The cross-hatched area represents the ionisation zone. The acceleration zone is located between metal surface and the ionisation zone where in practice, the two adjacent zones overlap. The area directly below the cathode spot is molten. Its temperature reaches a high value, determined by the metal material. As indicated previously, the crater after arcing has diameter of approximately 20µm. The distance from metal surface to the centre of the ionisation zone is represented by l_{MFP}, which represents the mean free path (MFP), which is very short due to local high pressure (many atmospheres). Thus, the ionisation zone is a very thin disk [14]. Consequently the electrons and vapour released from the incandescent surface will energetically interact to ionise the neutral materials in the ionisation zone. The ionisation zone has high local pressure as it is dense with particles, the concentration of which dominates the pressure. Figure B.7 illustrates the fluxes of the different species. Cathode spots with high temperature act as emission sites, injecting electrons, positive-ions and neutral vapour across the acceleration region to the ionisation region, where they mix together by interaction to sustain current flow. In the ionisation zone, it is generally assumed that all neutral metal atoms are completely ionised. Since the mass of electrons is significantly less than that of ions, the electron is considered as having higher mobility than an ion. This causes most of ions to remain in the ionisation region, which introduces a positive space charge.
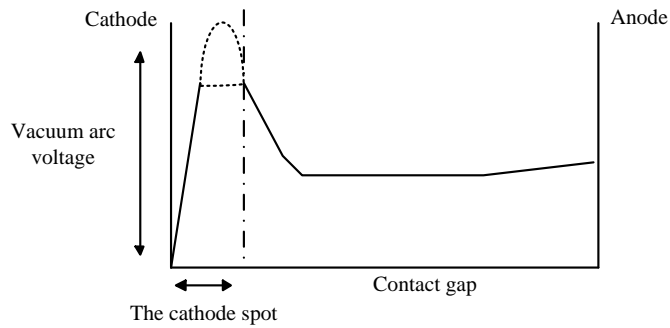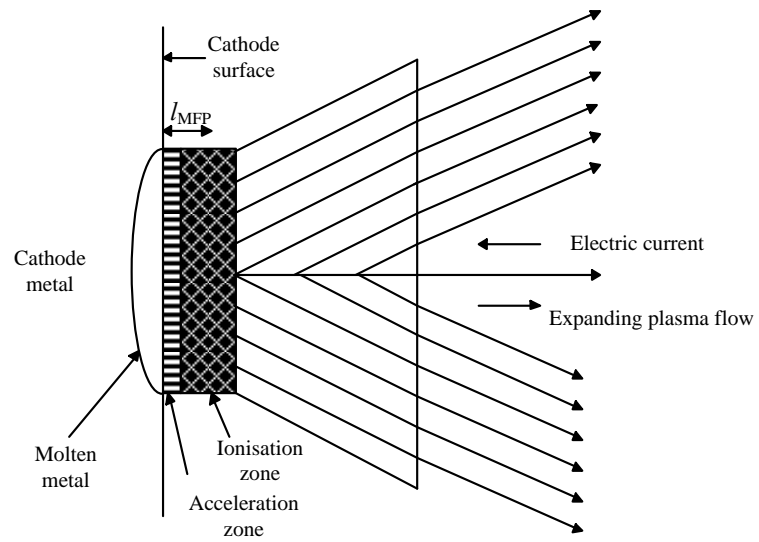
Figure B.6 Cathode cell geometry and arc voltage distribution.
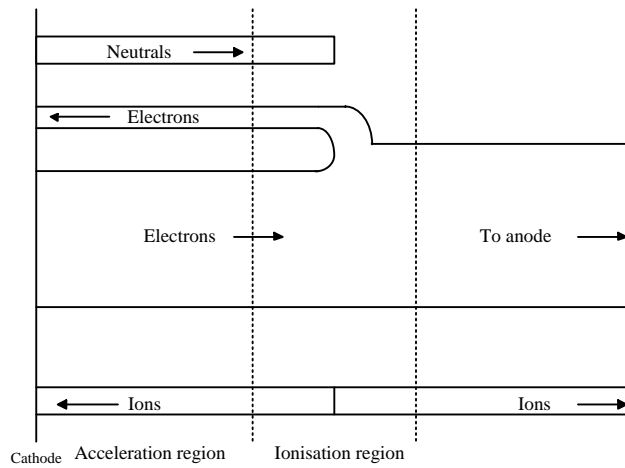
Figure B.7 Particle fluxes in cathode region of vacuum arc [15].

The positive space charge accelerates electrons escaping from the cathode, while the high-temperature in the cathode spots is maintained due to the bombardment of

positive metal ions accelerated by the positive space charge. Thus, the resulting high field and high temperature surface introduces T-F emission, indicated earlier, giving rise to vigorous electron emission from the cathode surface. Then the resulting plasma enters into an expanding zone with a cone shape from the ionisation region to the anode providing a barely luminous, neutral plasma diffuse low-pressure region, which is able to sustain current flow with a small voltage drop. Consequently, most of the voltage drop is concentrated across the cathode spot, as shown in Figure B.6.

In Figure B.7, the cathode spot model is divided into three parts, namely the cathode spot surface, the acceleration zone, and the ionisation zone. For conservation of energy, the energy balance in the cathode spot model is complex. Harris [16] stated that, at the cathode surface, energy flows owing to ion bombardment, electrons and atoms emission and the thermal conduction are considered in balance. A continuous check is used to monitor and calculate the emission of electrons, while the vapour pressure characteristic is utilised to calculate evaporation of atoms from the surface. In the acceleration zone, conservation is between charge and particle numbers and balance between forces and energies. The development of electric fields causes positive space charge, which approximately observes Poisson's equation. In the ionisation zone, charge and mass are conserved, and forces and energy are balanced. This region is electrically neutral, while its features are the net creation of charged particles and high temperature plasma due to ionisation.

If the quantity of electrons through the acceleration zone is assumed s_q, the ion current therefore is $(1 - s_q)I$. In the ionisation zone, the anode ion current has the same magnitude but opposite direction. To maintain current continuity, the electron current in the expanding region must be $(2 - s_q)I$. The current density is:

$$J = n \times e \times v \tag{B.2}$$

where n and v represent the concentration and velocity of the electrons or ions.

If assuming that ions are singly ionised and the plasma is essentially neutral $n_- = n_+$, then:

$$\frac{v_-}{v_+} = \frac{J_-}{J_+} = \frac{(2 - s_q)}{(1 - s_q)} \qquad \text{(B.3)}$$

B.2.2 Plasma between cathode spot and anode electrode

As described, once the vacuum arc is established, it is stable with the luminous plasma penetrating the inter-electrode region to sustain current flow. The cathode electrode acts as the source of electrons, positive-ions, neutral-vapour and micro-particles, meanwhile the adjacent anode electrode acts as a passive collector of electrons. Davis and Miller [17] stated that the voltage drop across the plasma, after the cathode spot, to anode electrode, could be ignored if the contact spacing is 1-2mm. This means the arc voltage is concentrated across the cathode spot, as shown in Figure B.6. In a diffuse vacuum arc, the voltage drop across vacuum electrodes can reach approximately 20 to 45V when the current passing through the electrodes is up to 3,150A for a contact spacing of 8-20mm.

Table B.1 Cathode spot erosion rates and arc voltage for metals used in vacuum interrupter [1].

Material	Erosion rate (μgC^{-1})	Arc voltage (V)
Ag	140,150	12.5
Cu	115,130	15.5
Cr	22-27,40	15.5
W	55,62,64	23.2

Since the cathode spots provide all the material in the vacuum arc to satisfy the needs of the external circuit, the cathode surface is eroded. Table B.1 tabulates the arc erosion (grams per coulomb) for some pure metals which are commonly utilised as vacuum interrupter contacts. Experiment results [18, 19] established that there are up to 80% metal particles in the bulk of erosion, which probably result from reformation of the cathode spots and their movement around the cathode surface. These metal particles have diameters that range from less than 1μm to a few tens of μm. Such particles within the inter-electrodes not only have a velocity ranging from 10 to

800m/s but also have a temperature greater than the melting point but less than the boiling point of the cathode material. The residual substance in the bulk of the erosion is metal vapour, which is ionised when it enters the ionisation zone. It is possible to evaporate the particles as they penetrate into the high-pressure plasma region immediately above the cathode spot. It has been shown that the evaporation rate of these particles having a high molten temperature, such as W, is faster than those with a low molten temperature, Cu [20].

Kimblin [21] has analysed the diffuse arc by performing experiments on the ion current flowing to the shield when biasing the shield potential. When interrupting a 275A arc current with an electrode distance of 35mm, the experimental results revealed the performance difference between 25mm and 50mm diameter electrodes. The final value of ion current is the same in both cases, but the rate of current rise for the 25mm electrodes is faster, i.e. the ion current initially increases linearly as the electrodes separate, then reaches a saturated value at spacing of approximately 15mm for the 25mm diameter electrodes and 30mm for the 50mm electrodes. A similar measurement of ion current with same electrode spacing revealed that the saturated ion current values increase from 8% of the total arc current at 100A to 20% at 3000A. There is ion current flow in the vacuum arc, and its maximum value depends on a given current, but it is independent of the shield wall diameter and the electrode diameter.

The previous sections illustrated that the diffuse arc is an expanding diameter cone shape plasma from the cathode spot, as electrode gap increases. When the cathode spots random motion reaches the edge, some plasma escapes from the gap and reaches the shield, such as Figure B.8 (a). The dashed line represents sequential plasma positions during separation. An increase in g (gap distance) results in more plasma escaping from within the inter-electrode and collected by the shield. This is why the ion current increases as electrodes separate.

(a)   (b)
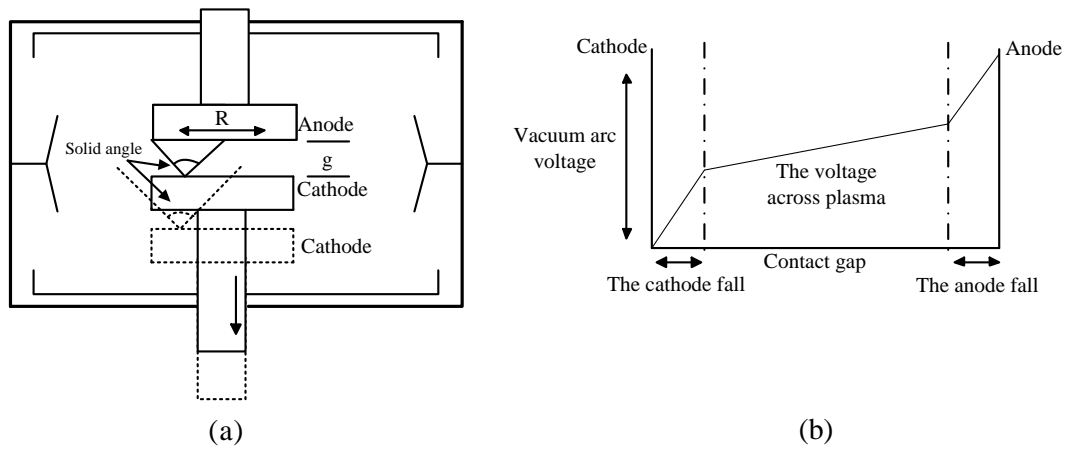
Figure B.8 Separating contacts with plasma plume and arc voltage.

The plasma fraction passing to the shield and what is collected by the anode are determined by the solid angle subtended at the anode, which is determined by the ratio g/R. The smaller the electrodes the smaller the solid angle for a given gap. The fraction of current $(1 - s)$, in equation (B.3), determines the ion current in the plasma, which saturates once it arrives at the shield, due to the negative bias. As Mitchell [22] found, in high currents and/or small anode diameter electrodes, vapour 'starvation' occurs when the plasma expands away from the cathode spot leading to a reduction in ions and electrons. Thus, to maintain the current flow, an anode potential fall occurs to attract sufficient electrons, such as shown in Figure B.8 (b). The energy of the electrons will be extremely high since they are firstly powered in the ionisation zone and then are accelerated through the anode field. Thus, the anode surface temperature increases with the arrival of these electrons. With this anode temperature rise, there will be an ever-increasing metal vapour above the anode; where the metal vapour is non-ionised until it reaches a threshold pressure. Thus, a visible plasma plume is observed. This description is the formation of an *anode spot*, which unlike cathode spots, does not move around the electrode surface. This gives rise to increased anode erosion, as well as the cathode surface. The occurrence of anode spot indicates the plasma transition from the diffuse to the constricted mode, where the arc voltage is reduced. The anode spot plays the same role as cathode spot in releasing metal vapour to sustain current flow. It also causes current concentration in the region where anode vapour ionisation develops, thus the arc voltage drops. The

200

arc voltage normally increases as the conducting current is increases before the anode spot formation. In summary, as an anode spot occurs, it not only results in erosion of both electrode surfaces during arcing, but also leaves a mass of metal vapour within the inter-electrodes after arcing. This vapour reduces the recovery strength of the post-arc. However Rich [23] established that the arc can remain in the diffuse mode, even for currents up to 72kA, provided the electrode diameter is appropriately large.

Figure B.9 The effect of the overlapping plasma plumes from the cathode spot as the current.

At higher current densities, there will be an increasing number of cathode spots appearing and spreading over the cathode surface, as shown in Figure B.9. As mentioned, a diffuse arc has a cone shape expanding from the cathode electrode to the anode. Cone can overlap before reaching the anode electrode if each spot has a high current density. If overlapping is just above the cathode spots as current density increases the local ionisation distribution of ions and electrons changes due to increased collisions. This change is dominated by the level of the arc current and the electrode diameters. Experimental results from Rusteberg [24] considered the transition from collision-less to collision plasma with an increase in arc current. Once the collision occurs, the plasma appears to be a well-defined column due to effect of the azimuthal magnetic field B_θ, which results from the circuit current passing through the electrodes, as shown in Figure B.9. Thus, a current density increase

causes an increase in the plasma resistivity, and also results in a vacuum arc voltage increase, as shown in Figure B.9 (b) [25].

B.2.3 Arc voltage

Unlike the gaseous arcs, the voltage of a vacuum arc presents an extremely low value, which generally is in the order of a few tens of volts. According to reference [17], with calcium electrodes interrupting 200A, the arc voltage is approximately 13V, and for refractory materials, molybdenum it is 26V. Other arc sustaining voltages for elements are shown in Table 2.1. The reason seems to be that when the arc is in the diffuse mode it is independent of arc length. As mentioned previously, the arc voltage is concentrated across the cathode spot, and between the cathode spot and the anode electrode it could be ignored if the contact spacing is 1-2mm.

As the current is increased, the vacuum arc voltage presents a positive resistance characteristic that slowly increases due to overlapping plasma plumes. This is contrary to the gaseous arc in which the arc voltage decreases as current increases. As the current increases further, a point is reached when anode spots are formed. When this occurs, the arc voltage drops.

B.2.4 Current chop

Initially there is a molten metal bridge which is formed at the last protrusion of contact. As the electrodes continued to part, a bridge column arc forms with high-pressure and high-temperature, its duration depending on the circuit current and contact dimensions after metal bridge rupture. Since the pressure around the bridge column reduces, the components from the ejected point of the bridge column no longer compensate the loss of metal vapour from the expanding column. The vacuum arc transitions into the diffuse mode. The characteristic of the plasma between the electrodes changes as the number of cathode spots increases, where the number of cathode spots is proportional to the current passing through the contacts.

In most AC current interruption situations, the current rarely reduces to zero smoothly. A few amperes before current reaches zero, the arc becomes unstable and

drops to zero abruptly and prematurely, producing an extremely high *di/dt*. This event is termed the *current chop* and the phenomenon is termed *current chopping*.

Current chopping is observed in any arc medium [26], such as air and oil. It appears that the current passing through the contact drops to zero in a short time due to a lack of conducting components, such as electrons and ions. In a vacuum, the number of cathode spots decreases as current reduces, where when a cathode spot disappears the corresponding energy transmission is broken and the temperature around cathode spot quickly drops to that of the surrounding contact metal, due to the short thermal time constant (in the order of microseconds). Therefore, the extinguished cathode spot no longer takes part in the vacuum arc process. As current reduces further to a certain level which depends on the electrodes material, only one cathode spot remains. To keep the cathode spot stable, the area below it must have a high temperature to delivering enough electrons and metal vapour to produce positive ions in the ionisation zone. Then the ionisation zone will send ions back to bombardment the cathode surface to maintain the high temperature. Thus, the unstable diffuse arc arises from the occurrence of ion starvation [27]. The decrease of electrons and metal evaporation results in the decrease of ions, provided the current passing through the electrodes decreases below a certain value.

The current chopping *di/dt* creates over-voltage, *v=Ldi/dt*, across the contacts that could damage these breakers. Figure B.10 illustrates the experimental results for current chopping and the vacuum arc voltage, as the current decreases to near zero.
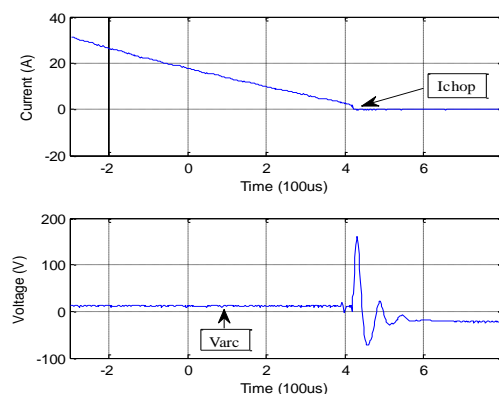
Figure B.10 Experimental voltage and current traces showing current chopping and overshoot voltage for copper contacts, 50A peak current.

When current chopping occurs, the vacuum arc voltage overshoot quickly reaches 160V beyond the normal arc voltage of 12V. The overshoot voltage is independent of the DC supply. The amount of magnetic energy in the circuit dominates the overshoot voltage. Consider a transformer circuit. Since the characteristic of an inductor is to maintain continuous current flow, the energy stored in the leakage and magnetising inductance of a transformer must be transferred to the transformer stray capacitance, thus the overshooting voltage is:

$$\frac{1}{2} \times C \times V^2 = \frac{1}{2} \times L_M \times I_0^2 \tag{B.4}$$

or

$$V = I_0 \times \sqrt{\frac{L_m}{C}} \tag{B.5}$$

For example, consider a 1000kVA, 27.6kV transformer where the magnetising is current 2A. Thus, at 50Hz

$$L_M = \frac{V}{\omega \times I_m} = \frac{27600}{\sqrt{3} \times 314 \times 2} \approx 25\text{H} \tag{B.6}$$

The type of winding and insulation of the transformer dominates the effective capacitance. Assume 6nF, then

$$Z_0 = \left(\frac{L_m}{C}\right)^{1/2} = \left(\frac{25}{6 \times 10^{-9}}\right)^{1/2} \approx 64.5(\text{k}\Omega) \tag{B.7}$$

For a 1A chopping current, the over-voltage is 64.5kV.

The chopping current average value decreases as the vapour pressure of the metal increases [1], (see Table B.2). Reference [4] indicated that current chopping not only occurs with low current but also appears at high power ratings when the vacuum arc is still diffused. Normally, refractory metals are used as vacuum interrupter electrode material for high power ratings. However, experiment results [28] illustrate refractory metals have more unstable arcs than other metals and tend to chop due to their low vapour pressure. This is normally resolved by combining a refractory metal with a higher vapour pressure metal. A cathode spot is not a fixed, unmovable structure, with a variable lifetime depending on electrode material. A new spot

appears to replace an old one on the rim of any crater left by previous spots. Thus, ions starvation in the diffuse arc is not the only reason to produce the chopping phenomenon. Another reason is unsuccessful continuation of repetitive cathode spot formation. In general, there are two solutions to keep the diffuse arc stable from current chopping. First, the electrode surface has a high density of field-enhancing protrusions. Second, an axial magnetic field (AMF) is utilised in the vacuum interrupter [29].

Table B.2 Chopping current for some pure metals [1]

Metal	Average chop current (A)	Maximum chop current (A)
Ag	3.5	6.5
Cu	15	25
Cr	7	16
Ni	7.5	14
W	16	350

B.3 Columnar and transition vacuum arc

The bridge column arc occurs with one atmosphere pressure after molten metal bridge rupture, in air, oil or a vacuum. Normally, as electrodes part, the bridge column arc transitions into a diffuse arc. However, if the current through the electrodes is high enough, there can be enough power to keep the arc root region excited thereby compensating for the loss produced by the slow expansion of the bridge column arc. There is still high pressure in the inter-electrode plasma, which will result in direct transition into a high-pressure columnar arc, called a *constricted arc*, as shown in Figure B.11.
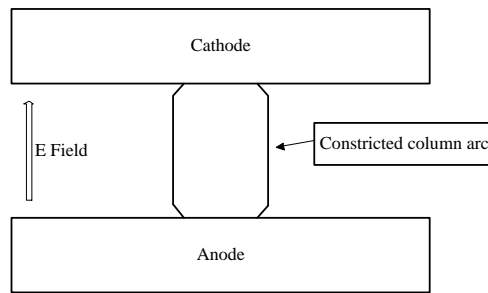
Figure B.11 The constricted column vacuum arc.

Normally a constricted column arc is accompanied by an anode spot, which tends to focus on an anode electrode region, not moving around either electrode surface. This results in considerable erosion of the contact. The arc voltage becomes less as the current passing through the contacts concentrates in the region where ionisation of the anode vapour develops. Mitchell [30] pointed out that the erosion is only observed in the cathode surface if the current through the arc is below 10kA. However, as current increases, the constricted column arc forms. The erosion rate becomes greater than before and appears with a similar rate on both electrode surfaces. As a consequence, some means should be utilised to keep the arc in a diffuse mode.

Heberlein and Gorman [31] described the constricted arc's development as vacuum contact separates with current flowing. The arcs described are illustrated in Figure B.12.
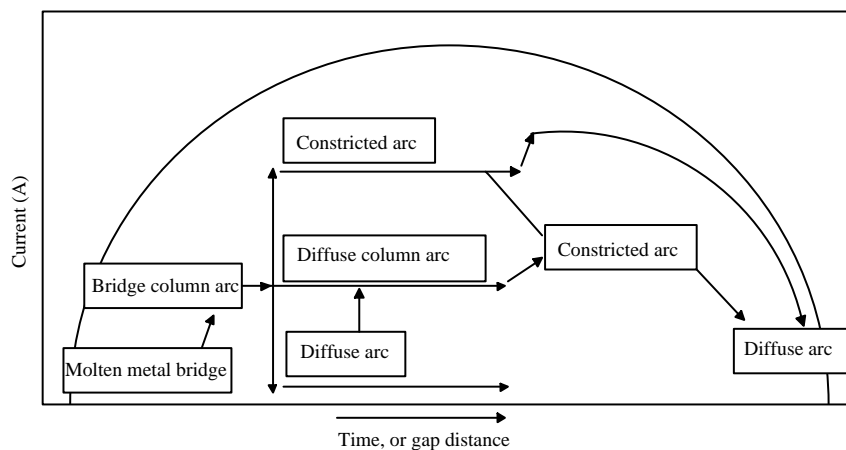
Figure B.12 Appearance of the high-current columnar vacuum arc; note gap distance is time dependent.

206

1. The molten metal bridge: as described in Section B.1. For interruption in any medium, it is the first stage of the arc and occurs between the electrodes as the contacts separate. During this stage, the voltage across the contact is small, lasting for a short period.

2. The bridge column arc: arises with high-pressure as the molten metal bridge breaks. In a few tens of nanoseconds, after the molten metal bridge rupture, the voltage across the contacts increases to the voltage greater than the expected arcing voltage. The voltage falls back to the metal's minimum arc voltage for a duration dependant on the electrode material and circuit current. For a low current level (depending on the circuit current being to proportional electrode diameter), the bridge column arc gradually reduces in diameter until a diffuse arc occurs. For a high current level (where the power into the contact surfaces at the arc roots accommodates the slow expansion of the bridge column arc and material being lost to the surrounding vacuum is compensated), the bridge column arc can directly transfer into a high-pressure columnar arc, such as diffuse columnar arc or a constricted arc, without a diffuse arc stage.

3. The diffuse arc: as introduced in Section B.2. It occurs with bright cathode spots that maintain constant motion over the cathode electrode with variable lifetime and appear to repel each other resulting in some surface erosion. With copper electrodes, each spot can sustain approximately 100A. Since the plasma from the cathode spot to the anode is neutral, the voltage across the interrupter is focused on the cathode spot. As the current increases further, it will reach the diffuse column arc stage associated with an ever-increasing number of cathode spots.

4. The diffuse column arc: as in Figure B.9 (b). When it occurs, the arc is still in diffuse mode. But the inter-electrode plasma was overlapping regions, where this plasma characteristic is different from previous single plasma. It becomes more ionised with a glowing appearance due to an increase in ion collisions and an increase in resistivity. Thus, as the conducting current increase, the vacuum arc voltage increases until an anode spot forms, which results in a constricted arc.

5. The constricted arc: as the current increases further, the diffuse column arc suddenly focuses to a small area on both electrodes, with less movement than in the diffuse mode - thus it is referred to as constricted mode. The metal ions from the anode to the cathode are deflected inwards owing to the pinch effect. Since all cathode spots are grouped together, the plasma through the arc becomes most bright. However, at this time, the arc voltage becomes less than in the diffuse mode. Erosion occurs in both electrodes, at a higher rate than before.

In summary, based on the conducting current level and the diameter of the electrode, there are three plasma arc states, including diffuse arc, diffuse column arc, and the constricted arc after bridge column arc rupture. The constricted arc becomes weak as the current falls. When the current reduces to a certain level, the anode spots disappear as cathode spots appear.

B.4 The diffuse arc in a magnetic field

There are two magnetic fields that effect vacuum arcs, namely transverse and axial magnetic fields, as shown in Figure B.13.

(a)
B_T: Transverse magnetic fields

(b)
B_A: Axial magnetic fields
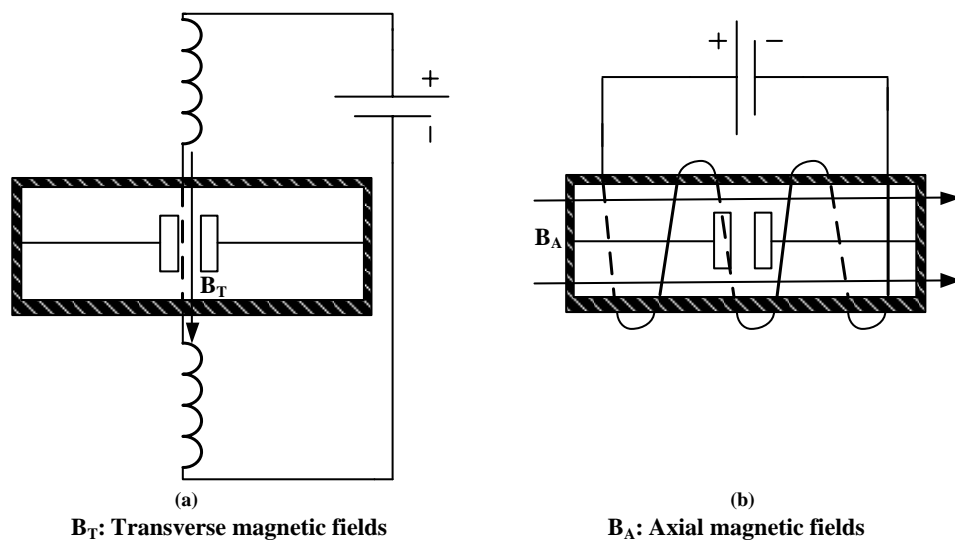
Figure B.13 Configurations for producing transverse magnetic fields and axial magnetic fields.

B.4.1 Interaction of the diffuse arc and a transverse magnetic field

The transverse magnetic field (TMF), as its name implies, is when the magnetic field is applied across the contacts perpendicular to the principal plasma direction.

When a TFM is applied on a diffuse arc, the cathode spots are still in retrograde motion, repelling each other while moving over the cathode surface. The force produced by the background pressure for retrograde motion is greater than the ampere force [32]. Meanwhile the expanding plasma above the cathode spot through the electrodes is barely luminous as the neutral plasma sustains current to flow from the anode to the cathode, where the ions in the neutral plasma experience an ampere force produced by the TFM. Thus, Emtage and Kimblin [33] illustrated that most of the current is restricted to a thin shell on the retrograde side of the plasma as shown in Figure B.14. A gap between the neutral plasma and the anode electrode is formed as the ions within the boundary move in a direction parallel to the anode surface. To keep the circuit current flow from the anode, the electrons will expend more power to pass through the gap. Thus, the voltage across the contact gap will increase to a voltage of several kV, possibly above the DC supply to attain zero current. The high voltage VCB built by Gorman and Kimblin [34] interrupted currents up to 15kA for circuit voltages up to 80kV.
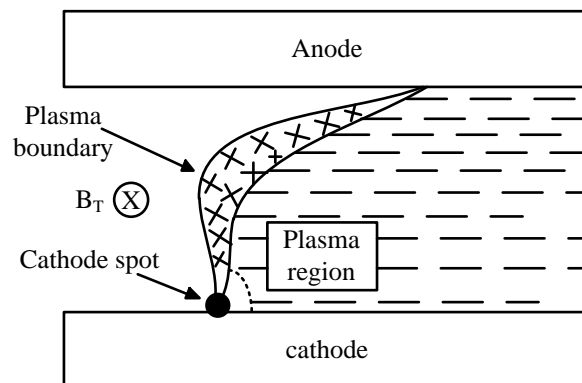
Figure B.14 A sketch of the calculated plasma structure [2.39].

Normally, once arc current increases beyond the point where the arc transitions from diffused to constricted, the constricted arc is almost motionless, damaging both

electrodes due to a high erosion rate. References [35-37] illustrate that the erosion rate is decreased if a TMF is applied, because the constricted arc is influenced by the normal orientated ampere force that maintains movement around the inter-electrodes. The arc does not move immediately in the TMF, when it transitions into a constricted arc [38, 39]. It dwells at the location where the arc originally appeared. Once the arc starts to move, an opposing force produced by the arc roots at both electrodes will be applied on the constricted arc. Thus, the arc roots cannot move momentarily and its speed is limited. In a vacuum, the formation of drag forces arises from momentum lost by neutral atoms flying away from the arc column as it moves, while there is reluctance of the arc roots to move to new locations. As a consequence, it is difficult for arc to reach its maximum velocity, except when the drag force and the TMF driving force balance.

B.4.2 Interaction of the diffuse arc and an axial magnetic field

An axial magnetic field (AMF) is generated such that it passes through the electrodes from the cathode to the anode, i.e. in a direction that is opposite to that of the arc current which flows from anode to cathode.

The application of an AMF [40] is shown in Figure B.15. The overlapping plasmas above each cathode spot introduce an increase in the plasma density, an increase in probability of collision, and an increase in the plasma's resistivity. Consequently the arc voltage increases as current through inter-electrode increases until a constricted arc forms. However, as soon as the AMF is applied, the electrons ejected from the cathode spot into the inter-contact gap move around a helix along the magnetic flux lines due to interaction of the AMF and the electron characteristics involving their charge, velocity and mass. The electrons diameter of encirclement enlarges as the electrons move toward the anode. Once the electrons are localised, there is a high electric field that forces the ions escaping from the cathode spot to stay with the electrons. The ion current travelling to a surrounding shield of the interrupter reduces by 60% as the AMF increases to 80mT [41].
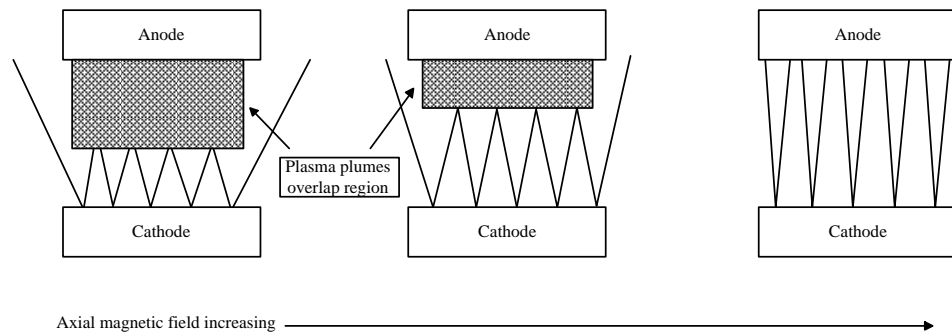
Figure B.15 Diagrams showing the effect of an increasing AMF in reducing the overlap region of the plasma plumes above the cathode spots.

As the AMF increases, the electrons move to the anode in a more direct path. Thus, the plasma plume overlapping reduces near the anode electrode, creating less movement. The arc voltage gradually decreases as the AMF increases. Rondeel and Anders [42, 43] found a slight increase in erosion rate of the cathode surface when the AMF is employed. The cathode spots become less mobile owing to the increasing AMF. As the AMF continues to increase, the plasma plumes become more columnar and finally separate as more electrons move helically along the magnetic flux lines. Each independent plume causes an increase in plasma density and energy loss due to collisions between the ever-increasing confinements of the plasma components. Thus, the arc voltage increases as the AMF increases. As the AMF increases further, erosion is observed at both electrodes due to the confined arc roots. Klimblin and Voshall [44], established that, with an AMF increasing from zero to a high value, the arc voltage first decreases to a minimum and then increases. In summary, enlargement of the electrode surface is not the only method that can be used to maintain the arc in a diffuse mode: application of an AMF can introduce the same results where current levels are higher.

References

[1]   P. G. Slade, "The Vacuum Interrupter: Theory, Design, and Application," *CRC Press and Taylor & Francis Group,* pp. 130-170, 2008.

[2]   Y. Niwa, T. Funahashi, K. Yokokura, J. Matsuzaki, M. Homma and E. Kaneko, "Basic investigation of a high-speed vacuum circuit breaker and its vacuum arc characteristics," *Generation, Transmission and Distribution, IEE Proceedings,* vol. 153, pp. 11-15, 12 Jan. 2006.

[3]   P. Slade, and M. Nahemow, "Initial separation of electrical contacts carrying high currents," *Journal of Applied Physics,* vol. 49, pp. 3290-3297, 1971.

[4]   F. Llewellyn-Jones, "The Physics of Electrical Contacts," *Clarendon Press, Oxford,* 1957.

[5]   A. Anders, "Ion charge distributions of vacuum arc plasmas: the origin of the species," *Physical Review,* vol. 55, pp. 969-981, January 1997.

[6]   P. Slade, "The consequences of arcing, in Electrical Contacts: Principles and Applications," *Marcell Dekker, Inc. New York,* pp. 463-509, 1999.

[7]   P. Malkin, "The vacuum arc and vacuum interruption," *Phys. D,* pp. 1005-1019, Appl. 1989.

[8]   J. E. Daalder, "Diameter and current density of single and multiple cathode discharges in vacuum," *IEEE Trans.,* vol. PAS-93, pp. 1747-1757, 1974.

[9]   J. Daalder, "Erosion structures on cathodes arced in vacuum," *Journal of Physics D: Applied Physics,* vol. 12, pp. 1769–1779, 1979.

[10]   J. Daalder, "Random walk of cathode arc spots in vacuum," *Journal of Physics D: Applied Physics,* vol. 16, pp. 17-27, 1983.

[11]   J. Heberlein, and D. Porto, "The interaction of vacuum arc ion currents and axial magnetic fields," *IEEE Transactions on Plasma Science,* vol. PS-11, pp. 152-159, 1983.

[12]   J. Daalder, "Cathode spots and vacuum arcs," *Physical Review,* vol. 104C, pp. 91-106, 1981.

[13]   T. H. Lee, and A.N. Greenwood, "Theory for the cathode mechanism in metal vapor arcs," *J. Appl. Phys.,* vol. 32, pp. 916-923, 1961.

[14]   J. D. Cobine, "Gaseous conductors," *McGraw-Hill,* p. 20, 1941.

[15]   James M. Lafferty, "Vacuum arcs - theory and application," *wiley,* p. 255, 1980.

[16]   L. P. HARRIS, "A mathematical model of cathode spot operation," *Proceedings of 8th international symposium on Discharges and electrical instalation in vacuum, Albuquerque, NM, USA* 1978.

[17]   Davis, D. William, and H.C. Miller, "Analysis of the electode products emitted by DC arcs in a vacuum ambient," *J. Appl. Phys.,* vol. 40, pp. 2212-2221, 1969.

[18]   G. Mesyats, "Cathode Phenomena in a Vacuum Discharge," *Nauka, Moscow,* 2000.

[19]   P. Slade, W.P. Lee, L. Loud, and R. Haskins, "The unusual electrical erosion of high tungsten content, W-Cu contacts switching load current in vacuum," *IEEE Transactions on CMPT,* vol. 24, pp. 320-330, September 2001.

[20]   A. Kozyrev, and A. Shishkov, "Movement, heating and evaporation of droplets in near cathode region of vacuum arc," *IEEE Cat. No. 04CH37565,* pp. 229–232, 09/10 2004.

[21]   C. W. KIMBLIN, "Vacuum arc ion currents and electrode phenomena," *Proceedings of the IEEE,* vol. 59, pp. 546–555, April 1971.

[22]   G. R. Mitchell, "High-current vacuum arcs part 2 - theoretical outline," *Proc. IEE,* vol. 117, pp. 2327-2332, 1970.

[23]   J. A. Rich, "A means for raising the current for anode spot formation in metal vapor arcs," *Proc. IEEE,* vol. 59, pp. 539-545, 1971.

[24]   C. Rusteberg, M. Lindmayer, B. Juttner, and H. Pursch, "On the ion energy distribution of high current arcs in vacuum," *IEEE Transactions on Plasma Science,* vol. 23, pp. 909-914, December 1995.

[25]   G.R. Mitchell, "High-current vacuum arcs, part 1 - an experimental study," *Proc. IEE,* vol. 117, pp. 2315-2326, 1970.

[26]   I. Paulus, R. Holmes, and H. Edels, "Vacuum arc response to current transients," *Journal of Physics D: Applied Physics,* vol. 16, pp. 17-27, 1983.

[27]   R. Smeets, "The origin of current chopping in vacuum arcs," *IEEE Transactions on Plasma Science,* vol. 17, pp. 303-310, April 1989.

[28] G. A. Farrall, "Recovery of dielectric strength after current interruption in vacuum," *IEEE Transacitons on Plasma Science,* vol. PS-6, pp. 360-369, Decenmber 1978.

[29] E. Hantzsche, "Mysteries of the arc cathode spot: a retrospective glance," *IEEE Transactions on Plasma Science,* vol. 31, pp. 799-808, October 2003.

[30] G.R. Mitchell, "High current vacuum arcs: Part I and Part II," *Proceedings of the IEE,* vol. 117, pp. 2315-2332, 1970.

[31] J. Heberlein, and J. Gorman, "The high current metal vapor arc column between separating electrodes," *IEEE Transactions on Plasma Science,* vol. PS-8, pp. 283-289, December 1980.

[32] C. G. Gallagher, "The retrograde motion of the arc cathode spot," *J. Appl. Phys.,* vol. 21, p. 768, 1950.

[33] P. Emtage, C. Kimblin, J. Gorman, F. Holmes, J. Heberlein, R. Voshall, and P. Slade, "Interaction between vacuum arcs and transverse magnetic fields with application to current limitation," *IEEE Transactions on Plasma Science,* vol. PS-8, pp. 314-319, December 1980.

[34] J. Gorman, C. Kimblin, R. Voshall, R. Wein, and P. Slade, "The interaction of vacuum arcs with magnetic fields and applications," *IEEE Transactions on Power Apparatus and Systems,* vol. PAS-102, pp. 257-266, February 1983.

[35] R. Michal, "Theoretical and experimental determination of the self-field of an arc," *Proceedings of the 26th Holm Conference on Electrical Contacts (Chicago, IL),* pp. 265-270, September 1980.

[36] A. Lee, Y. Chien, P. Koren, and P. Slade, "High current arc movement in a narrow insulating channel," *IEEE Transactions on CHMT,* vol. CHMT 5, pp. 51-55, March 1982.

[37] R. Boxman, "High current vacuum arc column motion on rail electrodes," *Journal of Applied Physics,* vol. 48, pp. 1885-1889, May 1977.

[38] P. Slade, "Electrical Contacts: Principles and Applications," *Marcell Dekker, Inc. New York,* pp. chap. 12, p.630, 1999.

[39] J. Teichmann, M. Romheld, and W. Hartman, "Magnetically driven high current switching arcs in vacuum and low pressure gas," *Transactions on IEEE Plasma Science,* vol. 27, pp. 1021-1025, August 1999.

[40] C.W. Kimblin, and R.E. Voshall, "Interruption ability of vacuum interrupters subjected to axial magnetic fields," *Electrical Engineers, Proceedings of the Institution of,* vol. 119, pp. 1754-1758, 1972.

[41] J. Heberlein, and D. Porto, "The interaction of vacuum arc ion currents and axial magnetic fields," *IEEE Transactions on Plasma Science,* vol. PS-11, pp. 152-159, September 1983.

[42] W. Rondeel, "The vacuum arc in an axial magnetic field," *Journal of Physics D: Applied Physics,* vol. 8, pp. 934-942, 1975.

[43] S. Anders, A. Anders, K.M. Yu, X.Y. Yao, and Ian G. Browne, "On the macroparticle flux from vacuum arc cathode spots," *Transactions on IEEE Plasma Science,* vol. 21, pp. 440-446, October 1993.

[44] C. Kimblin, and R. Voshall, "Interruption ability of vacuum interrupters subjected to axial magnetic fields," *Proceedings of the IEE,* vol. 119, pp. 1754-1758, December 1972.

Appendix C

List of figures and tables

C.1 List of figures

217

C.2 List of tables